Cell Sorting in Pillar Arrays based on Electrokinetics and Morphology

BAO DANG HO
FACULTY OF ENGINEERING | LUND UNIVERSITY

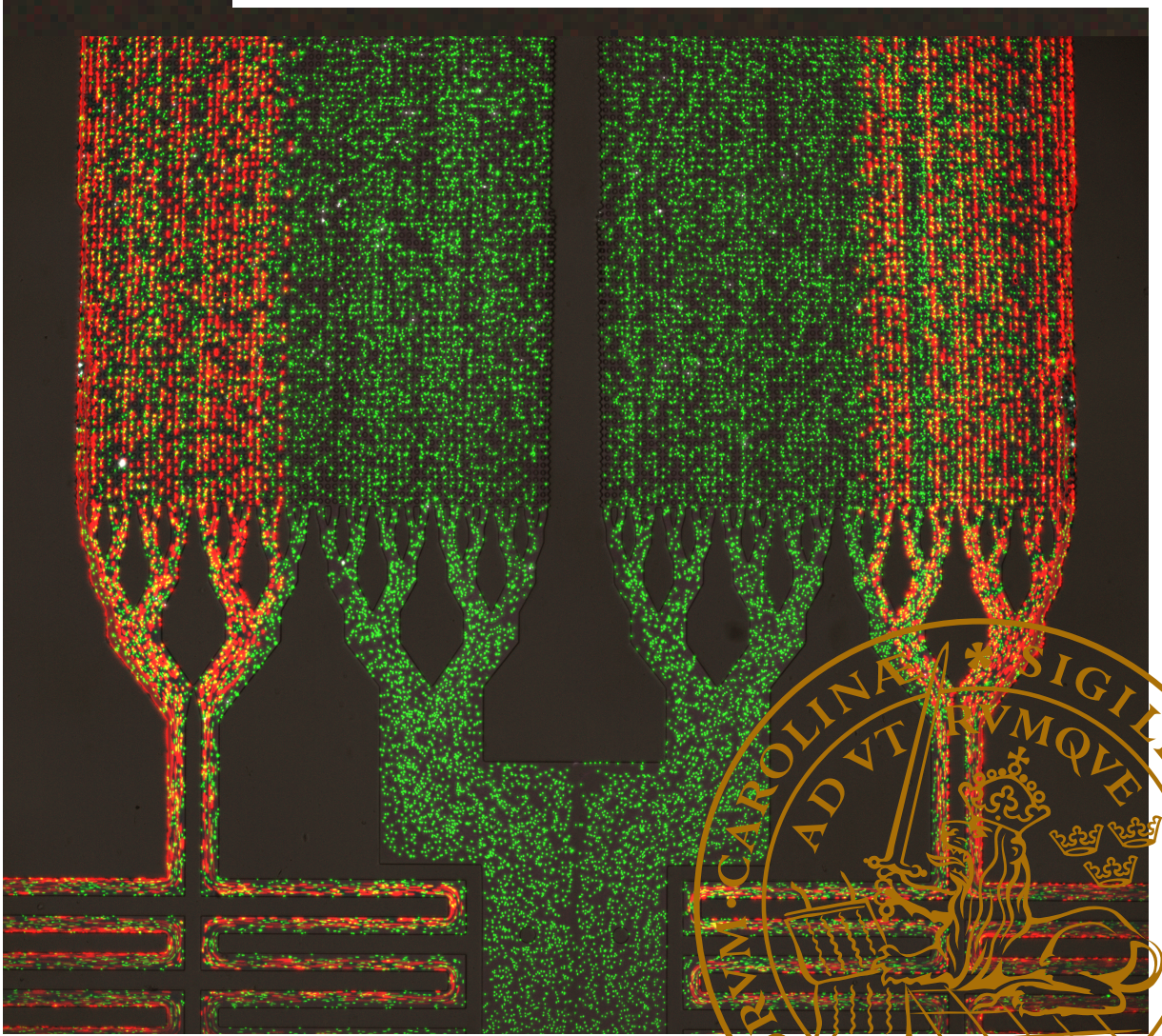

Cell Sorting in Pillar Arrays based on Electrokinetics and Morphology

Bao Dang Ho

LUND
UNIVERSITY

DOCTORAL DISSERTATION

by due permission of the Faculty of Engineering, Lund University, Sweden.
To be defended at Rydbergssalen, Sölvegatan 14,
on Friday 23rd of November 2018 at 9:15.

Faculty opponent:
Prof. Michael Hughes
University of Surrey, Guildford, Surrey, UK

Organization	Document name
LUND UNIVERSITY Department of Physics Professorsgatan 1 223 63 Lund Sweden	**DOCTORAL DISSERTATION** Date of disputation 2018-11-23 Sponsoring organization
Author(s) Bao Dang Ho	

Title and subtitle

Cell Sorting in Pillar Arrays based on Electrokinetics and Morphology

Abstract

Deterministic Lateral Displacement (DLD) is a method capable of sorting cells based on size where mechanical interactions between a sufficiently large particle and obstacles in a microfludic *pillar array* force the particle to follow a different trajectory than their smaller counterparts, resulting in continuous lateral separation. To extend the capability of DLD, electrical interaction between particles and pillars can be employed to complement the mechanical interaction, making electrical/dielectric properties additional parameters for sorting. Another idea is to exploit the morphologies of cells and as a concequence, their dynamical properties, to sort them in DLD. The development of DLD cell sorting methods based on those two ideas has brought forth five papers appended to this thesis: paper I, III, and V (combination of electrokinetics and DLD), and paper II and IV (exploiting morphology in sorting by DLD).

In the first topic, differences in electric properties or dielectric properties of particles and cells are employed to extend the capability of DLD. In Paper I, an AC electric field was applied across DLD devices having insulating pillars to sort similar-sized polystyrene particles having different surface charge, viable from non-viable yeast cells, and viable from non-viable *E. coli* bacteria. In Paper III, the same method was utilised on open channel DLD devices, showing unaltered effectiveness but offering the ability to flexibly change the distance between the electrodes. Also in the topic of combining electrokinetics and DLD, Paper V introduced a new type of DLD device where the electrodes were defined locally on every pillar, making it easier to generate a high electric field strength.

Besides electrical properties, morphology is another useful accompaniment to DLD. In Paper II, pathogenic *Streptococcus pneumoniae* bacteria were fractionated in DLD devices according to the difference in their morphology, viz. their chain length. It was also demonstrated, in paper IV, that an AC field can be used to rotate non-spherical red blood cells and in turn, change their trajectory in a DLD device. This implies an opportunity to sort red blood cells from cells having different morphology, either spherical cells or parasites like trypanosomes.

Key words

Label-free separation, Deterministic Lateral Displacement, Electrokinetics

Classification system and/or index terms (if any)

Supplementary bibliographical information	Language
	English
ISSN and key title	ISBN
	978-91-7753-888-2 (print) 978-91-7753-889-9 (pdf)
Recipient's notes	Number of pages: 199 / Price
	Security classification

Cell Sorting in Pillar Arrays based on Electrokinetics and Morphology

Bao Dang Ho

LUND
UNIVERSITY

Cover illustration front: Purification of 1.1 μm polystyrene microspheres from a mixture of 1.1 μm and 2.1 μm polystyrene microspheres. The device has 32 units like this in parallel and is intended for purifying *S. pneumoniae* single cocci from chains at high throughput.

Cover illustration back: DLD obsession. After four years working on DLD, you will see it everywhere.

Funding information: The thesis work was financially supported by grants from the European Union, under the Seventh Framework Programme FP7/2007-2013/ within the project LAPASO (project number 607 350) and under Horizon2020/HEALTH within the project BeyondSeq (project number 634 890).

Faculty of Engineering, Department of Physics

ISBN: 978-91-7753-888-2 (print)
ISBN: 978-91-7753-889-9 (pdf)

Printed in Sweden by Media-Tryck, Lund University, Lund 2018

Media-Tryck is an environmentally certified and ISO 14001 certified provider of printed material. Read more about our environmental work at www.mediatryck.lu.se

To my parents and my sister

Contents

Abstract

Deterministic Lateral Displacement (DLD) is a method capable of sorting cells based on size where mechanical interactions between a sufficiently large particle and obstacles in a microfludic *pillar array* force the particle to follow a different trajectory than their smaller counterparts, resulting in continuous lateral separation. To extend the capability of DLD, electrical interaction between particles and pillars can be employed to complement the mechanical interaction, making electrical/dielectric properties additional parameters for sorting. Another idea is to exploit the morphologies of cells and as a concequence, their dynamical properties, to sort them in DLD. The development of DLD cell sorting methods based on those two ideas has brought forth five papers appended to this thesis: paper I, III, and V (combination of electrokinetics and DLD), and paper II and IV (exploiting morphology in sorting by DLD).

In the first topic, differences in electric properties or dielectric properties of particles and cells are employed to extend the capability of DLD. In Paper I, an AC electric field was applied across DLD devices having insulating pillars to sort similar-sized polystyrene particles having different surface charge, viable from non-viable yeast cells, and viable from non-viable *E. coli* bacteria. In Paper III, the same method was utilised on open channel DLD devices, showing unaltered effectiveness but offering the ability to flexibly change the distance between the electrodes. Also in the topic of combining electrokinetics and DLD, Paper V introduced a new type of DLD device where the electrodes were defined locally on every pillar, making it easier to generate a high electric field strength.

Besides electrical properties, morphology is another useful accompaniment to DLD. In Paper II, pathogenic *Streptococcus pneumoniae* bacteria were fractionated in DLD devices according to the difference in their morphology, viz. their chain length. It was also demonstrated, in paper IV, that an AC field can be used to rotate non-spherical red blood cells and in turn, change their trajectory in a DLD device. This implies an opportunity to sort red blood cells from cells having different morphology, either spherical cells or parasites like trypanosomes.

Popular Summary in English

Most of the visible objects and tools around us are made from solid materials, which have definite shape and high strength to withstand external forces from the surrounding environment. Fluids, on the other hand, are highly deformable and change shape easily under an applied force, making it difficult to control or manipulate them. Nevertheless, there are areas of science and technology where fluids can be constrained, controlled, and made use of to bring out useful applications for human life. Microfludics is one such field.

Microfluidics refers to the study of liquids and gases at the micrometric scale – the scale of things that are smaller than the resolution limit of a human's eyes, the world of tiny bio-particles like bacteria, parasites or red blood cells. There are several good reasons for studying and engineering tools at such a minute scale. Firstly and straightforwardly, in order to deal with cells and pathogens, we need to shrink our tools and devices down to their size. Secondly, making tiny devices also means more economical use of rare samples from patients or expensive reagents required for analysis, making diagnosis more affordable and less painful. Last but not least, we might integrate many tiny tools and devices into a small handheld chip which can perform a complete diagnostic task, a lab-on-a-chip, and distribute them to the patients' home where they perform their own diagnostic procedures. This is similar to the development where centralised building-sized computers became individual handheld smartphones, with equal importance to the well-being in our society.

In the theme of microfludics for bio-medical applications, this work focuses on separating different kinds of cells by their physical properties, with the goal of making biomedical tools that are simpler, cheaper and more accessible to everyday life. The three properties of interest in this work are size, electrical/dielectric properties, and morphology of the cells that need sorting. Thanks to the disposability of the material, the simplicity of the mechanism (no complicated chemical treatments needed), the prospects are bright for making the devices available to each person's home for them to perform the diagnosis by themselves or to distant regions of the world to help local people conduct useful medical tests which are currently inaccessible to them. The study presented here is a modest step in the journey to that future.

Acknowledgements

It has been more than four years since my first visit to Lund for the interview of my current PhD position and my first participation in LAPASO, the Label-free Particle Sorting consortium funded by the European Commission, even before I was officially admitted to the project. During the challenging but interesting journey thus far, I am immensely thankful to my supervisor, Prof. Jonas Tegenfeldt, who enrolled me into his team and introduced to me the field of cell separation. While giving me much freedom to try any ideas I could think of, he provided me with every necessary guidance and support, networked me with experts in the fields he was not quite an expert on, and gave me almost instant feedback on my work, manuscripts, and thesis.

I would also like to thank my co-supervisor, Dr. Jason Beech, who has taught me tremendous practical knowledge and skills in, for example, microfludics and soft lithography, cleanroom expertise, and microscopy. When things did not seem right in the lab, Jason would be the first person I turned to and he never refused to give a hand.

The work in this thesis would never be complete without collaboration and support from LAPASO principle investigators and fellows: Prof. Hywel Morgan, Dr. Daniel Spencer, and Carlos Honrado from the University of Southampton; Prof. Birgitta Henriques Normark, Dr. Genevieve Garriss, and Vitor Oliveira from Karolinska Institute; Anke, Miguel, Clement, Elisabeth, Walter, Laura, and other LAPASO partners and fellows who have shared great times with me during every LAPASO meeting.

I have also received tremendous help from my group mates, who are also my good friends and lunch companions: Trung, Stefan, Kushagr and Oskar. Trung has been my close friend and collaborator from the first day in Lund and provides me with a lot of help during my PhD. Stefan is my DLD advisor, who is also my most frequent BMC lunch buddy. Oskar is my source of inspiration and optimism. Kushagr is the guy who gives you the impression that he knows everything, which may be true. In general, it is a group of buddies I can get advice about anything, from science to every matter in life.

Within the division of Solid State Physics, I would like to thank Gerda for her great help during my three years with LAPASO, Christelle for her kindness and the cosy dinners at her and Jonas' home, Elke and Martin for the energy and fun they bring, Damiano and

my office buddies throughout the years: Enrique, Michael, Pyry, Steve, Reza, Ivan, for the warm atmosphere they create at C366. All of them have made FTF my pleasant workplace.

I am grateful to be part of the biogroup: Christelle, Heiner, Jonas, Laura, Elke, Fei Fei, Rebehkah, Mercy, Martin, Frida, Inga, Zhen, Regina, Kalle, Therese, Roman, Jingyuan, Pradheebha, who have given constructive comments about my work and have taught me a lot in biomedical field during our weekly meetings. I also feel thankful to the faculty, administrative, and technical staff at FTF, who have directly helped me during my PhD or have contributed to building a supportive working environment I enjoy every day: Dan, Jonas Johansson, Anneli, Anders Gustafsson, Maria, Johanna, Janne, Bengt, Håkan, Marica, Mia, Sara, Mariusz, Abdul-Rehman, and Charlotte. And the list goes on. Thank you all for the good four years I have had at FTF.

Outside work, I would like to thank Hoa for his daily encouragement on my PhD research, Hong for being my good corridor friend, Ngoc, Dana, Tu, Hien, Van, Jasmine for all the great dinners and the delicious meals I enjoy (I now realise that most of my Vietnamese friends are excellent cooks), and Quan, Vinh, Minh, Thao for all the talks and advice for my PhD. Thank you all for building such a great Vietnamese community here in Lund.

Big thanks also go to all my corridor friends at Sparta 39B, who have contributed to a friendly and lively atmosphere I enjoy since 2016. Christina Naum, Julia von Treskow, Jiyan, and Isabel frequently asked me about my PhD work and encouraged me when my experiments did not go as planned. Jiyan even cooked dinners for me during my busy writing time. I sure will miss you all when I move out at the end of this year. Also, I want to thank Magnus, for giving me a comfortable accommodation when I first started my PhD in Lund, four years ago.

Lastly and most importantly, I want to express my gratitude to my parents and my younger sister, who have given me unconditional love, support and encouragement, from very far away in Vietnam.

List of Publications

This thesis is based on the following papers and manuscripts:

I **Cell Sorting using Electrokinetic Deterministic Lateral Dispalcement**
B. D. Ho, J. P. Beech, C. Honrado, D. Spencer, H. Morgan, and J. O. Tegenfeldt
Manuscript

I designed and made the masters and the devices. I performed all the experiments, analysed the data, and did the simulations. I wrote the manuscript.

II **Separation of Pathogenic Bacteria by Chain Length**
J. P. Beech, B. D. Ho, G. Garriss, V. Oliveira, B. Henriques-Normark, and J. O. Tegenfeldt
Analytica chimica acta, 2018, **1000**, 223-231

I designed the devices. I made the masters and devices, together with J. Beech. I characterised the devices with polystyrene beads (Figure 2E,F). I manually measured the size of the bacteria (the data for Figure 4). I processed the videos for Figure 7. I took part in most of the experiments and discussions.

III **Open channel Deterministic Lateral Displacement for Particle and Cell Sorting**
T. S. H. Tran, B. D. Ho, J. P. Beech, and J. O. Tegenfeldt
Lab Chip, 2017, **17**, 3592

I took part in the electrokinetic experiments (Fig 6), the initial experiments (Figure 3C), and the flow resistance experiments (Section "Flow resistance" in the ESI).

IV **Electrokinetic Rotation of Red Blood Cells in Deterministic Lateral Displacement devices**
B. D. Ho, H. Yavari, S. H. Holm, T. S. H. Tran, J. P. Beech, and J. O. Tegenfeldt
Manuscript

I conceived the idea. I made the devices, performed the experiment, analysed the data together with H. Yavari. I wrote most of the manuscript (section 2, half of section 3, section 4, and section 5).

V **Active Posts in Deterministic Lateral Displacement Devices**
J. P. Beech, K. Keim, B. D. Ho, C. Guiducci, and J. O. Tegenfeldt
Manuscript

I contributed to the design of the microfluidic part of the device. I took part in the experiments with particle sizes over $2\mu m$ (Figure 4, Figure 8 of the main text and Figure 5 of the ESI). I helped with setting up the numerical simulations.

The following manuscript is related but beyond the scope of this thesis:

VI **Integrated Separation and Readout - Towards Field-diagnosis of Trypanosomiasis**
C. Honrado, S. H. Holm, J. P. Beech, B. D. Ho, D. Spencer, M. P. Barrett, J. O. Tegenfeldt, and H. Morgan
Manuscript
I contributed in the experimental work and the design of the integrated device.

All papers are reproduced with permission of their respective publishers.

List of Abbreviations

AC	Alternating Current
BOP	Bipolar Operational Power
CAD	Computer-Aided Design
CFU	Colony-Forming Unit
CTC	Circulating Tumour Cell
DC	Direct Current
DEP	Dielectrophoresis
DLD	Deterministic Lateral Displacement
DNA	Deoxyribonucleic Acid
EOF	Electroosmotic Flow
EP	Electrophoresis
ESI	Electronic Supplementary Information
FACS	Fluorescence-Activated Cell Sorting
FEM	Finite Element Method
FFF	Field Flow Fractionation
FSI	Fluid-Structure Interaction
GUI	Graphical User Interface
IBM	Immersed Boundary Method
LAPASO	Label-free Particle Sorting
LBM	Lattice Boltzmann Method
LED	Light-Emitting Diode

MACS	Magnetic-Activated Cell Sorting
MCF-7	Michigan Cancer Foundation-7
MEMS	MicroElectroMechanical System (a.k.a. Microsystem Technology)
MFCS	Microfluidic Control System
PDMS	PolyDiMethylSiloxane
PEG	PolyEthylene Glycol
PFOTS	Trichloro (1H,1H,2H,2H-PerFluoroOcTyl) Silane
PLL	Poly(L-Lysine)
POC	Point-Of-Care
RMS	Root Mean Square
RNA	RiboNucleic Acid
sCMOS	scientific Complementary Metal Oxide Semiconductor
SDPD	Smoothed Dissipative Particle Dynamics
RBC	Red Blood Cell
WBC	White Blood Cell

List of Symbols

Roman alphabet

D	Material derivative
D_C	Critical diameter of DLD
$\mathbf{D_{dir}}$	Direction toward the nearest wall (unit vector)
d_p	Diameter of particle
D_w	Distance to wall
$\mathbf{E}$	Electric field
e	Euler's number ($e \simeq 2.71828$)
$\mathbf{E_{rms}}$	Electric field (root mean square)
E_t	Tangential component of electric field
$\mathbf{F}$	Force
f	Frequency of electric field
$\mathbf{f}$	Total body force per unit mass
$\mathbf{F_t}$	Total force acting on particle
$\mathbf{F_d}$	Stokes drag force acting on particle
$\mathbf{F_{DEP}}$	Dielectrophoretic force acting on particle
$\mathbf{F_w}$	Steric wall force acting on particle
f_{CM}	The Clausius-Mossotti factor
G	Gap between two pillars of DLD
$\mathbf{I}$	Identity matrix
i	The imaginary unit ($i = \sqrt{-1}$)

Roman alphabet (continued)

$\mathbf{J}$	Current density
j	(Subscript) Type of ions
K	Surface conductance
k_B	Boltzmann constant
L	Characteristic dimension of microfludic channel
m	Mass
m	(Subscript) Medium
N	Period of a DLD array
n	Number density of ions
n_0	Number density of ions in the bulk solution
$\mathbf{P}$	Dipole moment
p	(Subscript) Particle
p	Pressure
q	Elementary charge ($q \simeq 1.602 \times 10^{-19}$)
r	Particle radius
Re	Reynolds number
$Re\,()$	The real part of ...
r_p	Particle radius
s	(Subscript) Surface
$step\,()$	Step function

Roman alphabet (continued)

T	Absolute temperature
T	(Superscript) Transpose of a matrix
t	Time
$\mathbf{u}$	Velocity of fluid
U_E	Electric potential energy
u_{eof}	Electroosmotic flow velocity
u_{ep}	Electrophoretic velocity of particle
V	Electric potential
$\mathbf{v}$	Velocity of particle
w	(Subscript) Wall
z	Charge number

Greek alphabet

∇	Del operator
ε	Permittivity
ζ	Zeta potential
η	Dynamic viscosity
κ	Inverse of Debye length
λ_D	Debye length
μ_{eof}	Electroosmotic flow mobility
μ_{ep}	Electrophoretic mobility of particle
ρ	Mass density of fluid
ρ_q	Volume charge density
ρ_p	Mass density of particle
σ	Conductivity
τ_p	Particle velocity response time in Stokes flow
ϕ	Electric potential
ω	Angular velocity

Chapter 1

Introduction

There is plenty of room at the bottom.
— Richard Feynman

1.1 Microfluidics

HUMANS have the tendency of miniaturizing their tools, making things smaller yet better and even cheaper. One excellent example is the computer. The replacement of bulky mechanical shafts and disks, or electromagnetic relays and vacuum tubes with semiconductor components has helped miniaturizing a computer from a room-sized machine to a cell phone in people's pockets nowadays, with far better performance at much lower price. Microfluidics has developed in a way that is analogous to that of microelectronics: microelectronics studies and makes use of solid state electronic circuits at micro and nano scale, while microfluidics investigates and manipulates fluids in channels whose sizes are smaller than the width of a human hair. In fact, just like microelectronics, microfludics has emerged as a field, encompassing a large number of research publications, enormous technological development and bringing about many patents and start-up companies.

Microfludics started in the late 70s with IBM ink jet printer nozzles[1] and Stanford University's miniaturized gas chromatography[2]. The early works in microfludics till the early 90s were closely related to Microsystem Technology (MEMS). In fact, most of the

early microfludic products were made in silicon or glass, the familiar materials of the MEMS industry. A large portion of the research was focused on theory, modeling/simulation, or the technological aspects (*e.g.* making of valves and pumps in silicon). Applications were narrow and limited to flow sensors, ink jet printer nozzle arrays, micro-dosing systems and microchemical analysis systems[3]. The next stage of microfludics was marked with the introduction of soft lithography using polydimethylsiloxane (PDMS)[4] to fabricate devices, transferring microfludics from a branch of MEMS into a distinct field of its own. The main advantage of soft lithography is the ease to replicate new devices from an original mold. Also, the transparency of PDMS to visible and ultraviolet light and its compatibility to cells have made microfludics more friendly to biological and medical applications. The "softness" of PDMS has also enabled the fabrication of flexible miniature pneumatic valves, mixers, and pumps, broadening the capability of microfludic devices. Besides silicon, glass, and PDMS, other materials like thermoplastics (polystyrene, cyclic olefin copolymer, polymethyl methacrylate, and polycarbonate) or familiar materials (paper, wax, and cloth), have also been exploited for specific requirements.

Thanks to the maturity of the technology and the diversity of the materials used for fabrication, microfluidics has found various applications in biological and medical research[5,6]. Following are just some of the key applications:

- ▷ *Point-of-care diagnostics (POC)* is a promising area for microfludic applications since it fits with the key aspect of microfludics: making low-cost and even disposable lab-on-a-chip devices that can complete a specific task. There have been several microfludic POC products on the market[7] with limited success. The development of paper-based microfludics[8], together with the innovations in optical microfluidic technologies[9], for example cell phone microscopy[10], will conceivably make microfluidic POC devices readily available in everyday life.
- ▷ *Droplet microfludic devices*[11,12] can generate, at high speed, a large amount of microscopic single-droplet containers that can be considered as tiny test tubes for a wide range of applications such as: chemical reactions, therapeutic agent delivery, cell culture, or molecular synthesis.
- ▷ *Cell and bioparticle sorting devices* fractionate a heterogeneous population of cells and bioparticles into homogeneous ones, for preparative and analytical purposes. This will be discussed in more details in the next section.

- ▷ *Sensor applications* cover a wide range of physical and chemical sensors, electrochemical sensors, and biosensors. Examples include thread-based strain or pH sensors[13], paper-based electrochemical sensor[14], or yeast cell growth sensor using polymer microcantilever[15].

- ▷ *Cell biology*[16] is a fast-growing area of microfludics. Applications are diverse and include: cell culture[17], neuroscience, stem cell or cancer cell research, drug discovery and screening, microbiology, and clinical diagnostics, just to name a few. A typical example is the immobilisation of *C. elegans* using microfluduics, which offers the unprecedented ability to conveniently trap, manipulate, and image the worms[18–21].

- ▷ *Organ-on-a-chip*[22] mimics and constructs the complex structures of tissues or organs on microfludic chips, for example: liver on chip[23], kidney on chip[24], or lung on chip[25].

The above-mentioned diverse applications of microfluidics substantiate its importance and visibility in today's society. However, a phenomenal "killer application", like the personal computers or the smart phones as with microelectronics, has not yet arrived[5,6]. A large proportion of research in microfluidics is still in the engineering fields[6]. Sackmann *et al.*[6] made some well founded suggestions for making microfluidics a mainstream in biomedical research: offering fundamentally new capabilities instead of only improving upon existing methods, keeping the devices as simple as possible, fostering collaborations between physicists/engineers and biologists/medical experts, and finding the right problems. The following section will attempt to convince the readers that biological particle sorting is one of the right problems.

1.2 Particle Sorting

Sorting is the process of regaining the order of a system, a quantity which universally decreases over time. This can mean either arranging individual objects in a predefined sequence or grouping similar objects together into specific groups. In biological and medical fields, the latter definition is normally assumed. The objects of biomedical sorting are normally micro- or nanoscale bioparticles and cells, for example tissue-derived cells, blood cells, bacteria, parasites, and micro/nano vesicles. In terms of purpose, biomedical particle sorting can be a preparative step where the sorted populations are reserved for further study or analysis, or an analytical process where the distributions of the sorted populations provide useful information for clinical diagnosis. To set the background for the rest of the thesis, this section will briefly introduce some of the most popular sorting techniques employed in biomedical applications nowadays.

The simplest yet most prevalent cell sorting techniques are *filtering* and *centrifugation*. The first method makes use of filters which have pore sizes in the micrometer range to only allow cells of a predefined upper size limit to pass through. Examples of such filters are disposable filter papers used in preparation of samples for cell culture or flow cytometry analysis or nylon filters used in sorting adipocytes by size[26,27]. The second method, centrifugation, takes advantage of the difference in sedimentation speed of particles, which is a function of size and mass density, to sort them accordingly. Centrifuge machines are indispensable in most clinical or research labs for separation of blood components or for concentrating and collecting of particles in a liquid medium. Despite being simple, fast, and easy to use, filtering and centrifugation only target size or density of the cells and as a result, sorting by other physical properties or functional properties is impossible. Centrifuge machines are also rather bulky and require electric power to operate.

To target functional properties of cells, other methods, *magnetic-activated cell sorting (MACS)* and *fluorescence-activated cell sorting (FACS)*, make use of labeled probes to identify the cells of interest. In these methods, antibodies are coated on magnetic nanoparticles (MACS) or attached to fluorophores (FACS). The antibodies then bind to specific antigens on the surface of the cells of interest, thereby tagging them with magnetic nanoparticles or fluorophores. In MACS, the tagged cells may be retained in a magnetic column by magnetic force while other cells are eluted away. In FACS, by emitting and detecting the fluorescence

signals, tagged cells can be detected individually. They are then selectively charged and sorted out from other cells by electrostatic force. While MACS and FACS are effective and can target a wide range of cells, they also have limitations. For example, MACS requires the use of magnetic nanobeads and magnetic columns, which are expensive. Furthermore, since it only targets functional properties of cells, specifically surface-expressed proteins, sorting by size or other physical properties is difficult. In case of FACS, besides the high cost of reagents and equipment, the FACS machines are bulky, difficult to operate, and as a result, cannot be deployed in remote areas. Many of those limitations of MACS and FACS can be avoided by using microfluidic cell sorting techniques.

In general, microfluidic particle sorting technology makes use of micro- and nano-fabrication to produce features as small as cells or biological particles to easily manipulate them. In principle, cell sorting in microfludic devices can also exploit labels as in the case of MACS or FACS, for example using magnetic beads to alter the size and compressibility of cells for acoustophoretic sorting[28]. However, a large proportion of research in microfluidic particle sorting pursues the concept of *label-free sorting*. Instead of tagging the cells with magnetic or fluorescence label, this group of techniques exploit intrinsic physical properties to separate or enrich cells, and can be divided into two groups: active and passive methods. Active methods require an externally applied force field, for instance dielectrophoresis or acoustophoresis. Passive methods, on the other hand, rely on the internal intrinsic forces – the steric force between the particles and the devices' walls and the hydrodynamic force that the fluid exerts on the particles – together with careful geometrical designs to perform the sorting task. Below are some of the most popular microfluidic active and passive cell sorting methods. More extensive reviews can be found elsewhere[29,30].

Active methods:

- *Electrophoresis* exploits the difference in particles' electrophoretic mobility in an electric field to sort them accordingly. *Gel electrophoresis*[31] has long been used to sort DNA in agarose or polyacrylamide gels according to their size since mobility of longer molecules is reduced significantly due to their increased interaction with the pores of the gel. *Capillary electrophoresis,* on the other hand, sorts particles based on their effective charge (or more precisely, their zeta potential) as they travel along a long, thin glass capillary under an applied DC electric field. Capillary electrophoresis has also been successfully miniaturised on a glass chip[32].

- ▷ *Dielectrophoresis (DEP)*[33,34] makes use of the dielectrophoretic force acting on the particles in a non-uniform electric field. The force is dependent on the particles' size and effective polarisability (or more precisely, the Clausius-Mossotti factor, see Section 2.5). Therefore, the particles can be sorted by their sizes and/or their effective polarisability. An example is shown in Figure 1.1.

- ▷ *Acoustophoresis*[35] employs an acoustic standing wave force to induce lateral displacement of particles, perpendicular to the direction of flow. The force is dependent on the particles' size, density, and compressibility. Therefore, the particles can be sorted according to size, density, and compressibility (Figure 1.1).

- ▷ *Field Flow Fractionation (FFF)*[36] utilises a force field perpendicular to the flow to migrate particles into streams of different velocity in a parabolic flow profile, resulting in separation in retention time at the end of the channel.

Passive methods:

- ▷ *Pinched Flow Fractionation*[37] makes use of the fact that a particle cannot be closer to a wall than its radius to separate particles based on size (Figure 1.1).

- ▷ *Deterministic Lateral Displacement (DLD)*[38] is in principle a size-based method with the advantage of being continuous and high-resolution. A detailed description of DLD can be found in Section 2.2.

- ▷ *Inertial microfluidics*[39] operates in the middle range of Reynolds number where the flow is still laminar but the inertia of fluid and particles is considerable (see Section 2.1 for a description of laminar flow and Reynolds number). The inertial Dean flow in a curved channel and/or the inertial lift forces on particles are utilised to separate particles based on their size (Figure 1.1).

Let us now examine the possibility of *label-free particle sorting* being a mainstream practice in biomedical research, according the criteria proposed by Sackmann *et al.*[6]. First, considering fundamental novelty, it can be seen that while some techniques, for example microscale filters, improve upon the ideas which have been used to make their macro counterparts, other approaches, for instance Inertial Sorting or Deterministic Lateral Displacement, were completely new discoveries. When it comes to keeping the devices as simple as

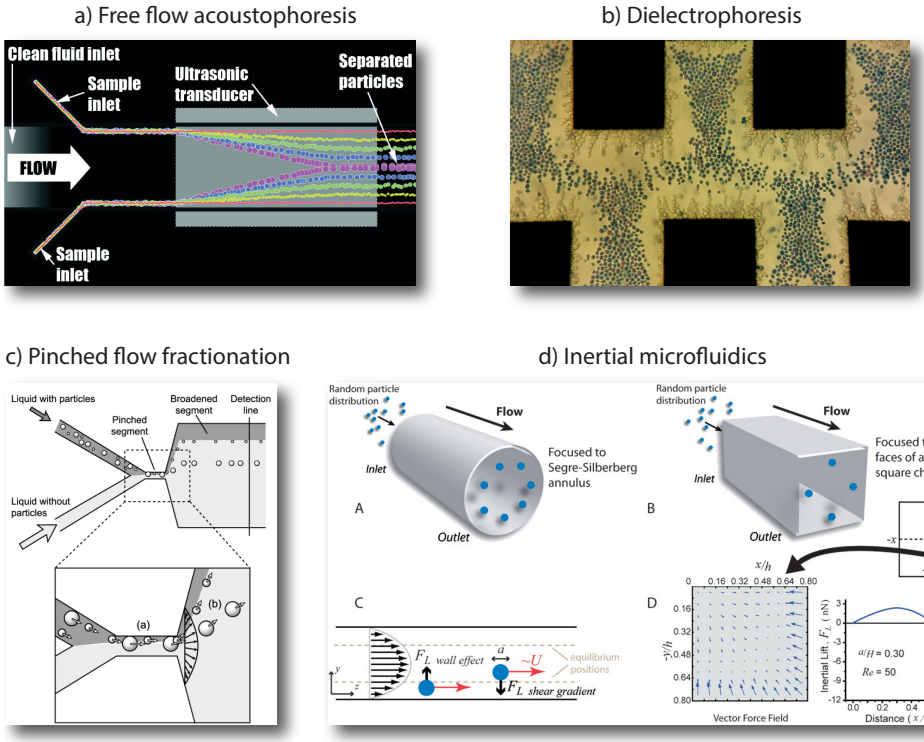

Figure 1.1: Examples of active (a,b) and passive (c,d) microfluidic label-free particle sorting methods. a) In free flow acoustophesis, particles are sorted laterally based on their size, density, and compressibility. Reprinted (adapted) with permission from Petersson *et al.* [35]. Copyright 2007 American Chemical Society. b) Under dielectrophoresis, non-viable yeast cells (stained dark blue) and viable yeast cells (transparent) migrate to different areas in a castellated electrode device, according to the sign of the dielectrophoretic force acting on them. c) With pinch flow fractionation, particles of different size can be sorted because the centre of small particles can be closer to the wall than that of big particles. Reprinted (adapted) with permission from Yamada *et al.* [37]. Copyright 2004 American Chemical Society. d) When the Reynolds number is larger than unity, particles experience inertia lift forces that are dependent on their size and their position in the cross-section of a channel. This can be exploited to focus particles of different sizes at different positions an separate them. Republished (adapted) with permission from Di Carlo [39]. Copyright 2009, the Royal Society of Chemistry.

possible to lower the entrance threshold for biomedical technicians or end-users, most of the passive techniques are good candidates since they usually need only a pressure generator, which can be as simple as a syringe. Active mechanisms often need some sort of apparatus to generate the required force field. However, those apparatuses can be redesigned and simplified to adapt to the local infrastructure. The third and forth criterion – fostering collaborations between physicists/engineers and biologists/medical experts and finding the right problems to solve – are open questions, since they are not dependent on the techniques but rather are determined by the needs and the incentives of the professionals involved. Nevertheless, as the most important purposes of label-free particle sorting are to avoid using ex-

pensive reagents and to produce cheap and more widely available biomedical devices, this is a promising yet challenging area, which can stimulate collaborations between scientists and companies in multidisciplinary fields. An example of such collaborations was LAPASO, the Label-free Particle Sorting research project funded by the People Programme (Marie Curie Actions) of the European Union's Seventh Framework Programme. The LAPASO project has brought together a multidisciplinary consortium of eight full partners and seven associate partners in Europe and Africa to solve current problems in the fields of bacteriology, parasitology, and rare cells sorting, using label-free methods. Further information can be found at its website: `http://lapaso.org`.

The work in this thesis is narrowed down to Deterministic Lateral Displacement. The main focus is on extending the capabilities of this technique by exploiting, besides size differences, the electrical/dielectric properties and the morphology of the cells. The thesis is structured as follows. After this introduction, Chapter 2 presents the theory and modeling of Deterministic Lateral Displacement and Electrokinetics. Chapter 3 describes the methods and the practical details of the work. Chapter 4 summarizes the results of the thesis work, the related published articles and manuscripts intended for publications, and concludes the thesis. The appendix and the related papers are located at the end of the thesis.

Chapter 2

Theory and Modelling

It's easy to be complicated
but very difficult to be simple.
— Debasish Mridha

This chapter presents the theory of microfludics and electrokinetics, the two central topics of this research work. It also gives an overview of the related modelling and simulation work.

2.1 Fluid Dynamics in Microfluidic Systems

Following is a brief summary of the physics of fluid dynamics in microfludic systems. Further comprehensive reading may be found in several textbooks in fluid dynamics [40–42] or theoretical microfluidics [43,44].

The physics of continuum fluid dynamics is described by the Navier-Stokes equations. Despite their essence to many scientific and engineering fields, whether the general solutions to them exists is an unsolved mathematical problem [45]. Fortunately in many cases, the equations can be simplified. The Navier-Stokes equations for an incompressible flow, which is the case for microfluidic applications, consist of one vector equation describing momentum conservation and one scalar equation describing mass conservation [40]:

$$\rho\frac{D\mathbf{u}}{Dt} = \rho\mathbf{f} - \nabla p + \eta\nabla^2\mathbf{u} \tag{2.1}$$

$$\nabla \cdot \mathbf{u} = 0 \tag{2.2}$$

Here, ρ is the density of the fluid, $\mathbf{u}$ is the velocity field, $\frac{D}{Dt} = \frac{\partial}{\partial t} + \mathbf{u} \cdot \nabla$ is the material derivative, t is the time, $\mathbf{f}$ is the total body forces per unit mass, p is the pressure, and η is the dynamic viscosity of the fluid. Essentially, Equation 2.1 is the Newton's second law applied to a unit volume of fluid: the term on the left hand side is the rate-of-change of momentum while the terms on the right hand side are the body force (for example gravity or dielectrophoretic force) and the surface forces (pressure force and viscous sheer force). Since the density ρ is often uniform and known, the four unknowns (p and the three components of $\mathbf{u}$) can in principle be solved using Equation 2.1 and Equation 2.2. Nevertheless in practice, solving the general Navier-Stokes equations is hard because of the nonlinerity coming from the convective derivative of the velocity, $(\mathbf{u} \cdot \nabla)\mathbf{u}$.

Fortunately, Equation 2.1 can be reduced in microfluidic systems where the ratio between inertial effects and viscous effects, $Re = \frac{\rho u L}{\eta}$ (the Reynolds number), is normally under unity. Here, L is the characteristic dimension of the microfluidic channel. In a typical microfluidic device, assuming $\rho = 1000\ \frac{kg}{m^3}$, $\eta = 0.001\ \frac{kg}{m.s}$, $u = 100\ \frac{\mu m}{s}$, and $L = 10\ \mu m$, the Reynolds number is 10^{-3}, well below unity. In this case, the inertial term on the left hand side of Equation 2.1, $\rho\frac{D\mathbf{u}}{Dt}$, is negligible and the equation can be simplified into the *Stokes equation*, which is linear:

$$0 = \rho\mathbf{f} - \nabla p + \eta\nabla^2\mathbf{u}$$

The flow described by the Stokes equation is called *Stokes flow* or *creeping flow*. In such a scheme, the flow consists of non-mixing, turbulent-free parallel layers of fluid. In fact, the Stokes flow is a subset of a broader *low-Re* flow regime called *laminar flow*, where the Reynolds number is low enough for the fluid to be smooth, orderly, and free of any turbulent vortices ($Re \leq 800$[46]) . Laminar flow is the underlying mechanism for Deterministic Lateral Displacement (DLD), which will be discussed in the next section,

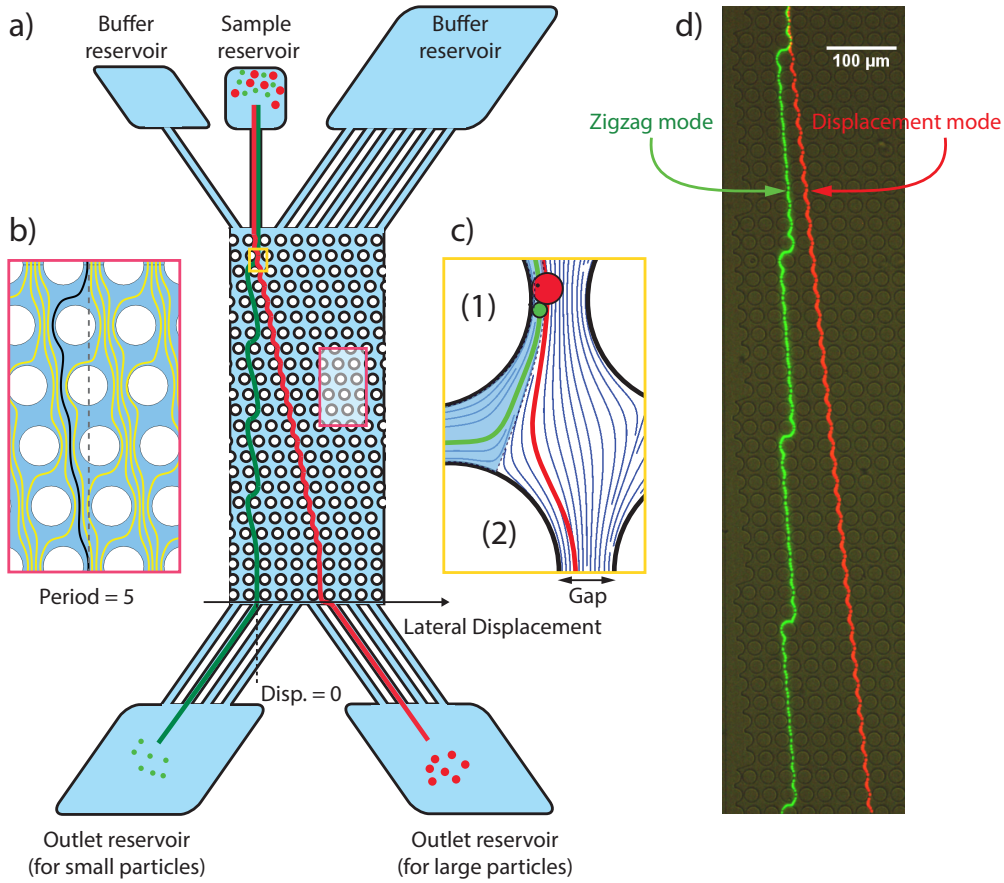

Figure 2.1: Principle of Deterministic Lateral Displacement. a) A schematic of a typical DLD device. The device consists of three parts: the inlet reservoirs on the top, the pillar array in the middle, and the outlet reservoirs at the bottom. It is capable of sorting a mixture of big (red) and small (green) particles into homogeneous populations. b) Periodic streamlines in the channel due to the pillar array. c) The underlying mechanism of size-dependent separation in DLD. The centre of mass of the green particle resides within the blue stream, whereas the centre of mass of the red one locates outside of the blue stream. Therefore, the two particles follow two different trajectories. (The streamlines in b) and c) are based on actual simulations.) d) Colour-coded micrograph of polystyrene beads, $2.1\ \mu m$ (green) and $4.3\ \mu m$ (red), in a pillar array having an estimated critical diameter, $D_C = 2.8\ \mu m$.

to be "deterministic". As DLD is a continuous hydrodynamic particle sorting technique, it relies on the flow behaviour being predictable in time and space. Consequently, DLD relies on being operated in the laminar flow regime.

2.2 Deterministic Lateral Displacement - Basic Principle

A typical device based on deterministic lateral displacement (DLD) (Figure 2.1a, not to scale) consists of three parts: the inlet reservoirs on the top, the sorting array in the middle, and the outlet reservoirs at the bottom. The middle inlet reservoir – the sample reservoir – contains a heterogeneous sample suspended in a running medium. The two inlet reservoirs on the sides – the buffer reservoirs – help maintain straight flow throughout the sorting array. The sorting takes place in a section consisting of an array of micrometre-sized pillars in a shallow channel of rectangular cross-section. The pillars are positioned so that the principle direction of the pillar array lattice forms an angle with respect to the channel wall. The outlet reservoirs accommodate the homogeneous populations being separated. The size of a DLD device is dependent on the intended application but its dimensions are typically on the order of $length \sim 1\ cm$, $width \sim 1\ mm$, and $depth \sim 10\ \mu m$. Detailed information about the devices in this thesis work is given in the Appendix (Chapter 5).

The arrangement of the pillars and the laminar nature of the flow are fundamental to the operation of DLD. The presence of the pillar array, tilted with a specific angle with respect to the overall flow direction, bifurcates and diverts the otherwise straight flow into many "zigzagging" streams around the pillars, as illustrated by the simulated streamlines in Figure 2.1b. If the pillar array is periodic, thanks to the turbulence-free and predictable nature of laminar flow, a flow stream would appear at the same lateral position after every period, as exemplified by the black streamline in Figure 2.1b.

This laminar and periodic flow pattern is the underlying mechanism for particle separation. As can be seen in Figure 2.1c, since pillar 2 is shifted to the right of pillar 1, it bifurcates the flow into two streams: one to its left (light blue) and one to its right (white). When spherical particles are transported near to the surface of pillar 1, the distance from the wall to the centre of a small particle is less than to the centre of a large particle. Depending on whether the centres of the particles reside within the blue stream (the green particle) or outside the blue stream (the red particle), they will travel through the DLD array in either a zigzag trajectory or a displacement/bumping trajectory, repectively. Particles traveling in zigzag mode return to the same lateral position after each period while particles traveling in displacement mode are transported along the tilting angle of the pillar array. This results in separation. As an example, Figure 2.1d shows the trajectories of 2.1 μm (green) and 4.3 μm

(red) polystyrene beads in a DLD array having the gap width between pillars of 6 μm and the period of 10.

The *critical diameter* above which particles traveling in displacement mode can be calculated assuming laminar flow with parabolic velocity profile between two posts of a row[47]. Beech and Tegenfeldt came up with a close-form analytical approximation for the critical diameter[48]:

$$D_C = 1.2GN^{-0.5} \tag{2.3}$$

where D_C is the critical diameter, G is the gap between two posts in a row (Figure 2.1c), and N is the period of the array. Another estimation for the critical diameter was proposed by John Davis[49], based on an empirical study:

$$D_C = 1.4GN^{-0.48} \tag{2.4}$$

For the pillar array shown in Figure 2.1d, Equation 2.3 and Equation 2.4 give $D_C = 2.3\mu m$ and $D_C = 2.8\mu m$, respectively, differing by around 20%. For the case exemplified in Figure 2.1d, the actual critical diameter was experimentally found to be larger than 3.1 μm, meaning that Equation 2.4 in this case gives a more realistic estimation of the resulting separation. This equation is also more commonly used when fabricating DLD devices. However, it should be stressed that both equations only give approximations of the resulting separation. Further studies are required to reveal a more accurate relationship between the critical size and the device geometries and the properties of the liquid and the particles.

2.3 Deterministic Lateral Displacement - Status of Theory, Technology, and Applications

2.3.1 Theory and Simulation

Theoretical work on DLD can be categorised broadly into two main branches. One branch focuses more on the structure of the flow and the other focuses more on the particle-obstacle interaction. In the first approach, the authors base their calculations on laminar flow to determine the flow profile and the distribution of flow streams in a pillar array. The flow profile and flow stream distribution are then employed to infer the trajectories of particles according to their size, without any explicit assumption about the interaction between the particles and the obstacles besides the impenetrability condition. This approach was employed in the first DLD paper[38] to explain the working principle of DLD and later in other works to estimate the critical diameter in a circular pillar array[47] or in a triangular pillar array[50]. The second theoretical approach, on the other hand, attempts to describe the irreversible particle-obstacle contact by a characteristic parameter while making no reference to the structure of the flow. This approach, so called "directional locking", was also successful in correlating theoretical calculations with experimental results, obtained in macro scale DLD arrays[51–61]. In addition, a model based on advection-diffusion theory claiming to bridge the two main aforementioned approaches has been published.[62].

Numerical simulation research on particle separation using DLD can be sorted into two main groups: Finite Element Method or a combination of Lattice Boltzmann Method (LBM), Finite Element Method (FEM), and Immersed Boundary Method (IBM). In the first approach, the Navier-Stokes equations are solved for the fluid flow, the mechanical deformation of the solid particles is also solved, and the fluid and the solid phase are connected using Fluid-Structure Interaction (FSI) algorithms[63,64]. In cases where the particles are hard spheres and are small compared to the gap between pillars, the two-way coupling scheme (FSI) can be simplified into a one-way coupling scheme where the particles were modeled as point-like objects whose minimum distance to pillar walls equals the actual particles' radius[62,65–69]. The second simulation approach employs the Lattice Boltzmann Method to resolve fluid velocity instead of solving the Navier-Stockes equations. The membranes/surfaces of the particles are modeled as a spring network and solved using FEM whereas the fluid-structure interaction is solved using the Immersed Bound-

ary Method[70–73]. In addition to the FEM or LBM/FEM/IBM approach, researchers also employed Finite Difference Method + IBM[74], Fictitious Domain Method[75], or Smoothed Dissipative Particle Dynamics (SDPD)[76] for numerical studies of DLD. Most notably, Henry *et al.*[76] showed qualitative agreement between the dynamics of Red Blood Cells in their models with the dynamics of the cells in DLD.

Future works on numerical simulations of DLD should preferably attempt to correlate with experimental data to help with the designing and optimising process. It is also of interest to accurately capture the behaviour of arbitrary particles (*e.g.* bacteria or other bioparticles with complex properties) in DLD devices to explore new sorting schemes.

2.3.2 Technology

Chip materials

The two most popular materials for fabrication of DLD devices are silicon[38,77,78] and polydimethylsiloxane (PDMS)[79–81]. Silicon etching techniques allow fabrication of well-defined pillars and very narrow gaps but the process can be complicated and difficult to replicate. Soft lithography using PDMS, on the other hand, allows for rapid and cheap device prototype fabrication, but high-aspect ratio pillars can often be difficult to achieve due to limitations in the processing steps. To reduce the cost of making chips and to improve scalability, attempts have also been made to produce DLD chips in plastic[82,83].

Design

Much of the attention on the design of DLD has been paid to optimising pillar shape, both experimentally and numerically. In general, it has been proven that if the cross-section of the pillars is a triangle[50,84–90], a square[72,87], an I shape/L shape[72,91–93], a diamond shape[87], an egg shape[94], or a specific topological optimised shape[95], the same critical diameter is achieved at a larger gap width than in the case of circular pillars. As a consequence, the DLD array is less prone to clogging and at the same time, the volumetric throughput will increase. There are also other added benefits of using special shapes. For example, the airfoil shape[96] was believed to reduce deformation of soft particles. The I-shape/L-shape pillars were found to induce rotational movement of non-spherical cells[91,92], which in turn helps distinguish particles based on their morphology. Another way which has been successful at sorting

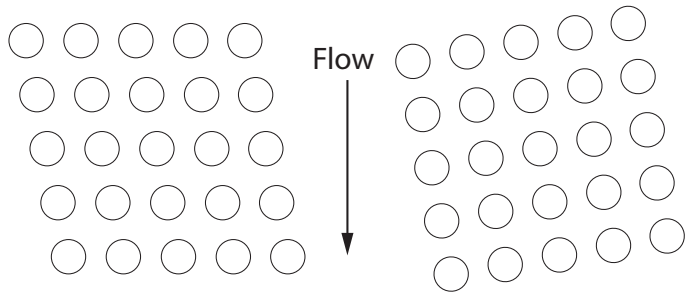

Figure 2.2: Two ways of implementing array's tilting angle: rhombic array (left), where the rows are perpendicular to the flow, and rotated square array (right), where the rows are perpendicular to the columns.

particles based on their morphological differences is to impose an orientational constraint by decreasing the channel depth down to below the largest dimension of a particle with aspect ratio larger than unity (*i.e.* long or thin particles). This has been employed to sort trypanosomes from blood[97,98] or Circulating Tumour Cell (CTC) clusters from blood[93].

At a larger scale, researchers have been working on improving the performance of the whole pillar array. There are two ways of implementing the tilting angle of the array: rhombic configuration and rotated square configuration (Figure 2.2). The majority of DLD publications use the rhombic configuration. The advantage is that it is easier to correct for boundary effects near the edges of the device, as well as, to interface two sections having arrays of different angles. However, it has been pointed out recently that the rotated square configuration is more immune to anisotropic permeability[99].

Attempts have been made to reduce unwanted effects in DLD caused by the tilting angle of the array, including the wall effect[100] and the anisotropic permeability effect[99,101–103]. The wall effect is due to the finite width of the array while the anisotropic permeability effect is because of the array tendency to induce a lateral pressure gradient perpendicular to the overall flow direction. To increase throughput, Loutherback *et al.* proposed mirroring an array next to the other[50] and this idea has been appreciated by other researchers[104,105].

Driving Mechanisms

While most of DLD experiments employ a pressure difference across the device to induce the flow and in turn to transport the particles, it has been demonstrated that other driving mechanisms also have their benefits. For example, gravity-driven[55,61], centrifugal force-

driven[60], or capillary force-driven DLD[106] may conceivably be useful in distant places where pressure pumps or syringe pumps are impractical. Electroosmotic-driven DLD[38,58], due to the plug flow profile, can yield smaller critical diameters than in the pressure-driven DLD[47].

Tuning critical diameter or sorting by parameters other than size

Not limited to improving DLD by optimising design or employing new physical mechanisms, researchers have also attempted to extend its capabilities by adding tunability. Interesting examples include tuning the critical diameter of a DLD array by deforming the device[80] or by applying electrokinetic forces[107]. These implementations on one hand complicate the operation of DLD devices, but on the other hand, extends the dynamical range of the device. The critical diameter can also be altered if a non-Newtonian fluid is used instead of aqueous media[63].

It has further been shown that DLD is capable of discriminating between particles based on properties additional to size. For example, the deformability of Red Blood Cells has been shown experimentally[108] and numerically[70,73,76,87] to affect their trajectories in a DLD device. Similarly, morphology of RBCs and trypanosome[97], *S. pneumoniae*[109], or 3D-printed macro objects[59] has been shown to be an effective marker for separation using DLD.

2.3.3 Applications

Since its inception, DLD has been employed to effectively separate a wide range of particles for biological and medical research. At the lower spectrum of size, around and below 1 μm, DLD has been used to concentrate exosomes[78], separate microvesicle from blood[110,111], sort DNA of different length[38], or fractionate bacteria based on chain length[109]. On the order of 10 μm, the technique has been employed for separation of nucleated RBC from blood[112], trypanosomes from blood[97,98], epithelial cells from fibroblasts[113], fungal spores from debris background[114], cardiomyocytes from heart tissue digest[115], MCF-7 cancer cells by size[89], viable Jurkat cells from nonviable apoptotic cells and their remnants[104], or droplets based on size[116,117].

A large part of DLD applications have been focused on the preparative or analytical separations of blood samples. Preparative separations comprise separations where the common goal is to enrich a certain subpopulation of the samples for further processing or downstream analysis. Examples include the separation of WBC from RBC or from blood as a whole[79,81,118] and furthermore, to take different blood components apart[77,119,120]. The other direction is analytical particle sorting where the sorting itself is the end goal of the analysis. This includes either analysing the distribution of a certain property among the cells in the sample, or detecting the presense of a certain cell in the sample, such as in the case of rare cell isolation and detection. A wide range of rare cells including parasites[97,98], PC3 cancer cells[88], or Circulating Tumour Cells (CTC)[85,90,93,94,121] have been enriched and detected using DLD.

In summary, during fourteen years, DLD has been central to a wide range of theoretical, engineering, and biomedical studies. Thanks to the relative maturity of the field, it can be hypothesised that future work will lean towards development of products based on DLD. Examples could be inexpensive point-of-care diagnostic chips[98], integrated chips where DLD is one component[94], or high throughput DLD chips which can process whole blood[81,88,94]. From a technological point of view, DLD devices which can sort nanoparticles or DLD devices which can specifically enrich rare cells from background would be highly appreciated. It should be noted that although the throughput of DLD devices can be improved by running at high pressures and/or by using parallelisation, the main strength of DLD is high resolution and this should be exploited in more applications.

2.4 Electrokinetics

In this section, the term *Electrokinetics* is used as an umbrella term to refer to three phenomena which can be used for transport (*-kinetics*) under application of an electric field (*Electro-*):

- ▷ Electroosmotic flow: the transport of aqueous solutions using an electric field
- ▷ Electrophoresis: the transport of a charged particle using an electric field
- ▷ Dielectrophoresis: the transport of a dielectric particle using a non-uniform electric field

Electrophoresis is fundamentally caused by electroosmotic flow around a particle. Both electroosmotic flow and electrophoresis are related to the charges at the interfaces between an electrolyte solution and a solid wall, which can be the wall of a device or the surface of a particle. Dielectrophoresis is related to the polarisation the particles and the medium and does not require the particles to be charge. To keep this section at reasonable length, dielectrophoresis will be discussed in the section. More detailed treatment of AC electrokinetics can be found in the book by Morgan and Green[122].

2.4.1 The Electrical Double Layer

The electrical double layer is the basic concept underlying electroosmotic flow and electrophoresis. When a charged object is embedded into an electrolyte solution, the ions of opposite polarity from the solution, counter-ions, are attracted to the surface of the object and electrically screen it[1]. Over a century, scientists have proposed, developed and refined theories to explain and quantify the double layer. The most commonly used model nowadays was proposed by Bockris *et al.*[123 124]. According to this model, as illustrated in Figure 2.3a), the region of electrolyte solution closest to the object surface consists of solvent dipoles, usually water molecules, and ions of both polarities (co-ions and counter-ions). The plane passing through the loci of bounded dipoles and ions is called *the inner*

[1]Even a neutral object, for example a glass or PDMS surface, can become charged in aqueous solution. In case of glass or PDMS, the terminated –OH group will dissociate into $-O^-$ and H^+ in an aqueous solution. This creates the necessary asymmetry between the stationary charge (the negative ionised hydroxyl groups) and the mobile ions in the double layer.

Helmholtz plane. Farther away from the surface is a region of hydrated counter-ions. The plane passing through the loci of hydrated ions is named *the outer Helmholtz plane.* The layer residing between the object surface and the outer Helmholtz plane, consisting of molecules and ions bounded to the object surface, is called *the Stern layer*. Outside the Stern layer, hydrated ions can move relative to the object surface. The counter-ions in this outer layer "diffuse" into the bulk electrolyte solution, or in other words, the charge density reduces exponentially to zero, reaching neutrality. Therefore, this layer is called the *the diffuse layer*. The term *double layer* refers to the Stern layer and the diffuse layer.

The electric potential in the electrical double layer – the Poisson - Boltzman equation.

The electric potential in the diffuse layer can be described by the Possion equation:

$$\nabla^2\phi = -\frac{\rho_q}{\varepsilon} \tag{2.5}$$

Where ρ_q is the volume charge density and ε is the permittivity of the medium. The volumetric charge density can be calculated applying the statistical *Boltzman law,* which states that the likelihood that a particle possesses an energy U_E is proportional to $e^{-\frac{U_E}{k_B T}}$, where e is the Euler's number, k_B is the Boltzmann constant, and T is the absolute temperature. Therefore the number density of the ions can be written as:

$$n = n_0 e^{-\frac{U_E}{k_B T}} \tag{2.6}$$

Where U_E is the electric potential energy of the ions, and n_0 is the number density of ions in the bulk solution. The electric potential energy can be expressed in the electric potential by: $U_E = zq\phi$, where z is the charge number, and q is the elementary charge. Equation 2.6 becomes:

$$n = n_0 e^{-\frac{zq\phi}{k_B T}} \tag{2.7}$$

And since $\rho_q = nzq$, Equation 2.5 becomes:

$$\nabla^2\phi = -\frac{zq}{\varepsilon} n_0 e^{-\frac{zq\phi}{k_B T}} \tag{2.8}$$

When there are many ionic species in the electrolyte solution, one has:

$$\nabla^2\phi = -\frac{q}{\varepsilon}\sum z_j n_{0j} e^{-\frac{z_j q\phi}{k_B T}} \tag{2.9}$$

which is known as *the Poisson-Boltzman equation*. Here the subscript j denotes the ions of type j. Since the potential ϕ appears at both sides of the equation, an analytical solution is difficult. However, approximations can be made in some special cases.

The Debye-Hückel theory. If we assume that the potential ϕ is small, we can approximate the exponential term by first order Taylor approximation: $e^x \approx 1 + x$ for small x. Thus, Equation 2.9 becomes:

$$\nabla^2\phi = -\frac{q}{\varepsilon}\sum z_j n_{0j}(1 - \frac{z_j q\phi}{k_B T}) \tag{2.10}$$

Due to the charge balance, $\sum z_j n_{0j} = 0$, we come up with a linear ordinary differential equation:

$$\nabla^2\phi = \frac{\phi}{k_B T}\frac{q^2}{\varepsilon}\sum z_j^2 n_{0j} \tag{2.11}$$

Denoting $\kappa^2 = \frac{q^2}{\varepsilon k_B T}\sum z_j^2 n_{0j}$, Equation 2.11 can be simplified to:

$$\nabla^2\phi = \kappa^2\phi \tag{2.12}$$

The Debye-Hückel theory is equivalent to the thick double layer limit, applied for ions. Thus, it should be solved using spherical coordinates. To illustrate, we simplify the problem to 1D, then Equation 2.12 has solution of the form: $\phi(r) = \phi_1 e^{\kappa r} + \phi_2 e^{-\kappa r}$. Solving this ODE with appropriate boundary conditions ($\phi(r = \infty) = 0$ and $\phi(r = 0) = \phi_0$) yields[2]:

$$\phi_r = \phi_0 e^{-\kappa r} = \phi_0 e^{-r/\lambda_D} \tag{2.13}$$

[2]Here a model simpler than the one in Figure 2.3a is assumed. The outer Helmholtz plane is supposed to coincide with the surface, and so: $\phi_d = \phi_0$.

One can see that at a distance of λ_D, called *the Debye length*, the potential falls off to $\frac{1}{e}$ of its maximum value. Also, λ_D is inversely proportional to $\sqrt{\frac{1}{2}\sum z_j^2 n_{0j}}$, the square root of the *ionic strength* of the electrolyte solution. Increasing the concentration of the electrolyte will increase the ionic strength of the solution and as a result, decrease λ_D.

For a symmetric monovalent electrolyte solution like *KCl*, the Debye length can be calculated as:

$$\lambda_D = \kappa^{-1} = \sqrt{\frac{\varepsilon k_B T}{2q^2 n_0}} \tag{2.14}$$

where ε is the permittivity of the solution, k_B is the Boltzmann constant, T is the absolute temperature, q is the elementary charge, and n_0 is the number density of the ions in the bulk. For a 1M KCl solution at room temperature: $\varepsilon = 80 \times 8.85 \times 10^{-12}\ F/m$, $k_B = 1.38 \times 10^{-23}\ J/K$, $T = 293\ K$, $q = 1.60 \times 10^{-19}\ C$, $n_0 = 6.02 \times 10^{26}\ m^{-3}$, the Debye length is $0.305\ nm$. For a $1\ mM$ KCl solution at room temperature ($\sigma \simeq 15\ mS/m$), $\lambda_D = 9.6\ nm$.

The Gouy-Chapman theory. If we assume that the thickness of the double layer is much smaller than the curvature of the charged object (the think double layer limit), the object can be considered planar, then Equation 2.12 can be reduced to 1D problem and solved analytically. The solving method can be referenced from the book "Colloidal Dispersions" of Russel *et. al.*[125] (page 101). The potential is found to be:

$$\phi = \frac{2k_B T}{q} ln\left(\frac{1+\gamma e^{-\kappa y}}{1-\gamma e^{-\kappa y}}\right) \approx \frac{4k_B T}{q}\gamma e^{-\kappa y} \tag{2.15}$$

where $\gamma = tanh\left(\frac{q\phi_0}{4k_B T}\right)$. We can see that when $\phi_0 \to 0$, Equation 2.15 becomes Equation 2.13, the Debye-Hückel approximation with 1D assumption.

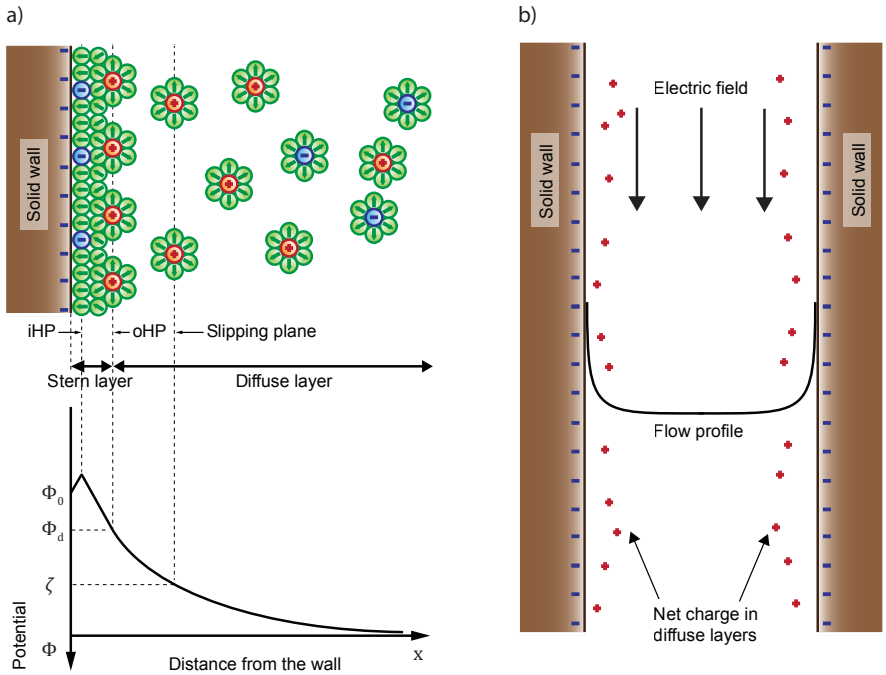

Figure 2.3: The electrical double layer and its relation to electroosmotic flow. a) Structure of the electrical double layer; b) Mechanism of the electroosmotic flow

2.4.2 Electroosmotic Flow

It has been known for more than two hundred years that an applied voltage can be used to transport an electrolyte solution in a channel with charged walls[126]. This phenomenon can be explained by the theory of the *electrical double layer*. Due to the structure of the electrical double layer, for the case in Figure 2.3a, the potential drops exponentially (in absolute value) from the outer Helmholtz plane into the bulk electrolyte solution. The charge density also decreases exponentially from the outer Helmholtz plane into the bulk electrolyte solution. Therefore, there is a net charge in the diffuse layer. If an electric field is applied tangential to the wall, as illustrated in Figure 2.3b, at some certain plane in the diffuse layer, called the *slipping plane*, the counter charges will move, dragging the fluid with them to form a plug-like flow profile. In essence, the slipping plane separates mobile fluid from stationary fluid that remains attached to the surface. The potential at the slipping plane is called the *zeta potential* ($\zeta - potential$). The electroosmotic flow velocity is related to the zeta potential of the wall via the Helmholtz– Smoluchowski equation:

$$u_{eof} = -\frac{\varepsilon \zeta_w}{\eta} E_t \tag{2.16}$$

Here u_{eof} is the electroosmotic flow velocity, ε is the permittivity of the fluid, ζ_w is the zeta potential of the wall, η is the viscosity of the fluid, and E_t is the electric field component tangential to the wall.

It is convenient to define the *electroosmotic mobility,* which is the ratio between the electroosmotic velocity and the tangential electric field:

$$\mu_{eof} = \frac{u_{eof}}{E_t} = -\frac{\varepsilon \zeta_w}{\eta}$$

2.4.3 Electrophoresis

The electrical double layer also forms when a charged particle is in contact with an electrolyte solution. In this situation, the relation between the size of the particle and the thickness of the double layer needs to be considered. If the particle is roughly one micrometer or bigger, which is typically much larger than the thickness of the double layer (several nanometers), similar arguments as with electroosmotic flow can be used and the electrophoretic velocity can be calculated as[127,128]:

$$u_{ep} = \frac{\varepsilon \zeta_p}{\eta} E \tag{2.17}$$

Here u_{ep} is the electroosmotic flow velocity, ε is the permittivity of the fluid, ζ_p is the zeta potential of the particle's surface, η is the viscosity of the fluid, and E is the applied electric field. This equation is very similar to the equation of electroosmotic flow (2.16), only with the difference in sign. It is because in both cases, the physical chemistry effects are the same, only that Equation 2.16 expresses fluid velocity with respect to a wall while Equation 2.17 calculates the particle (wall) velocity with respect to the fluid, hence the sign difference.

It is, again, convenient to define the *electrophoretic mobility,* which is the ratio between the electrophoretic velocity and the electric field:

$$\mu_{ep} = \frac{u_{ep}}{E} = \frac{\varepsilon \zeta_p}{\eta}$$

When the particle size is comparable to the Debye length, which is in the limit of a thick double layer, a different equation for electrophoresis should be used[128]:

$$u_{ep} = \frac{2\varepsilon \zeta_p}{3\eta} E \tag{2.18}$$

which has similar form to the case of the thin double layer, only that the coefficient has changed from 1 to $\frac{2}{3}$.

2.4.4 Measurement of Phase Lag between Electroosmotic Flow and Electric Field

The normal situation in electrokinetics, which is also the case in capillary electrophoresis, is that electroosmotic flow and electrophoresis take place simultaneously. Conceivably, they must have different response time because the inertia of the volume of a fluid is much larger than that of a single particle. If there is any phase lag between the movement of a bead when applying, for example, an AC sinusoidal field, it would be attributed to the slower response of electroosmotic flow.

To investigate this matter, electrokinetic experiments were performed in a DLD device with carboxylate-modified beads of 2 μm in diameter suspended in a 1.7 mM KCl solution, having the conductivity of $25 mS/m$. No electroosmotic suppressor (PVP or Pluronic F127) was used and the device was not exposed to elevated temperature after bonding (Section 3.1), all is to enhance the electroosmotic flow during the experiments. The high intensity LED lamp used to expose the fluorescent beads was synchronised with the AC voltage applied across the device. The electrical setup performing this task is shown in Figure 2.4.

The output sinusoidal signal from a function generator (15 MHz function/arbitrary waveform generator, model 33120A, Hewlett Packard, Palo Alto, CA, USA) was amplified

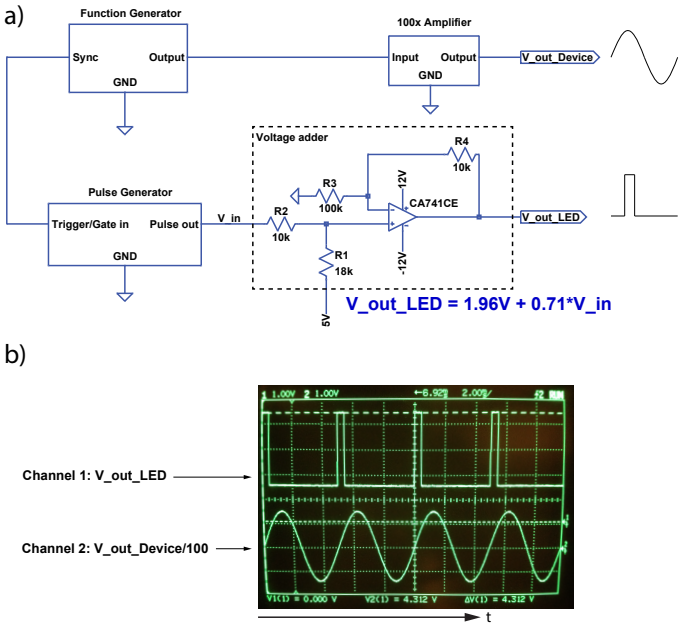

Figure 2.4: Synchronisation of the rectangular pulses of the LED light and the AC voltage applied to the device. a) Schematic of the electrical setup. b) Oscilloscope screen showing the syncronised voltages fed to the LED and to the device

100 times by a Bipolar operational power supply/amplifier (BOP 1000M, Kepco, Flushing, NY, USA) whose output was applied across the device. The sinusoidal signal from the function generator was synchronized with a rectangular signal from a pulse generator (TGP110 10MHz Pulse generator, Thurlby Thandar). The duty cycle of the rectangular signal was adjustable, capable of providing a very short pulse to the LED. An op-amp voltage adder circuit was used to raise the lower level of the rectangular signal to a value above zero, making the beads visible even between the peaks. As a result, an observer would see the beads at high intensity of light for a short period of time and at low intensity between peaks. The trigger of the pulse generator was adjusted to coincide with the beginning of the sine wave (Figure 2.4b). The phase lag between the electrokinetic oscillation of the beads (due to electroosmotic flow and particle electrophoresis) and the sinusoidal signal, if exists, can be pinpointed by the phase lag between the high intensity period and the starting point of each oscillation.

The results are shown in Figure 2.5. First of all, since the electroosmotic flow has positive mobility in PDMS channels[129], and since the terminal electrode was on the left and the ground electrode was on the right, the electroosmotic flow would be from the left

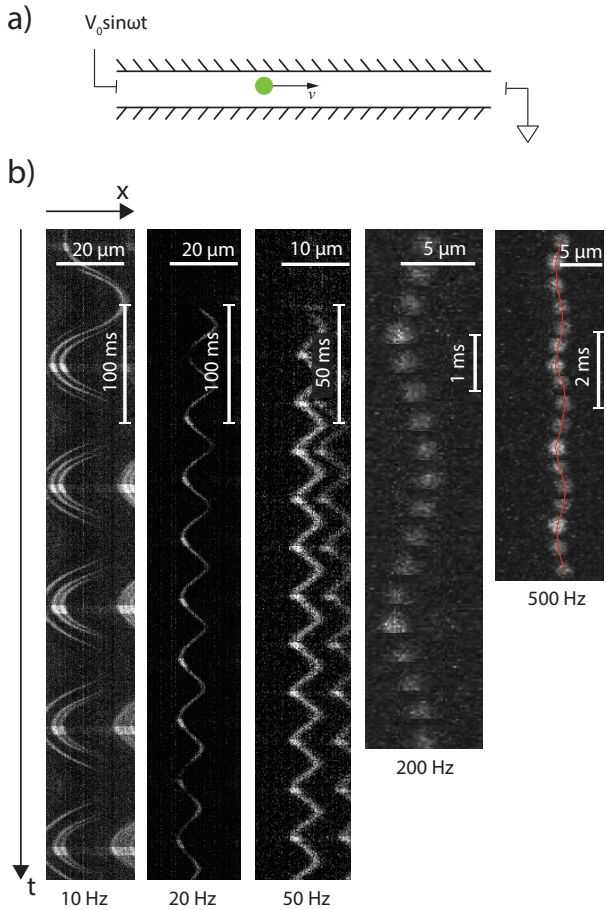

Figure 2.5: Experiments to measure the phase lag between electroosmotic flow and electric field. a) Schematic of the setup. b) Kymographs showing the positions of the beads as a function of time. The original videos were taken at 2100 frames per second. The spatial and temporal scales are different for each graph. In all cases, the terminal electrode was on the left and the ground electrode was on the right. For the case $f = 500\ Hz$, lines connected the centres of the bead at different time points have been drawn to guide the eyes.

to the right during the positive half cycle of the sinusoidal signal applied on the device. Here we also see the beads lit up before they move from the left to the right (most visible at 20 Hz), which confirms that the electroosmotic flow was dominant over the particle electrophoresis, which is in the opposite direction for the negatively charged beads used here. Second of all, the beads lit up precisely at the beginning of their motion from the left to the right at all frequencies up to 200 Hz, which implies that there was no visible lagging between the beads' oscillation (mainly due to electroosmotic flow) and the electric field. This may also be valid at 500 Hz, although the small amplitude of the oscillation at this

frequency made it difficult to confirm. In conclusion, electroosmotic flow is fast enough to keep pace with the electric field at all frequencies up to 200 Hz.

2.5 Dielectrophoresis

This section aims to give a brief overview of dielectrophoresis. More detailed treatments of the topic can be found in several textbooks in this field[122,130].

2.5.1 Simple Picture - a Dielectric Particle in a Dielectric Medium in a Static Electric Field

When a neutral dielectric particle is immersed into a dielectric fluid under a static electric field, both the particle and the fluid are polarised and charge of opposite sign accumulates at either sides of the interface. If the particle is so small that the electric field does not vary significantly across its dimensions, the induced polarisability can be approximated as a dipole moment and the force acting on it can be written using a linear approximation of the field:

$$\mathbf{F} = (\mathbf{P} \cdot \nabla)\mathbf{E} \tag{2.19}$$

Here $\mathbf{P}$ is the dipole moment and $\mathbf{E}$ is the electric field. Equation 2.19 shows that the force is non-zero only if the field is non-uniform.

To approximate the particle as a dipole, the *effective moment method* is employed[131]. The effective dipole moment of a spherical particle, for example, is the moment of a dipole which will produce an identical electrostatic potential, if placed at the centre of the particle. This method has been used to derive the effective dipole moment of a spherical dielectric particle in a dielectric medium[131]:

$$\mathbf{P} = 4\pi r^3 \varepsilon_m \frac{\varepsilon_p - \varepsilon_m}{\varepsilon_p + 2\varepsilon_m}\mathbf{E} \tag{2.20}$$

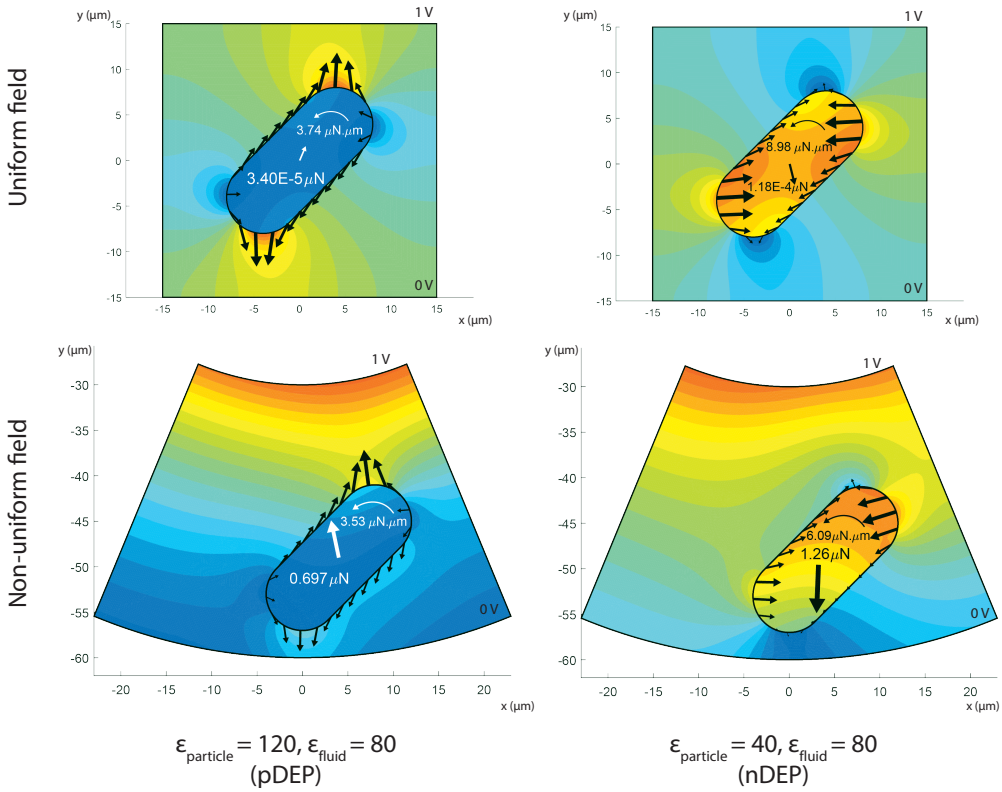

Figure 2.6: Numerical simulation of a rod-shape particle in a uniform or a non-uniform electric field. On the background is the magnitude of the field, on the boundary of the particle is the Maxwell surface stress tensor. Inside the particle, the DEP force and the torque acting on it are annotated. The arrows on the particle boundary has the same scale for all subfigure, while the arrows representing the DEP force and the torque are not for scale.

Here r is the particle radius, ε_m and ε_p are the permittivity of the fluid medium and the particle, respectively. It can be seen that the effective dipole moment is proportional to the volume of the particle and a term representing the "contrast" in permittivity between the particle and the medium, known as the *Clausius-Mossotti factor:* $f_{CM} = \frac{\varepsilon_p - \varepsilon_m}{\varepsilon_p + 2\varepsilon_m}$. Since $\nabla \times \mathbf{E} = 0$ and $\nabla(\mathbf{A} \cdot \mathbf{B}) = (\mathbf{A} \cdot \nabla)\mathbf{B} + (\mathbf{B} \cdot \nabla)\mathbf{A} + \mathbf{A} \times (\nabla \times \mathbf{B}) + \mathbf{B} \times (\nabla \times \mathbf{A})$, Equation 2.20 and Equation 2.19 can be combined to yield:

$$\mathbf{F_{DEP}} = 2\pi r^3 \varepsilon_m \frac{\varepsilon_p - \varepsilon_m}{\varepsilon_p + 2\varepsilon_m} \nabla |\mathbf{E}|^2 \tag{2.21}$$

When the particle has complicated shape or when the field varies significantly across the particle, the effective moment approximation can be erroneous. Instead, the dielectrophoretic force can be integrated from the Maxwell surface stress acting on the particle. Such calculations can be done in a numerical Finite Element Analysis software, for example COMSOL Multiphysics (Figure 2.6). Figure 2.6 illustrates the 2D simulation of a hypothetical rod-shape particle in a uniform and a non-uniform field. Several remarks can be made regarding the simulated results. First of all, it is clear that the DEP force in the uniform field is negligibly small, four to six orders of magnitude smaller than in the non-uniform field, although the Maxwell stress at the surface has comparable magnitude. Second of all, the DEP force points to the region of higher field when the permittivity of the particle is larger than that of the fluid (positive DEP) and to the region of lower field when the permittivity of the particle is smaller than that of the fluid (nDEP). Lastly, in all cases there are torques of the same order of magnitude which tend to rotate the particle counter-clockwise so that its length aligns parallel with the field.

2.5.2 Practical picture - the Particle and the Medium have Non-zero Conductivity, and an AC Field is Applied

In a typical microfludic device, the medium is an electrolyte solution and the ions within the solution contributes to its conductivity. The particle may also have a surface conductance (polystyrene beads) or internal conductivity (cells). Furthermore, the field is normally not a simple DC static field but an AC field, whose frequency in the range of kHz or MHz. Therefore, the dielectrophoretic force in Equation 2.21 is modified to include the conductivity of the particle and medium and the time average value of the field:

$$\mathbf{F_{DEP}} = 2\pi\varepsilon_m r^3 Re\left(\frac{\tilde{\varepsilon}_p - \tilde{\varepsilon}_m}{\tilde{\varepsilon}_p + 2\tilde{\varepsilon}_m}\right)\nabla|\mathbf{E_{rms}}|^2 \tag{2.22}$$

where $\tilde{\varepsilon}_m$, $\tilde{\varepsilon}_p$ are the complex permittivities of the particle and the suspending medium, defined as: $\tilde{\varepsilon} = \varepsilon - i\sigma/\omega$ (ε denotes the permittivity, σ denotes the conductivity, and ω is the angular frequency of the electric field).

For polystyrene beads, the bulk conductivity σ_b is negligibly small and their conductivity comes from the surface conductivity σ_s[122]:

$$\sigma_p \simeq \sigma_s = \frac{2K}{r} \tag{2.23}$$

where r is the radius and K is the surface conductance of the beads.

In the cases where cells are studied, their complicated structures can be modeled as a two-shell or three-shell sphere and the effective Clausius-Mossotti factor can be calculated from the contribution of each layer[130].

2.6 Simulation

When the geometry is complicated or when the mathematics is too complex to produce an analytical solution, especially when many physical mechanisms are involved, a numerical simulation based on differential equations and proper boundary conditions provides a rather direct, engineering way to look at the problems at hand. Simulation is also advantageous for approving or disproving novel ideas, since prototyping in microfludics is costly and time consuming. All the simulations in this work were built using COMSOL Multiphysics. The *physics*[3] used are summarized below and more details can be found in Table 2.1.

i. Stokes flow is used for calculating the velocity profile of the fluid in the devices. Since the Reynolds number of microfluidic devices is well below unity, the inertial component can be neglected. Also, since the fluid velocity is well below the speed of sound, the flow is assumed incompressible. The wall boundary condition can be non-slip (pressure driven flow) or slip boundary condition (electroosmotic flow).

ii. Wall distance is useful when calculating the distance from the centre of mass of a particle to a wall to apply a wall force. It is described using an *Eikonal equation.*

[3] *The physics* here are the names of the modules in COMSOL, which do not necessarily coincide with the concepts they suggest.

Table 2.1: Physics used in simulations. Meaning of symbols can be found at the List of Symbols on page xiii.

Physics	Differential equations/Boundary conditions	Meaning
Stokes flow	$0 = \nabla.\left[-p\mathbf{I} + \eta\left(\nabla\mathbf{u} + (\nabla\mathbf{u})^T\right)\right] + \rho\mathbf{f}$	Inertial term neglected (left hand side); surface forces and body forces adds up to zero (right hand side).
	$\rho\nabla.\mathbf{u} = 0$	Incompressible flow
	$\mathbf{u} = 0 \mid_{walls}$	No-slip boundary condition
	$\mathbf{u} = \mu_{eof}\mathbf{E}_t \mid_{walls}$	Electroosmotic flow boundary condition
	$p = p_0 \mid_{inlet}, p = 0 \mid_{outlet}$	Pressure at the inlet and outlet of the device
Wall distance	$\lvert\nabla D_w\rvert = 1$	The norm of the gradient of wall distance is unity
	$D_w = 0 \mid_{wall}$	Wall distance is zero for the points on the wall
Electric current	$\nabla.\mathbf{J} = 0$	Continuity equation of current
	$\mathbf{J} = \sigma\mathbf{E}$	Ohm's law in steady state
	$\mathbf{J} = (\sigma + i\omega\varepsilon_0\varepsilon_r)\,\mathbf{E}$	Ohm's law in frequency domain
	$\mathbf{J} = \left(\sigma + \varepsilon\varepsilon_r\frac{\partial}{\partial t}\right)\mathbf{E}$	Ohm's law in transient state
	$\mathbf{E} = -\nabla V$	Definition of electric potential
	$V = V_0 \mid_{inlet}, V = 0 \mid_{outlet}$	Voltage at the inlet and outlet of the device
Particle tracing for fluid flow	$\frac{d}{dt}(m_p\mathbf{v}) = \mathbf{F_t}$	Newton's second law
	$\mathbf{F_d} = \frac{1}{\tau_p}m_p\,(\mathbf{u} - \mathbf{v})$	Drag force, Stokes form used for laminar flow
	$\tau_p = \frac{\rho_p d_p^2}{18\eta}$	Particle velocity response time for spherical particles in a laminar flow
	$\mathbf{F_w} = F_{w0} \times step\left(D_w - r_p\right) \times (-\mathbf{D_{dir}})$	Wall repulsive force
	$\mathbf{F_{DEP}} = 2\pi r_p^3\varepsilon_m Re\{f_{CM}\}\nabla\lvert\mathbf{E_{rms}}\rvert^2$	Dielectrophoresis force
	$f_{CM} = \frac{\tilde{\varepsilon}_p - \tilde{\varepsilon}_m}{\tilde{\varepsilon}_p + 2\tilde{\varepsilon}_m}$	The Clausius-Mosotti factor
	$\tilde{\varepsilon} = \varepsilon - j\frac{\sigma}{\omega}$	Complex permittivity

iii. Electric current provides solutions to the electric field in the device, which will be used later as an input to calculate electroosmotic flow and dielectrophoretic force. In this work, it is assumed that there is no current source or external current density.

vi. Particle tracing for fluid flow provides a computationally reasonable way to simulate dynamics of the particles in a DLD device under the combined action of pressure driven flow, electroosmotic flow, electrophoresis and dielectrophoresis.

Chapter 3

Device Fabrication and Experimental Setup

If you optimise everything,
you will always be unhappy.
— Donald Knuth

The research methodology is illustrated in Figure 3.1. The research ideas can come from either *a technological-driven approach* (literature and our previous work) or *an application-driven approach* (biological or medical needs). To probe the feasibility of the ideas, a modelling or simulation step can be performed (Section 2.6), but can be skipped if the implementation of the ideas is straightforward. The next step, device fabrication, includes several sub steps: designing and making photolithographic masks, making moulds, and finally casting and bonding devices. The details can be found in section 3.1. The experiments are then performed on the fabricated devices with model particles (*e.g.* polystyrene microspheres) or with cells and bioparticles. The results will be documented and recorded via a microscope equipped with optics and cameras (Section 3.2). In the next step, experimental data will be processed, analysed, and compared with simulation results. Normally, it takes several iterations through the previous steps before the results of the study can be ready for dissemination.

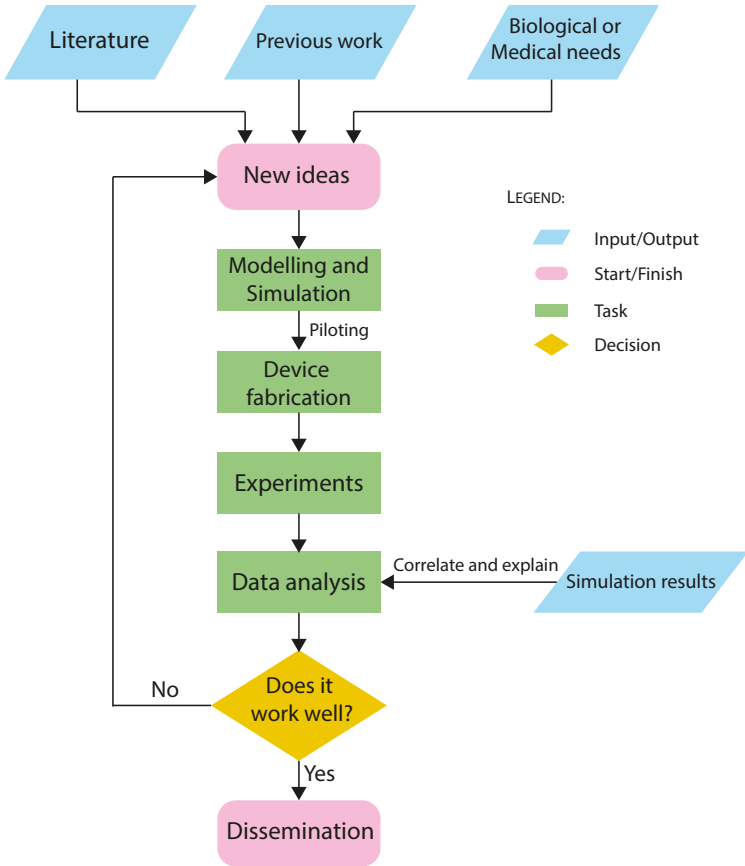

Figure 3.1: Typical methodology flow chart used for the work presented within this thesis.

3.1 Device Fabrication

All devices were cast from a silicon-based organic polymer called *polydimethylsiloxane*, normally abbreviated as PDMS. The material is transparent, non-toxic, impermeable to water but permeable to air and other gases, making it suitable for biomedical microfluidic devices. The making of a PDMS device is termed *soft lithography*[4]. It is relatively simpler and less equipment intensive than a conventional lithography process. However, to make the mould for soft lithogaphy, a conventional clean room lithography process using a photosensitive resist is required. The complete device fabrication procedure includes:

- Drawing of the devices' features on an electronic file. The CAD software named Tanner L-Edit (Mentor Worldwide LLC, Santa Barbara, California, USA) was used.

- ▷ Fabrication the chromium-coated glass mask. For the work presented within this thesis, the masks were outsourced to a mask manufacturing company (Delta Mask B.V., Enschede, The Netherlands). The mould for soft lithography was fabricated in Lund NanoLab by using a $10 - 50\ \mu m$ thick layer of the negative photoresist SU-8 on a silicon wafer. The SU-8 layer has the counterpart features of the features of the device, for example holes on the SU-8 mould correspond to pillars in the device. An antisticking step with *trichloro (1H,1H,2H,2H-perfluorooctyl) silane* (PFOTS) (Sigma Aldrich, Saint Louis, MO, USA) in vapour phase on the mould is needed to facilitate demoulding of PDMS. Several moulds can be fitted on a single 3-inch wafer, as illustrated in Figure 3.2.

- ▷ Generation of the PDMS imprint by soft lithography. This was carried out by mixing the monomer (Sylgard 184, Dow Corning Inc., USA) with its curing agent at a ratio of $10 : 1\ (w/w)$ and pouring it on the mould. The liquid PDMS on the mould is then cured at $80°C$ for an hour. The hardened PDMS layer is then peeled off from the mould, trimmed, perforated with access holes, treated with oxygen plasma, and bonded on a PDMS-coated glass slide. Thereafter, silicon tubing is added to act both as liquid reservoirs and as an interface to the pressure controller (Figure 3.2).

- ▷ An additional surface treatment of the DLD devices may be required for specific applications. In Paper II, to reduce sticking of *S. pneumoniae* to the PDMS walls, the devices were filled with PLL(20)-g[3.5]-PEG(2) solution after bonding for 20 minutes. In Paper I, the bonded devices were left in an oven at $120°C$ for 24 hours[132] to bring the PDMS surface back to its native hydrophobic state, making it stable for electrokinetic experiments.

The last three steps described above have been developed and optimised previously in our group and more details can be found in other publications[48,133]. The first step, the drawing and designing of DLD devices, is often the most time-consuming step due to the vast amount of features of a DLD array which need to be positioned precisely. However, this step can be sped up significantly by the implementation of software script into L-Edit, which automate the process. The script also reduces human errors when designing the separation arrays.

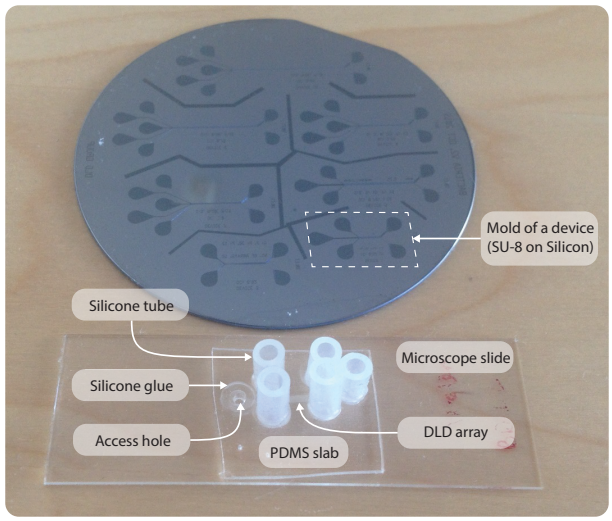

Figure 3.2: An SU-8 silicon wafer and a bonded PDMS device on a standard microscope slide.

3.1.1 Implementing Scripts for Automated Device Drawing

Although the finer details can be more complicated, a typical design of a DLD device is illustrated in Figure 3.3a. Unless internal electrodes are needed (Paper V), the device can be drawn on one single layer, corresponding to one single lithography mask. The green areas are hollow space where liquid can flow while the white areas are PDMS obstacles or walls. A typical device consists of inlet and outlet reservoirs, a pillar array where separation takes place, and channels connecting the array and the reservoirs. Within the array, the pillars are arranged inclined to the overall flow direction, facilitating deterministic lateral displacement (more details can be found in Section 2.1). Edge correction[100] is implemented to minimise wall effects and to ensure a symmetric flow pattern throughout the array. Two additional straight pillar arrays are positioned between the tilted array and the connecting channels to ensure that the particles move as they are expected when they enter and exit the tilted arrays.

L-Edit is a CAD software which allows users to draw basic shapes (rectangulars, circles, polygons, *etc.*) whose dimensions can be specified precisely, via a graphic user interface (GUI). It also provides various functions to transform these shapes. A complicated geometry, for example a DLD array, can be constructed from basic shapes via a hierarchical organisation. In this organisation, every design feature, from a basic shape to a whole

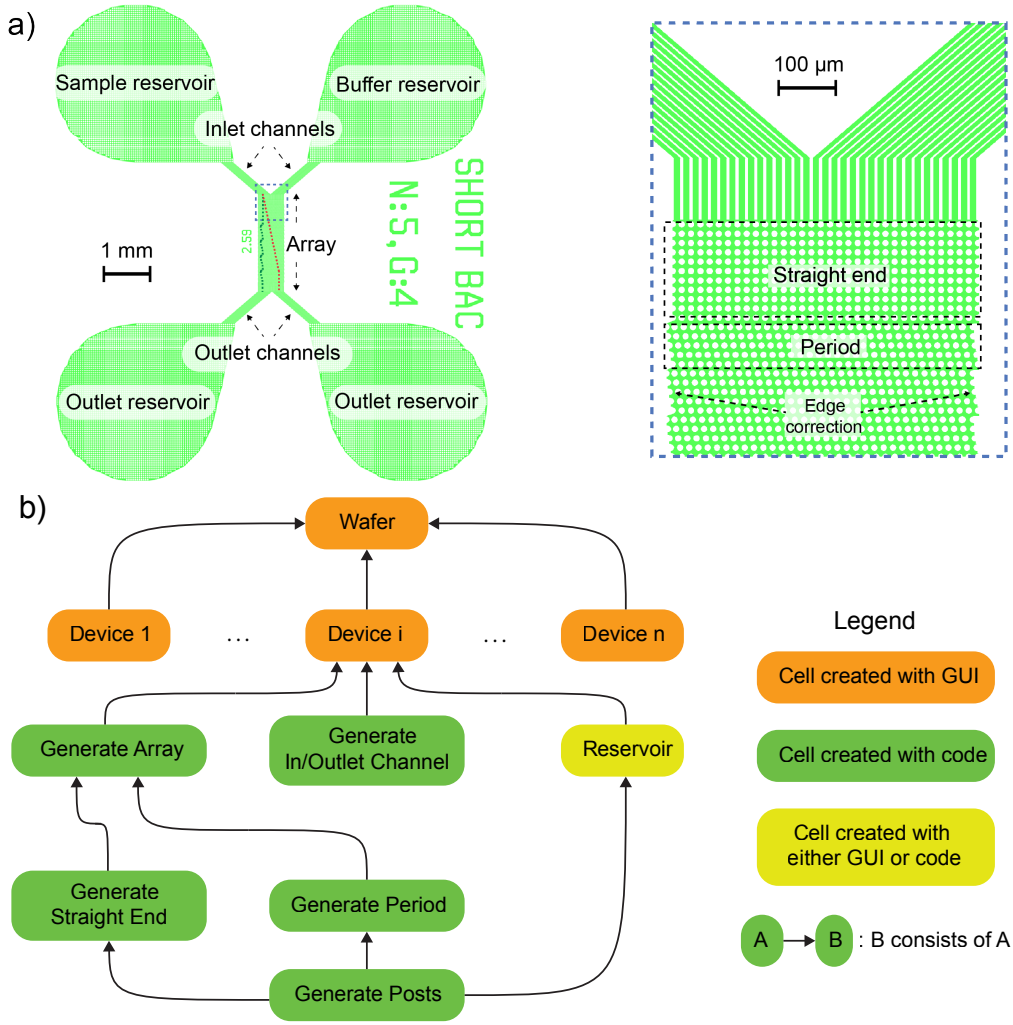

Figure 3.3: Design of DLD device. a) A typical design of a DLD device, b) The design is structured in a hierarchical order using cells in L-Edit.

device, is called *cell* and a cell at a higher hierarchical level can be built by populating it with instances of cells at a lower level, making it easy to modify or reuse a design. It also supports programmable drawing mode via *T-cell* (Template cell), in *C* language, allowing users to draw shapes of parameterised size or clone an array of shapes with parameterised quantity. Both the GUI and the programmable interface have their own advantages. The GUI provides flexible drawing and positioning of shapes in specific cases where programming is impossible, whereas the programmable interface enables designing and placing features in

a parametric and automatic manner. The two approaches can be combined to optimise the designing process.

A simplified process of designing the devices is described in the diagram of Figure 3.3b. The cells with green background are T-cells while the cells with orange background are created using the GUI. The reservoirs can be drawn either by code or by the GUI, depending on the specific situation. The design task starts with creating posts (pillars) (*Generate Posts*) and then arranging posts into arrays without or with a tilt with respect to the overall fluid direction (*Generate Straight End* and *Generate Period*). The straight ends and the periods are then combined into the array (*Generate Array*) and the connecting channels are also generated (*Generate In/Outlet Channel*). The reservoirs have some parts which can be programmed, but also some parts which can be done easier with GUI. A *Device* is then constructed by combining the array, the connecting channels, and the reservoirs. Finally, the devices are arranged so that they fit onto a *Wafer* of suitable size (*e.g.* a 3-inch wafer).

Although the procedure was described in a bottom up manner, when all the modules (T-cells) have been prepared, the designing process is carried out top down. For example, generating an array is performed by calling the corresponding T-cell with its own parameters without paying any attention to the T-cells at a lower levels (*Generate straight end*, *Generate period* or *Generate posts*), which makes the designing task easy and convenient. [1]

3.2 Experimental Setup

A typical experimental setup is shown in Figure 3.4. A pressure gradient was created by letting the outlet reservoir be open to the ambient air while connecting inlet reservoirs to an overpressure controller or a syringe pump. The setup presented here uses a $MFCS - 4C$ pressure controller (Fluigent, Paris, France), connected to the reservoirs of the device via silicone tubes and T-connectors. To bias the device with a voltage, holes were drilled through the elbow connectors and platinum electrodes were pushed through the holes, glued and embedded into the fluid in the reservoirs (Figure 3.4a).

[1] The source code for the T-cells used in this work to draw a DLD array can be found at bit.ly/DLDScript (case sensitive), and is free to use under CC 4.0 BY-NC.

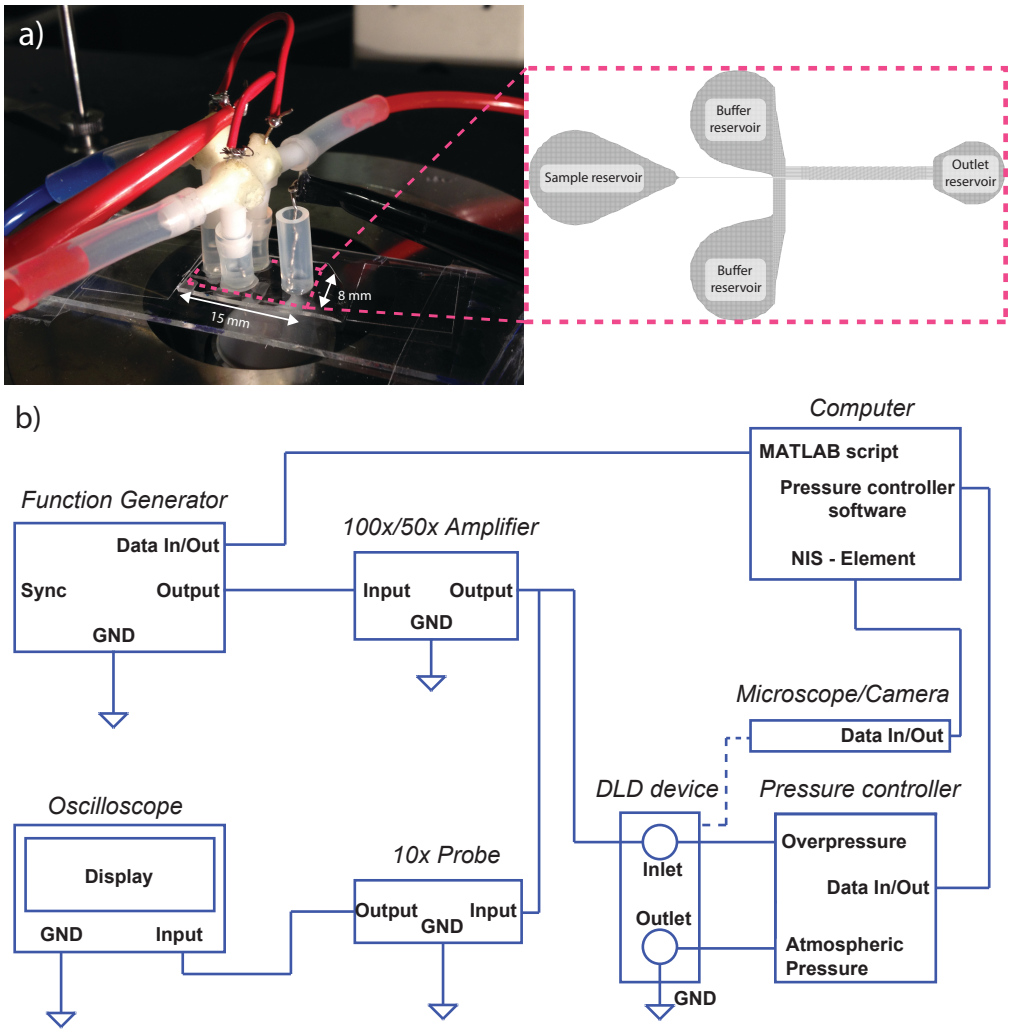

Figure 3.4: Experimental setups. a) Picture of a DLD device connected to tubing and electrical wiring (left), along with an overview of the layout of the device (right). b) Schematic of the full setup (Paper I, III, and IV). In Paper V, the amplifier was omitted. In Paper II, no electrical equipment was used.

To generate DC or AC fields, a function generator (15 *MHz* function/arbitrary waveform generator, model 33120A, Hewlett Packard, Palo Alto, CA, USA) was used and the signals were amplified 100 times by a Bipolar operational power supply/amplifier (BOP 1000M, Kepco, Flushing, NY, USA) to give a maximum voltage of 1000 V_{pp} at 1 *kHz*. Alternatively, a high-frequency, 50× amplifier (WMA-300, Falco Systems, Amsterdam, The Netherlands) can be used to give a maximum voltage of 300 V_{pp} at 1 *MHz*.

The voltage was measured using an oscilloscope (Hewlett Packard 54603B 60MHz), via a 10× probe (Kenwood PC-54, 600 V_{pp}). An inverted microscope (Nikon Eclipse TE2000-U, Nikon Corporation, Tokyo, Japan) and an Andor Neo sCMOS camera (DC-152Q-FI, Andor Technology, Belfast, Northern Ireland) were used to acquire the images and videos of the experiments. A colour camera (Exmor USB 3.0, USB29 UXG M) was used to capture colour video if necessary, for example in the experiments with non-fluorescen viable/non-viable yeast cells or with fluorescence viable/non-viable *E. coli*. The images captured from the camera were recorded into a computer hard drive using NIS Element software (NIS Element Advanced Research v4.51, Nikon).

Chapter 4

Summary of Results and Outlook

If I have seen further than others,
it is by standing upon the shoulders of giants.
— Isaac Newton

This chapter summarises the motivations and the main results of the papers and of the ongoing adipocyte sorting project, and discusses some conclusions and outlook.

4.1 Electrokinetic Deterministic Lateral Displacement (Paper I)

Size is probably the most common parameter in label-free particle sorting. Nevertheless, particles derived from an initial population, for example viable and non-viable cells of some kind, can be quite homogeneous in size. In those situations, parameters other than size need to be employed. Although DLD was originally a size-based method, it has been demonstrated that the effective size of polystyrene beads in a DLD device could be tuned with an AC voltage[107]. This suggests that electrical and dielectric properties of particles can be exploited as new parameters for separation in DLD devices.

In Paper I, we employed surface electric properties and dielectric properties of particles and cells to sort them in a DLD device. We have shown that by combining electrokinetics with DLD (Section 3.2) and tuning the AC frequency, similar-sized polystyrene particles

of differently modified surface properties could be sorted. Interestingly, using the same principle, viable and non-viable yeast cells and viable and non-viable *E. coli* bacteria could also be separated with high purity.

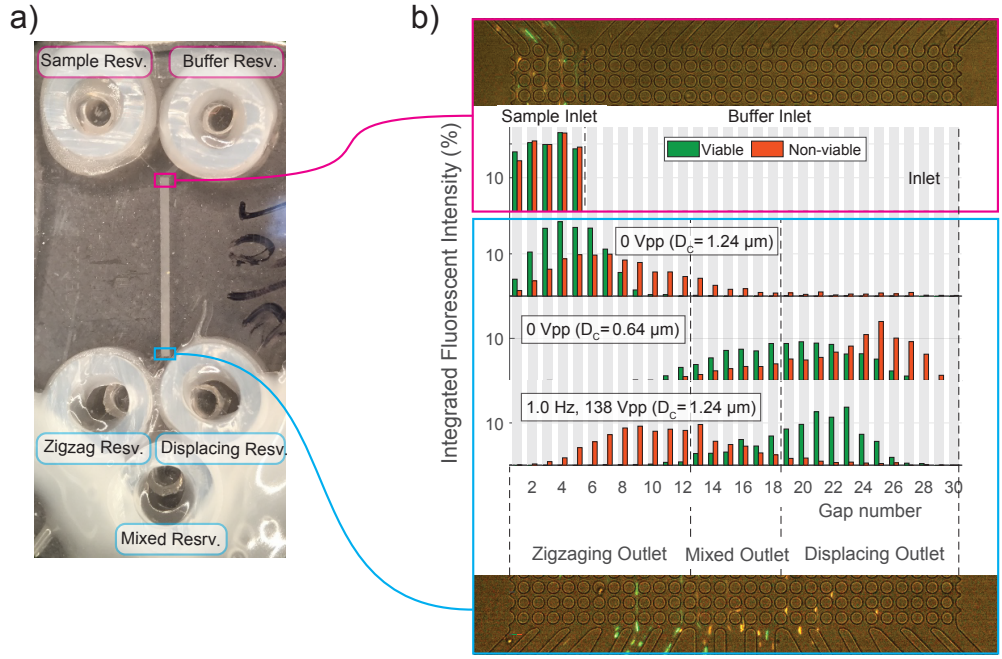

Figure 4.1: Separation of viable and non-viable *E. coli* using Electrokinetic DLD. a) Actual device sorting viable from non-viable *E. coli*. b) Distribution of *E. coli* at different gaps. First graph: inlet; second graph: outlet of a device having $D_C = 1.24\ \mu m$, no applied voltage; third graph: outlet of a device having $D_C = 0.64\ \mu m$, no applied voltage; fourth graph: outlet of a device having $D_C = 1.24\ \mu m$, when a voltage of $1\ Hz$, $138\ Vpp$ was applied.

Figure 4.1b illustrates the benefit of electrokinetic DLD in sorting viable and non-viable *E. coli*. A mixture of bacteria was injected into the DLD array through five lanes close to the left wall. In the normal DLD mode (pressure driven flow, no voltage applied), at the outlet of a device having $D_C = 1.24\ \mu m$, both types of cells displayed zigzagging tendency, with non-viable cells appearing to be slightly larger and having a broader distribution. On the other hand, in a device having $D_C = 0.64\ \mu m$, also in normal DLD mode, both types of cells displayed displacing tendency, with non-viable cells appearing to be slightly larger and both types of cells having broad distributions. In both cases, separation of viable and non-viable *E. coli* at high purity was deemed to be difficult. However, if an AC voltage of $1\ Hz$, $138\ Vpp$ was applied along the device having $D_C = 1.24\ \mu m$, viable and non-viable bacteria could then be separated laterally with a small overlap at the outlet. In this case, non-viable cells, interestingly, exhibited lower effective size.

4.2 Sorting Bacterial by Chain Length (Paper II)

Many bacteria are pathogenic, causing serious diseases in humans. Among them, *S. pneumoniae* is a major cause of pneumonia which leads to more than one million deaths worldwide annually, and is thus the subject of many biomedical studies. *S. pneumoniae* bacteria exist in their colonies as either single bacteria (cocci), diplococci, or chains of many cocci with varying length. It is believed that longer chains can adhere more to epithelial cells in the lung while shorter chains and single cocci are able to evade the immune system[134,135]. It is therefore of strong interest to sort these different morphologies of *S. pneumoniae* for further microbiological studies.

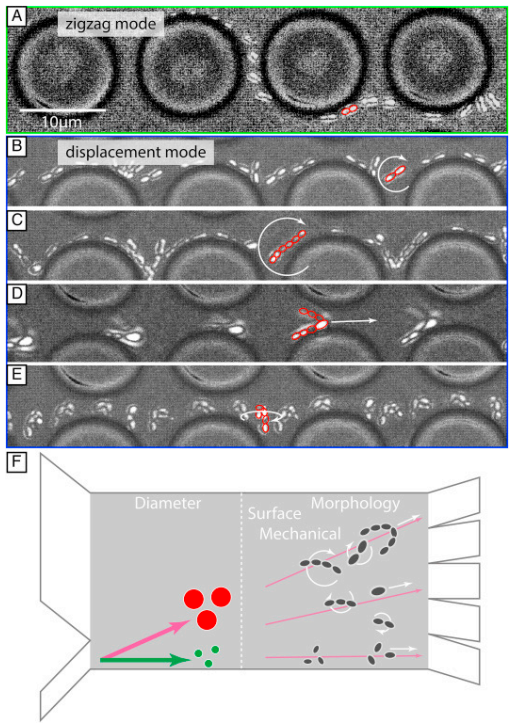

Figure 4.2: Sorting of *S. pneumonia* based on chain length. A)-E) Different trajectories of *S. pneumoniae* bacteria in a DLD device. F) Summary of the position a *S. pneumoniae* morphology can appear at the outlet, as a result of its width, length, and shape. Image taken from [109] (https://doi.org/10.1016/j.aca.2017.11.050, Creative Commons Attribution License (CC BY).

Different hydrodynamic behavior of long and short chains of *S. pneumoniae* in a DLD device, besides size, can be exploited for separation. It has been observed previously that in DLD a non-spherical particle would rotate to minimise its hydrodynamic resistance

and the smallest dimension would decide the particle's trajectory (*i.e.* zigzag or displacement)[76,97]. This is the case for the zigzagging thin diplococci exemplified in Figure 4.2A. However, when the length of the bacterial chains increase, the effective sizes of the chains are no longer their smallest dimension, due to their dynamical motions. For example, in Figure 4.2B and Figure 4.2C, the difference of fluid velocity between the two ends of a chain induces a flipping motion and leads to a displacement trajectory. In Figure 4.2D and Figure 4.2E, the chain became bent and appeared much larger than its width and as a result, travel in the displacement trajectory. In conclusion, the position of a single cocci or a chain at the outlet is dependent on its width, length, and shape (*i.e.* straight or bent chain) (Figure 4.2F).

In Paper II, with a device having the critical diameter approximately the size of a single coccus, we were able to enrich single cocci in the outlets corresponding to small effective sizes and long chains in the outlets corresponding to large effective sizes, for two different strains of *S. pneumoniae*: R6 (non-encapsulated) and D39 (encapsulated). During the experiments, we also managed to separate the two strains from each other. The separation might be contributed by their difference in size (width and chain length) or their surface property (R6 was found to be much more hydrophobic than D39).

Paper II proves that separation of different morphologies of *S. pneumoniae* is feasible with DLD. The next step is to scale up the number of bacteria sorted. A high throughput device is desirable due to two main reasons. First of all, to study a population of single cocci or a population of chains using RNA extraction and analysis, a large quantity of bacteria needs to be sorted, which is around 1-10 million colony-forming unit (CFU), within a time scale shorter than the bacteria's doubling time, which is around 20-30 minutes. This is far beyond the capability of the device presented in Paper II. Second of all, due to the inherent overlapping between the size distribution of singles and diplos and betweet chains and diplos, to obtain sufficiently pure population of single cocci, the critical diameter needs to be sufficiently small so that most of, if not all, diplo cocci are filtered out. Similar argument applies to sorting chains, but in this case the critical diameter should be large enough to remove diplo cocci from longer chains. This requirement on purity further reduces the quantity of bacteria can be collected after sorting. Inspired by the benefits a high throughput DLD device can bring, we have designed and fabricated such a device and tested it with polystyrene beads (Figure 4.3). The device was able to enrich 1.1 μm beads at high purity from a mixture of 1.1 μm and 2.1 μm beads (Figure 4.3c). The volumetric throughput

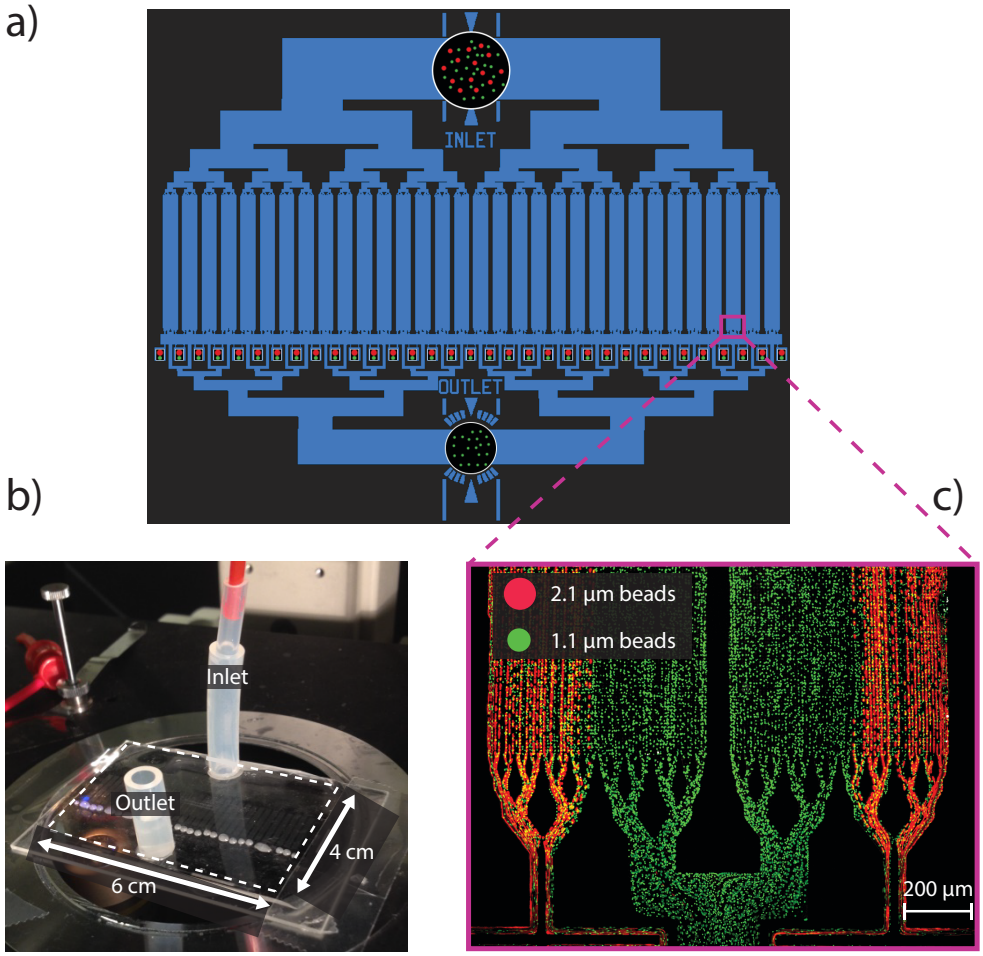

Figure 4.3: A high throughput DLD device intended for enrichment of single cocci. a) Design of device. The device has only one inlet reservoir and one outlet reservoir, with its sole purpose to enrich around half of all small particles in the mixture from the inlet reservoir into the outlet reservoir. There are 64 DLD arrays placed in parallel to increase the throughput. b) Actual image of the device. c) 1.1 μm beads were successfully enriched from the mixture into the outlet reservoir.

when running at 200 *mBar* over pressure was $43mL/minute$ and the quantitative throughput into the outlet reservoir is roughly 25000 $beads/second$. This means to obtain a million beads, the running time is only 40 seconds, which is a promisingly short running time, with regards to the bacteria doubling time of around $20 - 30$ *minutes*.

4.3 Electrokinetic Deterministic Lateral Displacement on an Open Channel Device (paper III)

Conventional DLD devices, and microfluidic devices in general, employ pressure pumps or syringe pumps to drive fluid through an enclosed channel. While this configuration provides stable and well-controlled fluid flow, in some cases, an open channel DLD device is preferable. In such device, one of the walls (*i.e.* the lid) is removed and the pillars and the fluid are open to the environment. This new configuration offers two main advantages: simplicity, since lid bonding and fluid pumping are avoided, and reusability, since the DLD channel can be washed and stored for reuse. When open DLD is combined with electrokinetics, an additional benefit emerges: adjustability of electrodes.

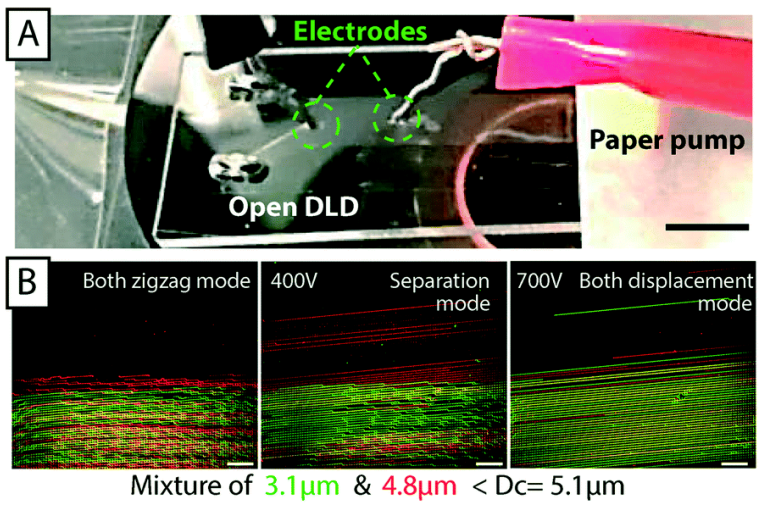

Figure 4.4: Combination of electrokinetics and open DLD. A) Setup of an electrokinetic open DLD where electrodes are placed directly on the pillar array surface. (Scale bar: $3\,mm$.) B) By tuning the voltage, $3.1\,\mu m$ and $4.8\,\mu m$ beads can be either separated or both displaced in a open DLD device with $D_C = 5.1\ \mu m$ (Scale bar: $100\ \mu m$). Image taken from [106], Published by The Royal Society of Chemistry.

The combination of electrokinetics and closed-channel DLD requires the electrodes to be embedded in the reservoirs (Beech *et. al* [107], paper I) and so, the distance between electrodes is fixed. In paper III, we tested the idea of placing electrodes directly on the surface of an open DLD device and as a result, were able to reduce the distance between electrodes from 30 mm down to 3 mm (Figure 4.4A). The placement of the electrodes on top of the array did not disturb the fluid flow and the separation of 3.1 μm and 4.8 μm beads in an open DLD device with $D_C = 5.1\ \mu m$ was demonstrated (Figure 4.4B).

4.4 Electrokinetic Rotation of Red Blood Cells in Deterministic Lateral Displacement (paper IV)

It has been proven that by controlling the depth of a DLD device, the orientation of red blood cells and thus their effective size can be changed. This effect was exploited to separate RBC from trypanosomes[97,98], the parasites which cause the *sleeping sickness* disease. Nevertheless, it is of interest to explore other methods which can also alter the orientation of red blood cells, as an alternative to fabricating DLD devices with the specific depth.

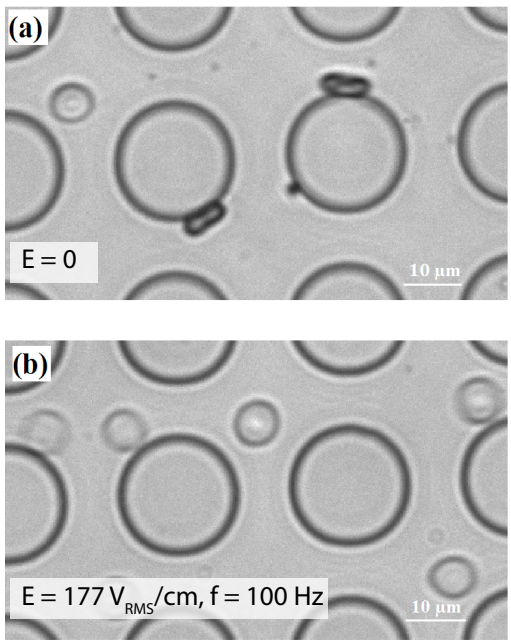

Figure 4.5: Effect of electric field on orientation of RBCs in a DLD device. a) In the absence of an electric field, when the cells travelled close to the pillars, they will lean against the pillars with their width, exhibiting a small effective size. b) When the field was on, the cells aligned horizontally like a disc, exhibiting larger effective size.

In paper IV, it was demonstrated that by applying a low frequency AC voltage (100 Hz) of a nominal value of around 177 V_{RMS}/cm, the orientation of red blood cells in deterministic lateral displacement (DLD) devices could be altered (Figure 4.5). Experiments showed that, due to this orientation change, the effective size of RBC can be increased by a factor of around 1.5, from below 3.47μm to 4.44 μm. In a future work, *Trypanosoma cyclops.* parasites can be tested in the same device and their displacement, as a function of voltage, can be compared with that of RBCs. If the difference in the effective

critical diameter of the RBCs and the parasites can be increased, then they can conceivably be separated by applying an AC voltage in DLD, as an alternative to fabricating DLD devices with specific depth. This would open up for deeper devices and therefore higher throughput.

4.5 Electrokinetic Deterministic Lateral Displacement with Metal-coated Pillar Array (paper V)

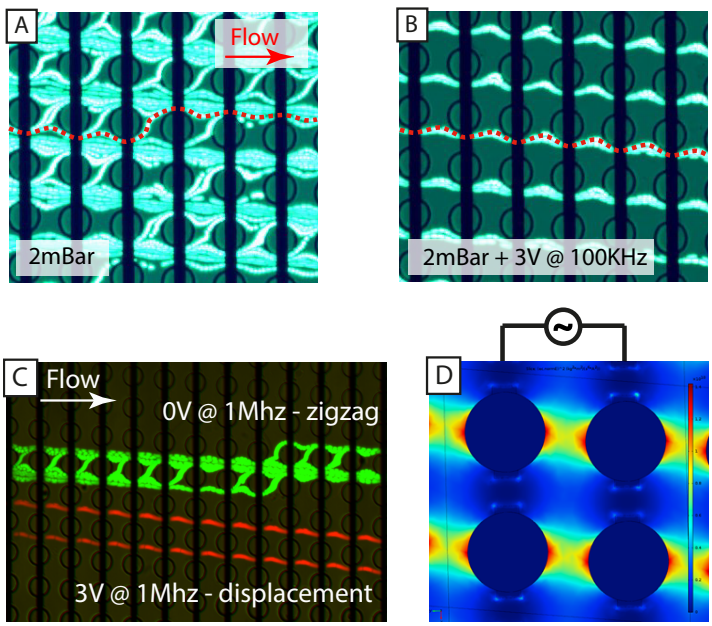

Figure 4.6: Trajectories of 2 μm carboxylate modified polystyrene particles in a metal DLD device having $D_C = 5.2\ \mu m$. A) The particles went zigzagging when no voltage was applied. B) The particles went displacing when a 3 V_{PP}, 100 kHz voltage was applied. C) Comparison of the trajectories of the same type of bead, with and without an applied voltage of 3 V_{PP}, 1 MHz. D) Numerical simulation of $|\mathbf{E}|^2$ in the metal-coated DLD array. Since the polystyrene beads experienced nDEP in our experimental conditions, they were repelled from the high field regions (red/yellow) and attracted to the low field regions (dark blue). If the flow is weak or the applied electric field is high, the beads will be trapped at the dark blue regions. Tweaking the flow and the applied field can result in particle being released from trapping, travelling with the flow but never crossing the red/yellow regions. Therefore, they will travel in displacing trajectories, following the orientation of the pillar array,

In Paper V, DLD devices with electrically connected metal-coated pillars were fabricated. Using this approach, a high field could be generated with a much smaller voltage than using macro electrodes embedded in reservoirs. By changing the applied voltage, tunable particle separations were achieved. At a voltage as low as 3 *Vpp*, it was possible to displace 2 μm polystyrene beads in a DLD device with a critical diameter of 5.2 μm, showing a large

dynamical range (Figure 4.6). Interestingly, by ramping up the voltage, separation of submicron polystyrene beads was achieved. This opens up the opportunity to sort bioparticles, for example viruses and exosomes, that are in the submicron range. The ability to displace exosomes with DLD has been demonstrated by Wunsch *et al.*[78] using a nano-DLD device, with a rather complicated fabrication process and low volumetric throughput.

4.6 Sorting of Adipocytes according to Size (project in progress)

Adipocytes (a.k.a. lipocytes or fat cells) are specialised cells making up the adipose tissue – the energy storage of humans and animals. The size of mature adipocytes vary significantly, $\sim 20\ \mu m - 200\ \mu m$ in diameter. Enlarged adipocytes are linked to insulin resistance and can be used to predict type 2 diabetes. Since the cells have lower mass density than water, to sort out different population of cells according to size, researchers allow the cells to float through nylon filters with appropriate pore size[26,27]. Although the method is practical and simple to perform, collecting of cells smaller than 50 μm is difficult since a large fraction of the smallest cells are lost in the process.

A setup has been built to fractionate adipocytes based on size using a DLD device[1]. It was demonstrated that by using a device[2] with $Gap = 50\ \mu m$, $Period = 14$, adipocytes larger and smaller than the critical diameter, $D_C = 20\ \mu m$, could be sorted (Figure 4.7). Near the outlet, most of the adipocytes, which were larger than 20 μm, were displaced toward the right wall, while a few cells which were smaller than 20 μm traveled in zigzag mode and stayed close to the left wall. In future work, a device with larger gap and as a result, larger critical diameter, can be used to fractionate the adipocytes into two separate populations of larger and smaller than 50 μm. In this way we can study the effects of adipocyte size on insulin resistance.

[1] In collaboration with Dr. Karin Stenkula, Faculty of Medicine, Lund University.

[2] The original master was designed and fabricated by Dr. Miguel Xavier, with help from Dr. Stefan Holm and Dr. Jason Beech.

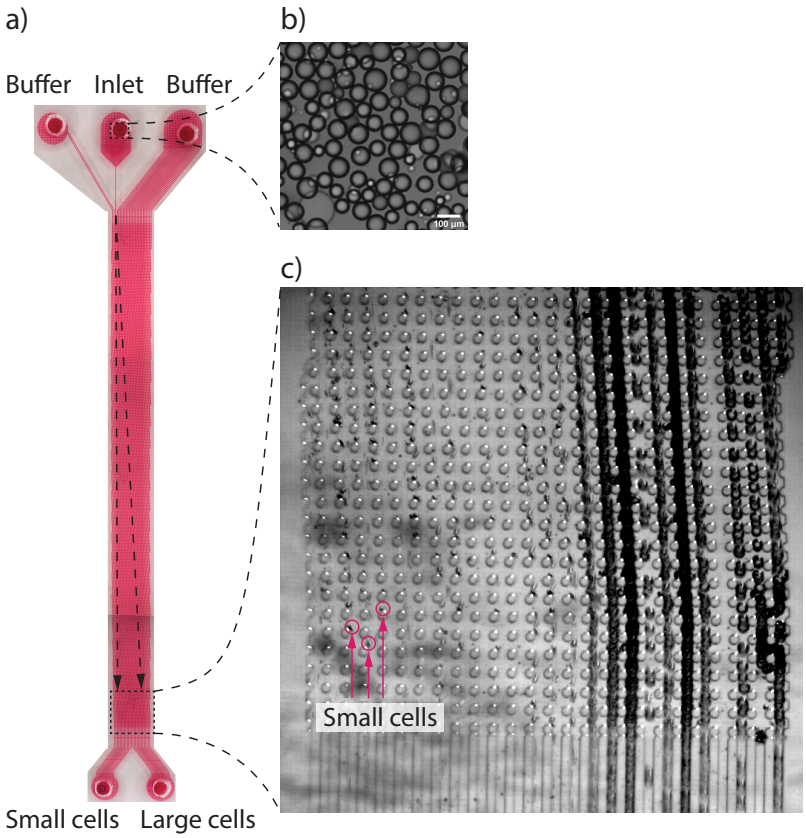

Figure 4.7: Sorting adipocytes by size using DLD. a) The device used to sort adipocytes has a gap width of $50\ \mu m$ and a critical diameter of $20\ \mu m$. b) The adipocytes have a wide size distribution, ranging from below $20\ \mu m$ to over $100\ \mu m$ in the sample at the inlet. c) Near the outlet, most of the cells, which have a diameter of larger than $20\ \mu m$ were displaced toward the right wall of the device while some of the cells which are smaller than $20\ \mu m$ traveled in zigzag mode and stayed closer to the left wall. The image is a "minimum projection" of 853 frames taken at the outlet, $33\ ms$ apart.

4.7 Conclusions and Outlooks

There is no "one-size-fit-all" approach in particle sorting. First of all, the parameters for sorting, which will decide the suitable methods, will be dependent on the intrinsic properties of the particles of interest. For example, while size can be an apparent criterion for sorting spherical cells, this parameter is somewhat ambiguous for *S. pneumoniae* (Paper II) since different morphologies of the bacteria have similar widths but different lengths. In other cases, for example viable/non-viable *E. coli* (Paper I), sorting by size is practically impossible and other properties must be exploited. Second of all, even when the same type of input samples and sorting parameters are given, different approaches can be used and each approach has its own advantages and disadvantages. An example could be sorting cells by their electrical/dielectric properties. While the metal DLD (Paper V) can offer a very high dynamical range to easily sort sub-micron particles, the fabrication is rather expensive and complicated. Insulating pillar electrokinetic DLD (Paper I) relaxes the need of metal layer deposition and etching, but requires a high voltage, and thus, an amplifier to operate. Electrokinetic open DLD (Paper III) requires simpler setup and offers reusability, but efforts should be made to stabilise the setups and the open device is prone to evaporation. In conclusion, the choice of the sorting methods should be considered based on both factors: the properties of the cells and bioparticles and the availability of sorting devices or equipment at the field.

Although my focus has been on applications (chain length sorting in Paper II and adipocyte sorting), the work described in this thesis concerns more the technical aspects of sorting techniques and efforts have been made to fractionate particles based on electrical/dielectric properties and morphologies. A future direction for this work could be applying the methods developed to sorting problems identified by researchers and professionals within the biomedical field. The adipocyte sorting project, which stemmed from discussions with diabetes researchers, is an example. In addition, there is room for improvement and development of the investigated techniques. For example, the device used to sort *S. pneumoniae* in Paper II has been enlarged and put in parallel to increase the throughput. Pilot experiments have been performed on the device with polystyrene microspheres and for the next step, bacterial sample can be tested. Paper III demonstrates a proof of principle of combining electrokinetic DLD with open DLD but to make this approach applicable for biological samples, more effort is required in designing an application-oriented integ-

rated device and improving the electrode-DLD channel contact, for example an electrode which has flat surface at the end would ensure better stability for running the experiments. The experimental work in Paper IV could be expanded to sorting *Trypanosoma cyclops* from RBCs, given the rotational effect induced on them by an AC field is different. Paper V is the beginning chapter of a promising series of study on employing the metal DLD device to sort a wide range of bioparticles, especially sub-micron ones like exosomes. For the adipocyte sorting project, new devices with larger gap and critical diameter have been made, targeting size thresholds required by biomedical researchers studying diabetes.

This chapter concludes the thesis but more details of the work can be found in the appendix and the papers attached at the end.

Chapter 5

Appendix: DLD devices

This chapter provides finer details into the DLD devices used throughout this work, mainly for Paper I and Paper II. The DLD devices used in Paper III and Paper V have been described in their ESI. The DLD device used in Paper IV has been documented by Holm[133].

DLD devices used in Paper I, for beads and yeast cells

Wafer level

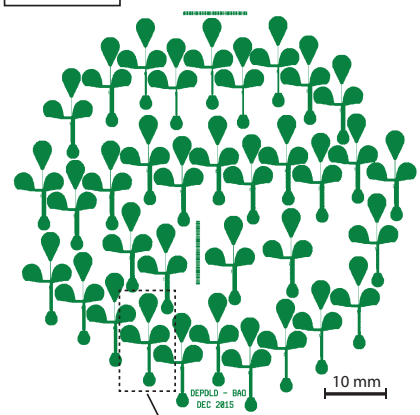

- The devices are for analytical purpose with only one single stream of inlet sample and one outlet reservoir.
- There are 33 different devices, having similar lengths and reservoir designs, but different gap widths (from 2 - 25 µm) and period (5, 10, and 20) to give a wide range of critical diameters (not all combinations were implemented). Four of them were used in Paper I.
- Device used in Paper I for polystyrene beads:

Gap width(µm)	Pillar diameter (µm)	Period	Critical diameter (µm)
6	20	10	2.8

- Devices used in Paper I for yeast cells:

Gap width (µm)	Pillar diameter (µm)	Period	Critical diameter (µm)
10	20	10	4.6
11	20	10	5.1
12	20	10	5.6

Device level

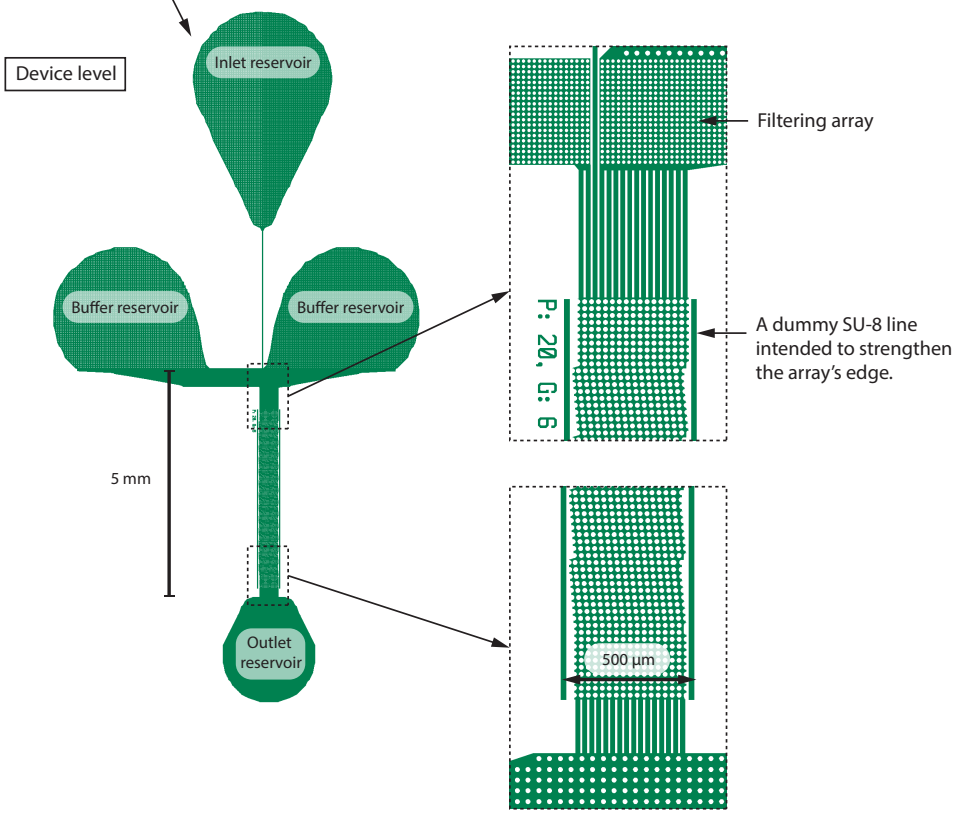

DLD devices used in Paper I and Paper II, for sorting *E. coli* and *S. pneumoniae*

Wafer level

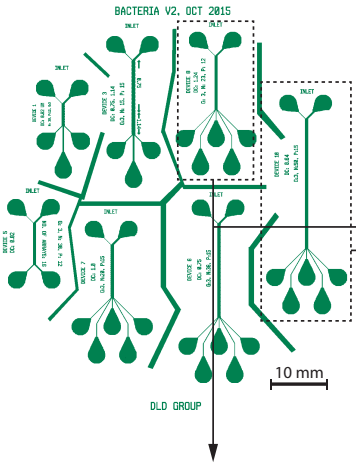

- The devices are for sorting and recovering sorted populations
- There are 7 different devices, having critical diameters varying around 1µm. Two of them were used for sorting *E. coli* and one for *S. pneumoniae.*
- Devices used in Paper I for *E. coli* :

Gap width (µm)	Pillar diameter (µm)	Period	Critical diameter (µm)
4	12	23	1.24
3	15	50	0.64

- Device used in Paper II for *S. pneumoniae* :

Gap width(µm)	Pillar diameter (µm)	Period	Critical diameter (µm)
4	12	23	1.24

Device level

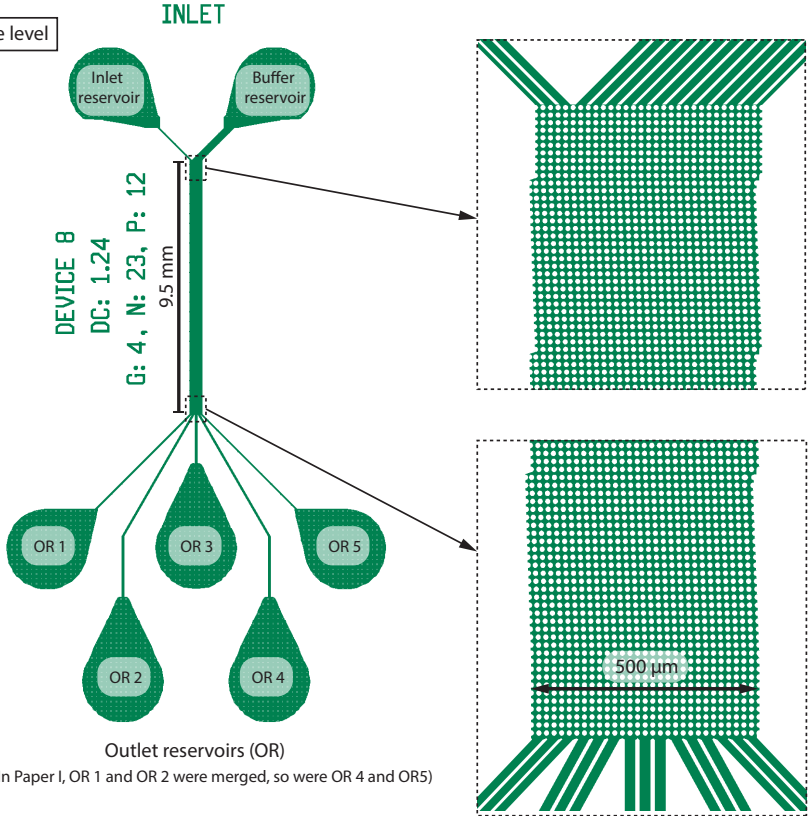

Outlet reservoirs (OR)

(In Paper I, OR 1 and OR 2 were merged, so were OR 4 and OR5)

Bibliography

[1] E. Bassous, H. H. Taub, and L. Kuhn. Ink jet printing nozzle arrays etched in silicon. *Applied Physics Letters*, 31(2):135–137, 1977.

[2] S. C. Terry, J. H. Jerman, and J. B. Angell. A gas chromatographic air analyzer fabricated on a silicon wafer. *IEEE Transactions on Electron Devices*, 26(12):1880–1886, 1979.

[3] Peter Gravesen, Jens Branebjerg, and O Søndergård Jensen. Microfluidics-a review. *Journal of Micromechanics and Microengineering*, 3(4):168, 1993.

[4] Younan Xia and George M Whitesides. Soft lithography. *Annual review of materials science*, 28(1):153–184, 1998.

[5] G. M. Whitesides. The origins and the future of microfluidics. *Nature*, 442(7101):368–73, 2006.

[6] E. K. Sackmann, A. L. Fulton, and D. J. Beebe. The present and future role of microfluidics in biomedical research. *Nature*, 507(7491):181–9, 2014.

[7] Curtis D Chin, Vincent Linder, and Samuel K Sia. Commercialization of microfluidic point-of-care diagnostic devices. *Lab on a Chip*, 12(12):2118–2134, 2012.

[8] Ali Kemal Yetisen, Muhammad Safwan Akram, and Christopher R Lowe. Paper-based microfluidic point-of-care diagnostic devices. *Lab on a Chip*, 13(12):2210–2251, 2013.

[9] Frank B Myers and Luke P Lee. Innovations in optical microfluidic technologies for point-of-care diagnostics. *Lab on a Chip*, 8(12):2015–2031, 2008.

[10] Derek Tseng, Onur Mudanyali, Cetin Oztoprak, Serhan O Isikman, Ikbal Sencan, Oguzhan Yaglidere, and Aydogan Ozcan. Lensfree microscopy on a cellphone. *Lab on a Chip*, 10(14):1787–1792, 2010.

[11] Shia-Yen Teh, Robert Lin, Lung-Hsin Hung, and Abraham P Lee. Droplet microfluidics. *Lab on a Chip*, 8(2):198–220, 2008.

[12] Samaneh Mashaghi, Alireza Abbaspourrad, David A Weitz, and Antoine M van Oijen. Droplet microfluidics: A tool for biology, chemistry and nanotechnology. *TrAC Trends in Analytical Chemistry*, 82:118–125, 2016.

[13] Pooria Mostafalu, Mohsen Akbari, Kyle A. Alberti, Qiaobing Xu, Ali Khademhosseini, and Sameer R. Sonkusale. A toolkit of thread-based microfluidics, sensors, and electronics for 3d tissue embedding for medical diagnostics. *Microsystems &Amp; Nanoengineering*, 2:16039, 2016.

[14] Zhihong Nie, Christian A Nijhuis, Jinlong Gong, Xin Chen, Alexander Kumachev, Andres W Martinez, Max Narovlyansky, and George M Whitesides. Electrochemical sensing in paper-based microfluidic devices. *Lab on a Chip*, 10(4):477–483, 2010.

[15] Yifan Liu, Lilian M Schweizer, Wenxing Wang, Robert L Reuben, Michael Schweizer, and Wenmiao Shu. Label-free and real-time monitoring of yeast cell growth by the bending of polymer microcantilever biosensors. *Sensors and Actuators B: Chemical*, 178:621–626, 2013.

[16] Georgette B. Salieb-Beugelaar, Giuseppina Simone, Arun Arora, Anja Philippi, and Andreas Manz. Latest developments in microfluidic cell biology and analysis systems. *Analytical Chemistry*, 82(12):4848–4864, 2010.

[17] Matthias Mehling and Savaş Tay. Microfluidic cell culture. *Current Opinion in Biotechnology*, 25:95–102, 2014.

[18] S Elizabeth Hulme, Sergey S Shevkoplyas, Javier Apfeld, Walter Fontana, and George M Whitesides. A microfabricated array of clamps for immobilizing and imaging c. elegans. *Lab on a Chip*, 7(11):1515–1523, 2007.

[19] Kwanghun Chung, Matthew M Crane, and Hang Lu. Automated on-chip rapid microscopy, phenotyping and sorting of c. elegans. *Nature methods*, 5(7):637, 2008.

[20] Trushal Vijaykumar Chokshi, Adela Ben-Yakar, and Nikos Chronis. Co 2 and compressive immobilization of c. elegans on-chip. *Lab on a Chip*, 9(1):151–157, 2009.

[21] Jan Krajniak and Hang Lu. Long-term high-resolution imaging and culture of c. elegans in chip-gel hybrid microfluidic device for developmental studies. *Lab on a Chip*, 10(14):1862–1868, 2010.

[22] Dongeun Huh, Yu-suke Torisawa, Geraldine A Hamilton, Hyun Jung Kim, and Donald E Ingber. Microengineered physiological biomimicry: organs-on-chips. *Lab on a Chip*, 12(12):2156–2164, 2012.

[23] Yosuke Nakao, Hiroshi Kimura, Yasuyuki Sakai, and Teruo Fujii. Bile canaliculi formation by aligning rat primary hepatocytes in a microfluidic device. *Biomicrofluidics*, 5(2):022212, 2011.

[24] Kyung-Jin Jang and Kahp-Yang Suh. A multi-layer microfluidic device for efficient culture and analysis of renal tubular cells. *Lab on a Chip*, 10(1):36–42, 2010.

[25] Dongeun Huh, Benjamin D Matthews, Akiko Mammoto, Martín Montoya-Zavala, Hong Yuan Hsin, and Donald E Ingber. Reconstituting organ-level lung functions on a chip. *Science*, 328(5986):1662–1668, 2010.

[26] Margareta Jernås, Jenny Palming, Kajsa Sjöholm, Eva Jennische, Per-Arne Svensson, Britt G. Gabrielsson, Max Levin, Anders Sjögren, Mats Rudemo, Theodore C. Lystig, Björn Carlsson, Lena M. S. Carlsson, and Malin Lönn. Separation of human adipocytes by size: hypertrophic fat cells display distinct gene expression. *The FASEB Journal*, 20(9):1540–1542, 2006.

[27] N. Franck, K. G. Stenkula, A. Öst, T. Lindström, P. Strålfors, and F. H. Nystrom. Insulin-induced glut4 translocation to the plasma membrane is blunted in large compared with small primary fat cells isolated from the same individual. *Diabetologia*, 50(8):1716–1722, 2007.

[28] Andreas Lenshof, Arshad Jamal, Josefina Dykes, Anke Urbansky, Ingbritt Åstrand Grundström, Thomas Laurell, and Stefan Scheding. Efficient purification of cd4+ lymphocytes from peripheral blood progenitor cell products using affinity bead acoustophoresis. *Cytometry Part A*, 85(11):933–941, 2014.

[29] D. R. Gossett, W. M. Weaver, A. J. Mach, S. C. Hur, H. T. Tse, W. Lee, H. Amini, and D. Di Carlo. Label-free cell separation and sorting in microfluidic systems. *Anal Bioanal Chem*, 397(8):3249–67, 2010.

[30] Andreas Lenshof and Thomas Laurell. Continuous separation of cells and particles in microfluidic systems. *Chemical Society Reviews*, 39(3):1203–1217, 2010.

[31] Edwin Mellor Southern. Detection of specific sequences among dna fragments separated by gel electrophoresis. *J mol biol*, 98(3):503–517, 1975.

[32] D Jed Harrison, Karl Fluri, Kurt Seiler, Zhonghui Fan, Carlo S Effenhauser, and Andreas Manz. Micromachining a miniaturized capillary electrophoresis-based chemical analysis system on a chip. *Science*, 261(5123):895–897, 1993.

[33] R. Pethig. Review article-dielectrophoresis: status of the theory, technology, and applications. *Biomicrofluidics*, 4(2), 2010.

[34] Michael P Hughes. Strategies for dielectrophoretic separation in laboratory-on-a-chip systems. *Electrophoresis*, 23(16):2569–2582, 2002.

[35] Filip Petersson, Lena Åberg, Ann-Margret Swärd-Nilsson, and Thomas Laurell. Free flow acoustophoresis: microfluidic-based mode of particle and cell separation. *Analytical chemistry*, 79(14):5117–5123, 2007.

[36] J Calvin Giddings. A new separation concept based on a coupling of concentration and flow nonuniformities. *Separation Science*, 1(1):123–125, 1966.

[37] Masumi Yamada, Megumi Nakashima, and Minoru Seki. Pinched flow fractionation: continuous size separation of particles utilizing a laminar flow profile in a pinched microchannel. *Analytical chemistry*, 76(18):5465–5471, 2004.

[38] L. R. Huang, E. C. Cox, R. H. Austin, and J. C. Sturm. Continuous particle separation through deterministic lateral displacement. *Science*, 304(5673):987–90, 2004.

[39] Dino Di Carlo. Inertial microfluidics. *Lab on a Chip*, 9(21):3038–3046, 2009.

[40] George Keith Batchelor. *An introduction to fluid dynamics*. Cambridge university press, 2000.

[41] G. Hauke. *An Introduction to Fluid Mechanics and Transport Phenomena*. Springer Netherlands, 2010.

[42] B. Lautrup. *Physics of Continuous Matter, Second Edition: Exotic and Everyday Phenomena in the Macroscopic World*. Taylor & Francis, 2011.

[43] Nam-Trung Nguyen, Steven T Wereley, and Steven T Wereley. *Fundamentals and applications of microfluidics*. Artech house, 2002.

[44] H. Bruus. *Theoretical Microfluidics*. OUP Oxford, 2008.

[45] Charles L Fefferman. Existence and smoothness of the navier-stokes equation. *The millennium prize problems*, 57:67, 2006.

[46] Bruno Eckhardt. Introduction. turbulence transition in pipe flow: 125th anniversary of the publication of reynolds' paper. *Philosophical Transactions of the Royal Society A: Mathematical, Physical and Engineering Sciences*, 367(1888):449–455, 2009.

[47] D. W. Inglis, J. A. Davis, R. H. Austin, and J. C. Sturm. Critical particle size for fractionation by deterministic lateral displacement. *Lab Chip*, 6(5):655–8, 2006.

[48] Jason Beech. *Microfluidics Separation and Analysis of Biological Particles*. PhD Thesis. Lund University, 2011.

[49] J. A. Davis. *Microfluidic Separation of Blood Components through Deterministic Lateral Displacement*, volume Doctors of *Electrical Engineering*. PhD Thesis. Princeton University, 2008.

[50] Kevin Loutherback, Jason Puchalla, Robert H Austin, and James C Sturm. Deterministic microfluidic ratchet. *Physical review letters*, 102(4):045301, 2009.

[51] M. Balvin, E. Sohn, T. Iracki, G. Drazer, and J. Frechette. Directional locking and the role of irreversible interactions in deterministic hydrodynamics separations in microfluidic devices. *Phys Rev Lett*, 103(7):078301, 2009.

[52] Joelle Frechette and German Drazer. Directional locking and deterministic separation in periodic arrays. *Journal of Fluid Mechanics*, 627:379–401, 2009.

[53] John Herrmann, Michael Karweit, and German Drazer. Separation of suspended particles in microfluidic systems by directional locking in periodic fields. *Physical Review E*, 79(6):061404, 2009.

[54] T. Bowman, J. Frechette, and G. Drazer. Force driven separation of drops by deterministic lateral displacement. *Lab on a Chip*, 12(16):2903–2908, 2012.

[55] R. Devendra and G. Drazer. Gravity driven deterministic lateral displacement for particle separation in microfluidic devices. *Analytical Chemistry*, 84(24):10621–10627, 2012.

[56] T. J. Bowman, G. Drazer, and J. Frechette. Inertia and scaling in deterministic lateral displacement. *Biomicrofluidics*, 7(6), 2013.

[57] S. R. Risbud and G. Drazer. Directional locking in deterministic lateral-displacement microfluidic separation systems. *Phys Rev E Stat Nonlin Soft Matter Phys*, 90(1):012302, 2014.

[58] S. Hanasoge, R. Devendra, F. J. Diez, and G. Drazer. Electrokinetically driven deterministic lateral displacement for particle separation in microfluidic devices. *Microfluidics and Nanofluidics*, 18(5-6):1195–1200, 2015.

[59] M. L. Jiang, K. Budzan, and G. Drazer. Fractionation by shape in deterministic lateral displacement microfluidic devices. *Microfluidics and Nanofluidics*, 19(2):427–434, 2015.

[60] M. L. Jiang, A. D. Mazzeo, and G. Drazer. Centrifuge-based deterministic lateral displacement separation. *Microfluidics and Nanofluidics*, 20(1), 2016.

[61] S. Q. Du and G. Drazer. Gravity driven deterministic lateral displacement for suspended particles in a 3d obstacle array. *Scientific Reports*, 6, 2016.

[62] S Cerbelli. Separation of polydisperse particle mixtures by deterministic lateral displacement. the impact of particle diffusivity on separation efficiency. *Asia-Pacific Journal of Chemical Engineering*, 7(S3), 2012.

[63] Gaetano D'Avino. Non-newtonian deterministic lateral displacement separator: theory and simulations. *Rheologica Acta*, 52(3):221–236, 2013.

[64] F. Khodaee, S. Movahed, N. Fatouraee, and F. Daneshmand. Numerical simulation of separation of circulating tumor cells from blood stream in deterministic lateral displacement (DLD) microfluidic channel. *Journal of Mechanics*, 32(4):463–471, 2016.

[65] M. Heller and H. Bruus. A theoretical analysis of the resolution due to diffusion and size dispersion of particles in deterministic lateral displacement devices. *Journal of Micromechanics and Microengineering*, 18(7), 2008.

[66] B. R. Long, M. Heller, J. P. Beech, H. Linke, H. Bruus, and J. O. Tegenfeldt. Multidirectional sorting modes in deterministic lateral displacement devices. *Physical Review E*, 78(4), 2008.

[67] S. Cerbelli, M. Giona, and F. Garofalo. Quantifying dispersion of finite-sized particles in deterministic lateral displacement microflow separators through brenner's macrotransport paradigm. *Microfluidics and Nanofluidics*, 15(4):431–449, 2013.

[68] Stefano Cerbelli, Fabio Garofalo, and Massimiliano Giona. Effective dispersion and separation resolution in continuous particle fractionation. *Microfluidics and Nanofluidics*, 19(5):1035–1046, 2015.

[69] Junchao Wang, Victor GJ Rodgers, Philip Brisk, and William H Grover. Mopsa: A microfluidics-optimized particle simulation algorithm. *Biomicrofluidics*, 11(3):034121, 2017.

[70] Timm Krüger, David Holmes, and Peter V Coveney. Deformability-based red blood cell separation in deterministic lateral displacement devices—a simulation study. *Biomicrofluidics*, 8(5):054114, 2014.

[71] Rohan Vernekar and Timm Krüger. Breakdown of deterministic lateral displacement efficiency for non-dilute suspensions: A numerical study. *Medical Engineering and Physics*, 37(9):845–854, 2015.

[72] Jianhui Wei, Hui Song, Zaiyi Shen, Ying He, Xianzhi Xu, Yong Zhang, and Bing Nan Li. Numerical study of pillar shapes in deterministic lateral displacement microfluidic arrays for spherical particle separation. *IEEE transactions on nanobioscience*, 14(6):660–667, 2015.

[73] Q. Wei, Y. Q. Xu, X. Y. Tang, and F. B. Tian. An ib-lbm study of continuous cell sorting in deterministic lateral displacement arrays. *Acta Mechanica Sinica*, 32(6):1023–1030, 2016.

[74] Raymond Quek, Duc Vinh Le, and K-H Chiam. Separation of deformable particles in deterministic lateral displacement devices. *Physical Review E*, 83(5):056301, 2011.

[75] Shangjun Ye, Xueming Shao, Zhaosheng Yu, and Wenguang Yu. Effects of the particle deformability on the critical separation diameter in the deterministic lateral displacement device. *Journal of Fluid Mechanics*, 743:60–74, 2014.

[76] E. Henry, S. H. Holm, Z. M. Zhang, J. P. Beech, J. O. Tegenfeldt, D. A. Fedosov, and G. Gompper. Sorting cells by their dynamical properties. *Scientific Reports*, 6, 2016.

[77] J. A. Davis, D. W. Inglis, K. J. Morton, D. A. Lawrence, L. R. Huang, S. Y. Chou, J. C. Sturm, and R. H. Austin. Deterministic hydrodynamics: taking blood apart. *Proc Natl Acad Sci U S A*, 103(40):14779–84, 2006.

[78] B. H. Wunsch, J. T. Smith, S. M. Gifford, C. Wang, M. Brink, R. L. Bruce, R. H. Austin, G. Stolovitzky, and Y. Astier. Nanoscale lateral displacement arrays for the separation of exosomes and colloids down to 20 nm. *Nature Nanotechnology*, 11(11):936–940, 2016.

[79] S. Y. Zheng, Y. C. Tai, and H. Kasdan. A micro device for separation of erythrocytes and leukocytes in human blood. *2005 27th Annual International Conference of the IEEE Engineering in Medicine and Biology Society, Vols 1-7*, pages 1024–1027, 2005.

[80] J. P. Beech and J. O. Tegenfeldt. Tuneable separation in elastomeric microfluidics devices. *Lab Chip*, 8(5):657–9, 2008.

[81] David W Inglis, Megan Lord, and Robert E Nordon. Scaling deterministic lateral displacement arrays for high throughput and dilution-free enrichment of leukocytes. *Journal of Micromechanics and Microengineering*, 21(5):054024, 2011.

[82] B. Bilenberg, M. Hansen, D. Johansen, V. Ozkapici, C. Jeppesen, P. Szabo, I. M. Obieta, O. Arroyo, J. O. Tegenfeldt, and A. Kristensen. Topas-based lab-on-a-chip microsystems fabricated by thermal nanoimprint lithography. *Journal of Vacuum Science & Technology B*, 23(6):2944–2949, 2005.

[83] C. I. Civin, T. Ward, A. M. Skelley, K. Gandhi, Z. P. Lee, C. R. Dosier, J. L. D'Silva, Y. Chen, M. Kim, J. Moynihan, X. C. Chen, L. Aurich, S. Gulnik, G. C. Brittain, D. J. Recktenwald, R. H. Austin, and J. C. Sturm. Automated leukocyte processing by microfluidic deterministic lateral displacement. *Cytometry Part A*, 89A(12):1073–1083, 2016.

[84] K. Loutherback, K. S. Chou, J. Newman, J. Puchalla, R. H. Austin, and J. C. Sturm. Improved performance of deterministic lateral displacement arrays with triangular posts. *Microfluidics and Nanofluidics*, 9(6):1143–1149, 2010.

[85] K. Loutherback, J. D'Silva, L. Liu, A. Wu, R. H. Austin, and J. C. Sturm. Deterministic separation of cancer cells from blood at 10 ml/min. *AIP Adv*, 2(4):42107, 2012.

[86] Z. Liu, F. Huang, J. Du, W. Shu, H. Feng, X. Xu, and Y. Chen. Rapid isolation of cancer cells using microfluidic deterministic lateral displacement structure. *Biomicrofluidics*, 7(1):11801, 2013.

[87] Z. M. Zhang, E. Henry, G. Gompper, and D. A. Fedosova. Behavior of rigid and deformable particles in deterministic lateral displacement devices with different post shapes. *Journal of Chemical Physics*, 143(24), 2015.

[88] J. D'silva, R. H. Austin, and J. C. Sturm. Inhibition of clot formation in deterministic lateral displacement arrays for processing large volumes of blood for rare cell capture. *Lab on a Chip*, 15(10):2240–2247, 2015.

[89] Z. B. Liu, Y. Lee, J. H. Jang, Y. Li, X. Han, K. Yokoi, M. Ferrari, L. D. Zhou, and L. D. Qin. Microfluidic cytometric analysis of cancer cell transportability and invasiveness. *Scientific Reports*, 5, 2015.

[90] Zongbin Liu, Rui Chen, Ying Li, Jianqiao Liu, Ping Wang, Xuefeng Xia, and Lidong Qin. Integrated microfluidic chip for efficient isolation and deformability analysis of circulating tumor cells. *Advanced Biosystems*, 0(0):1800200, 2018.

[91] K. K. Zeming, S. Ranjan, and Y. Zhang. Rotational separation of non-spherical bioparticles using i-shaped pillar arrays in a microfluidic device. *Nature Communications*, 4, 2013.

[92] S. Ranjan, K. K. Zeming, R. Jureen, D. Fisher, and Y. Zhang. Dld pillar shape design for efficient separation of spherical and non-spherical bioparticles. *Lab on a Chip*, 14(21):4250–4262, 2014.

[93] S. H. Au, J. Edd, A. E. Stoddard, K. H. K. Wong, F. Fachin, S. Maheswaran, D. A. Haber, S. L. Stott, R. Kapur, and M. Toner. Microfluidic isolation of circulating tumor cell clusters by size and asymmetry. *Sci Rep*, 7(1):2433, 2017.

[94] Nezihi Murat Karabacak, Philipp S. Spuhler, Fabio Fachin, Eugene J. Lim, Vincent Pai, Emre Ozkumur, Joseph M. Martel, Nikola Kojic, Kyle Smith, Pin-i Chen, Jennifer Yang, Henry Hwang, Bailey Morgan, Julie Trautwein, Thomas A. Barber, Shannon L. Stott, Shyamala Maheswaran, Ravi Kapur, Daniel A. Haber, and Mehmet Toner. Microfluidic, marker-free isolation of circulating tumor cells from blood samples. *Nature Protocols*, 9:694, 2014.

[95] J. C. Hyun, J. Hyun, S. Wang, and S. Yang. Improved pillar shape for deterministic lateral displacement separation method to maintain separation efficiency over a long period of time. *Separation and Purification Technology*, 172:258–267, 2017.

[96] M. Al-Fandi, M. Al-Rousan, M. A. K. Jaradat, and L. Al-Ebbini. New design for the separation of microorganisms using microfluidic deterministic lateral displacement. *Robotics and Computer-Integrated Manufacturing*, 27(2):237–244, 2011.

[97] S. H. Holm, J. P. Beech, M. P. Barrett, and J. O. Tegenfeldt. Separation of parasites from human blood using deterministic lateral displacement. *Lab Chip*, 11(7):1326–32, 2011.

[98] S. H. Holm, J. P. Beech, M. P. Barrett, and J. O. Tegenfeldt. Simplifying microfluidic separation devices towards field-detection of blood parasites. *Anal. Methods*, 8(16):3291–3300, 2016.

[99] Rohan Vernekar, Timm Krüger, Kevin Loutherback, Keith Morton, and David W Inglis. Anisotropic permeability in deterministic lateral displacement arrays. *Lab on a Chip*, 17(19):3318–3330, 2017.

[100] David W Inglis. Efficient microfluidic particle separation arrays. *Applied Physics Letters*, 94(1):013510, 2009.

[101] T Kulrattanarak, RGM Van der Sman, YS Lubbersen, CGPH Schroën, HTM Pham, PM Sarro, and RM Boom. Mixed motion in deterministic ratchets due to anisotropic permeability. *Journal of colloid and interface science*, 354(1):7–14, 2011.

[102] T Kulrattanarak, RGM Van Der Sman, CGPH Schroën, and RM Boom. Analysis of mixed motion in deterministic ratchets via experiment and particle simulation. *Microfluidics and Nanofluidics*, 10(4):843–853, 2011.

[103] S. C. Kim, B. H. Wunsch, H. Hu, J. T. Smith, R. H. Austin, and G. Stolovitzky. Broken flow symmetry explains the dynamics of small particles in deterministic lateral displacement arrays. *Proceedings of the National Academy of Sciences of the United States of America*, 114(26):E5034–E5041, 2017.

[104] N. Tottori, T. Nisisako, J. Park, Y. Yanagida, and T. Hatsuzawa. Separation of viable and nonviable mammalian cells using a deterministic lateral displacement microfluidic device. *Biomicrofluidics*, 10(1), 2016.

[105] S. L. Feng, A. M. Skelley, A. G. Anwer, G. Z. Liu, and D. W. Inglis. Maximizing particle concentration in deterministic lateral displacement arrays (vol 11, 024121, 2017). *Biomicrofluidics*, 11(3), 2017.

[106] Trung SH Tran, Bao D Ho, Jason P Beech, and Jonas O Tegenfeldt. Open channel deterministic lateral displacement for particle and cell sorting. *Lab on a Chip*, 17(21):3592–3600, 2017.

[107] J. P. Beech, P. Jonsson, and J. O. Tegenfeldt. Tipping the balance of deterministic lateral displacement devices using dielectrophoresis. *Lab Chip*, 9(18):2698–706, 2009.

[108] J. P. Beech, S. H. Holm, K. Adolfsson, and J. O. Tegenfeldt. Sorting cells by size, shape and deformability. *Lab Chip*, 12(6):1048–51, 2012.

[109] Jason P Beech, Bao Dang Ho, Geneviève Garriss, Vitor Oliveira, Birgitta Henriques-Normark, and Jonas O Tegenfeldt. Separation of pathogenic bacteria by chain length. *Analytica chimica acta*, 1000:223–231, 2018.

[110] A. J. Laki, L. Botzheim, K. Ivan, T. Szabo, V. Tamasi, E. Buzas, and P. Civera. Microvesicle fractionation using deterministic lateral displacement effect. *2014*

9th IEEE International Conference on Nano/Micro Engineered and Molecular Systems (Nems), pages 490–493, 2014.

[111] A. J. Laki, L. Botzheim, K. Ivan, V. Tamasi, and P. Civera. Separation of microvesicles from serological samples using deterministic lateral displacement effect. *Bio Nanoscience*, 5(1):48–54, 2015.

[112] R Huang, TA Barber, MA Schmidt, RG Tompkins, M Toner, DW Bianchi, R Kapur, and WL Flejter. A microfluidics approach for the isolation of nucleated red blood cells (nrbcs) from the peripheral blood of pregnant women. *Prenatal diagnosis*, 28(10):892–899, 2008.

[113] James V. Green, Milica Radisic, and Shashi K. Murthy. Deterministic lateral displacement as a means to enrich large cells for tissue engineering. *Analytical Chemistry*, 81(21):9178–9182, 2009.

[114] D. W. Inglis, N. Herman, and G. Vesey. Highly accurate deterministic lateral displacement device and its application to purification of fungal spores. *Biomicrofluidics*, 4(2), 2010.

[115] B. Y. Zhang, J. V. Green, S. K. Murthy, and M. Radisic. Label-free enrichment of functional cardiomyocytes using microfluidic deterministic lateral flow displacement. *Plos One*, 7(5), 2012.

[116] H. N. Joensson, M. Uhlen, and H. A. Svahn. Droplet size based separation by deterministic lateral displacement-separating droplets by cell-induced shrinking. *Lab on a Chip*, 11(7):1305–1310, 2011.

[117] N. Tottori, T. Hatsuzawa, and T. Nisisako. Separation of main and satellite droplets in a deterministic lateral displacement microfluidic device. *Rsc Advances*, 7(56):35516–35524, 2017.

[118] Y. Chen, J. D'Silva, R. H. Austin, and J. C. Sturm. Microfluidic chemical processing with on-chip washing by deterministic lateral displacement arrays with separator walls. *Biomicrofluidics*, 9(5), 2015.

[119] N. Li, D. T. Kamei, and C. M. Ho. On-chip continuous blood cell subtype separation by deterministic lateral displacement. In *2007 2nd IEEE International Conference on Nano/Micro Engineered and Molecular Systems*, pages 932–936.

[120] D. Holmes, G. Whyte, J. Bailey, N. Vergara-Irigaray, A. Ekpenyong, J. Guck, and T. Duke. Separation of blood cells with differing deformability using deterministic lateral displacement. *Interface Focus*, 4(6), 2014.

[121] H. Okano, T. Konishi, T. Suzuki, T. Suzuki, S. Ariyasu, S. Aoki, R. Abe, and M. Hayase. Enrichment of circulating tumor cells in tumor-bearing mouse blood by a deterministic lateral displacement microfluidic device. *Biomedical Microdevices*, 17(3), 2015.

[122] H. Morgan and N.G. Green. *AC Electrokinetics: Colloids and Nanoparticles*. Research Studies Press, 2003.

[123] JO'M Bockris, MAV Devanathan, and K Müller. *On the structure of charged interfaces*, pages 832–863. Elsevier, 1965.

[124] J.O.M. Bockris, A.K.N. Reddy, and M.E. Gamboa-Aldeco. *Modern Electrochemistry 2A: Fundamentals of Electrodics*. Springer US, 2007.

[125] W.B. Russel, W.B. Russel, D.A. Saville, and W.R. Schowalter. *Colloidal Dispersions*. Cambridge University Press, 1991.

[126] FF Reuss. Charge-induced flow. In *Proceedings of the Imperial Society of Naturalists of Moscow*, volume 3, pages 327–344.

[127] Jean-Louis Viovy. Electrophoresis of dna and other polyelectrolytes: Physical mechanisms. *Reviews of Modern Physics*, 72(3):813–872, 2000.

[128] David Erickson. *Electroosmotic Flow (DC)*, pages 560–567. Springer US, Boston, MA, 2008.

[129] Brian J Kirby and Ernest F Hasselbrink Jr. Zeta potential of microfluidic substrates: 2. data for polymers. *Electrophoresis*, 25(2):203–213, 2004.

[130] R.R. Pethig. *Dielectrophoresis: Theory, Methodology and Biological Applications*. Wiley, 2017.

[131] Thomas B. Jones. *Electromechanics of Particles*. Cambridge University Press, Cambridge, 1995.

[132] Lung-Hsin Hung and Abraham P Lee. Optimization of droplet generation by controlling pdms surface hydrophobicity. In *ASME 2004 International Mechanical Engineering Congress and Exposition*, pages 47–48. American Society of Mechanical Engineers.

[133] Stefan Holm. *Microfluidic Cell and Particle Sorting Using Deterministic Lateral Displacement*. PhD Thesis. Lund University, 2018.

[134] A. B. Dalia and J. N. Weiser. Minimization of bacterial size allows for complement evasion and is overcome by the agglutinating effect of antibody. *Cell Host Microbe*, 10(5):486–96, 2011.

[135] J. L. Rodriguez, A. B. Dalia, and J. N. Weiser. Increased chain length promotes pneumococcal adherence and colonization. *Infect Immun*, 80(10):3454–9, 2012.

Electrokinetic DLD

Paper I

Cell sorting using Electrokinetic Deterministic Lateral Displacement †

Bao D. Ho[1], Jason P. Beech[1], Carlos Honrado[2], Daniel Spencer[2], Hywel Morgan[2] and Jonas O. Tegenfeldt[1*]

†*Electronic Supplementary Information available*

[1]*Division of Solid State Physics and NanoLund, Physics Department, Lund University, PO Box 118, 221 00, Lund, Sweden*

[2]*Faculty of Physical Sciences and Engineering and Institute for Life Sciences, University of Southampton, Southampton, UK, SO17 1BJ*

[*]*Corresponding author. Telephone: +46 46 222 8063. E-mail: jonas.tegenfeldt@ftf.lth.se*

Keywords

Deterministic Lateral Displacement; Label-free separation; Cell sorting; Yeast; *E. coli*.

Abstract

We report a thorough investigation of the combination of Electrokinetics and Deterministic Lateral Displacement (DLD). We show how an Electrokinetic DLD device can sort polystyrene particles by the difference in their surface charge. We also demonstrate that this type of device can sort viable from non-viable yeast cells and viable from non-viable *E. coli* bacteria. In particular for the case of *E. coli,* a 50/50 ratio of viable/non-viable cells population can be separated into different reservoirs with more than 90% purity. We experimentally realise that each type of particles has its own range of optimised sorting frequencies: $\sim 1\ Hz$ for viable/non-viable *E. coli*, $\sim 100\ Hz$ for different types of polystyrene beads, and $\sim 20\ kHz$ for viable/non-viable yeast cells. We present our best understanding of the mechanism underlying sorting, which may involve various contributing phenomena.

1. Introduction

The separation, sorting, and enrichment of cells and bioparticles are important to many biomedical applications, especially diagnostics, therapeutics, and cell biology. Conventional cell sorting methods, including fluorescence-activated cell sorting (FACS) and magnetic-activated cell sorting (MACS) [1], have been available for several decades and are familiar to biomedical researchers and technicians. However, those methods have several limitations: they require user specialization and training; the initial costs, operating costs, and reagent costs are high; and labelling with antibodies and fluorophores may alter the functions of cells. For this reason, alternative cell sorting methods that are simple, low cost, and reagent-free are highly attractive.

Label-free cell sorting, instead of tagging the cells with chemical labels, exploits intrinsic physical properties of the cells to fractionate them. There exists a wide range of different label-free techniques targeting different physical properties of cells and bioparticles, including but not limited to size [2-5], shape, compressibility [5], density [5, 6], dielectric properties [7], and surface charge [6, 8]. In 2004, Huang *et al.* proposed a novel label-free method named Deterministic Lateral Displacement (DLD) for sorting particles based on size [3]. In a DLD device, sorting is made possible by an array of pillars placed inside a shallow rectangular channel (Figure 1, not for scale). The pillar array is arranged in a rhombic configuration, tilted with an angle to the flow direction of the fluid (from top to bottom in Figure 1). This asymmetric arrangement of the pillars splits the flow into many streams. Particles which are small enough to fit into a single stream travel zigzagging along the channel and exhibit zero displacement at the outlet. Large particles, on the other hand, will continuously bump into the pillars they encounter, switch from one stream to another and exit at different positions than the small particles. At the end of the array, the large and the small particles can be collected in two different outlets. The critical diameter, the threshold diameter at which particles are separated, can be estimated by the empirical formula proposed by Davis [9]:

$$D_C = 1.4GN^{-0.48} \quad (1)$$

Where D_C is the critical diameter, G is the gap between two pillars, and N is the period of the pillar array.

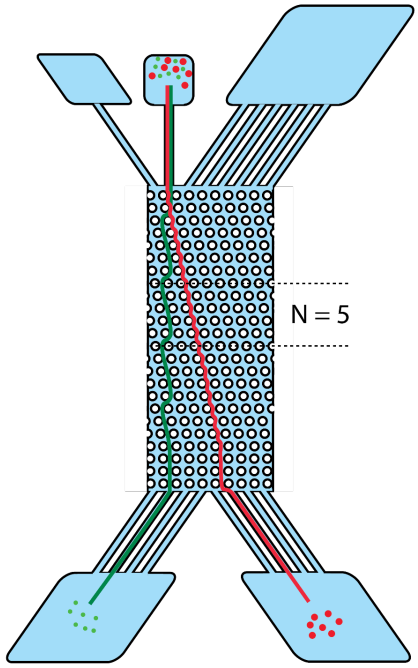

Figure 1: *Schematic of a DLD device capable of sorting a mixture of big (red) and small (green) particles into two sub-populations. The particles that are smaller than the critical diameter travel in a zigzag trajectory, having zero displacement at the end of the array, while the ones larger than the critical diameter travel in a displacement trajectory. The two size fractions are collected in different outlet reservoirs.*

DLD has been employed in various microfluidic devices to sort a wide range of cells and bioparticles, for example WBC from RBC and plasma [10-12], circulating tumour cells from blood [13, 14], or trypanosomes from blood [15, 16]. Although originally being a size-based method, DLD has also been enhanced to sort particles based on other properties, for example shape [15-17], length [18], deformability [17, 19], and electrical properties [20, 21]. In this article, we employ a hybrid device combining AC electrokinetics and DLD to sort particles based on electrical and dielectric properties, with the focus on its application to cells and bioparticles.

Electrokinetics has previously been used in combination with DLD to transport media and particles. It was in the first DLD paper that bacterial DNAs of different sizes (61 and 158 kb) were transported by a DC field along a DLD channel and separated at the end of the device [3]. Similarly, Hanasoge *et al.* employed a DC voltage to drive silica and glass beads of different sizes through a pillar array and found that the angles between the trajectory of the beads and the direction of the field are size-dependent [21]. Not limited to DC field, Beech *et al.* combined AC electrokinetics with DLD to flexibly tune the critical diameter at which separation occurs, by up to 50% [20]. Different from the

aforementioned DC methods, the flow was driven by pressure instead of DC field while the AC field, applied simply via platinum wires dipped inside inlet and outlet reservoirs, provided the tuneable nudging force. Similarly, Tran *et al.* separated different-sized beads in an open channel DLD device where the beads were transported by capillary driven flow and the AC field was applied directly on the surface of the DLD pillars via platinum electrodes [22]. In another work, Chang and Cho combined AC electrokinetics with DLD in their virtual pillar array devices where 2D circular gold electrodes, instead of 3D pillars, were deposited at the bottom of a microfluidic channel to displace particles using dielectrophoretic force [23].

Previous research on Electrokinetic DLD hybrid devices chiefly employed particle size as the sorting criterion and electric field strength as the tuneable physical variable. Our work extends the usability of the device by showing that surface charge and dielectric properties can be additional sorting parameters and in this case, the frequency of the field is an important factor. We demonstrate separation of similar-sized polystyrene beads having different surface modifications, similar-sized viable/non-viable yeast cells, and similar-sized viable/non-viable *E. coli* bacteria. In the case of *E. coli*, we sorted a 50/50 mixture of viable/non-viable cells into separated populations with purity of more than 90 %.

2. Results and Discussion

2.1. Sorting of polystyrene microspheres based on surface charge

2.1.1. Characterization of polystyrene microspheres

To study the effect of surface charge, six types of polystyrene beads of similar size but different surface charge coating were used (Table 1). There are three groups of beads in the table: plain beads, having sulphate groups on their surface due to the nature of polystyrene sphere production; carboxylate modified beads, having carboxylate groups grafted on the surface; and amine beads, with grafted amine groups. The bead diameters were reported by the vendors, while the zeta potential were measured with a Zetasizer NanoZS instrument (Malvern Instruments, Ltd., Worcestershire, U.K.). The zeta potentials correlate with the surface charge density at the shear plane – the effective surface charge – of the particles. In the zeta potential measurements, the beads were suspended in 1.7 mM KCl, 0.1% w/v Pluronics F127 (σ = 25 mS/m).

Surface type	Diameter	Zeta potential	Product number, Vendor	Emission colour
Sulphate #1	2.1 µm	-32.1 ± 0.9 mV	B0200, Duke Scientific	Blue
Sulphate #2	2.1 µm	-35.5 ± 0.6 mV	B0200, Fisher Scientific	Blue
Carboxylate #1	2.0 µm	-15.9 ± 0.3 mV	F8888, Invitrogen	Green
Carboxylate #2	1.9 µm	-13.5 ± 0.4 mV	F8827, Invitrogen	Green
Carboxylate #3	2.1 µm	-22.2 ± 0.7 mV	09847, Polyscience	Green
Amine	2.0 µm	+22.9 ± 0.1 mV	L9529-1ML, Sigma	Orange

Table 1: Polystyrene spheres used in this work

Besides surface electrical properties, dielectric property of particles is also of interest for studying their behaviours in sorting device. The method for characterising dielectric property using dielectrophoretic (DEP) force is described in Section 3.4 (The theory of dielectrophoresis is presented briefly in Subsection 2.4.1.). The polarity of the DEP force on the Sulphate #2 and the Carboxylate #2 beads at different frequencies (Figure 2) reveals that both types of beads experienced negative DEP at almost all combination of conductivity and frequency, with the exception of the sulphate beads at very low conductivity (1 mS/m) from 1 kHz to 200 kHz experiencing positive DEP.

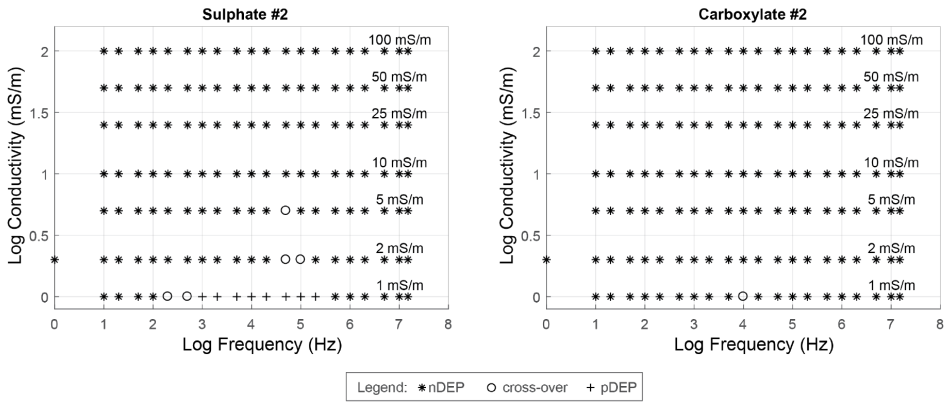

Figure 2: *Polarity of DEP force on Sulphate beads #2 and Carboxylate beads #2 in either a DLD device, a castellated device, or a quadrupole device. The force is of negative polarity (nDEP) in most cases.*

2.1.2. Sorting of polystyrene microspheres

The beads of six different types, all having diameters close to 2 μm, were run in analytical DLD devices having critical diameter $D_C = 2.8\,\mu m$, at pressure $P = 10\,mBar$ and applied voltage $V_{PP} = 300\,V$ (See Subsection 3.1.1 and Figure S7 of the ESI). The frequency of the voltage was scanned from 10 Hz until 5 kHz. Videos of the beads' trajectories at the end of the DLD array were captured as image stacks. The image stacks were then processed to produce the plots that show the integrated fluorescence intensity of each type of beads at each gap (Figure 3). For fluorescence polystyrene beads, the integrated fluorescence intensity is proportional to the bead count. Details of the data analysis are presented in Section 3.2.

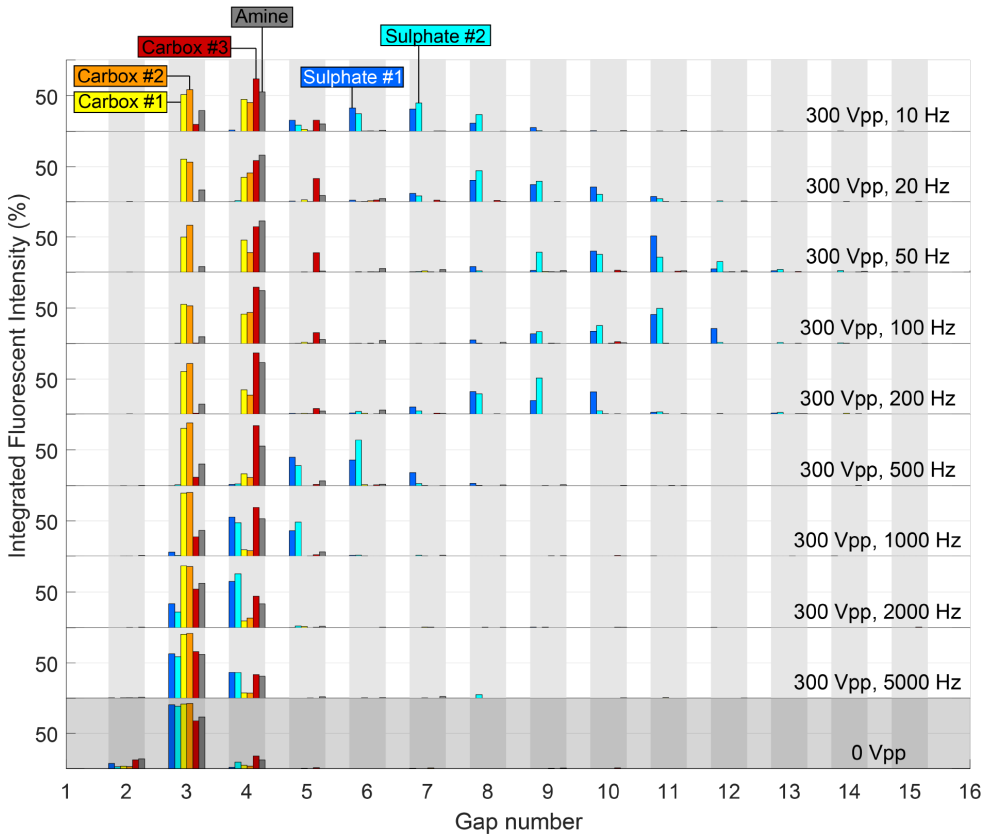

Figure 3: *Displacement of six types of bead when varying frequencies while the applied pressure and the applied peak-to-peak voltage were kept the same.*

It was clear that there is a correlation between zeta potential (Table 1) and the beads' displacement (Figure 3). The Sulphate #1 and Sulphate #2 beads, which have much higher absolute values of zeta potential, displace much more than the carboxylate beads. Among the carboxylate beads, the carboxylate #3 beads, having slightly higher zeta potential than carboxylate #1 and #2 beads, show slightly higher displacement but not enough to make the switch to a displacing tendency like that of sulphate beads. The amine beads, which have a positive zeta potential, show little displacement.

The results suggest that beads with different zeta potential/surface coating can be sorted out in an Electrokinetic DLD, at frequencies from 20 Hz to 200 Hz. At the frequencies from 1 kHz and above, there is almost no displacement although the same peak-to-peak voltage was applied.

2.2. Sorting of viable and non-viable yeast cells

2.2.1. Characterization of viable and non-viable yeast cells.

Yeast cells can be modelled as a sphere of cytoplasm coated with either a single shell, two shells, or even three shells externally. In this paper, we adopt the two-shell model, which assumes that the cytoplasm is enveloped by a plasma membrane and a cell wall (Figure S1 of the ESI). The size/thickness and the permittivity of the cytoplasm, the plasma membrane, and the cell wall appear to change insignificantly after the cells are heat-treated. Their electrical conductivities, on the other hand, change and contribute to the difference in electrical properties of viable and non-viable cells. After the cells have been heat-treated, their cytoplasmic conductivity decreased while their membrane conductivity increased. This fact, according to Pethig [24], is a result of membrane damage due to heat: high temperature degrades the structure of the cell membrane, decreases its resistance to the leakage of ions from the cytoplasm down the concentration gradient into the surrounding medium. Therefore, the membrane conductivity increases and the cytoplasmic conductivity decreases after heat treatment. The conductivity of the cell wall is dependent on that of the external medium. Asami *et al.* [25] pointed out that the ratio of the cell wall conductivity to the medium conductivity can vary from 0.1 to 0.24, depending on the medium conductivity.

As a basis for separation of viable and non-viable yeast cells using Electrokinetic DLD, we first characterise and compare their DEP response at different combinations of medium conductivities and voltage frequencies (Figure 4). Figure 4a shows examples of the DEP characterisation experiments of yeast cells in the three devices used for this task: a DLD device, a quadrupole device, or a castellated electrode device (see Section 3.4 for details). In Figure 4b, the results of these experiments, plotted as star (nDEP), plus (pDEP), and circle (cross-over between nDEP and pDEP) data points, are shown on the background of the DEP force signs – green for nDEP and red for pDEP – calculated using parameters measured by Hölzel *et al.* [26]. Hölzel *et al.* reported a wide varying range of the membrane conductivity of both viable and non-viable yeast cells. In plotting the graphs of Figure 4b, we chose the membrane conductivity to be 0.02 mS/m and 0.16 mS/m for viable and non-viable cells, respectively. In Figure S2 (ESI), we also plot the same graph but choose the lowest values in the reported ranges (2×10^{-5} mS/m and 0.01 mS/m, for viable and non-viable cells, respectively). In that case, our data do not match with the model for some values of medium conductivity (5 – 10 mS/m for viable cells, and 10 – 25 mS/m for non-viable cells) at low frequency range (up to roughly 100 kHz), but correlate with the model at other data points.

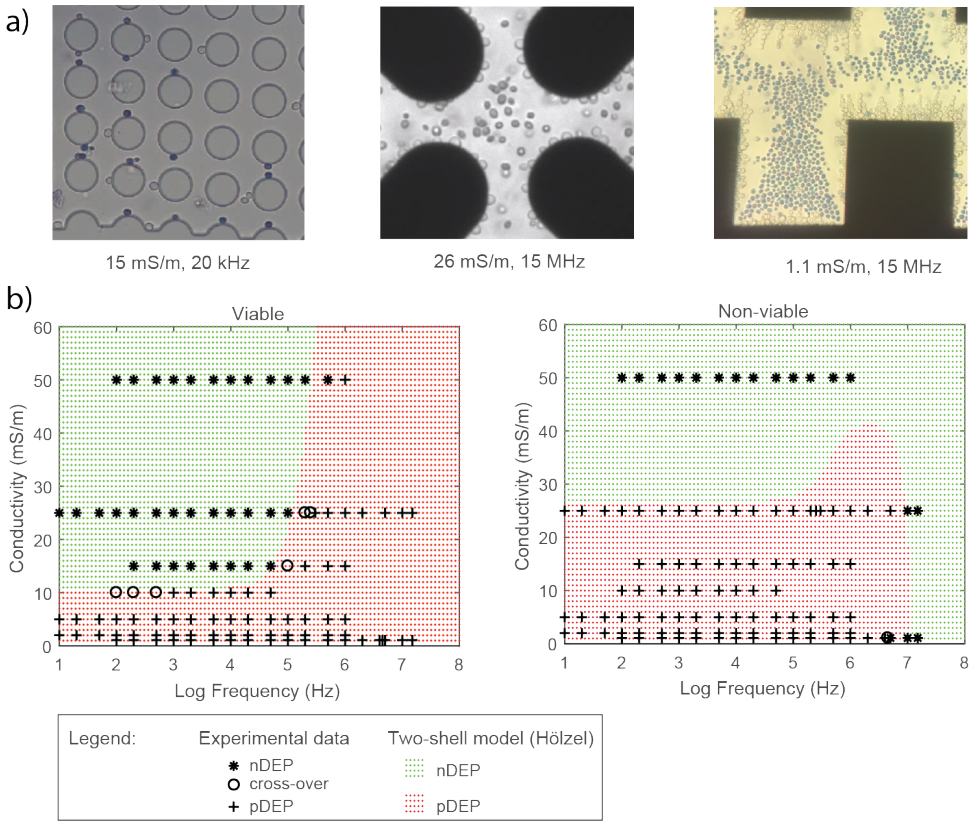

Figure 4: *Electrical characterisation of yeast cells based on DEP.* ***a)*** *Images of viable/non-viable yeast cells being characterised in a DLD device, a quadrupole device, and a castellated device, respectively.* ***b)*** *The sign of DEP force on viable/non-viable yeast cells, from our experiments versus from calculations using the parameters measured by Hölzel et al. [26]. The conductivity of membrane was chosen to be 0.02 mS/m and 0.16 mS/m for viable and non-viable cells, respectively.*

2.2.2. Sorting of viable and non-viable yeast cells

From Figure 4b, it can be assumed that separation of viable/non-viable yeast cells in a DLD device based on DEP is most effective at medium conductivity ranging from 15 to 25 mS/m and at frequency ranging from 100 Hz to below 100 kHz, where there DEP force signs are different. During experiments in DLD, at 100 Hz both viable and non-viable yeast cells were displaced with displacement proportional to the applied voltage (Figure 5a). Separation was, however, infeasible at this frequency. When the frequency was increased while the voltage was kept unchanged, the displacement was decreased, as exemplified in Figure 5b and by comparing Figure 5b with Figure 5a. By varying the medium conductivity from $10 - 50\,mS/m$ and the frequency from $100\,Hz - 50\,kHz$, we observed that the separation was best achieved at a combination of $\sigma = 50\,mS/m, f = 20\,kHz$, as shown in Figure 5c.

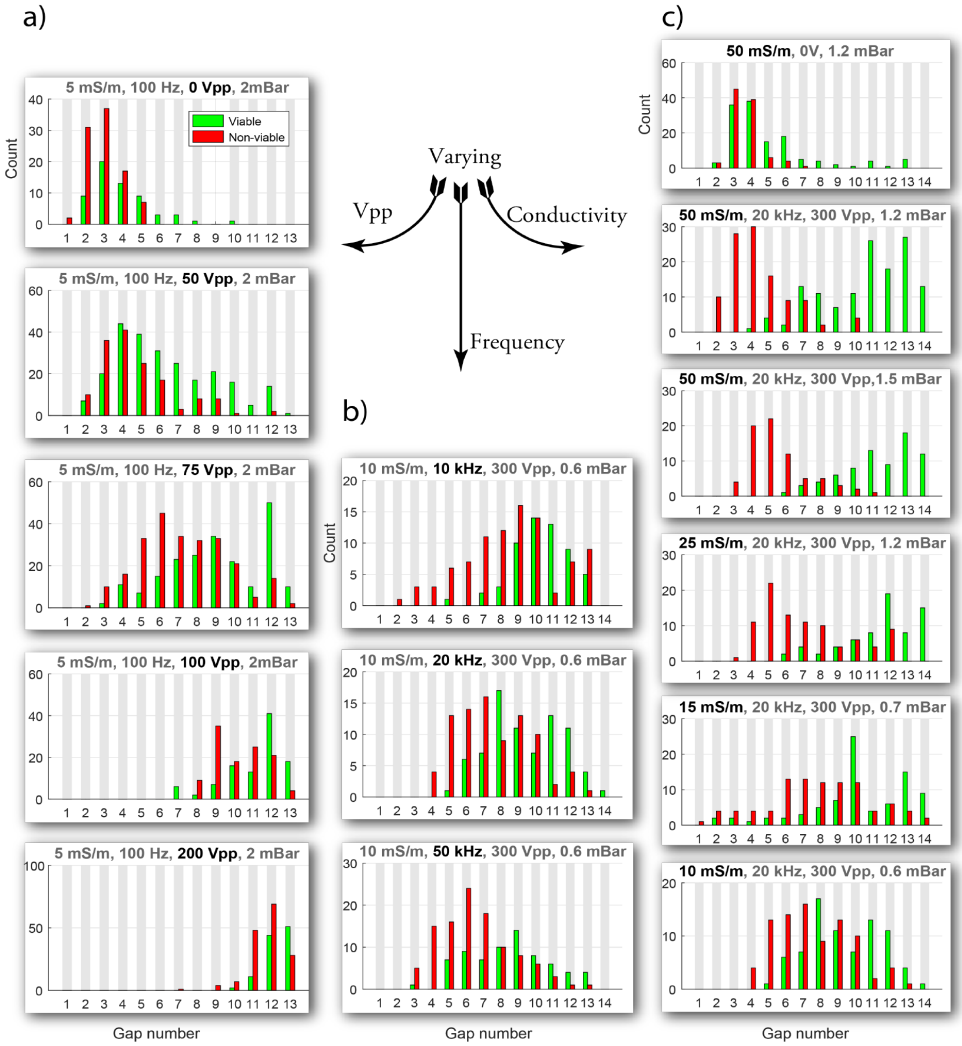

Figure 5: *Displacement of viable/non-viable yeast cells when either voltage, frequency, or conductivity was varied. The critical diameters of the device used in Figure 5a: D_C = 5.6 µm, Figure 5b: D_C = 4.6 µm, Figure 5c: the first two graphs D_C = 5.1 µm, the last four graphs D_C = 4.6 µm.*

2.3. Sorting of viable and non-viable *E. coli*

Non-viable (heat-treated) *E. coli* appear to be slightly larger than viable ones in a DLD device; however, the difference is inadequate to separate them using a conventional DLD device. In a device having the critical diameter of 1.24 µm (Gap = 4 µm, Period = 23), both types of cells would travel in a zigzag manner (Figure 6b, plot #2 from the top). On the other hand, in a device having the critical diameter of 0.64 µm (Gap = 3 µm, Period = 50), both types of cells would travel in a displacing manner (Figure S4a, ESI, plot #2 from the top). Details of the devices can be found in Section S8 of the ESI.

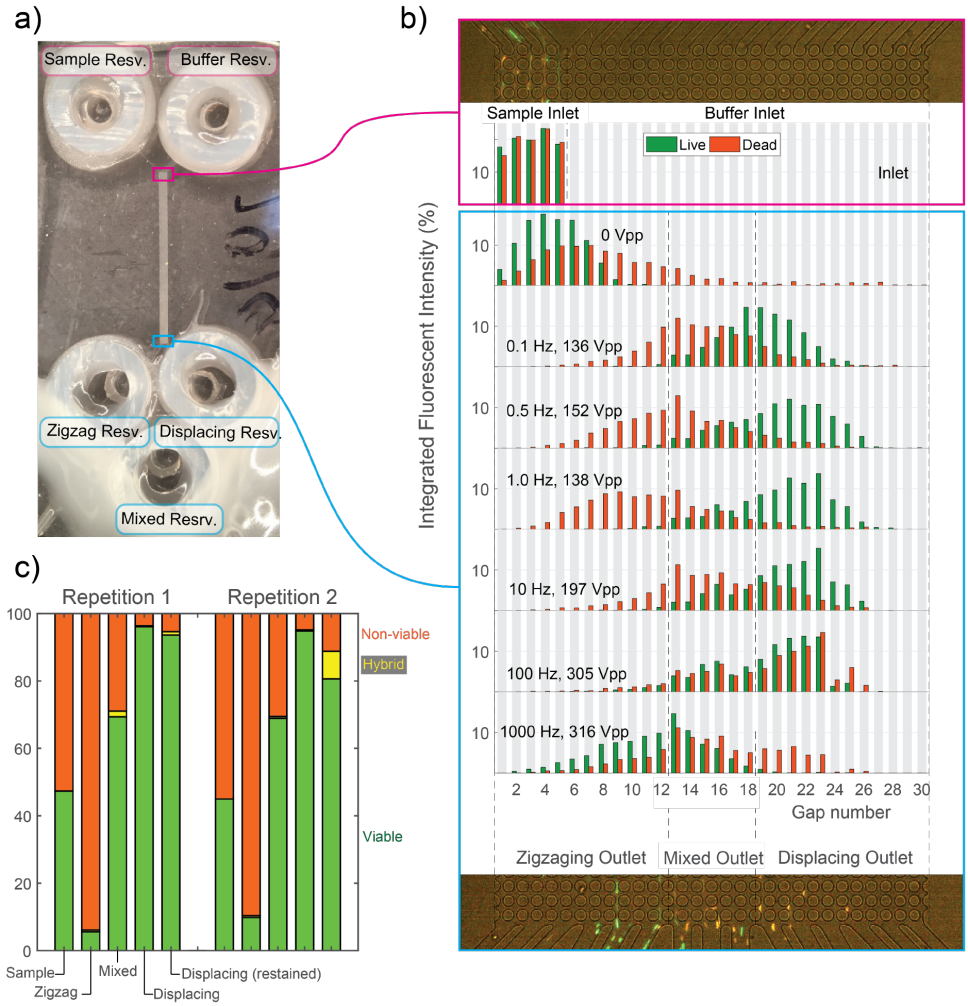

Figure 6: *E. coli sorting with Electrokinetic DLD.* ***a)*** *Image of the device,* ***b)*** *Distribution of viable and non-viable cells at the end of the DLD array at different combinations of frequency and voltage. The conductivity here is 100 mS/m.* ***c)*** *Ratio between viable and non-viable cells recovered from different outlet reservoirs. Each repetition was performed on a different device (of the same design but can vary slightly due to manual fabrication steps)*

Therefore, it is of great interest to explore the potential of electrokinetics in extending the capability of DLD. For this purpose, a DLD device capable of sorting sample into three reservoirs at the outlet was used (Figure 6a). The reservoirs are named: “zigzag reservoir”, “mixed reservoir”, and “displacing reservoir”, corresponding to the trajectories of the particles they can collect. Efforts were made to first sort bacteria into the reservoirs and later recover them and test for viability.

The whole set of experiments includes two steps: scanning and searching for an optimised combination of conductivity and frequency for sorting, and then running actual sorting experiment at the optimised combination just found. In the first step, three values of conductivity were tested (20 mS/m, 100 mS/m, and 500 mS/m) in a DLD device having a critical diameter of 1.24 μm and the applied pressure was 20 mBar. During those experiments, it was observed that in general the viable cells were displaced more than the non-viable ones. Therefore, at each frequency, the voltage was adjusted so that almost all viable cells were displaced into the "displacing outlet" or the "mixed outlet". The degree of displacement of the non-viable cells would then indicate the efficiency of sorting (the more zigzag tendency, the higher sorting efficiency). The plots for the experiments performed at σ = 100 mS/m – the conductivity giving the best sorting – are shown in Figure 6b.

There are two interesting revelations from the plots of Figure 6b. First of all, as the frequency was increased from 1 Hz, a higher voltage was needed to keep the viable cells at the same degree of displacement. At 1 kHz, even a voltage of more than 300 Vpp (the limit of our amplifier) could not fully displace viable bacteria. Second of all, although the non-viable cells, when the power was off, tend to displace slightly more than viable cells, the trend was reversed when the power was on, allowing collecting of non-viable cells into the "zigzag reservoir" and the "mixed reservoir", and the viable ones into the "mixed reservoir" and the "displacing reservoir". It can be seen that 1 Hz was the best frequency for sorting, at the conductivity of 100 mS/m. At the conductivity of 20 mS/m or 500 mS/m, similar trends were observed but the sorting capability was not as good as at 100 mS/m (Figure S4b, S4c in the ESI). We therefore chose the conductivity of 100 mS/m for the second step – actual sorting experiments.

In the second step, we ran a new device at the parameters found in the first step, in 1 hour 30 minutes (D_C = 1.24 μm, P = 20 mBar, σ = 100 mS/m, f = 1 Hz, Vpp = 130 $\pm$10 V. The variation of the optimised voltage for separation is due to the variation between devices, since for example, the holes for the reservoirs were perforated manually.). The populations of the bacteria in the three outlet reservoirs were recovered and counted. Furthermore, an additional re-staining step with propidium idode (dead cell stain) was performed on the population in the "displacing reservoir", which was expected to contain mostly viable cells. The results are shown in Figure 6c, showing high purity of non-viable cells in the "zigzag reservoir" and high purity of viable cells in the "displacing reservoir".

2.4. Mechanism of sorting

The mechanism of sorting is intricate and may be a combination of many phenomena. A short review of the possibly involved phenomena is presented below. After that, we will discuss the contribution of each phenomenon into sorting mechanism.

2.4.1. Review of involved phenomena

a) *Dielectrophoresis* (DEP) refers to the transport of dielectric particles in a non-uniform electric field [7]. The DEP force on a spherical particle of radius r in a non-uniform electric field $\boldsymbol{E}$ is calculated as:

$$\boldsymbol{F}_{DEP} = 2\pi\varepsilon_m r^3 Re\left(\frac{\tilde{\varepsilon}_p - \tilde{\varepsilon}_m}{\tilde{\varepsilon}_p + 2\tilde{\varepsilon}_m}\right)\nabla|\boldsymbol{E}_{\boldsymbol{rms}}|^2 \qquad (2)$$

where $\boldsymbol{E}_{\boldsymbol{rms}}$ is the root mean square value of the field, $\tilde{\varepsilon}_p$, $\tilde{\varepsilon}_m$ are the complex permittivity of the particle and the suspending medium, defined as: $\tilde{\varepsilon} = \varepsilon - i\sigma/\omega$. Here ε is the permittivity, σ is the conductivity, and ω is the angular frequency of the electric field. The term in the brackets is called the Clausius-Mossotti factor.

For polystyrene beads, the bulk conductivity σ_b is negligibly small and their conductivity comes from the surface conductivity σ_s [27]:

$$\sigma_p \approx \sigma_s = \frac{2K}{r} \qquad (3)$$

where r is the radius and K is the surface conductance of the beads.

In the cases where cells are studied, their complicated structures can be modelled as a two-shell or three-shell sphere and the effective Clausius-Mossotti factor can be calculated from the contribution of each layer [24].

b) *Electroosmotic flow* and *electrophoresis* refer to the transport of an electrolyte or a charged particle, respectively, using an electric field. Both phenomena can be explained by the theory of the *electrical double layer*. The term electrical double layer refers to the two layers of charge at the interface between a charged surface (charged wall, charged particle) and an electrolyte in contact with this surface. The first layer is the charge layer attached to the surface while the second layer consists of mainly the charges of the opposite polarity to the first layer, coming from the electrolyte and screening the first layer. The applied electric field exerts electrostatic force on the excessive charges in the second layer, and these charges in turn transfer the momentum they acquire via viscous drag to the element that is mobile in relation to the field (the liquid medium in the case of electroosmotic flow and the particles in the case of electrophoresis). This results in the movement of the liquid medium relative to the wall (electroosmotic flow) or the movement of charge particles relative to the liquid (electrophoresis).

The electroosmotic velocity or the electrophoretic velocity is quantified by the Helmholtz–Smoluchowski equation [28, 29]:

$$\boldsymbol{u}_{eof} = -\varepsilon\zeta_w \boldsymbol{E}/\eta \quad (4)$$

$$\boldsymbol{u}_{ep} = \varepsilon\zeta_p \boldsymbol{E}/\eta \quad (5)$$

where ε is the permittivity of the medium, ζ is the zeta potential at the shear plane, the plane between the immobilised and the mobilised charge layers (the subscripts w and p denote the wall and the particle, respectively), η is the viscosity of the medium, and $\boldsymbol{E}$ is the applied field.

Electroosmotic flow and electrophoresis cause the fluid and the particles to oscillate at low AC frequencies. At high frequencies, they are damped. It was observed in our experiments with a high frame rate camera that the oscillation of polystyrene beads are visible at up to 2 kHz.

c) Saffman lift force.

The velocity of the particles in the device, in both cases of pressure driven flow and electrokinetic motion, is on the order of several hundred microns per second. Therefore, the Reynolds number is well below unity and inertial effects [30] on the fluid and on the particles can be neglected. However, in case the velocity of the particles is different from the bulk fluid (due to electrophoresis) and the fluid velocity has a gradient (*i.e.* parabolic flow profile), a Saffman lift force may exist [31]. The formula for the Saffman lift force is given as [32]:

$$F_S = 81.2r^2 u_r \sqrt{\gamma/\nu} \quad (6)$$

where r is the radius of the particle, u_r is the velocity of the particle relative to that of the fluid, γ is the shear rate (velocity gradient), and ν is the kinematic viscosity. The effect of the Saffman lift has been reported in case a DC voltage and a pressure difference is applied across a microfluidic channel [32, 33].

d) Dielectrophoretic-like wall force

It has been reported that due to the presence of an insulating wall, there is a repulsive, dielectrophoretic-like force acting on particles close to the wall [34-38]:

$$F_W \propto f(r, D_w) r^2 E^2 \quad (7)$$

where r is the radius of the particle, D_w is the wall distance, and E is the applied electric field. The wall force decays quickly as the particles evade the wall.

2.4.2. Opinions on sorting mechanism

a) Dielectrophoresis

It has been proposed by Beech *et al.* [20] that the mechanism behind sorting in Electrokinetic DLD is dielectrophoresis. This is a valid argument, since we observed that beads and yeast cells, depending on the frequency of the applied voltage, were attracted to either high field regions (pDEP) or low field regions (nDEP). In simulation (Section 6, ESI), a lateral shift of the beads away from the wall is visible when a DEP force is applied. However, the DEP force might not be the dominant phenomenon, or at

least not the only phenomenon that contributes to the sorting mechanism, based on the following two arguments.

First of all, the displacement of the beads (Figure 3) appears to vary with frequency. This can also be seen from the trajectories in Figure 7a and the outlet distribution in Figure 7b of 2 µm carboxylate-modified polystyrene beads in a DLD device having $Dc = 2.3\ \mu m$, when the frequency and the applied voltage were varied.

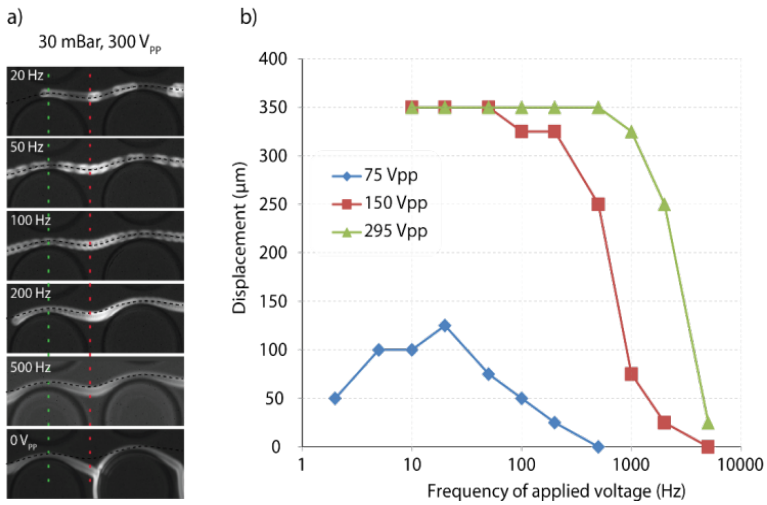

Figure 7: *Trajectories of a 2 µm carboxylate-modified beads in a DLD device having D_c=2.3 µm are dependent on frequency. a) Influence of AC frequency on trajectories of a bead. The trajectory of the bead at 100 Hz (dotted black line) was added to all images as a reference. b) Displacement of the beads at the outlet of the device, as a function of the AC frequency, at different voltages.*

Similar trend can also be seen in the video: "Oscillation of beads – 100 Hz (red) – 500 Hz (green) – 5000 Hz (white).wmv" (ESI). The video was superimposed from three videos of the experiments at three different frequencies. In these experiments, the beads were first transported by a pressure driven flow towards the walls of the pillars. The pressure was then turned off, leaving the beads near the walls, before an AC voltage was switched on. The videos were captured just after the AC voltage was switched on, showing the electrokinetic oscillation of the beads. The video illustrates that the lower the frequency, the faster the beads evade the pillar. If it was only DEP force, the trajectories of the beads should be frequency-independent, as will be shown below.

From Figure 2, it can be deduced that the conductivities of the beads are around 1 mS/m. The charge relaxation time can be calculated as:

$$\tau = \frac{\varepsilon}{\sigma} \quad (8)$$

For beads and for fluid, $\tau_p \sim 20\,ns$ and $\tau_m \sim 30\,ns$, respectively, which correspond to a frequency well above 10 MHz. The applied frequencies shown in Figure 3 are well below this value and thus, the DEP force in Equation (2) becomes:

$$\boldsymbol{F}_{DEP} = 2\pi\varepsilon_m a^3 \left(\frac{\sigma_p - \sigma_m}{\sigma_p + 2\sigma_m}\right) \nabla |\boldsymbol{E}_{\boldsymbol{rms}}|^2 \qquad (9)$$

Which is independent of frequency. Therefore, DEP force may not be the only factor.

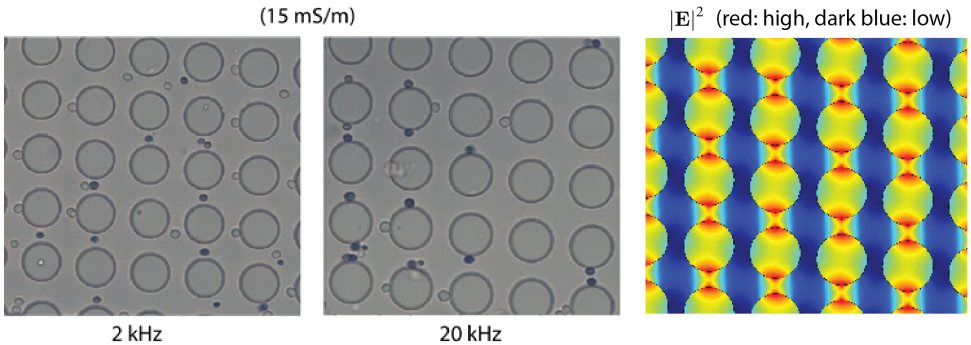

Figure 8: *Anomalous behaviour of non-viable yeast at 2 kHz: instead of going to the high field regions like the non-viable cells at 20 kHz or to the low field regions like the viable cells at 2 kHz and 20 kHz, the non-viable cells at 2 kHz were located at the medium field regions in the middle of the gaps. The simulation of the square of the field strength is shown on the right for reference. The voltage was applied between the left and the right side of each figure (See Section 3.1 for the detailed experimental setup).*

Second of all, during experiments with yeast (Figure 8), it was observed that at low frequencies, while the non-viable cells appeared to experience pDEP, there is an unknown force pushing them into the middle of the gaps. This may be the combination of the pDEP towards the pillars and some other force away from the pillars.

b) *Electroosmotic flow* and *electrophoresis*

In general, in a symmetric sinusoidal AC field, the time average effect of electroosmotic flow or electrophoresis should be zero. This can be seen in the simulation in Section 6, ESI.

c) *Saffman force*

Similarly, the Saffman lift force is alternating in the direction perpendicular to the flow. The simulation in Section 6 of the ESI shows that this lift force has small effect on overall trajectory of particles.

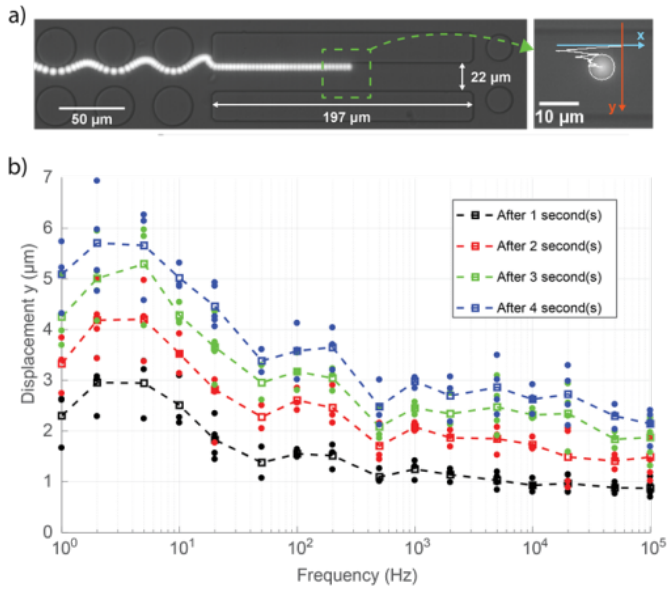

Figure 9: *Frequency dependence of particle motion away from a straight wall. (a) Setup of the experiments. A particle was transported by a pressure driven flow into the straight channel, close to the wall. The flow was then turned off, leaving the particle stationary close to the wall before an AC voltage was turned on and the motion of the particle due to the applied field was recorded. (b) The distance the particles travelled in the direction perpendicular to the wall, after 1, 2, 3, and 4 seconds. The distance was zero at time 0. At each frequency, three different particles were investigated. Their displacements are represented by the closed circular markers. Each open squared marker was the average of three different closed circular markers.*

d) Dielectrophoresis-like wall force

The wall effect can be investigated by an experimental setup shown in Figure 9a). Carboxylate beads (6.3 µm) were led into a straight channel by a pressure driven flow. The pressure was then switched off so that the beads remain stationary and close to the channel wall before an AC voltage was applied. High-magnification, high-speed videos were acquired and the MosaicSuite Particle Tracker [39] was used to extract the positions of the particles as a function of time. The results are shown in Figure 9b). It was clear that the wall force pushes the particles away from the wall and it decays quickly away from the wall. However, since the y-displacement at 5 kHz and at 100 Hz is not so different, this may not explain the result observed in Figure 3. Note that the particles in experiments in Figure 9 have been chosen to be three times larger than the ones used in Figure 3 to enhance the DEP-like wall force (In Equation 7, the force is proportional to the square of the radius).

In conclusion, since the displacement of the polystyrene beads in Electrokinetic DLD is strongest at below 1 kHz, coinciding with the range of electroosmotic flow and electrophoresis, it may be related to these two electrokinetic effect, besides DEP. However, the exact mechanism is still open

and can be a topic of interest. It should be noted that Burt *et al.* [40] observed similar trend of high (arguably) DEP response at low frequency of yeast cells, bacteria, and silicon powder. The authors hinted that the *low frequency dielectric dispersion* (LFDD) can be the cause. However, we were unable to relate this phenomenon with our experimental data.

3. Materials & Methods

3.1. Experimental setups

3.1.1. Devices

The DLD devices used throughout this paper were fabricated in polydimethylsiloxane (PDMS) using soft lithography [41] (specific details can be found in Section 3 "Device fabrication" in the ESI), including two types of design: analytical devices and sorting devices. In an analytical device, only a narrow, single stream of sample is allowed to enter the DLD array and is buffered on the sides (Figure 10b). If the sample is monodisperse in size and in electrical/dielectric properties, they would exit as a single stream at the outlet, allowing precise quantification of displacement. There is only one outlet for the sake of simplicity and also to ensure well-balanced outlet fluidic resistance. In the second type of device – the sorting device – there are five parallel streams of sample entering the DLD array to increase throughput, comparing to the analytical device, and at the outlet, there are three reservoirs to collect particles experiencing different degree of displacement (Figure 6a). The designs of the two types of devices are shown in Section 7 of the ESI.

3.1.2. Equipment and setup

Both pressure and electrical interconnections are required for each Electrokinetic DLD experiment. An over pressure (1 – 100 mBar), regulated by a pressure controller (MFCS-4C, Fluigent, Paris, France, check this), was applied to all inlet reservoirs while an ambient pressure was applied to the outlet reservoirs (Figure 10a). Electrical signals, generated by a function generator (33120A, Hewlett Packard, Palo Alto, CA, USA) and amplified using either a bipolar operational power supply/amplifier (BOP 1000M, Kepco, Flushing, NY, USA) or a high-frequency amplifier (WMA-300, Falco Systems, Amsterdam, The Netherlands), were applied along the length of devices via platinum wires embedded inside the inlet and the outlet reservoirs. The voltage is measured using an oscilloscope (54603B 60MHz, Hewlett Packard) with a 1x/10x probe (Kenwood PC-54, 600Vpp). The conductivities of the media and the suspensions used in all experiments are measured using a B-771 LAQUAtwin Compact Conductivity Meter (Horiba Instruments).

The device was positioned on the stage of an inverted microscope (Nikon Eclipse TE2000-U, Nikon Corporation, Tokyo, Japan). Image sequences of fluorescence particles/cells exiting the DLD array into the outlet reservoirs were captured using an Andor Neo CMOS camera (Andor Technology, Belfast, Northern Ireland) and transferred into a lab computer via NIS Element software (NIS Element

Advanced Research v4.60, Nikon). A colour camera (Exmor USB 3.0, USB29 UXG M) was also used to capture colour video if necessary, for example in the experiments with non-fluorescent viable/non-viable yeast cells or with fluorescent viable/non-viable *E. coli*. They were then analysed using FIJI (ImageJ 1.52f, Nation Institutes of Health, USA), as described below.

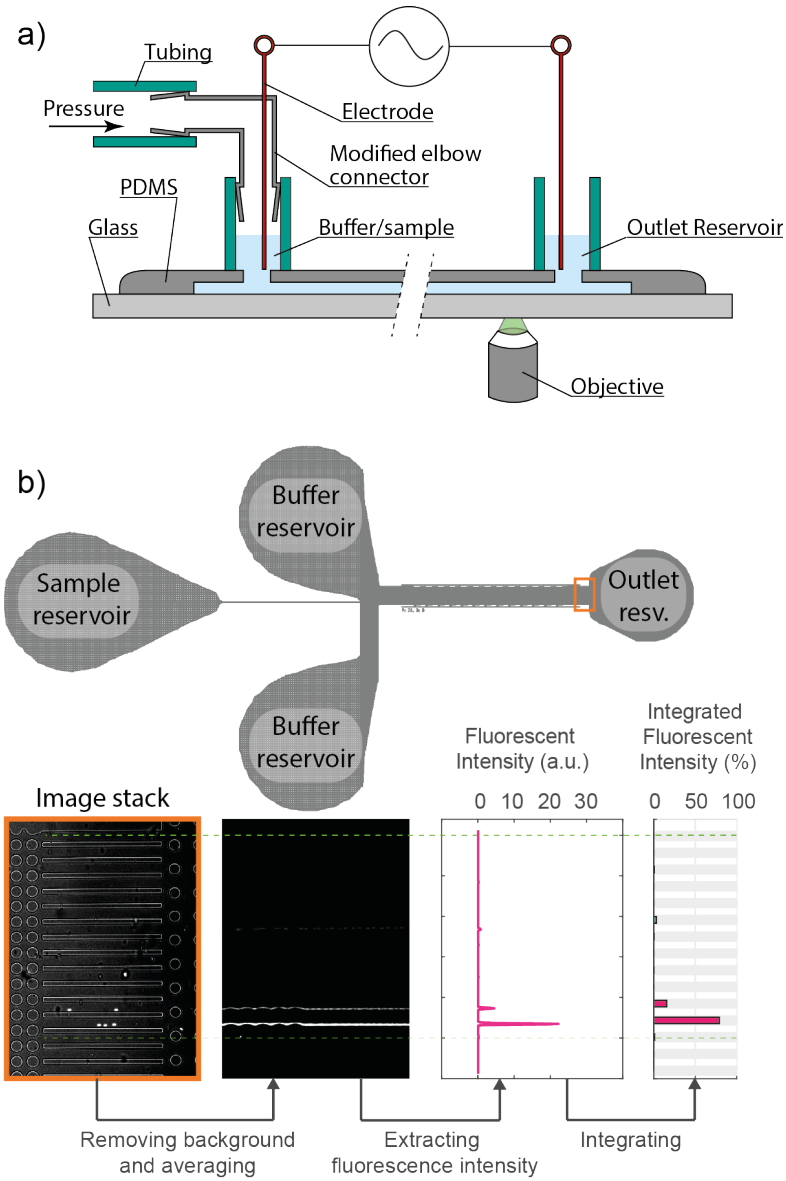

Figure 10: *Details of the experimental setup. a) Side view of a device and the experimental setup. b) Sketch of a DLD device of the analytical type, and a summary of the data analysis steps.*

3.2. Data Analysis

Performance of a sorting experiment was assessed at the end of the array or in the outlet reservoirs.

3.2.1. Particle distribution at the end of the array

The particle distribution at the end of the DLD array can be quantified by manual counting or by assessing average fluorescence intensity of image stacks. In the first method, the number of particles exiting at each outlet gap was counted and a "gap number – count" graph can be constructed. This was done for viable/non-viable yeast cells. However, counting of the moving particles can be a daunting task when the number of image stacks to work on is large and/or the concentration of the particles is high. If the particles are fluorescent, the average fluorescence intensity of the image stacks can be used to quantify the number of particles. More specifically, given the background noise is low and the particles are uniform in size and fluorescent intensity, the fluorescence trace of each particle exiting the DLD array contributes equally to the average fluorescent intensity of the image stack. Therefore, the number of particles exiting at each gap is proportional to the integration of the average fluorescent intensity across the gap. The image processing was done with ImageJ and MATLAB as follows: (also see Figure 10b)

- To remove the background, the average of an image stack is subtracted from the image stack itself. Furthermore, a threshold is applied to make the new image stack binary.
- The new binary image stack is then averaged into a single image where the brightness of a trace at each gap reflects the number of particles contributing to the trace.
- The average fluorescence intensity was integrated across each gap and plotted.

A comparison between manual counts and integrals of fluorescence intensity of different types of beads and at different randomly chosen voltage frequencies (Figure S3 in the ESI) show satisfactory agreement between the two methods. In general, integration of intensity slightly over estimate the number distribution of the beads at the gaps corresponding to high lateral displacement because the particles exiting there usually have larger size than average and thus, contributing a wider trace, as can be observed during experiments with Carboxylate #3 beads.

In the case of fluorescence viable/non-viable *E. coli*, one would expect that the integration of intensity deviates further away from the actual counts due to higher dispersity of their size and their fluorescence intensity than polystyrene beads. Nevertheless, this measure can still give useful estimation of the number distribution to help select the most appropriate parameters for separation. When such parameters are chosen, more time consuming yet more accurate assessing method can be performed on the sorted populations – manual counting of the population collected from the outlet reservoirs.

3.2.2. Particle distribution in the outlet reservoirs

In the experiments with *E. coli*, the ratio of viable/non-viable cells in the outlet reservoirs was assessed by manual counting.

3.3. Sample Preparation

3.3.1. Polystyrene beads

Beads were suspended into a medium containing 1.7 mM KCl, 0.1% w/v Pluronic F127 at the concentration of 0.02 % v/v (48×10^6/mL). Pluronic was found to markedly reduce non-specific sticking of polystyrene beads to PDMS device walls and also suppress electroosmotic flow [42]. The conductivity of the medium with or without beads was 25 mS/m.

3.3.2. Yeast cells

Baker's yeast cells (*Saccharomyces cerevisiae*) in dry form (Jästbolaget AB, Sollentuna, Sweden) was suspended in Glucose 5% w/v at 32 ^{0}C in 30 minutes, for activation. Half of the sample was then heat treated at 62 ^{0}C in 15 minutes to kill the cells. The viable and heat treated sample was mixed at ratio 1:1 and stained with Trypan Blue at concentration of 0.2% w/v, in 5 minutes. Trypan Blue is a popular dead cell stain, which permeate compromised cell membrane and leaves the dark blue colour on the cells, enabling distinguishing between viable and non-viable cells. The mixed sample was then washed several times with the running media, consisting of KCl and Pluronic F127 0.1% w/v at different conductivities. The conductivity of the running media can be adjusted by changing the molar concentration of KCl. The sample was then pipetted into the inlet reservoir and the running medium into the buffer reservoirs and the device was run at low pressure (1 – 2 mBar) at different voltages and frequencies. Videos were captured at the end of the array. Viable and non-viable cells exiting at different gaps were manually counted.

3.3.3. E. coli

Green fluorescent *E. coli* (2566/pGFP) was cultured and stored at -80 ^{0}C in culture medium + 20% w/v glycerol. Prior to experiments, the bacteria were allowed to thaw naturally to room temperature. The concentration of the bacteria was measured at 8.2E8/mL. The bacteria were then spinned down and suspended in running medium (6.8 mM KCl + 0.1% w/v Pluronic F127, σ = 100 mS/m) at the same concentration. Half of the sample was heated at 70 ^{0}C in 20 minutes to kill the cells and then both halves were stained with Propidium Iodide (PI) at the concentration of 20 µg/mL in 5 minutes. Propidium Iodide is a dead cell stain which can penetrate compromised cell membranes. Viable *E. coli* bacteria will appear green due to the GFP, prior and after PI staining. The heat treated *E. coli* bacteria will appear dark prior PI staining and orange after PI staining, enabling distinguishing between viable and non-viable heat treated cells. The viable and non-viable population were mixed with the ratio 1:1 and pipetted into the inlet reservoir. The running medium was also pipetted into the buffer reservoir and the

device was run at an applied pressure of 20 mBar and an applied voltage of 130 ± 10 Vpp, 1 Hz. The variation in the applied voltage is due the variation between devices.

After running for 90 minutes, the sorted populations in the three outlet reservoirs were pipetted out on a glass slide, covered with a cover slip. Pictures of the bacteria were taken and later manually counted. To check the viability of the sorted cells in the displacing reservoirs, an additional PI staining step was also performed.

3.4. Particle Dielectric Characterisation based on Dielectrophoresis

The sign of the dielectrophoretic force acting on particles, given the electric field is known, can gives information about the dielectric or electrical properties of the particles. A particle experiencing negative DEP will travel to regions of low electric field strength whereas a particle experiencing positive DEP will migrate to the places where the field strength is high. The characterisation can be done either in a DLD device [20], a quadruple or a castellated electrode device [27]. While a quadruple or a castellated device, which has microelectrodes fabricated on the bottom of an enclosed microfluidic chamber, has been a standard in characterising DEP forces acting bioparticles, they are prone to AC Electroosmosis at low frequency [43]. A DLD device with insulating pillars is immune to AC Electroosmosis and thus, can bridge the gap at low frequency (< 100 kHz). An illustration of the DEP characterisation experiments on yeast cells in three different devices has been shown in Figure 4a.

4. Conclusion and Outlook

We have presented an application of an integrated device that combines DLD and electrokinetics to sort particles of different surface charge; viable from non-viable yeast cells; and viable and non-viable *E. coli*. We have successfully demonstrated proof of principle. We envision that our approach can be used in applications such as drug screening. However, we understand that further investigations are necessary to ensure that microorganisms killed by drugs can also be detected using our methods, as the heat treatment may not have the same effect.

References

1. Gossett, D.R., et al., *Label-free cell separation and sorting in microfluidic systems.* Anal Bioanal Chem, 2010. **397**(8): p. 3249-67.
2. Yamada, M., M. Nakashima, and M. Seki, *Pinched flow fractionation: continuous size separation of particles utilizing a laminar flow profile in a pinched microchannel.* Analytical chemistry, 2004. **76**(18): p. 5465-5471.

3. Huang, L.R., et al., *Continuous particle separation through deterministic lateral displacement.* Science, 2004. **304**(5673): p. 987-90.

4. Di Carlo, D., et al., *Continuous inertial focusing, ordering, and separation of particles in microchannels.* Proceedings of the National Academy of Sciences, 2007. **104**(48): p. 18892-18897.

5. Petersson, F., et al., *Free flow acoustophoresis: microfluidic-based mode of particle and cell separation.* Analytical chemistry, 2007. **79**(14): p. 5117-5123.

6. Southern, E.M., *Detection of specific sequences among DNA fragments separated by gel electrophoresis.* J mol biol, 1975. **98**(3): p. 503-517.

7. Pethig, R., *Review article-dielectrophoresis: status of the theory, technology, and applications.* Biomicrofluidics, 2010. **4**(2).

8. Harrison, D.J., et al., *Micromachining a miniaturized capillary electrophoresis-based chemical analysis system on a chip.* Science, 1993. **261**(5123): p. 895-897.

9. Inglis, D.W., et al., *Critical particle size for fractionation by deterministic lateral displacement.* Lab Chip, 2006. **6**(5): p. 655-8.

10. Davis, J.A., et al., *Deterministic hydrodynamics: taking blood apart.* Proc Natl Acad Sci U S A, 2006. **103**(40): p. 14779-84.

11. Siyang, Z., et al. *Deterministic lateral displacement MEMS device for continuous blood cell separation*. in *18th IEEE International Conference on Micro Electro Mechanical Systems, 2005. MEMS 2005.* 2005.

12. Li, N., D.T. Kamei, and C.M. Ho. *On-Chip Continuous Blood Cell Subtype Separation by Deterministic Lateral Displacement*. in *2007 2nd IEEE International Conference on Nano/Micro Engineered and Molecular Systems*. 2007.

13. Loutherback, K., et al., *Deterministic separation of cancer cells from blood at 10 mL/min.* AIP Adv, 2012. **2**(4): p. 42107.

14. Liu, Z., et al., *Rapid isolation of cancer cells using microfluidic deterministic lateral displacement structure.* Biomicrofluidics, 2013. **7**(1): p. 11801.

15. Holm, S.H., et al., *Separation of parasites from human blood using deterministic lateral displacement.* Lab Chip, 2011. **11**(7): p. 1326-32.

16. Holm, S.H., et al., *Simplifying microfluidic separation devices towards field-detection of blood parasites.* Anal. Methods, 2016. **8**(16): p. 3291-3300.

17. Beech, J.P., et al., *Sorting cells by size, shape and deformability.* Lab Chip, 2012. **12**(6): p. 1048-51.

18. Beech, J.P., et al., *Separation of pathogenic bacteria by chain length.* Analytica chimica acta, 2018. **1000**: p. 223-231.

19. Henry, E., et al., *Sorting cells by their dynamical properties.* Sci Rep, 2016. **6**: p. 34375.

20. Beech, J.P., P. Jonsson, and J.O. Tegenfeldt, *Tipping the balance of deterministic lateral displacement devices using dielectrophoresis.* Lab Chip, 2009. **9**(18): p. 2698-706.

21. Hanasoge, S., et al., *Electrokinetically driven deterministic lateral displacement for particle separation in microfluidic devices.* Microfluidics and Nanofluidics, 2014. **18**(5-6): p. 1195-1200.

22. Tran, T.S., et al., *Open channel deterministic lateral displacement for particle and cell sorting.* Lab on a Chip, 2017. **17**(21): p. 3592-3600.

23. Chang, S. and Y.H. Cho, *A continuous size-dependent particle separator using a negative dielectrophoretic virtual pillar array.* Lab Chip, 2008. **8**(11): p. 1930-6.

24. Pethig, R.R., *Dielectrophoresis: Theory, Methodology and Biological Applications*. 2017: Wiley.

25. Asami, K. and T. Yonezawa, *Dielectric behavior of wild-type yeast and vacuole-deficient mutant over a frequency range of 10 kHz to 10 GHz.* Biophysical journal, 1996. **71**(4): p. 2192-2200.

26. Hölzel, R. and I. Lamprecht, *Dielectric properties of yeast cells as determined by electrorotation.* Biochimica et Biophysica Acta (BBA) - Biomembranes, 1992. **1104**(1): p. 195-200.

27. Morgan, H. and N.G. Green, *AC Electrokinetics: Colloids and Nanoparticles*. 2003: Research Studies Press.

28. Viovy, J.-L., *Electrophoresis of DNA and other polyelectrolytes: Physical mechanisms.* Reviews of Modern Physics, 2000. **72**(3): p. 813-872.

29. Erickson, D., *Electroosmotic Flow (DC)*, in *Encyclopedia of Microfluidics and Nanofluidics*, D. Li, Editor. 2008, Springer US: Boston, MA. p. 560-567.

30. Di Carlo, D., *Inertial microfluidics.* Lab on a Chip, 2009. **9**(21): p. 3038-3046.

31. Saffman, P., *The lift on a small sphere in a slow shear flow.* Journal of fluid mechanics, 1965. **22**(2): p. 385-400.

32. Yuan, D., et al., *Tunable particle focusing in a straight channel with symmetric semicircle obstacle arrays using electrophoresis-modified inertial effects.* Micromachines, 2016. **7**(11): p. 195.

33. Kim, Y.W. and J.Y. Yoo, *Axisymmetric flow focusing of particles in a single microchannel.* Lab on a Chip, 2009. **9**(8): p. 1043-1045.

34. Yariv, E., *"Force-free" electrophoresis?* Physics of fluids, 2006. **18**(3): p. 031702.

35. Liang, L., et al., *Wall-induced lateral migration in particle electrophoresis through a rectangular microchannel.* Journal of colloid and interface science, 2010. **347**(1): p. 142-146.

36. Liang, L., S. Qian, and X. Xuan, *Three-dimensional electrokinetic particle focusing in a rectangular microchannel.* Journal of colloid and interface science, 2010. **350**(1): p. 377-379.

37. Yariv, E., *Dielectrophoretic sphere–wall repulsion due to a uniform electric field.* Soft matter, 2016. **12**(29): p. 6277-6284.

38. Liu, Z., et al., *Surface-conduction enhanced dielectrophoretic-like particle migration in electric-field driven fluid flow through a straight rectangular microchannel.* Physics of Fluids, 2017. **29**(10): p. 102001.

39. Sbalzarini, I.F. and P. Koumoutsakos, *Feature point tracking and trajectory analysis for video imaging in cell biology.* Journal of structural biology, 2005. **151**(2): p. 182-195.

40. Burt, J.P., T. Al-Ameen, and R. Pethig, *An optical dielectrophoresis spectrometer for low-frequency measurements on colloidal suspensions.* Journal of Physics E: Scientific Instruments, 1989. **22**(11): p. 952.

41. Xia, Y. and G.M. Whitesides, *Soft lithography.* Annual review of materials science, 1998. **28**(1): p. 153-184.

42. Barnes, T.J. and C.A. Prestidge, *PEO−PPO−PEO Block Copolymers at the Emulsion Droplet−Water Interface.* Langmuir, 2000. **16**(9): p. 4116-4121.

43. Green, N.G., et al., *Fluid flow induced by nonuniform ac electric fields in electrolytes on microelectrodes. I. Experimental measurements.* Physical review E, 2000. **61**(4): p. 4011.

Competing Interests

The authors declare no competing interests.

Funding

This work was carried out within NanoLund at Lund University. It was funded by European Union, under the Seventh Framework Programme FP7/2007-2013/ within the project LAPASO (project number 607350) and under Horizon2020/HEALTH within the project BeyondSeq (project number 634890). All device processing was conducted within Lund Nano Lab, Lund University and the Southampton Nanofabrication Centre, University of Southampton.

Acknowledgements

We are thankful to:

- Karin Schillén, Solmaz Bayati, Guanqun Du for instruction on zeta potential measurement,
- Lars T. Hederstedt for helping with culturing of *E. coli*
- Nicolas G Green for the original design of the quadrupole and castellated devices

(Electronic Supplementary Information)

Bio-particle sorting using Electrokinetic Deterministic Lateral Dispalcement †

Bao D. Ho[1], Jason P. Beech[1], Carlos Honrado[2], Daniel Spencer[2], Hywel Morgan[2] and Jonas O. Tegenfeldt[1*]

†*Electronic Supplementary Information available*

[1]*Division of Solid State Physics and NanoLund, Physics Department, Lund University, PO Box 118, 221 00, Lund, Sweden*

[2]*Faculty of Physical Sciences and Engineering and Institute for Life Sciences, University of Southampton, Southampton, UK, SO17 1BJ*

[*]*Corresponding author. Telephone: +46 46 222 8063. E-mail: jonas.tegenfeldt@ftf.lth.se*

1. Electrical properties of Yeast cells

The table in Figure S1 lists dimensions and dielectric/electrical properties of yeast cells, obtaining from the work of Hung *et al.* [1], Höltzel *et al.* [2], and Asami *et al.* [3].

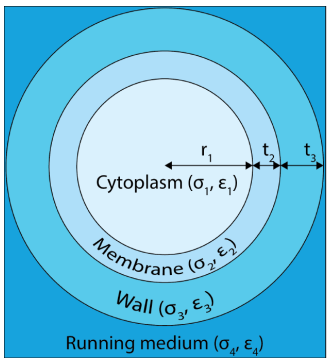

Source	Huang 1992		Hölzel 1992		Asami 1996
Parameters	Viable	Non-viable	Viable	Non-viable	Viable
r_1 (μm)	3.772	3.242	-	-	2.343
t_2 (μm)	0.008	0.008	-	-	0.007
t_3 (μm)	0.22	0.25	0.11 - 0.21	-	0.25
σ_1 (mS/m)	200	7	550	10 - 80	310 - 1500
σ_2 (mS/m)	2.5×10^{-4}	0.16	2.5×10^{-5} - 0.45	> 0.01	0
σ_3 (mS/m)	14	1.5	10 - 50	30	$0.1\sigma_4$ - $0.24\sigma_4$
σ_4 (mS/m)	3	0.5	2.2 - 220	2.2 - 220	145 - 1000
ε_1	50	50	51	51	50
ε_2	6	6	9.9	-	5.1
ε_3	60	60	60	60	60
ε_4	78	78	80	80	77

Figure S1: *Properties of yeast cells.*

2. Comparison between our data with Hölzel *et al.* [2]'s model at the lowest values of membrane conductivity in the ranges they reported

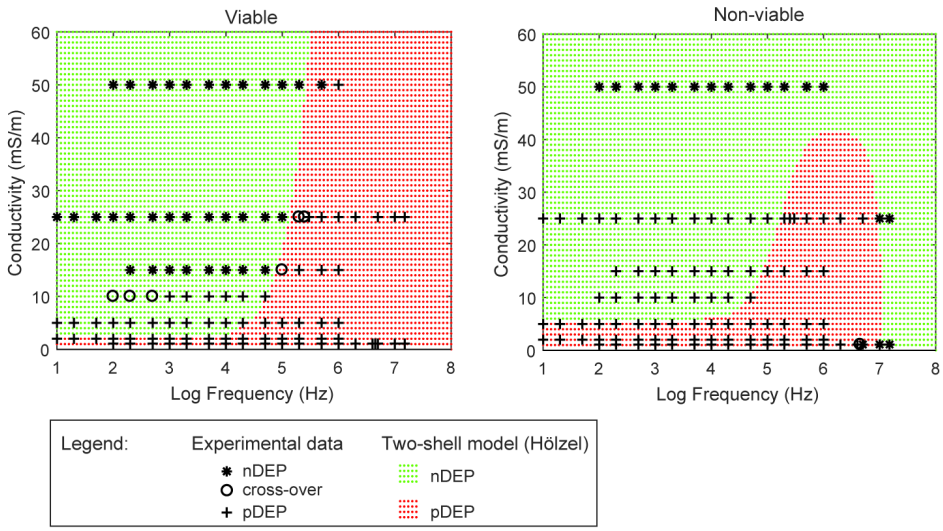

Figure S2: *Comparison between our data with Hölzel et al.'s model at the lowest values of membrane conductivity in the ranges they reported (2×10^{-5} mS/m and 0.01 mS/m, for viable and non-viable yeast cells, respectively).*

3. Device fabrication

There are two steps in making a device: fabricating SU-8 mould using lithography and moulding a PDMS device using soft lithography. In the first step, SU-8 (MicroChem, Newton, MA, USA) was dispensed onto a 3-inch silicon wafer and spun at a well-defined speed according to the manufacture's manual to obtain the desired thickness of the SU-8 layer, which is also the depth of the devices that will be moulded later. The wafer was then exposed to UV-light in a contact mask aligner (Karl Suss MJB4 soft UV, Munich, Germany) with a mask designed using L-Edit 2016 (Mentor Graphics Corporation, Wilsonville, Oregon, United States) and printed by an external mask making company (Delta Mask, Enschede, The Netherlands). After the SU-8 was exposed and developed, a monolayer of trichloro (1H,1H,2H,2H-perfluorooctyl) silane (PFOTS) (Sigma Aldrich, Saint Louis, MO, USA) was applied by molecular vapour deposition onto the wafer to reduce surface energy, preventing PDMS from sticking to the mould later. In the second step, PDMS base and PDMS curing agent (Sylgard 184, Dow Corning, Midland, MI, USA) was mixed at the ratio of 10:1, poured onto the SU-8 mould, and cured in an oven at 80 ^{0}C in 1 hour. The moulded device on the cured PDMS slab was cut out, perforated at reservoir positions, and oxygen plasma bonded on a PDMS-covered glass slide (ZEPTO, Diener Plasma-Surface Technology). Silicone tubes of 5 mm outer diameter (228-0707, VWR International LLC, Radnor, PA, USA) were glued (Elastosil A07, Wacker Chemie AG, Munich, Germany) onto the

device as inlet and outlet reservoirs. The bonded devices were left in an oven at 120^0C for 24 hours to bring the PDMS surface back to its native hydrophobic state, making it stable for electrokinetic experiments [4]. Finally, the devices were stored for future use.

4. Comparison between counting by hand and integrating average fluorescence intensity

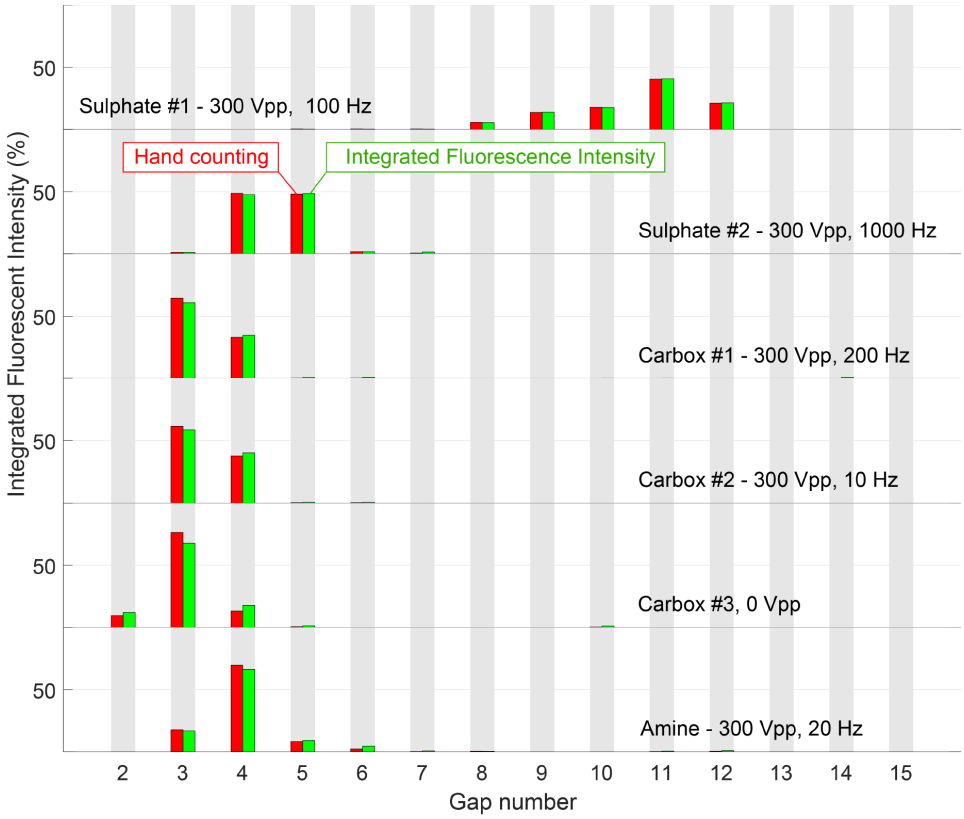

Figure S3: *Comparison between manual counts and integrals of fluorescence intensity.*

5. Soring of *E. coli* in other DLD device or at other conditions

In the main text, sorting of *E. coli* bacteria in a DLD device with $D_C = 1.24\ \mu m$ at the medium conductivity $\sigma = 100\ mS/m$ was presented. Here we presented sorting results in other cases.

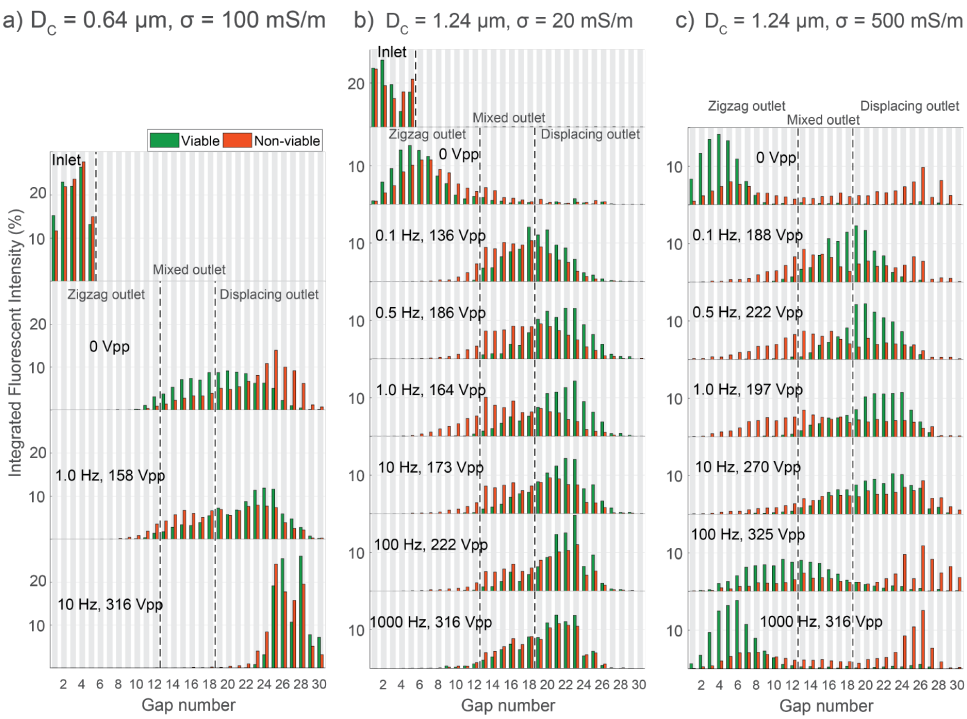

Figure S4: *Viable and non-viable E. coli outlet distribution in different devices and at different conductivities.* ***a)*** *In a device having small Dc, both viable and non-viable cells were displaced even when there is no applied voltage.* ***b)*** *and* ***c)*** *When the medium conductivity was either 20 mS/m or 500 mS/m, both viable and non-viable cells were displaced but their separation was not as good as in the case σ = 100 mS/m (See main text).*

6. Simulation

The simulations was done using COMSOL Multiphysics 5.3a and in 2D instead of 3D to reduce complexity, taking advantage of the fact that the device has a uniform cross section in the z-direction. Three dimensional simulations are needed if the position of the particle in the z-direction matters. For simplicity, we can assume that the particles are neutrally buoyant and flowing at mid-pillar height.

The simulations (Table 1) was done at different length scales (Figure 5) to compromise between accuracy and computational resources. The most computationally expensive simulation was done at the *device scale* to obtain the actual pressure and voltage drop on the DLD array. It also solves the electric field at the inlet channel, which together with experimental data, is needed for calculating the particle electrokinetic mobility. At the smaller scale – the *array scale* – electric currents, pressure driven flow, and electroosmotic flow were resolved. This scale is needed to reflect the actual anisotropic permeability of the device. If only few periods are simulated, the flow is pushed more to the displacing side than what would be the case in a real experiment. The smallest scale, *several periods,* is where the particle trajectories were simulated, at different experimental conditions, using the "Particle tracing for fluid flow" module. A "Wall distance" study is needed for application of wall force.

Scale	**Physics**	**Study type**
Device	Electric current	Frequency dependent
	Pressure driven flow	Stationary
Array	Electric current	Frequency dependent
	Pressure driven flow	Stationary
	Electroosmotic flow	Stationary
Several periods	Wall distance	Stationary
	Particle tracing for fluid flow	Time dependent

Table S1: *Simulation scheme. Different physics (i.e. modules in COMSOL) were explored.*

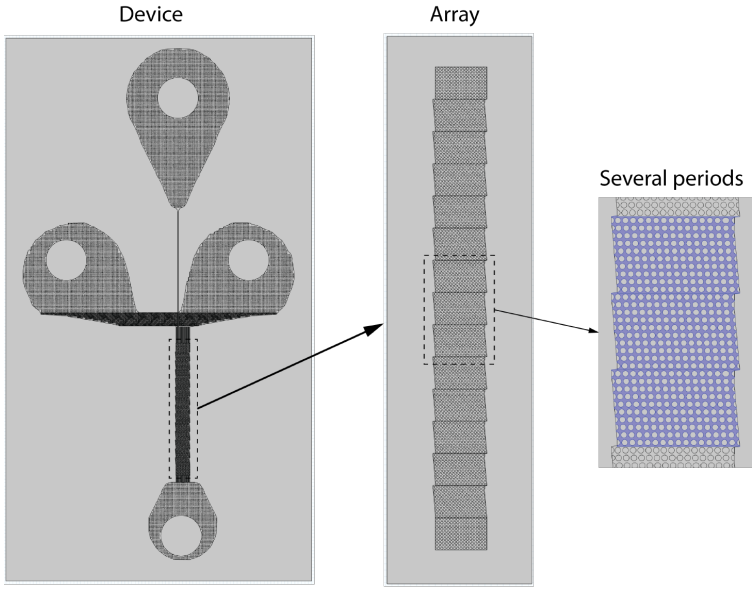

Figure S5: *Simulations were done at different spatial scales to optimise the computing time.*

The "Particle tracing for Fluid flow" module used the electric field and the flow field calculated in at the array scale to apply appropriate forces on the particle. In all cases, a fictitious wall force was applied when the centres of the particles are one radius apart from the pillar wall to keep them from penetrating the wall. Also in all cases, a Stokes drag force was applied on the particles. Figure 6 shows simulations in four different cases:

- Case 1 (PD): Pressure driven flow only (10 mBar), no voltage applied: the Stokes drag used velocity field from the pressure driven flow physics.
- Case 2 (DEP): Pressure driven flow, an AC field was applied and the DEP force was added: the DEP force on a sphere was applied on the particle, in this case a polystyrene bead. The value of its conductivity was chosen to be 1 mS/m, based on Figure 2 in the main text.
- Case 3 (EK): Pressure driven flow, an AC field was applied but only electrokinetic (EK) effects was added. Here we use the term "electrokinetics" to refer to both electrophoresis and electroosmotic flow. An electrophoretic mobility (deduced from the zeta potential of Sulphate #2) was used to prescribe the relative velocity of the particle to the fluid. The electroosmotic flow was setup by imposing a wall slipping velocity with an electroosmotic mobility (this value was calculated based on the

velocity of the Sulphate #2 beads when a -50 VDC was applied). The Stokes drag is derived from the velocity field from the sum of pressure driven flow velocity and the electroosmotic flow.

- Case 4 (EK+Saffman): Like case 3, but the Saffman lift force was also added.

Results and discussion:

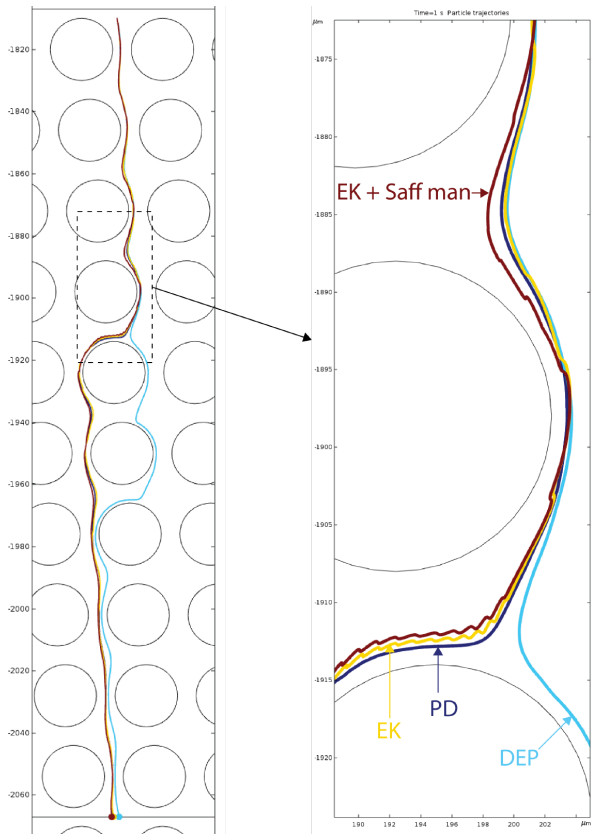

Figure S6: *Simulations result for four cases stated above. The beads was 2.1 µm Sufphate beads. The pressure was 10 mBar, the voltage was 300 Vpp, 100 Hz.*

It can be seen in Figure 6 that overall, all beads go zig-zagging, except for DEP bead has some displacing tendency. In the zoomed view, the EK and PD trajectories are quite close to each other, confirming that the time average of the AC electroosmotic and electrophoretic effects is close to zero. Also, the Saffman trajectory is close to the EK trajectory, showing that the time average of the Saffman force is close to zero.

However, there is room for improvement. In order for the simulation results to be conclusive, more extensive studies should be carried out:

- More values of frequency and electrophoretic mobility should be studied and compared with the results shown in Figure 3 of the main text.
- Since the trajectories of the particles are dependent on their initial releasing position and time, different releasing positions and time should be investigated.
- Here only one period of the DLD array is simulated. This should be extended to more periods, so that a larger picture of the trajectories of the particles can be observed.

7. Devices

7.1. Analytical DLD devices

Analytical DLD devices used for beads and yeast cells

- The devices are for analytical purpose with only one single stream of inlet sample and one outlet reservoir.

- Four devices have been used, and are listed on the right hand side. The device with Gap = 6 is shown below for demonstration. The other devices have similar lengths and outlet designs.

• Device used for polystyrene beads:

Gap width(μm)	Pillar diameter (μm)	Period	Critical diameter (μm)
6	20	10	2.8

• Devices used for yeast cells:

Gap width (μm)	Pillar diameter (μm)	Period	Critical diameter (μm)
10	20	10	4.6
11	20	10	5.1
12	20	10	5.6

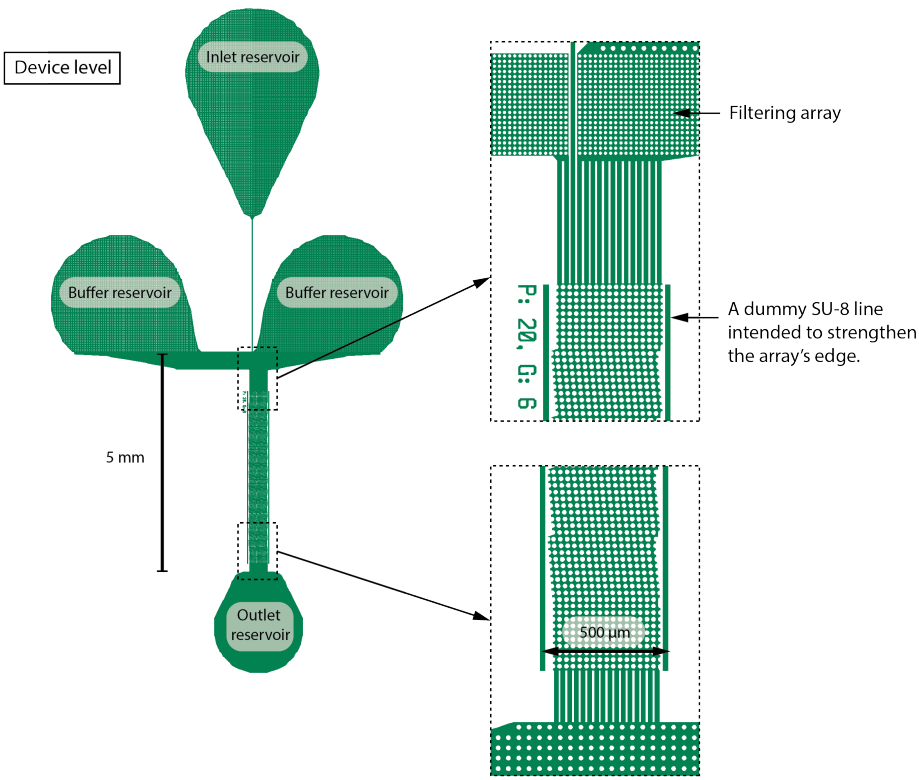

Figure S7: *Analytical DLD devices having only one inlet stream and one outlet reservoir.*

7.2. Sorting DLD devices

DLD devices used for sorting *E.coli*

- The devices are for sorting and recovering sorted populations of *E. coli* bacteria.
- Device with Gap = 4 is mainly used and is shown below.

Gap width (µm)	Pillar diameter (µm)	Period	Critical diameter (µm)
4	12	23	1.24
3	15	50	0.64

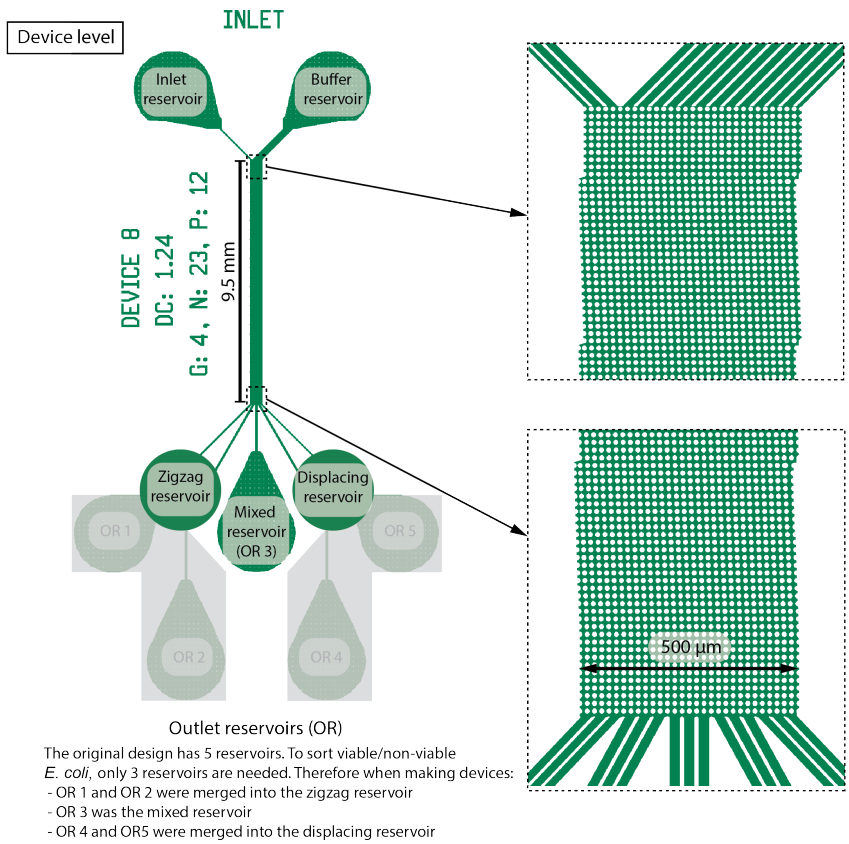

Figure S8: *Sorting DLD devices having only five inlet streams and five outlet reservoir.*

8. Videos

A selection of the videos of the results are available at: bit.ly/ElectrokineticDLDVideos (case sensitive)

- Polystyrene beads:
  - "Sulphate2 (red) – Carbox2 (green) - 100 Hz.avi": real-time, colour-coded video showing the separation of the Sulphate #2 (red) and Carboxylate #2 (green) beads at the end of the DLD array having D_C = 2.8 µm. The result has been plotted in Figure 3.
  - "Oscillation of beads – 100 Hz (red) – 500 Hz (green) – 5000 Hz (white).wmv": colour-coded, slow motion video showing the oscillation of the same type of bead at different frequencies, when an AC voltage was applied along a DLD device (no pressure applied).
- Yeast cells:
  - "50 mS_m - 0 Vpp - 1d2 mBar - 2x.wmv": viable (transparent) and non-viable (dark) yeast cells exiting at the end of a DLD array having $D_C = 5.1\ \mu m$. The video was cut out from the original video used to produce the first graph of Figure 5c (main text) and sped up 2 times. The original video is 10 times longer.
  - "50 mS_m - 20 kHz - 300 Vpp - 1d2 mBar - 2x.wmv": similar to the previous video, but an AC voltage of 20 kHz, 300 V_{PP} was applied. The video was cut out from the original video used to produce the second graph of Figure 5c (main text) and sped up 2 times. The original video is 7.5 times longer.
- *E. coli:*
  - "100 mS_m - 20 mBar - Inlet.wmv": viable (green) and non-viable (orange) *E. coli* bacteria entering a DLD array having $D_C = 1.24\ \mu m$. The video was recorded in real-time using the Exmor USB colour camera. In the same experiment, the Andor Neo monochrome camera was used to obtain the videos from which the results were processed and plotted in the first graph of Figure 6b (main text).
  - "100 mS_m - 20 mBar - Outlet.wmv": similar to the previous video, captured at the outlet.
  - "100 mS_m - 20 mBar - 138 Vpp - 1Hz - Outlet.wmv": video captured at the outlet, with an AC voltage applied. Separation of viable and non-viable cells is visible.

References

1. Huang, Y., et al., *Differences in the AC electrodynamics of viable and non-viable yeast cells determined through combined dielectrophoresis and electrorotation studies*. Physics in Medicine & Biology, 1992. **37**(7): p. 1499.
2. Hölzel, R. and I. Lamprecht, *Dielectric properties of yeast cells as determined by electrorotation.* Biochimica et Biophysica Acta (BBA) - Biomembranes, 1992. **1104**(1): p. 195-200.
3. Asami, K. and T. Yonezawa, *Dielectric behavior of wild-type yeast and vacuole-deficient mutant over a frequency range of 10 kHz to 10 GHz.* Biophysical journal, 1996. **71**(4): p. 2192-2200.
4. Hung, L.-H. and A.P. Lee. *Optimization of droplet generation by controlling PDMS surface hydrophobicity*. in *ASME 2004 International Mechanical Engineering Congress and Exposition*. 2004. American Society of Mechanical Engineers.

Bacteria chain length sorting with DLD

Paper II

Analytica Chimica Acta 1000 (2018) 223–231

Contents lists available at ScienceDirect

Analytica Chimica Acta

journal homepage: www.elsevier.com/locate/aca

Separation of pathogenic bacteria by chain length

Jason P. Beech [a], Bao Dang Ho [a], Geneviève Garriss [b], Vitor Oliveira [b], Birgitta Henriques-Normark [b, c, d], Jonas O. Tegenfeldt [a, *]

[a] Division of Solid State Physics and NanoLund, Lund University, SE-221 00, Sweden
[b] Department of Microbiology, Tumor and Cell Biology, Karolinska Institutet, SE-171 77 Stockholm, Sweden
[c] Department of Clinical Microbiology, Karolinska University Hospital, SE-171 76 Stockholm, Sweden
[d] SCELSE and LKC, Nanyang Technological University, NTU, Singapore 639798, Singapore

HIGHLIGHTS

- Fractionation of the human bacterial pathogen, *Streptococcus pneumoniae*, into subpopulations based on morphological type.
- The results open up for detailed studies of the association of morphology and virulence mechanisms among bacteria.
- The fractionation tool is based on microfluidics and deterministic lateral displacement.

GRAPHICAL ABSTRACT

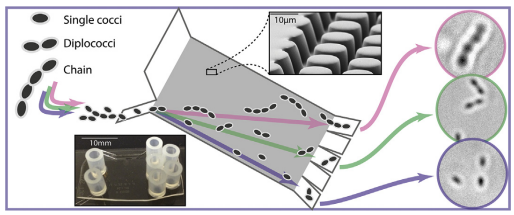

ARTICLE INFO

Article history:
Received 21 November 2017
Accepted 22 November 2017
Available online 25 November 2017

Keywords:
Deterministic lateral displacement
Separation
Bacterial virulence
Morphology

ABSTRACT

Using Deterministic Lateral Displacement devices optimized for sensitivity to particle length, we separate subpopulations of bacteria depending on known properties that affect their capability to cause disease (virulence). For the human bacterial pathogen *Streptococcus pneumoniae*, bacterial chain length and the presence of a capsule are known virulence factors contributing to its ability to cause severe disease. Separation of cultured pneumococci into subpopulations based on morphological type (single cocci, diplococci and chains) will enable more detailed studies of the role they play in virulence. Moreover, we present separation of mixed populations of almost genetically identical encapsulated and non-encapsulated pneumococcal strains in our device.

1. Introduction

1.1. Streptococcus pneumoniae

Streptococcus pneumoniae is a major human pathogen responsible for over a million deaths per year worldwide. The gram-positive *S. pneumoniae* is a round-shaped bacterium (coccus) that grows as a mixed population of various morphological types: single cocci, diplococci and chains of various lengths (Fig. 1). It is a common colonizer of the nasopharynx of preschool children but is also the causative agent of various invasive diseases such as pneumonia, septicemia and meningitis [1]. The different cell arrangements (single cocci, diplococci and chains), are thought to contribute differently to virulence and colonization. Previous studies show that long chains promote adherence to human lung epithelial cells *in vitro* and in colonization in a mouse model [2] while short chains better evade the complement, a component of the immune system [3]. One of the main virulence factors of *S. pneumoniae* is its

* Corresponding author.
E-mail address: jonas.tegenfeldt@ftf.lth.se (J.O. Tegenfeldt).

https://doi.org/10.1016/j.aca.2017.11.050

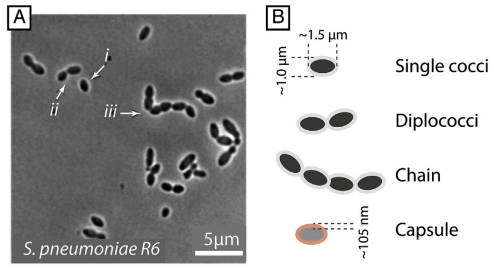

Fig. 1. Morphology of pneumococcal cells. (A) Phase-contrast micrograph of *S. pneumoniae* R6 (a non-encapsulated strain) showing i) single coccus ii) diplococcus and iii) chain of 4 cells (next to a diplococcus). (B) Definitions of different morphologies used in this work.

polysaccharide capsule that surrounds the bacterium [4]. More than 97 capsular serotypes of *S. pneumoniae* have been described to date, some of which are predominately associated with invasive disease or with colonization [5,6].

1.2. Microfluidics separation - deterministic lateral displacement

Deterministic Lateral Displacement (DLD) [7] is a microfluidic separation technique that has been applied to the label-free and continuous sorting of various biological particle systems. DLD devices contain ordered arrays of obstacles through which particles flow, see Fig. 2. As particles flow through the device, interactions with the obstacle arrays cause them to follow trajectories that depend on a combination of their size [7,8], shape [9–14], deformability [9,15,16] and dielectric properties [17]. Typically, the relative effects of these particle parameters on the particles' trajectories are determined by array parameters such as inter-obstacle distance and array tilt angle [7,8,18,19], obstacle shape [13,20,21] and device depth [9–11]. Tweaking these array parameters at the design stage allows us to choose which particle property (or properties) will dominate the particle behaviour and allows us to perform separations accordingly.

1.3. DLD for S. pneumoniae separations

Gaining a deeper understanding on how different morphological types contribute to the virulence of *S. pneumoniae* requires their separation into individual subpopulations. We designed DLD devices with the aim of sorting cultured *S. pneumoniae* cells into subpopulations based on cell size and morphological type, something that is otherwise impossible to achieve as this organism naturally grows as a mix of these morphological types. Ranjan et al. [12] showed some difference in the behaviour of differently shaped bacteria in DLD, using examples of cocci, coccobacilli and bacilli cells. They used H-shaped pillars and looked at how the rotation of single cells affected their trajectories. Many important human pathogens such as *Streptococcus pneumoniae*, *Staphylococcus aureus* and *Neisseria meningitidis* do not grow as single cells and are rather found in pairs, clusters or chains. We have previously separated trypanosomes (long thin microorganisms) from red blood cells (discoid cells) using DLD [10,11]. While hard spheres move in one of two trajectories determined by their diameter, long, thin particles (such as trypanosomes) move in a variety of modes with various rotational and morphological effects contributing to their trajectories, see Fig. 3. We used a similar approach here in designing a device that would be sensitive to different morphological types. We used the non-encapsulated *S. pneumoniae* strain R6 and the closely related encapsulated serotype 2 strain D39. Both are reference strains used as models for studying pneumococcal genetics and pathogenesis. In our device we separated genetically identical bacteria into morphological subpopulations and genetically similar strains from one another based on the presence of a capsule.

2. Methods

2.1. Device design

Our device was designed to focus a bacterial sample stream and collect 5 fractions that are laterally displaced by varying amounts, see Fig. 2 and the ESI for more details. The DLD array has circular posts with a diameter $D_p = 12$ µm with a gap width $G = 4$ µm. The period of the array $N = 23$. This gives us the critical diameter [18]:

$$D_C = 1.4 \times G \times N^{-0.48} = 1.24\ \mu m$$

The critical diameter was designed to be larger than single cocci (1 µm) but smaller than the length of diplococci and chains. The depth of the device was chosen to be 10 µm. Based on our previous experience of the behaviour of long thin particles in DLD devices we expected this depth to increase the effective size of the chains such

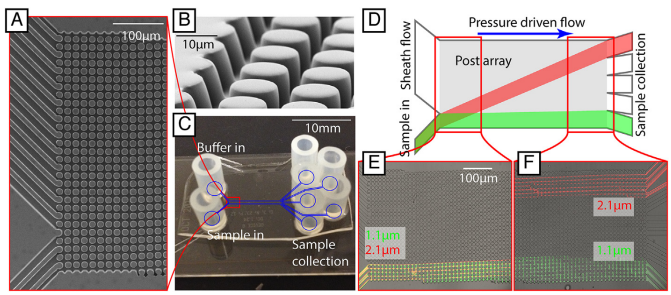

Fig. 2. Overview of a DLD device fabricated in PDMS. (A) and (B) DLD devices consist of pillar arrays through which particles flow. (C) Devices are fabricated in PDMS using replica moulding and bonded to glass slides. Tubes are attached to reservoirs and overpressure applied to both inlet reservoirs to generate flow. Separated fractions can be collected in the outlet reservoirs. (D) The mechanism of DLD causes particles to follow trajectories that depend primarily on their size and shape. (E) In this device 1.1 µm and 2.1 µm polystyrene beads are input into the array. The two different sized bead populations are completely separated and can be collected at different outlets (see ESI for more details).

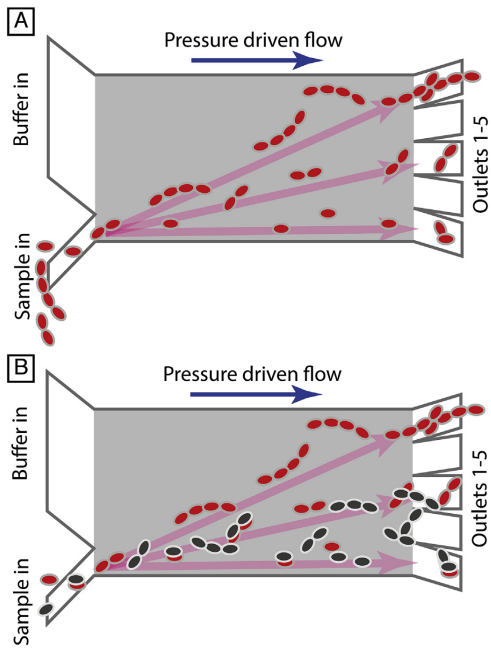

Fig. 3. Principles of sorting bacteria by morphology. (A) Displacement is a function of both cell width and chain length, longer particles are displaced more and fractions are generated at the device outlets. (B) Strains that grow in differing chain lengths can be separated. The presence of a capsule also affects trajectories (black colour illustrates non-encapsulated and red colour encapsulated cells). (For interpretation of the references to colour in this figure legend, the reader is referred to the web version of this article.)

that longer chains become more displaced than shorter chains, diplococci and single cocci of the same width.

The geometry of the DLD array and the positions of the outlet reservoirs were chosen such that the non-displaced fraction would be collected in reservoir 1, the fully displaced fraction (for hard spheres this would be the fraction with a diameter $> D_c = 1.24$ μm) would be collected in reservoir 5, and reservoirs 2–4 would collect the fractions with intermediate displacements.

2.2. Device fabrication

L-Edit 11.02 (Tanner Research, Monrovia, CA USA) was used for device design and photolithographic masks were ordered from Delta Mask (Delta Mask, Enschede, The Netherlands). Masters for replica moulding were fabricated in SU8 (SU8-2010, Microchem Corp., MA, USA) spun onto 3″ silicon wafers using UV-lithography (Karl Suss MJB4, Munich, Germany). After treatment of the master with an anti-adhesion layer of 1H,1H,2H, 2H-per-fluorooctyl-trichlorosilane (ABCR GmbH & Co. KG, Karlsruhe, Germany) [22] to facilitate demoulding, replicas were created in PDMS (Sylgard 184, Dow Corning, Midland, MI, USA) by standard replica moulding [23]. PDMS casts were oxygen plasma bonded to microscope slides spun with a thin layer of PDMS (Plasma Preen II-862, Plasmatic Systems Inc., North Brunswick, NJ, USA) to obtain devices with all internal surfaces consisting of PDMS. To prevent the sticking of cells to the internal surfaces of devices, their surfaces were treated immediately after bonding by filling the devices with 0.2% (w/v) PLL(20)-g [3.5]-PEG(2) (SuSoS AG, Dubendorf, Switzerland) in deionized water and allowing them to rest for at least 20 min before flushing them with deionized water for another 20 min. Silicon tubing with 3 mm inner and 5 mm outer diameter (228–0725 and 228–0707, VWR International LLC, Radnor, PA, USA) were glued (Elastosil A07, Wacker Chemie AG, Munich, Germany) onto the devices as reservoirs.

2.3. Experimental setup

Flow was generated in the device using an overpressure applied at the inlets with an MFCS-4C pressure controller (Fluigent, Paris, France) and the outlet reservoirs kept at ambient pressure. All images were taken through (1) An inverted Nikon Eclipse Ti microscope (Nikon Corporation, Tokyo, Japan) with an Andor NEO sCMOS camera (Andor Technology, Belfast, Northern Ireland) and Lumencor SOLA light engine™ (Lumencor Inc, OR, USA) with a FITC filter, or brightfield and (2) an inverted Nikon Eclipse Ts2 microscope (Nikon Corporation, Tokyo, Japan) with built in GFP optimized epifluorescence filter, or brightfield, and an Exmor USB 3.0 monochrome industrial camera (USB29 UXG M). In both cases 10x (Nikon, 0.25 NA, 7.23 WD), 20x (Nikon 0.40 NA, 3.9 WD), 60x water immersion (Nikon, 1.00 NA, 2.0 WD) or 100x oil immersion (Nikon 1.25 NA, 0.23 WD) objectives were used. All movies were acquired at 10 frames per second.

2.4. Bacterial strains, growth conditions and sample preparation

Streptococcus pneumoniae strains R6, R6 *hlpA-gfp*_Cam^r (BHN1226) and D39 *hlpA-gfp*_Cam^r (BHN1224) were grown in blood agar plates and incubated overnight at 37 °C in 5% CO_2. BHN1224 and BHN1226 were constructed by transforming a PCR product containing the *hlpA-gfp*_Cam^r locus [24] provided by J.-W. Veening into D39 and R6 as described in Ref. [24]. In order to minimize the adhesion of bacteria to the DLD device, cells were scraped from the plates and resuspended in a PBS +1% BSA solution at a final optical density (OD) of 1 (measured at 620 nm). Thanks to the surface coating of PLL-*g*-PEG (see above) we were able to run separations for several hours without any problematic clogging.

2.5. Hydrocarbon adherence assay

Pneumococcal surface hydrophobicity was determined by bacterial adherence to hexadecane as described elsewhere [25]. Briefly, three 5 mL cultures of each strain were grown to mid-log phase in Todd-Hewitt Broth supplemented with 0.5% Yeast Extract (THY), collected by centrifugation, washed twice and resuspended in 1 mL of PBS. The OD_{620nm} was measured and used as the control value (C0). 200 μL of hexadecane was added, the mixture was vortexed for 1 min and the phases allowed to separate. The OD_{620nm} of the aqueous phase was measured (CH). The percent hydrocarbon adherence (HA) was calculated as: HA = [(C0 - CH)/C0] x 100.

2.6. Bacterial cell count and viability

For counting bacterial cells, serial dilutions of the input sample and the fractions collected in the outlet were prepared in PBS. 10 μL of each dilution was spotted on blood agar plates and plates were incubated overnight at 37 °C in 5% CO_2. Colony forming units (CFU) were counted manually and the bacterial concentration (CFU/mL) was calculated. The impact of passage through the DLD device on bacterial cell viability was determined by counting the number of viable cells in the input sample and in each outlet. Survival was

expressed as the percentage of cells of the input sample recovered in the outlet. Survival was measured repeated twice with different input samples.

2.7. Bacterial cell size analysis

Size measurements of R6 and D39 cells were performed on microscopy images taken of the cells mounted on a standard microscope slide under a cover slip using a 100× oil immersion objective. A full description of the process can be found in the ESI.

2.8. Counting morphological types in separated fractions and unsorted samples

Separation results were determined by visual inspection of the cells collected in the outlet reservoirs of the device or from samples prior to separation. For counting in the outlets, images of 10s–100s of cells in each reservoir were randomized and analysed in a blind fashion (no knowledge of reservoir number) by experienced microbiologists. The microbiologists gave the cells the designation single cocci (for single cells), diplococci (for two cells attached together), or chains (for strings of 3 attached cells or more). The data was then compiled and plotted. More details can be found in the ESI. For experiments on the separation of R6 and D39 the fluorescence of the D39 cells was used to distinguish between the two strains.

3. Results

3.1. Morphology of S. pneumoniae

The D39 strain was found to have somewhat wider (1.09 ± 0.13 μm) and longer (1.43 ± 0.17 μm) cocci than R6 (0.92 ± 0.13 μm) and (1.32 ± 0.18 μm) respectively. D39 was also found to build longer chains (4.82 ± 1.17 μm) than R6 (3.78 ± 1.37 μm) in the culturing conditions used. The width and length distributions (irrespective of morphology) for the two strains are shown in Fig. 4A and B. Fig. 4C and D shows a breakdown of lengths for the different morphological types (single cocci, diplococci and chains). Interestingly there are significant overlaps

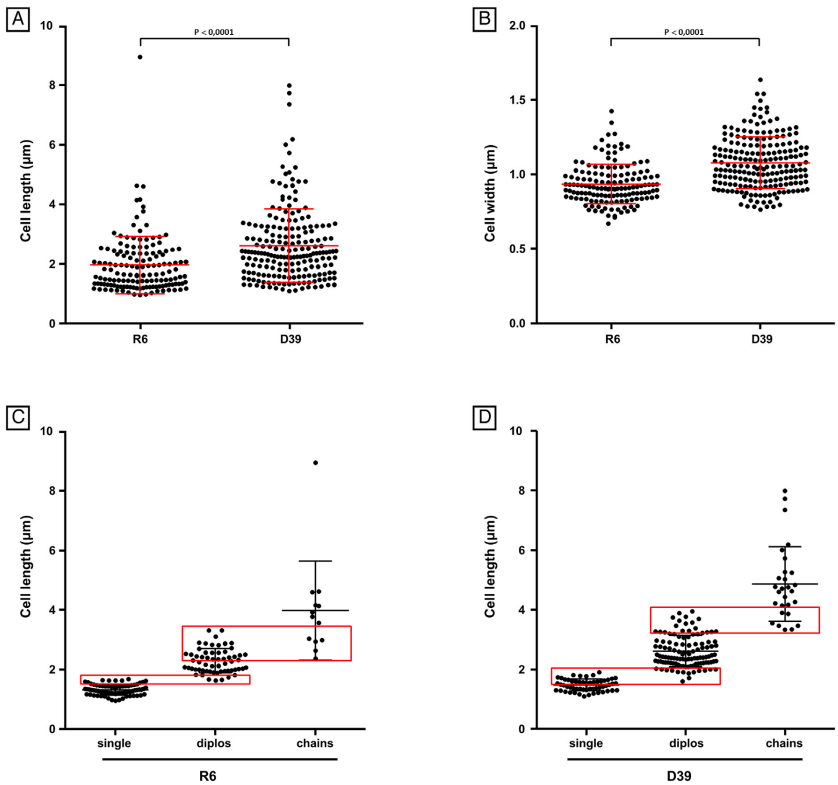

Fig. 4. Cell-size measurements. (A) Length of R6 and D39 cells. (B) Width of R6 and D39 cells. Each point represents a measured cell from 146 (R6) and 226 (D39) data points. The means are statistically different, based on an unpaired *t*-test analysis. The red lines represent the average and standard deviations for each group. (C) Length of R6 single cocci, diplococci and chains. (D) Length of D39 single cocci, diplococci and chains. Average and standard deviations are indicated. Red boxes indicate the overlap in sizes between different morphological types. (For interpretation of the references to colour in this figure legend, the reader is referred to the web version of this article.)

between the sizes of cocci and diploccoci, and diploccoci and chains for both D39 and R6. These differences might be due to cells being in various states of their replicative cycle and to variations in nutrient availability during growth and will be discussed in relation to the separation results in sections 3.5 and 3.6 below.

3.2. Surface properties of S. pneumoniae

Using a hydrocarbon adherence assay a previous study [25] showed that D39 and one of its non-encapsulated variant had significantly different hydrophobic characters, where the non-encapsulated strain was shown to be significantly more hydrophobic. We performed the same assay to confirm that we observed the same properties in our strains. As expected, the non-encapsulated strain R6 displayed much higher hydrophobicity (42.4 ± 2.10% adherence) than the encapsulated D39 strain (2.7 ± 0.16% adherence). These results corroborate the previously published data [25] and indicate that R6 and D39 could potentially be affected by different interactions with the device during separation.

3.3. Viability

We assessed the viability of two bacterial cell samples run through a device and collected during 2.5 h. We diluted the sample in the outlet and plated the bacterial cells on blood agar plates. Viability of both samples was >87%.

3.4. Sample recovery and throughput

We assessed the number of bacterial cells that could be recovered in the 5 outlets of our device by plating the samples recovered on blood agar plates and counting the CFU. After a 3-h run, during which the device was maintained upside-down (this facilitates sample recovery), we recovered between 15 and 1850 bacterial cells in the different outlets (specifically, outlet 1: 260; outlet 2: 250; outlet 3: 1850; outlet 4: 37; outlet 5: 15), in total 2412 bacterial cells. We estimated the volumetric throughput to approximately 1.0 μL/h based on measurements of the flow velocity of fluorescent beads in the device.

3.5. Chain length separations

For the non-encapsulated strain R6, specific morphological types were enriched in the different outlets of the device. Single cocci showed zero displacement and were enriched in outlet 1, whereas chains showed the most displacement and were enriched in outlet 5 (Fig. 5A). Diplococci, however, were found in all outlets (see discussion below in section 4). For the D39 strain results were similar (Fig. 5B). With both strains we significantly enriched single cocci and chains in outlets 1 and 5, respectively, when compared to unsorted samples (Fig. 5C and D).

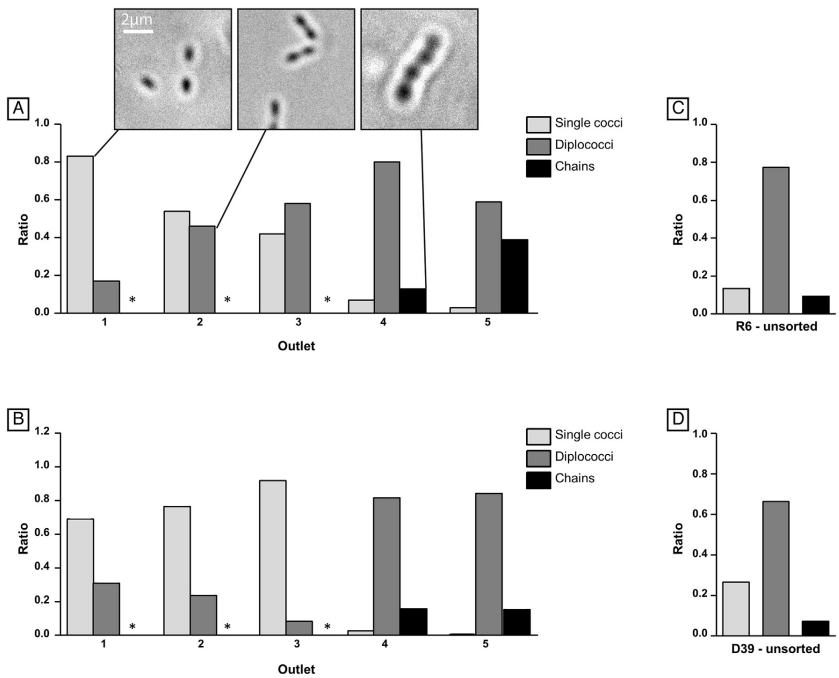

Fig. 5. Distributions of single cocci, diplococci and chains in outlet reservoirs after separation and in unsorted samples. (A) Distribution after separation, R6. Microscopy pictures of representative R6 single cocci, diplococci and chains in different outlets of the device are shown. (B) Distribution after separation, D39. Asterisks indicate that no chains were found. Distribution of each morphological type in unsorted R6 (C) and D39 (D) samples. Ratios were calculated by dividing the number of cells of each morphological type by the total number of cells in each sample or outlet.

3.6. Separation of R6 and D39

As shown in Fig. 6 the pneumococcal strains R6 and D39 could be separated. The majority of the D39 cells were displaced into outlet reservoirs 4 and predominantly 5, whereas almost all R6 were collected in reservoirs 1 to 3.

4. Discussion

Our device separates pneumococcal strains into morphologically different fractions. It is able to do this for both strains tested, R6 and D39, but the same approach should work for any bacteria that grow in chains, or indeed any long thin cells or particles. The mechanism of separation differs from that of hard, spherical particles that are bimodally separated into two fractions, one smaller than the critical size and one larger. Non-spherical entities move through the DLD array in a variety of modes, see Fig. 7, that lead to trajectories between zero displacement and maximum displacement. As shown in Fig. 7A, a diplococcus can move with zero displacement, despite one of its dimensions (length) being greater than D_c. This is due to a rotation of the cells (180° per row) that ensures that this dimension aligns with the flow and that the smaller width of the cells defines the effective size, which in this case is smaller than D_c. Fig. 7B and C shows a slightly larger diplococcus and a chain of 6 cells being displaced. In both cases the cells rotate 180° between each post in a motion that is reminiscent

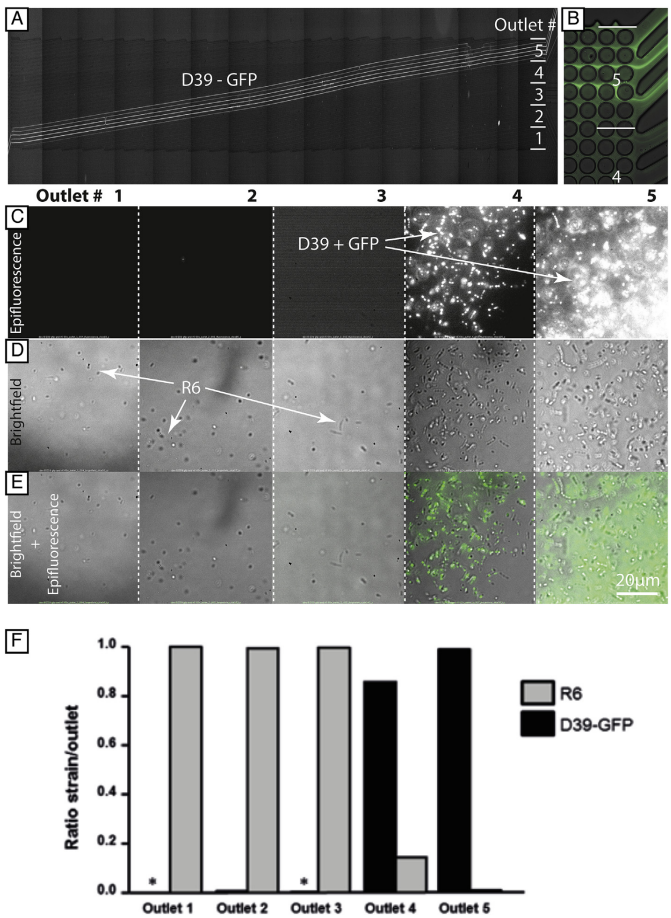

Fig. 6. Separation of R6 and D39. (A) A scanned image of the entire DLD array taken during a separation experiment. The mean trajectories of the fluorescent D39 cells can be seen. Note that the image is compressed in the x-direction. The length of the device is 9.5 mm and the width is 0.4 mm. (B) D39 cells predominantly exiting the device into outlet 5. (C) Fluorescent images taken in reservoirs show D39 cells. (D) In brightfield both R6 and D39 can be seen. (E) Strains can be identified by comparison of fluorescence and brightfield images. (F) Ratio of non-encapsulated (R6) and encapsulated (D39) cells in each of the 5 outlets of DLD device 8. Ratios were calculated by dividing the number of cells of each strain by the total number of cells in each outlet. Asterisks indicate that no D39 cells were found.

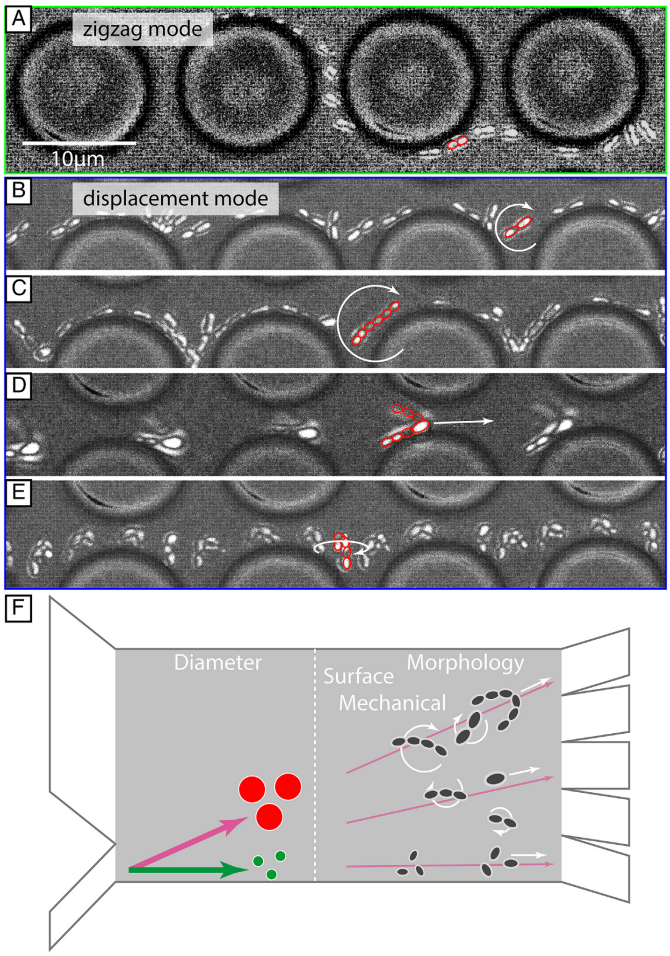

Fig. 7. Different transport modes for long thin particles in DLD. (A-E) Show a selection of the most common modes of transport for rod-like particles through the array (these images are extracted from movies that can be found in the ESI). (F) While hard spherical particles move in either displacement or zero displacement modes, rod-like diplococci and chains are distributed between the two based on length.

of a flick-flacking gymnast and has been called the flipping mode. Fig. 7D shows another mode that is common for very long and flexible particles. In this case a chain of 8–10 (narrow depth of focus compared to the length of the chain makes it hard to determine exactly) is bent into a parachute shape. Locked in this orientation the chain has the largest possible effective size. Fig. 7E shows a bent chain but in this case it appears to be too short or too bent to move in the parachute mode. The bent chain can be seen to rotate and move in the flipping mode. The movies from which the images in Fig. 7A–E were extracted can be found in the ESI.

The reason that a distribution of morphologies can be generated in a device with only two size-dependent modes can be understood in the following way. Long particles move in a variety of modes (flipping, parachuting), some of which cause displacement and some of which do not. The DLD array is long and a particle will sample several modes during transit through the device. Transitions from one mode to another can be triggered by random fluctuations of particle shape, by bending due to viscous forces, by interactions between particles or possibly by local fluctuations in the fluid flow. The wider or longer a particle is, the more likely it is to spend time in modes that lead to displacement and the greater the accumulated displacement will be at the end of the device as illustrated in Fig. 7F. This is evident in the greater displacement of the marginally larger D39 cells compared to the R6.

It is interesting that diplococci were found in all outlets in the experiments done with both R6 and D39. We were expecting some

overlap in the populations of cocci and diplococci and of diplococci and chains based on the size measurements shown in Fig. 4C and D where the sizes are seen to overlap. Upon analysis of the sizes of diplococci we found that we had actually separated the diplococci into size-based sub-populations. This difference in size was seen in the individual cells making up all morphological types (Figure S4 in the ESI). This size difference can likely be attributed to the cells being in various stages of their replicative cycle, or to varying levels of access to nutrients during growth. We can conclude that our approach has the power to resolve small differences in cells belonging to the same morphological type.

While we are able to greatly enrich the concentration of cocci in reservoir 1 and chains in reservoir 5 the presence of the diplococci is a problem. The performance of the device could be improved by emphasizing the purity of only one fraction. By increasing the size of the gaps in the array, diplococci would be less likely to displace than longer chains and purity could be improved. Conversely if a more pure fraction of cocci were required then a small decrease in the gap would cause diplococci to displace more and the purity of cocci would be improved. In both cases increasing the length and width of the array (with all other array parameters unchanged) would also improve separation since the probability that two morphologically different particles follow the same trajectory would decrease with the length of the path. A longer, wider device would also have space for a greater number of outlets and therefore a greater number of distinct populations could be resolved and collected.

The two strains of *S. pneumoniae*, R6 and D39, are almost genetically identical except for the presence of the capsule and a fluorescent marker: R6 (non-encapsulated, non-labeled) and D39 (capsulated, GFP-labeled). Despite this seemingly small difference the separation of the two strains was extremely efficient in our device, as can be seen in Fig. 6. While the separation results shown in Fig. 5 show that for each strain the different morphologies are distributed in all outlets this figure only shows the ratios of morphologies in each outlet, not the absolute number, which is harder to determine. The separation in Fig. 6 can be explained by a combination of the cell sizes and the distribution of morphologies for the two strains. Individual D39 cells are larger than R6 cells, as shown in panels A and B of Fig. 4 and, as can be seen in panels C and D, there is a much higher prevalence of larger diplococci and chains present for the D39 than the R6 strain. It is also possible that parameters other than size could influence the behaviour of the strains. It is unknown whether the mechanical properties of the diplococci and chains, specifically the stiffness, differs between the two strains. Further studies will show whether our method is sensitive to the rigidity of long particles or not but since DLD has been shown to be sensitive to the deformation of other particles [9,15], this is quite likely to be the case. What is more, as discussed in section 3.2, as measured by the hydrocarbon adherence assay, the presence of the capsule affects the hydrophobicity of the cells. Cells of the non-encapsulated R6 strain are much more hydrophobic than the capsulated D39 cells. Again, further studies will show whether hydrophobicity plays a role in the separation, or if it can be leveraged as a separation parameter. Here it is interesting to note that interactions between particles and posts, other than hard steric interactions, have been shown to greatly affect particle behaviour in DLD devices [17,26].

To summarize, Fig. 8 shows, by way of an illustration of a separation phase diagram, an overview of how our device works. Hard spherical particles fall along the diagonal line and are, if we neglect diffusion, either displaced (red zone) or not (green zone). Deformation causes particle to move away from the diagonal. Very deformable particles are able to move through the device even if they are larger than the gaps between the posts. Near to the critical

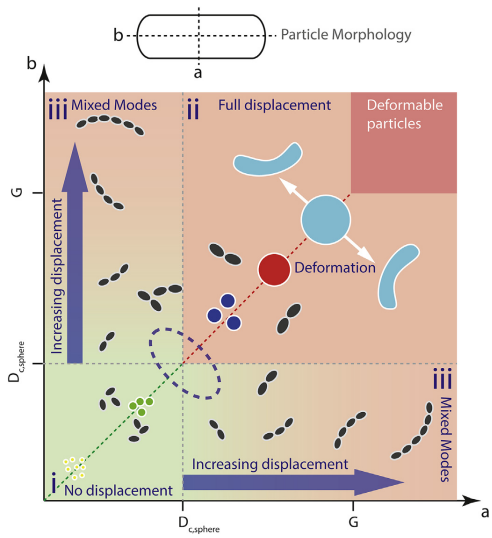

Fig. 8. An illustration of a separation phase diagram for a DLD device. On the axis are a and b, particle width and length. $D_{c,sphere}$ is the critical diameter in the device (the diameter at which a switch in trajectory occurs for hard spherical particles) and G is the gap between posts. The diagonal shows the bimodal separation of particles with $a = b < D_{c,sphere}$ from those with $a = b > D_{c,sphere}$. The coloured quadrants show i) Green, no displacement for particles with $a,b < D_{c,sphere}$. ii) Red, full displacement for particles with $a,b > D_{c,sphere}$. iii) Green/Red, mixed modes for a or $b > D_{c,sphere}$. As either a or b increases the trajectory of the particle approaches full displacement. The red area at top right ($a,b > G$) is unavailable for hard particles that are unable to pass between posts. However for deformable particles transit through the array is possible. Deformable particles become less spherical upon deformation and move away from the diagonal. This can cause them to move from the displacement to non-displacement modes. The blue dashed line illustrates where particles with a or b close to $D_{c,sphere}$ are sensitive to the effects of perturbations, particularly those arising from forces with a component perpendicular to the flow direction such as diffusion or non-steric interactions with posts.

size D_c trajectories are more likely to be sensitive to effects such as diffusion, particle post interactions and any other applied force, intentional or not. For long thin particles, even if they are narrow enough to theoretically move with zero displacement, the increasing length leads to higher probabilities that they spend time in modes that are associated with displacement.

5. Conclusions

We have shown the separation of cultured, pathogenic pneumococcal cells into fractions predominantly defined by their morphologies. We can enrich for single cocci or chains of 3 cells or longer and we describe strategies for the further improvement of future devices. We show the separation of two genetically similar strains, non-encapsulated R6 and encapsulated D39, based on small differences in size, possibly due to the presence of the capsule, and on differences in chain length. We successfully demonstrate collection of viable cells after sorting. While the throughput is moderate in this work, we expect it to be quite straightforward to increase the throughput to the levels necessary for detailed biomolecular studies of the resulting fractions by careful optimization of the device parameters, using wider devices, larger spacing between posts and parallelization. Overall, we believe that our work

will allow us to study virulence factors that have hitherto been difficult to study. What is more, our approach is not limited to the study of bacterial chains but opens up for separation of any high aspect ratio particles such as parasites and inorganic structures.

Acknowledgements

We thank Jan-Willem Veening for kindly providing us with the *hlpA-gfp*_Cam^r PCR product and Sulman Shafeeq for transformations yielding strains BHN1224 and BHN1226.

This work was carried out within NanoLund at Lund University with funding from LAPASO (EU FP7 project 607350) and the Swedish Research Council (VR) grants no. 2015-05426 and 2016-01861. In addition, the work was supported by funding from the Knut and Alice Wallenberg Foundation, the Swedish Foundation for Strategic Research and the Stockholm County Council with grant numbers SLL20170308 and SLL20160854. All device processing was conducted within Lund Nano Lab.

Appendix A. Supplementary data

Supplementary data related to this article can be found at https://doi.org/10.1016/j.aca.2017.11.050.

References

[1] N.F. Maraqa, Pneumococcal infections, Pediatr. Rev. 35 (7) (2014) 299–310.
[2] J.L. Rodriguez, A.B. Dalia, J.N. Weiser, Increased chain length promotes pneumococcal adherence and colonization, Infect. Immun. 80 (10) (2012) 3454–3459.
[3] A.B. Dalia, J.N. Weiser, Minimization of bacterial size allows for complement evasion and is overcome by the agglutinating effect of antibody, Cell Host Microbe 10 (5) (2011) 486–496.
[4] C. Hyams, et al., The Streptococcus pneumoniae capsule inhibits complement activity and neutrophil phagocytosis by multiple mechanisms, Infect. Immun. 78 (2) (2010) 704–715.
[5] J.Y. Song, M.H. Nahm, M.A. Moseley, Clinical implications of pneumococcal serotypes: invasive disease potential, clinical presentations, and antibiotic resistance, J. Korean Med. Sci. 28 (1) (2013) 4–15.
[6] S. Browall, et al., Intraclonal variations among Streptococcus pneumoniae isolates influence the likelihood of invasive disease in children, J. Infect. Dis. 209 (3) (2014) 377–388.
[7] L.R. Huang, et al., Continuous particle separation through deterministic lateral displacement, Science 304 (5673) (2004) 987–990.
[8] D.W. Inglis, et al., Critical particle size for fractionation by deterministic lateral displacement, Lab a Chip 6 (5) (2006) 655–658.
[9] J.P. Beech, et al., Sorting cells by size, shape and deformability, Lab a Chip 12 (6) (2012) 1048–1051.
[10] S.H. Holm, et al., Separation of parasites from human blood using deterministic lateral displacement, Lab a Chip 11 (7) (2011) 1326–1332.
[11] S.H. Holm, et al., Simplifying microfluidic separation devices towards field-detection of blood parasites, Anal. Methods 8 (16) (2016) 3291–3300.
[12] S. Ranjan, et al., DLD pillar shape design for efficient separation of spherical and non-spherical bioparticles, Lab a Chip 14 (21) (2014) 4250–4262.
[13] K.K. Zeming, S. Ranjan, Y. Zhang, Rotational separation of non-spherical bioparticles using I-shaped pillar arrays in a microfluidic device, Nat. Commun. (2013) 4.
[14] S.H. Au, et al., Microfluidic isolation of circulating tumor cell clusters by size and asymmetry, Sci. Rep. 7 (1) (2017) 2433.
[15] E. Henry, et al., Sorting cells by their dynamical properties, Sci. Rep. (2016) 6.
[16] D. Holmes, et al., Separation of blood cells with differing deformability using deterministic lateral displacement, Interface Focus 4 (6) (2014).
[17] J.P. Beech, P. Jonsson, J.O. Tegenfeldt, Tipping the balance of deterministic lateral displacement devices using dielectrophoresis, Lab a Chip 9 (18) (2009) 2698–2706.
[18] J.A. Davis, Microfluidic Separation of Blood Components through Deterministic Lateral Displacement, PhD thesis in Electrical Engineering, Princeton University, Princeton, NJ, USA, 2008.
[19] K.K. Zeming, et al., Asymmetrical deterministic lateral displacement gaps for dual functions of enhanced separation and throughput of red blood cells, Sci. Rep. (2016) 6.
[20] K. Loutherback, et al., Improved performance of deterministic lateral displacement arrays with triangular posts, Microfluid. Nanofluidics 9 (6) (2010) 1143–1149.
[21] J.C. Hyun, et al., Improved pillar shape for deterministic lateral displacement separation method to maintain separation efficiency over a long period of time, Sep. Purif. Technol. 172 (2017) 258–267.
[22] M. Beck, et al., Improving nanoimprint lithography stamps for the 10 nm features, Proc. 2001 1st Ieee Conf. Nanotechnol. (2001) 17–22.
[23] Y.N. Xia, et al., Replica molding using polymeric materials: a practical step toward nanomanufacturing, Adv. Mater. 9 (2) (1997) 147–149.
[24] M. Kjos, et al., Bright fluorescent Streptococcus pneumoniae for live-cell imaging of host-pathogen interactions, J. Bacteriol. 197 (5) (2015) 807–818.
[25] E. Swiatlo, et al., Contribution of choline-binding proteins to cell surface properties of *Streptococcus pneumoniae*, Infect. Immun. 70 (1) (2002) 412–415.
[26] K.K. Zeming, et al., Real-time modulated nanoparticle separation with an ultra-large dynamic range, Lab a Chip 16 (1) (2016) 75–85.

Electronic Supporting Information – Separation of bacteria by chain length

Jason P. Beech[a], Bao Dang Ho[a], Geneviève Garriss[b], Vitor Oliveira[b], Birgitta Henriques-Normark[b, c, d], Jonas O. Tegenfeldt[a]

[a] *Division of Solid State Physics and NanoLund, Lund University, SE-221 00, Sweden*
[b] *Department of Microbiology, Tumor and Cell Biology, Karolinska Institutet, SE-171 77 Stockholm, Sweden*
[c] *Department of Clinical Microbiology, Karolinska University Hospital, SE-171 76 Stockholm, Sweden*
[d] *SCELSE and LKC, Nanyang Technological University, NTU, Singapore 639798, Singapore*

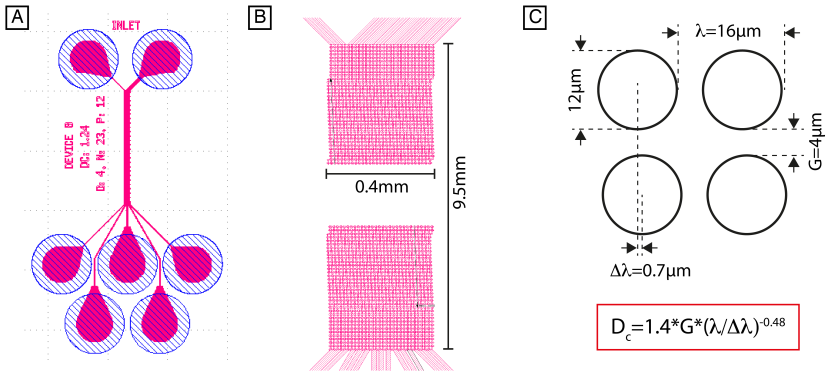

Figure S1. Device parameters. (A) An overview of the device taken from the mask design file. The blue circles indicate where inlet and outlet reservoirs are attached. (B) The DLD array dimensions. (C) The dimensions of the array itself and how they combine to give a give a critical diameter for particle separation.

1. DLD device parameters

Figure S1 gives an overview of our device parameters. Figure S1A shows the overall design with inlet and outlet channels. One of the inlet channel is denoted the sample inlet and the other the buffer inlet. The blue circles denote the positions of reservoirs that are attached to the PDMS/glass device. Figure S1B shows the dimensions of the separation array and Figure S1C shows the DLD array parameters.

Our device has gap width G = 4 μm and post diameter D_p = 12 μm. The center-to-center distance of the posts is given by $\lambda = G + D_p$ = 16 μm. Each row is shifted by $\Delta\lambda$ = 0.7 μm and the period of the array $N = \lambda/\Delta\lambda$ = 23. Using the equation for the critical diameter given by Davis [1]:

$$D_C = 1.4 \times G \times N^{-0.48} = 1.24\ \mu m$$

In order to test the device we first ran an experiment with fluorescent polystyrene microspheres 1.1 μm and 2.1 μm in diameter. A mixture of the two bead types in 0.1% SDS (to prevent adhesion of particles to the surface of the device) was introduced into the device via the sample inlet and a water solution of 0.1% SDS into the buffer inlet, both at 30 mBar. 400 frames @ 20 fps were captured using different

fluorescence filter sets to image each microsphere type individually. Averages were then created to show the trajectories of the particles. Colourised images of the particles at the beginning and end of the device are shown in Figure 2 of the main text. The 1.1 μm beads show zero displacement and the 2.1 μm beads are displaced by the maximum amount possible in this particular device geometry. We can conclude therefore that the critical size in the device lies between 1.1 μm and 2.1 μm. Due to lack of suitable sizes of microspheres we did not determine the exact critical size in the device. However, we conclude from our initial characterisation that the critical size in the device (in relationship to the size of the bacteria we are interested in) is in the correct range.

The depth of the device is 9.8 μm.

2. Morphology - Analysis of separated fractions

Separation results were determined by visual inspection of the cells collected in the outlet reservoirs of the device. Separations were run until the concentration of cells in the reservoirs was sufficiently high to obtain statistically significant results but low enough that individual cells could be identified. Movies of 200 frames were taken with a 60x long-working distance objective (Nikon, NA 1.00, WD 2.0). The focus was moved up and down slowly during the movie, which makes it easier to determine the morphology of cells that do not lie perfectly in the image plan. At least 4 movies per outlet reservoir were taken for each separation experiment with 10s to 100s of cells per movie. The movies were designated random names and then analyzed in a blind fashion by experienced microbiologists (coauthors: GG and VO). The microbiologists gave the cells the following designations: single cocci (for single cells), diplococci (for two cells attached together), or chains (for strings of 3 attached cells or more). The data was then compiled and plotted.

3. Cell size measurements

Size measurements of R6 and D39 cells were performed on microscopy images taken of the cells mounted on a standard microscope slide under a cover slip using a 100x oil immersion objective (Nikon 1.25 NA, 0.23 WD). The width and total length of units (cocci, diplococci and chains) was measured used NIS Elements software, as shown in Figure S2A. The pixel size was calibrated using an image of a ruler with 10 μm gradations using the same optical setup, Figure S2B. Cells appear larger when below or above the focal plane. In order to avoid errors due to this effect only in-focus cells were measured. Cells were deemed in-focus when they appeared dark with a minimal bright ring as shown in Figure S2A, inset, and the dark areas can be considered as the silhouettes of the cells where cell size can be measured, which can be confirmed in the superimposition of the bright field image and the fluorescence image of some R6-gfp bacteria in Figure S2C, where the green areas match with the dark areas in size.

To measure the width and the length of a cell, two pairs of parallel lines are positioned right at the boarder of the dark area of such cell, as shown in the inset of Figure S2A. If the cocci of a diplo or a chain did not line up, the length of each coccus were measured and then added up.

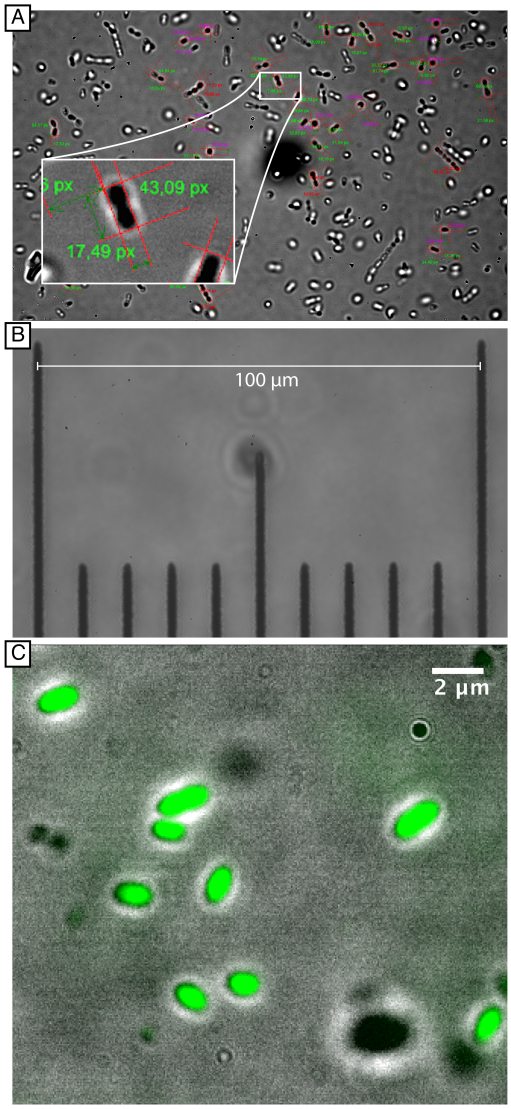

Figure S2. Cell-size measurements. (A) Both R6 and D39 were imaged on a microscope slide with a 100x oil immersion objective (Nikon 1.25 NA, 0.23 WD). To ensure that only cells in the correct focal plane were included, only those that appear dark with a small bright outlet were measured. (B) The pixel values were converted to lengths after calibration based on imaging of a ruler using the same imaging setup. (C) Superimposed bright field and fluorescence images of R6-gfp.

4. Hydrocarbon adherence assay

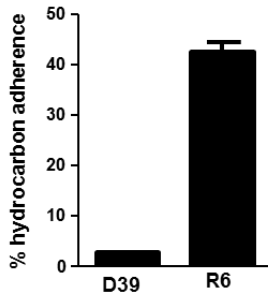

Figure S3. Pneumococcal surface hydrophobicity was determined by bacterial adherence to hexadecane as described elsewhere [2]. Bars represent the average of three measurements made on three cultures and standard deviations are indicated.

5. Size variation of diplococci in sorted fractions

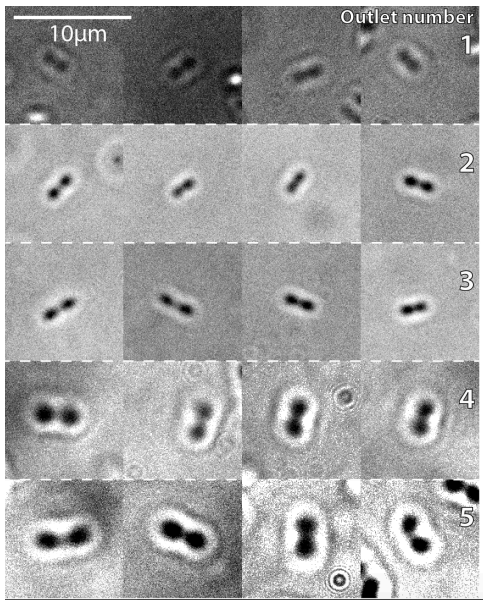

Figure S4. Size variation in sorted fractions of diplococci.

6. Movies

The movies in the ESI show the dynamics of the bacteria as they move through a device. They correspond to Figure 7A-E in the main text.

References

1. Davis, J.A., *Microfluidic Separation of Blood Components through Deterministic Lateral Displacement*, PhD thesis in *Electrical Engineering* (2008), Princeton University, Princeton, NJ, USA.
2. Swiatlo, E., et al., *Contribution of Choline-Binding Proteins to Cell Surface Properties of Streptococcus pneumoniae.* Infection and Immunity, 2002. **70**(1): p. 412-415.

Open DLD

Paper III

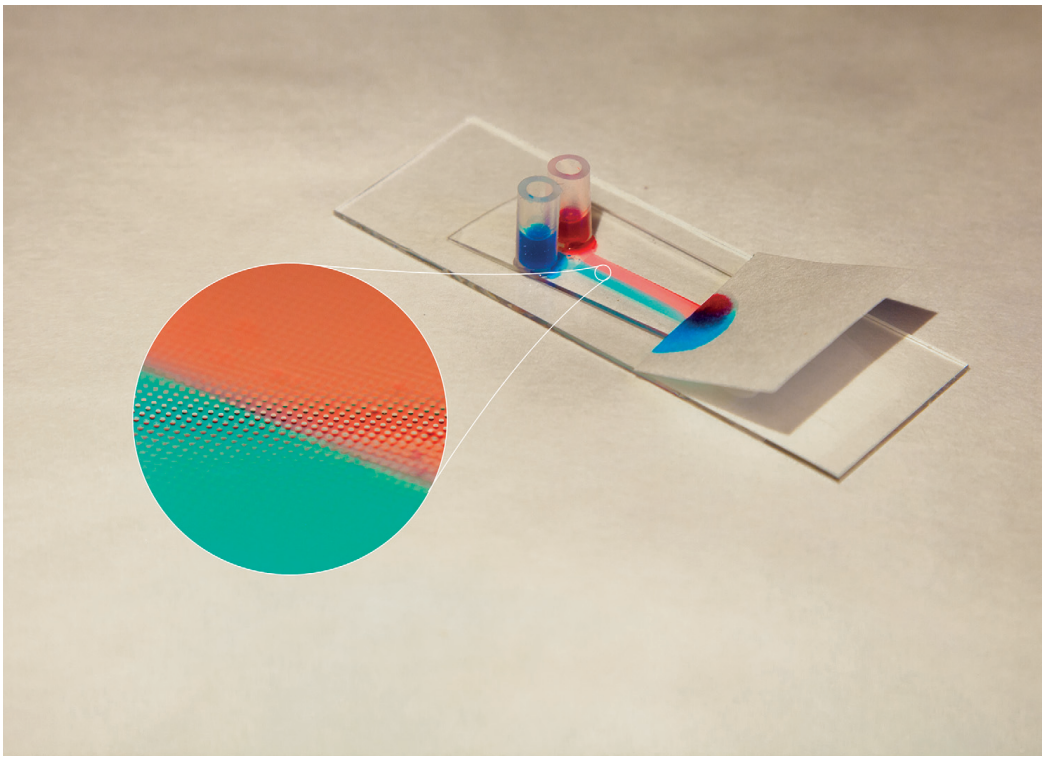

Featuring work from NanoLund, Prof. Jonas O. Tegenfeldt, Lund University, Sweden

A simple, low-cost and robust approach was developed for sorting complex samples using open-architecture fluidics. The liquid flow was driven by a paper capillary pump that doubles as a reservoir for collection of the sorted fractions.

Open channel deterministic lateral displacement for particle and cell sorting

Image reproduced by permission of Jason Beech/Tegenfeldt group

As featured in:

See Jonas O. Tegenfeldt *et al.*, *Lab Chip*, 2017, **17**, 3592.

ROYAL SOCIETY OF CHEMISTRY

rsc.li/loc

Registered charity number: 207890

Lab on a Chip

PAPER

View Article Online
View Journal | View Issue

Cite this: *Lab Chip*, 2017, **17**, 3592

Open channel deterministic lateral displacement for particle and cell sorting†

Trung S. H. Tran, Bao D. Ho, Jason P. Beech and Jonas O. Tegenfeldt *

Received 6th July 2017,
Accepted 18th September 2017

DOI: 10.1039/c7lc00707h

rsc.li/loc

We present the use of capillary driven flow over patterned surfaces to achieve cheap and simple, but powerful separation of biologically relevant particle systems. The wide use of microfluidics is often hampered by the propensity for devices to clog due to the small channel sizes and the inability to access the interior of devices for cleaning. Often the devices can only be used for a limited duration and most frequently only once. In addition the cost and power requirements of flow control equipment limits the wider spread of the devices. We address these issues by presenting a simple particle- and cell-sorting scheme based on controlled fluid flow on a patterned surface. The open architecture makes it highly robust and easy to use. If clogging occurs it is straightforward to rinse the device and reuse it. Instead of external mechanical pumps, paper is used as a capillary pump. The different fractions are deposited in the paper and can subsequently be handled independently by simply cutting the paper for downstream processing and analyses. The sorting, based on deterministic lateral displacement, performs equivalently well in comparison with standard covered devices. We demonstrate successful separation of cancer cells and parasites from blood with good viability and with relevance for diagnostics and sample preparation. Sorting a mixture of soil and blood, we show the potential for forensic applications.

Introduction

Cell separation is a critical process in cell biology, disease diagnostics and prognosis. While standard techniques such as FACS and MACS are widely used, there is a need to miniaturize systems in order to minimize sample and reagent use, simplify systems for the user, and integrate components into comprehensive analysis tools. Depending on the exact applications, different types of microfluidic sorting schemes may be utilized. Inertial[1] and acoustophoretic methods[2] give high volumetric throughput but with a relatively low size resolution and must be operated at low particle concentrations. Deterministic lateral displacement (DLD) is a method of particle separation, based on the continuous flow of particles through an array of obstacles that exhibits exceptional resolution in size-based separations.[3] DLD has been used for cell and bioparticle separations such as blood fractionation,[4–8] trypanosome enrichment from blood,[9,10] cancer cell isolation[11–13] and CTC cell cluster isolation from whole blood,[14] DNA and exosome separation,[15] and the separation of cells based on parameters other than size, namely shape and deformability,[16,17] and dielectric properties.[18] Early theoretical work by Inglis *et al.*[19] and Davis *et al.*[20] describing the critical size in DLD arrays has been improved upon by studying the effects of post shape.[21,22] Further improvements to theoretical descriptions have been made by considering other parameters such as diffusion,[23] dynamical properties,[17] and alternative trajectories through DLD arrays.[23–25] Being a passive method its basic operation does not require any application of external fields, like those used in acoustophoresis, and because it functions at high particle concentrations and low flow rates, relevant throughput can be achieved without the pressures required to generate the high particle velocities needed for inertial-effect based approaches. Even at high volume flow rates (10 mL min^{-1}) DLD has been shown to separate a variety of cells with minimal effect on viability.[12] Taken together, these qualities make DLD our method of choice for the development of a simple, cheap but effective approach to particle separation.

Here we show that by removing the lid of the DLD devices and using capillary flow we are able to perform separations, equally powerful as those in closed devices, but with many added advantages. While the benefits of open fluidics in general[26,27] and of capillary driven DLD has been demonstrated previously,[28,29] we here show proof of principle of their usefulness for sorting of biologically relevant particles not only based on size but also based on morphology and dielectric properties with relevance for *e.g.* medical diagnostics and

NanoLund and Division of Solid State Physics, Physics Department, Lund University, PO Box 118, 221 00, Lund, Sweden. E-mail: jonas.tegenfeldt@ftf.lth.se; Tel: +46 46 222 8063

† Electronic supplementary information (ESI) available. See DOI: 10.1039/c7lc00707h

forensics. What is more, this can be done in devices that are cheaper and easier to fabricate, since oxygen plasma and bonding is not required, and also cheaper and easier to run since pressure controllers are not required. A common limitation of standard fluidics devices, based on sealed small channels, is a propensity to clog, especially when handling complex samples. The difficulties to clean these closed devices make them unsuitable for prolonged and repeated use. We show that our open devices are easy to clean and reuse, which together with the use of the paper capillary pumps further contributes to the lowering of the costs. While standard pumps and pressure control units are ultimately more versatile, they are bulky, power consuming and expensive. We show that paper capillary pumps are compatible with open DLD devices allowing us to handle larger volumes than can fit into a device alone, and that they have the added advantage of doubling as sample collection substrates, further simplifying downstream process steps and analyses.

Results and discussion

Device fabrication and assembly

Both open and closed devices are fabricated in PDMS using replica molding on SU8 masters (see Materials and methods section). The final step in fabricating closed devices is to bond a glass slide to the PDMS cast and to then attach fluidics connectors. Open devices are much simpler in that they require neither of these two last steps. In order for the open device to function, PDMS must be rendered hydrophilic using *e.g.* oxygen plasma or, alternatively, prewetted by submersion in water. Fig. S3† in the supplementary material shows an overview of hydrophobic, hydrophilic and pre-wetted devices. Pre-wetting is much simpler to perform and negates the requirement of an oxygen plasma system, helping to keep the method cheap and simple. When a device is submerged in water the device features (channels and arrays) will fill with water after 5 minutes. When the PDMS slab is removed from submersion, water runs off of all flat areas and the only liquid remaining is that which is trapped within the patterned areas constituting the device. Sample can now be applied to the inlets and paper to the outlets and the sample will flow through the patterned areas of the device, confined to within the defined height of the features.

DLD devices in open configuration

Fig. 1A and B show a typical configuration of a closed DLD device. PDMS is bonded to glass to form closed channels and a pump or pressure control unit is used to drive flow through the device. As shown in Fig. 1C and D, our approach is to remove the glass lid and replace the pressure-driven flow with capillary flow. Provided the channels are hydrophilic, any aqueous solution placed at the inlet of the device will flow into the channels until they are filled. For our typical DLD devices (*e.g.* device 1, 20 mm length, 4 mm width and 24 μm depth, see ESI,† Fig. S1) the array volume is approximately 1.1 μL.

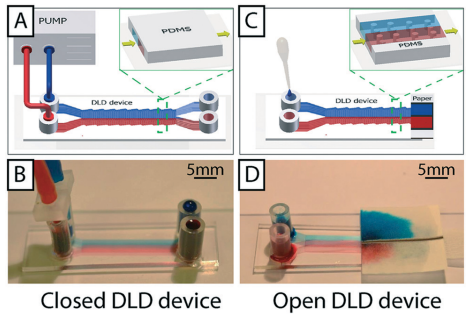

Fig. 1 Comparison of closed and open devices. (A and B) Conventional closed device where fluid is confined inside channels in a complicated setup of tubes and a pump or a pressure control unit. (C and D) Open DLD without lid. In these devices the interplay between surface tension and geometry keeps the fluid confined to the separation array and a paper reservoir at the outlet maintains flow, *via* capillary action, and collects the sample. We see, by observing the red and blue food coloring, that the flow is laminar in both devices.

To run the device, reservoirs are mounted at the device inlets and tested for volumes up to 60 μL using the paper capillary pump. At the beginning of the device there is a transition in liquid height from the reservoir to the bulk of the separation array. In this transition zone the sample flows across the top of the array, but the liquid height falls to that of the posts within 1–5 mm. Fig. 1D shows how we are able to maintain a stable, laminar flow (of red and blue food dye in this case) in the device using the paper capillary pump. The figure also shows how the fluids are collected in the paper. The resulting flow rates are measured to be 71 ± 19 nL s^{-1}, which is comparable to what we achieve with an applied pressure of 21 mBar in a corresponding closed device. This also compares well with a closed device driven by a paper capillary pump.

The liquid in the reservoirs gives a hydrostatic pressure that is less than 1 mBar and is therefore negligible in comparison with the equivalent driving pressure in a closed device. The result is that the liquid is pulled through the device by the negative pressure imposed by the capillary pump, minimizing any liquid build-up on top of the posts.

To estimate the liquid profile along the device we resorted to three approaches. Direct imaging (Fig. 2A and B) indicates that the liquid is indeed thicker at the beginning of the device close to the reservoirs and that it levels out rather quickly away from the reservoirs. Confocal imaging supports the conclusion giving a direct view of the profile (Fig. 2C–F). Finally we studied the flow in the channels. We measure the velocities of the flow (Fig. S4B†) and combine that with the cross sectional area of the device based on the design parameters to obtain a value of the volumetric flow. The resulting flow rate is consistent with what we obtain in direct measurements of the volumetric flow rate (Fig. S5†) and measurements of the average flow by measuring the elapsed time

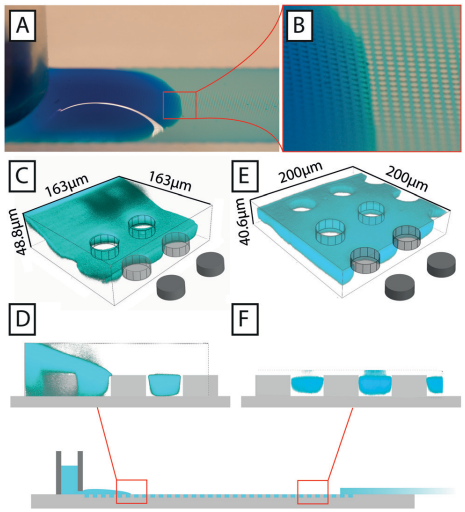

Fig. 2 Images of aqueous fluids in an open DLD device. A) Photograph of an aqueous solution of food color in an open device. B) Close-up of the transition between the area where the fluid forms a droplet and where it is confined to the post array. C) and D) 3d rendering and cross section, respectively, of confocal images of an aqueous solution of FITC in the same device, taken near to the reservoir. The drop formed by the reservoir can be seen to fall below the height of the posts. E) and F) 3d rendering and cross section, respectively, at the end of the device closest to the paper. The device is filled with liquid but no liquid can be seen above the posts.

between loading of a defined volume and the emptying of the reservoirs (Fig. S4D†) suggesting that the liquid is indeed filling the device to the top of the pillars. Note that there is a trend of lower flow velocities close to the reservoirs, in line with the local buildup of liquid on top of the post array that we observe by direct inspection.

The throughput of the paper capillary pump driven device is ultimately limited by the absorption rate of the paper. In a very simplified but illustrative picture the paper capillary pump can be viewed as a battery with an internal resistance and a hydromotive force in analogy to standard electrical batteries. If the external load is much less than the internal flow resistance, the flow rate is limited by the internal resistance. By measuring the flow rates in a free paper as well as a paper connected to a device (Fig. S5†), we could estimate the internal resistance, 16×10^{12} kg s^{-1} m^{-4}, which is within an order of magnitude of the resistance of our closed devices, 30×10^{12} kg s^{-1} m^{-4} (from Fig. S4†), and open devices 23×10^{12} kg s^{-1} m^{-4} (from Fig. S5†). From these data we could also estimate the hydromotive force to 32 mBar. Higher throughputs can now be realized by decreasing the device flow resistance through an increase in the depth of the devices or by using paper pumps with higher absorption rates. While the flow in narrow strips of paper follows the Washburn law[30] such that the flow rate is inversely proportional to the square root of time, we use wider strips of paper where the liquid fans out leading to a constant flow rate as shown by Mendez *et al.*[31] To obtain specific volumes and flow rates as a function of time, the paper capillary pumps can be programmed by selecting appropriate geometries of the paper.[32–34] Further details on the flow generated in our open devices by the paper capillary pump can be found in the ESI.†

In addition to the simplifications compared to standard DLD devices we can demonstrate good separation performance. Fig. 3B shows the separation of 3 μm and 7 μm polystyrene microspheres. The sample (a mixture of the two beads) was placed in one inlet and buffer placed in the other. As the sample stream flows through the device, in parallel with the buffer stream, the mechanism of DLD causes the 7 μm particles, which are larger than the critical size, D_c, to be displaced into the buffer stream while the 3 μm particles, which are smaller than D_c remain in the sample stream. This lateral displacement is caused by steric interactions between particles and posts, which cause particles to move with a component perpendicular to the flow direction. The net result is the continuous, spatial separation of particles, Fig. 3B, in this case based on size. We also show here how the particles are collected in the paper, in regions divided by wax lines, which we will return to below. Despite the lack of a lid in our open DLD devices, flow is well defined and confined to the pillar array, and high-resolution separations can be performed fully comparable to those demonstrated for closed DLD devices. Fig. 3C shows experimental comparison of 3 devices and 10 particle sizes run in open configurations. Filled circles show particles following the flow (as expected if they are below the critical size) and open circles show those that are displaced (above the critical size). These points fall on either side of the expected critical size (indicated by red double arrows) as calculated using the empiric expressions given by Inglis *et al.*[35] and Davis *et al.*[20] for closed devices demonstrating good correspondence between particle behavior in open and closed configurations.

Application areas – proof of principle

To show the applicability of open DLD devices to relevant bio-separations, we tested separation of a range of relevant bioparticles in different modalities, as described below.

Size-based separation. Deterministic lateral displacement provides a powerful mechanism for highly precise continuous sorting based on size. In addition to the size-based separation of polystyrene beads shown above (Fig. 3) we show the separation of cells of higher biological relevance. Fig. 4A shows the size-based separation of cells from a breast cancer cell line (MCF7 cells with diameter 17.3 ± 2.1 μm) from erythrocytes (red blood cells, RBC) (diameter 7.8 ± 0.6 μm) in an open device with D_c = 10.7 μm (device 2, see ESI,† Fig. S1) and Fig. 4B shows the size-based separation of white blood cells (WBC) (diameter 12.2 ± 0.9 μm) and RBCs in a device with D_c = 5.1 μm (device 1, see ESI,† Fig. S1). In both cases

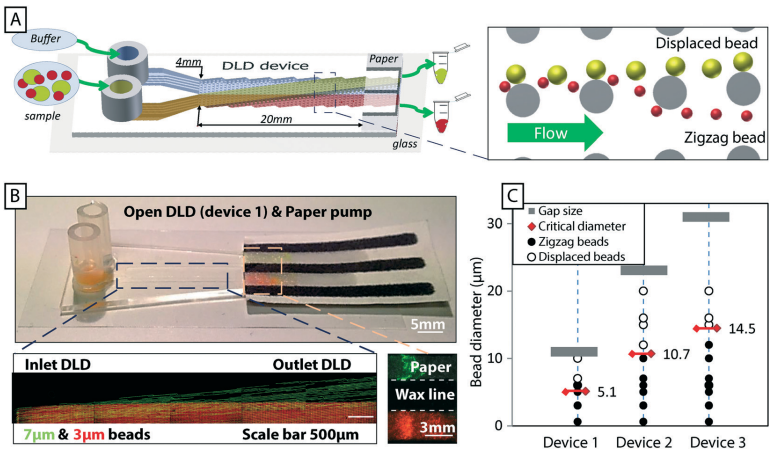

Fig. 3 An overview of open DLD, device layout and typical results. (A) Particles are introduced *via* one inlet and buffer *via* the other. The mechanism of deterministic lateral displacement pushes particles (yellow) larger than a critical size, D_c, from the sample stream to the co-flowing buffer stream as they move along the device. Smaller particles (red) remain in the sample stream. (B) Paper is used both as a capillary pump and as a method of sample collection. Here colored beads are visualized after separation and collected in zones in the paper pump defined with wax (yellow/green 7 μm and red 3 μm, black lines are wax). Time averaged images of fluorescent beads (green 7 μm and red 3 μm) in the beginning and end of the device show the trajectories of the beads in the device, which lead to separation. Note the collection of particles in separate, wax-delimited zones in the paper. (C) The behavior of open DLD devices is consistent with that of standard closed DLD devices. The red double arrows indicate theoretical critical sizes for a conventional closed device based on Davis' estimate.[20] The results for the open DLD are shown with filled black circles for particles in zigzag mode (following the flow), and open circles for particles in displacement mode (displaced into the buffer stream). The grey bars indicate the upper limit of the particle sizes as imposed by the gap sizes between posts.

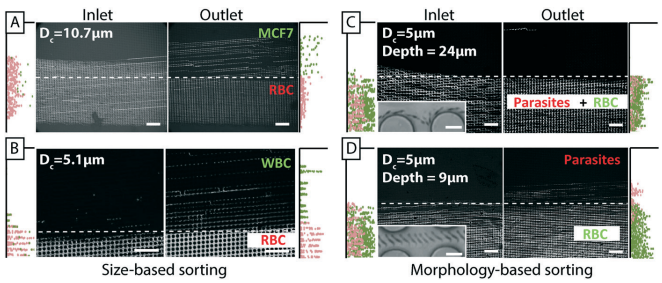

Fig. 4 Cell and parasite sorting in open DLD devices. All images show plots of inlet distributions (to the left) and outlet distributions (to the right) together with time-averaged micrographs of different cells moving through open DLD devices. The micrographs show the trajectories of the different cells in each case and the outlet distributions show the resulting separations. (A) Size-based separation of RBCs (red dots) and MCF7 cells (green dots) (B) sizebased sorting of RBCs (red dots) and WBCs (green dots) (C) in a 24 μm deep device RBCs (green dots) and parasites (*T. cyclops*) (red dots) have the same trajectories, but in a shallower device (9 μm deep) (D) they are separated. Scale bars 100 μm and 10 μm for the insets.

the performance of the devices in the simpler open configuration is equivalent to that of the same device with a lid and pressure-driven flow.

Morphology-based separation. To leverage the differences in morphology of bioparticles as a separation parameter, DLD devices can be made in which the orientation of non-spherical particles is controlled. In this way a specific aspect of the shape can be selected to influence the effective size of the particles.[9,36] As in previous work, but now in the open device, we control the orientation of parasites to optimize their separation from erythrocytes. In a 24 μm deep device 4 (Fig. 4C), both RBCs and parasites follow the flow, whereas in a 9 μm deep device 5 (Fig. 4D) RBCs follow the flow but parasites are displaced and separation is achieved based on the same principle as was shown in ref. 9 and 36. Device parameters are shown in ESI,† Fig. S1.

Complex samples. We demonstrate the robustness of the open DLD by introducing a mixture of soil and blood into a

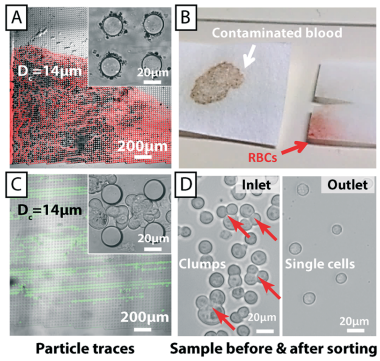

Fig. 5 Sorting of complex samples in open DLD devices. Even if large particles become trapped at the beginning of a device they do not block the flow of liquid and smaller particles as they would in a closed device. This allows extremely "dirty" samples to be analysed. A mixture of soil and RBCs is introduced into an open device. Despite the large amount of soil particles trapped at the beginning of the device (A), a clean fraction of RBCs is collected at the end of the device (B). (C) & (D) A combination of filtering and continuous separation of suspensions of cells containing large clusters that would otherwise block the inlets of a closed device.

device (Fig. 5). Soil sediments quickly and sticks in the separation array, as can be seen in Fig. 5A, but this does not cause the flow to stop. RBCs are still able to traverse the post array and a soil free fraction of RBCs is readily collected in paper at the end of the device (Fig. 5B).

A common challenge in microfluidics is the aggregation of cells that often lead to clogging even with careful surface passivation. Using the open DLD we clearly demonstrate the retention of cell aggregates of MCF7 cells while the individual cells are collected at the end of the device (Fig. 5C and D). While cell aggregates may be of interest in their own right,[37] in many cases, such as in cell culturing, drug screening and fluorescence activated cell sorting, it is often necessary to remove cell aggregates. Those experiments are conducted in device 3 with D_c = 14 μm (see ESI,† Fig. S1).

Application of electric fields

Electrokinetic effects can be utilized in DLD devices to widen the scope and add specificities associated with the distribution of charge on the particles of interest as shown previously by Beech *et al.*[18] in closed DLD devices. We added electrodes to the inlet and outlet reservoirs of a DLD device generating an electric field in the device. The electric field lines were "squeezed" between the insulating PDMS posts and field gradients were generated near the post surfaces. Polarizable particles interacted with the field gradient and the resulting dielectrophoretic (DEP) forces were used to modify the DLD-based behavior and tune size-based separations. Because there is no lid on an open device it is easy to access the fluid at any point in the device, during a separation. In the example shown in Fig. 6 electrodes are dipped into the fluid (KCl with a conductivity of 24 mS m^{-1}) and an AC electric field is applied. In a closed device the electrodes are usually mounted in the inlet and outlet reservoirs, which are 30 mm apart in this device. Here we could easily place them 3 mm apart allowing for the generation of much higher fields at a given voltage. In Fig. 6B we see the effects of adding an electric field. In the absence of an applied voltage, 3.1 μm sulphate-terminated polystyrene and 4.8 μm carboxy-terminated polystyrene microspheres are following the flow (zigzagging), which is to be expected in a device with a critical diameter of 5.1 μm (device 1, see ESI,† Fig. S1), showing that the electrodes do not greatly perturb the flow. At 400 V applied AC voltage (100 Hz) the 4.8 μm microspheres are displaced and separation is achieved. At 700 V, all microspheres are displaced.

Applying electrodes in this manner, rather than in the inlets and outlets, decouples the electrode geometry from the flow geometry in a very simple way, giving us freedom to apply any number of electrodes in any pattern and at any angle to the flow direction.

Sample collection and recovery

The paper at the end of the device functions not only as a capillary pump but also as a sample recovery matrix from which fractions can be cut in a manner similar to that shown by Osborn *et al.*[38] Filter paper with a thickness of 150 μm and a pore size of 25–60 μm has excellent absorption. Liquid reservoirs of the required volume can be defined using a wax printer. The wax lines serve to maintain the separation of collected fractions (Fig. 1, 3 and 7). Fluorescent samples with good signal can be imaged directly in the paper with low magnification (Fig. 3 and 7). For samples with lower, or no fluorescent signal, higher magnification together with transmitted light can be used to image cells. In Fig. 7 separated MCF7 cells and RBCs are imaged inside the paper reservoirs.

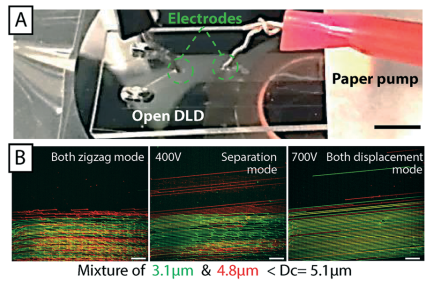

Fig. 6 Combination of electrokinetics and open DLD. (A) With direct access to the fluid it is straight-forward to position external electrodes at any point in the device. Scale bar 3 mm. An AC field at 100 Hz and various applied voltages (B) 0 V/400 V/700 V, change the trajectories of particles consistent with what was previously shown by Beech *et al.*[18] in closed DLD devices. Scale bars 100 μm.

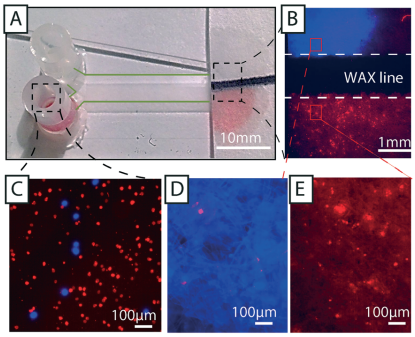

Fig. 7 Paper functions both as a capillary pump and as a collection reservoir for separated cells. (A and C) A sample containing RBCs (red fluorescence) and MCF7 cells (blue fluorescence) is introduced into an open DLD. RBCs (smaller than D_c) and MCF7 cells (larger than D_c) follow different trajectories through the device (from left to right) and can be collected to the right in two areas on the paper, separated by a printed wax line. The RBCs are more numerous than the MCF7 cells and can easily be seen in the paper through their red color (no fluorescence). Note the green dotted line that delineates the boarders of the device. (B) Trapped MCF7 cells and RBCs imaged in the paper. The high concentration makes it difficult to pick out individual cells in the image, but as (D) shows, very few RBCs were observed in the top zone where the MCF7 fraction dominates. (E) No MCF7 cells are seen in the RBC fraction.

To recover cells from the paper, we have developed a simple protocol that does not negatively affect viability or proliferation (Fig. 8). The desired fractions are cut out of the paper and placed inside a liquid medium of choice (*e.g.* in a 1.5 mL Eppendorf tube). Gentle vortexing releases most of the collected sample from the paper and subsequent centrifugation may then be performed to concentrate and/or collect the freed cells or particles. Fig. 8D shows a micrograph of MCF7 cells after separation in an open device, release from paper, and collection *via* centrifugation. Fig. 8E shows the recovery of 75% of cells from filter paper using this method.

While having good absorptive qualities, which is good for maintaining flow, fibrous filter paper with large pore size, is not ideal for sample collection due to trapping of particles and cells within the structure of the paper. Instead a two-layer paper system was used to increase the collection rate. By sandwiching a layer of filter membrane (1 μm pore size, polycarbonate membrane) between the filter paper and the device, the good absorptive qualities of the filter paper could be used while the polycarbonate membrane stopped the particles/cells from entering the paper and becoming trapped. Particles and cells captured on the surface of the polycarbonate membrane were easily resuspended with higher yields observed. Fig. 8E shows how 95% of cells could be recovered using the extra membrane layer.

To measure the effect of sorting in both open and closed devices on the health of cells, we performed viability and proliferation assays of MCF7 cells. Cell counting using viability dyes (trypan blue) was conducted to measure the percentage of viable cells and the rate of proliferation. Fig. 8F demonstrates viabilities of >90% for sorted cells. A small difference in the viability of cells (control, open, and closed devices) could be seen in our measurements but the difference has no practical significance and shows nothing more than the

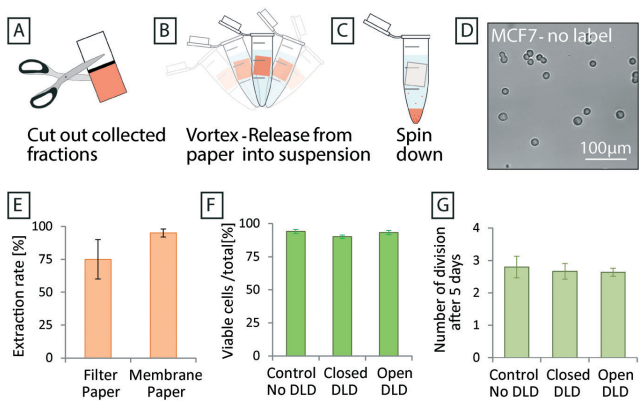

Fig. 8 Post-separation sample recovery. (A) Separated fractions are accumulated in the paper and kept separated by hydrophobic wax lines. The desired fractions are collected separately by dividing the paper along the wax line. (B) To re-suspend the collected fractions vortexing is used, which shakes the cells free of the paper matrix, followed by (C) centrifugation. (D) MCF7 cells after separation and collected using the process described in (A)–(C). (E) Recovery statistics for the filter paper and the two-layer system. Error bars show max/min values from 5 experiments. (F) Cell viability and (G) proliferation assay for MCF7 after separation in closed and open DLD. Error bars show the standard deviation in (F) and (G). No significant difference could be seen in the proliferation rates of sorted and non-sorted cells.

common variation between cultures using these cells. Furthermore, Fig. 8G shows that after 5 days of culturing, no difference in the proliferation rates of cells, (~2.5 divisions in 5 days), can be seen as a consequence of sorting.

The performance of the devices is qualitatively comparable to the conventional closed devices with clear separation of the different fractions. Purity and capture rate are performance parameters that do not depend on the DLD as much as on the overall design and will have to be optimized carefully for each specific application. For example the paper capillary pump in Fig. 3B can be extended to three lanes instead of two. In that way the purity of the sample collected in the two extreme lanes can be enhanced by discarding the central lane. The data in Fig. 4 shows clearly that by appropriate choice of cut-offs we would be able to achieve close to 100% purity of the separated fractions. With longer devices, this is expected to be done with minimum loss of capture efficiency.

Cleaning and reusing devices

The fouling of devices with particles and cells is the most common reason for device failure and limits device lifetime. Fouling can be due to several mechanisms. Particles can adhere to surfaces and they can become trapped because they are too large to move through constrictions. These mechanisms are also linked. For example, particles can stick to one another, forming agglomerations that are much more likely to get stuck. Fig. 9A shows an image of 4.5 and 10 μm particles that have become stuck in a closed device with a D_c = 5.1 μm and gap size of 11 μm after operating for 30 min (device 1, see ESI,† Fig. S1). At this point the device has ceased to work and particles are no longer able to enter the array. This kind of clogging is detrimental for all kinds of microfluidics devices, in particular for DLD devices since a well-defined flow direction is crucial for the successful operation. Even a small deviation of flow direction may change the critical size significantly.

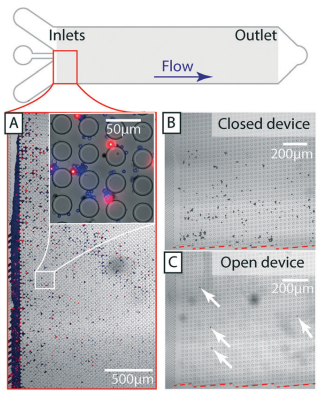

Fig. 9 Cleaning and reusing open DLD devices. (A) Depending on the array parameters, particle sizes and surface chemistries, devices eventually clog. (B) A closed device after attempted cleaning using sonication, high pressures and reversing the flow direction. (C) An open device after sonication and rinsing is almost completely free of particles (30 times fewer). Those remaining are highlighted with arrows. Channel walls are shown in red dashed lines.

Closed devices are most often irreversibly sealed (to avoid leaking) and are difficult to clean and reuse. Fig. 9B shows the same device after sonication, reversal of the flow direction and an increase in pressure in an effort to remove clogging. Despite these efforts many particles remain stuck in the device and the device is unusable. Open devices are considerably easier to clean and can be cleaned to a much higher degree. Fig. 9C shows the same kind of device as above after first being run in an open configuration and then cleaned by sonication and rinsing. This device is free of particles after rinsing and can be reused.

Conclusion

We have shown that by combining patterned surfaces in PDMS with paper based capillary pumps we can fabricate potentially cheap, simple to use, and reusable continuous flow separation devices. We have demonstrated proof-of-principle separations of samples based on size and morphology and what is more, in samples containing very large contaminant particles. Being open, access to flowing fluid is possible in these devices allowing for easy electric contact through electrodes. Flow rates can be held constant by choice of size and properties of the paper used in the capillary pump. Paper is not only useful as a pump but also as a matrix for the collection of separated fractions. The separational functionality of DLD is retained in open devices paving the way for simple, robust and clogging insensitive sorting using pillar arrays with potential applications in medicine and forensic science. Our device opens up for sample preparation applications in paper fluidics based diagnostics.[39,40]

The limitations and challenges introduced by working with open devices on the other hand include the risk for evaporation, contamination and biohazard.[41] These issues can be mitigated through a cover that is positioned in close proximity, yet not in contact with the actual device.

Materials and methods

PDMS device fabrication

In a contact mask aligner (Karl Suss MJB3 and MJB4, Munich, Germany), negative photoresist SU8 (MicroChem, Newton, MA, USA) spun on a 3″ silicon wafer was exposed with UV light through a chrome-mask designed in L-Edit 11.02 (Tanner Research, Monrovia, CA USA) and printed by Delta Mask (Delta Mask, Enschede, The Netherlands). Before casting of PDMS, a monolayer of 1*H*,1*H*,2*H*,2*H*-perfluorooctyltrichlorosilane (ABCR GmbH & Co. KG, Karlsruhe, Germany) was applied in the gas phase to the master

as an anti-adhesion agent to facilitate demoulding. A 10 : 1 mixture (monomer : curing agent) of PDMS (Sylgard 184, Dow Corning, Midland, MI, USA) was degassed, poured onto the master then baked for 2 hours at 80 °C. For the closed devices vias are punched and an oxygen plasma treatment step (Plasma Preen II-862, Plasmatic Systems, Inc., North Brunswick, NJ, USA) is performed to enable bonding to glass slides and the attaching of silicone tubes for fluidic connections, none of which are necessary for the open devices. In Fig. S2† (supplementary of device fabrication), a comparison among a protocol of closed DLD fabrication and optional protocol for open DLD fabrication (with and without oxygen plasma plus reservoir) is presented.

Paper capillary pump

A two-layer paper system was used as a capillary pump and for sample capture and collection for the experiments described in Fig. 8. For liquid absorption (Herzberg flow rate[42] 110 s/100 mL), filter paper of 0.15 mm thickness, a 25–60 μm pore size and 8 μm particle retention (Grade 600, VWR, Sweden) was used. For sample capture a layer of polycarbonate paper (Grade 28158, VWR, Sweden), (1 μm pore size) was sandwiched between the separation device and the lower grade filter paper. For the other experiments only the filter paper was used. Wax barriers were printed onto the filter paper using a wax printer (ColorQube 8570, Xerox, USA) followed by baking for 3 minutes at 100 ° C.

For the experiments characterizing the evaporation, a grid was printed onto the paper to facilitate measurement of the wetted area. The grid was printed using a standard laser writer (Canon iR-ADV C5250i).

Sample preparation (beads, RBCs, WBCs, parasites and MCF7 cells)

Fluorescently labeled polystyrene microspheres with varying diameters (from 1 μm to 20 μm) (Polyscience Inc., Warrington, PA, USA) were suspended in MilliQ water and 1% SDS and used in both closed and open DLD devices for calibration.

Small volumes of blood (10 μL) were obtained from healthy, consenting donors *via* finger pricking. Blood samples were diluted 20 times in autoMACS™ running buffer (Miltenyi Biotec, Auburn, CA, USA).

Trypanosoma cyclops parasites were thawed (after storage in 10% dimethyl sulfoxide (DMSO, Fluka, St. Louis, MO, USA: 41639) at −80 °C) and cultured in Cunningham's medium with 20% fetal calf serum (FCS, Sigma-Aldrich) at 28 °C. Parasites were harvested after proliferating to cover 80% of the culture dish and spiked into blood samples.

MCF-7 (breast carcinoma cell lines obtained from the American Type Culture Collection (ATCC)) was cultured at 37 °C and 5% CO_2. Cell culture medium was Dulbecco's modified Eagle's medium (DMEM), 10% FBS and 1% penicillin streptomycin (Sigma-Aldrich). After one week of subculture, the cells proliferated to fill more than 80% of the culture flasks and were considered ready for separation experiments.

Image acquisition and analysis

Particle and cell distributions were calculated from images acquired using an inverted epifluorescence microscope (Nikon Eclipse Ti, Nikon Corporation, Tokyo, Japan) and scientific CMOS camera (Flash4.0 V2, Hamamatsu, Japan). ImageJ 1.48v software downloaded from the National Institutes of Health, and NIS-elements 4.51 were used for image analysis and the preparation of figures. Images of particle trajectories are generated by time-averaging. Two color-images generated by adding color to separate images, taken in succession with different filter sets, and superimposing.

Conflicts of interest

There are no conflicts to declare.

Acknowledgements

We thank Stefan Holm and Bo Baldetorp for their kind donation of trypanosomes and MCF-7 cells respectively. This work was carried out within NanoLund at Lund University with funding from the Child Cancer Foundation (MT2013-0031), LAPASO (EU FP7 project 607350) and the Swedish Research Council (VR) grant no. 2015-05426. All device processing was conducted within Lund Nano Lab. We thank Christelle Prinz for valuable comments after carefully reading the manuscript.

References

1 D. Di Carlo, D. Irimia, R. G. Tompkins and M. Toner, *Proc. Natl. Acad. Sci. U. S. A.*, 2007, **104**, 18892–18897.
2 T. Laurell, F. Petersson and A. Nilsson, *Chem. Soc. Rev.*, 2007, **36**, 492–506.
3 L. R. Huang, E. C. Cox, R. H. Austin and J. C. Sturm, *Science*, 2004, **304**, 987–990.
4 J. A. Davis, D. W. Inglis, K. J. Morton, D. A. Lawrence, L. R. Huang, S. Y. Chou, J. C. Sturm and R. H. Austin, *Proc. Natl. Acad. Sci. U. S. A.*, 2006, **103**, 14779–14784.
5 D. W. Inglis, M. Lord and R. E. Nordon, *J. Micromech. Microeng.*, 2011, **21**, 054024.
6 C. I. Civin, T. Ward, A. M. Skelley, K. Gandhi, Z. P. Lee, C. R. Dosier, J. L. D'Silva, Y. Chen, M. Kim, J. Moynihan, X. C. Chen, L. Aurich, S. Gulnik, G. C. Brittain, D. J. Recktenwald, R. H. Austin and J. C. Sturm, *Cytometry, Part A*, 2016, **89A**, 1073–1083.
7 K. K. Zeming, T. Salafi, C. H. Chen and Y. Zhang, *Sci. Rep.*, 2016, **6**, 22934.
8 M. Yamada, W. Seko, T. Yanai, K. Ninomiya and M. Seki, *Lab Chip*, 2017, **17**, 304–314.
9 S. H. Holm, J. P. Beech, M. P. Barrett and J. O. Tegenfeldt, *Lab Chip*, 2011, **11**, 1326–1332.
10 S. H. Holm, J. P. Beech, M. P. Barrett and J. O. Tegenfeldt, *Anal. Methods*, 2016, **8**, 3291–3300.

11 Z. B. Liu, F. Huang, J. H. Du, W. L. Shu, H. T. Feng, X. P. Xu and Y. Chen, *Biomicrofluidics*, 2013, **7**, 011801.
12 K. Loutherback, J. D'Silva, L. Y. Liu, A. Wu, R. H. Austin and J. C. Sturm, *AIP Adv.*, 2012, **2**, 042107.
13 H. Okano, T. Konishi, T. Suzuki, T. Suzuki, S. Ariyasu, S. Aoki, R. Abe and M. Hayase, *Biomed. Microdevices*, 2015, **17**, 59.
14 S. H. Au, J. Edd, A. E. Stoddard, K. H. K. Wong, F. Fachin, S. Maheswaran, D. A. Haber, S. L. Stott, R. Kapur and M. Toner, *Sci. Rep.*, 2017, **7**, 2433.
15 B. H. Wunsch, J. T. Smith, S. M. Gifford, C. Wang, M. Brink, R. L. Bruce, R. H. Austin, G. Stolovitzky and Y. Astier, *Nat. Nanotechnol.*, 2016, **11**, 936–940.
16 J. P. Beech, S. H. Holm, K. Adolfsson and J. O. Tegenfeldt, *Lab Chip*, 2012, **12**, 1048–1051.
17 E. Henry, S. H. Holm, Z. M. Zhang, J. P. Beech, J. O. Tegenfeldt, D. A. Fedosov and G. Gompper, *Sci. Rep.*, 2016, **6**, 34375.
18 J. P. Beech, P. Jonsson and J. O. Tegenfeldt, *Lab Chip*, 2009, **9**, 2698–2706.
19 D. W. Inglis, J. A. Davis, R. H. Austin and J. C. Sturm, *Lab Chip*, 2006, **6**, 655–658.
20 J. A. Davis, *Doctoral thesis*, Princeton, 2008.
21 Z. Zhang, E. Henry, G. Gompper and D. A. Fedosov, *J. Chem. Phys.*, 2015, **143**, 243145.
22 K. Loutherback, K. S. Chou, J. Newman, J. Puchalla, R. H. Austin and J. C. Sturm, *Microfluid. Nanofluid.*, 2010, **9**, 1143–1149.
23 B. R. Long, M. Heller, J. P. Beech, H. Linke, H. Bruus and J. O. Tegenfeldt, *Phys. Rev. E*, 2008, **78**, 046304.
24 J. Frechette and G. Drazer, *J. Fluid Mech.*, 2009, **627**, 379–401.
25 S. C. Kim, B. H. Wunsch, H. Hu, J. T. Smith, R. H. Austin and G. Stolovitzky, *Proc. Natl. Acad. Sci. U. S. A.*, 2017, **114**, E5034–E5041.
26 J. Melin, W. van der Wijngaart and G. Stemme, *Lab Chip*, 2005, **5**, 682–686.
27 B. P. Casavant, E. Berthier, A. B. Theberge, J. Berthier, S. I. Montanez-Sauri, L. L. Bischel, K. Brakke, C. J. Hedman, W. Bushman, N. P. Keller and D. J. Beebe, *Proc. Natl. Acad. Sci. U. S. A.*, 2013, **110**, 10111–10116.
28 J. P. Beech and J. O. Tegenfeldt, Capillary driven separation on patterned surfaces, *microTAS 2009, The 13th International Conference on Miniaturized Systems for Chemistry and Life Sciences*, Jeju, Korea, November 1–5, 2009, pp. 785–787.
29 K. Morton, O. K. C. Tsui, C. K. Tung, J. C. Sturm, S. Y. Chou and R. Austin, *New J. Phys.*, 2010, **12**, 085008.
30 E. W. Washburn, *Phys. Rev.*, 1921, **17**, 273–283.
31 S. Mendez, E. M. Fenton, G. R. Gallegos, D. N. Petsev, S. S. Sibbett, H. A. Stone, Y. Zhang and G. P. Lopez, *Langmuir*, 2010, **26**, 1380–1385.
32 E. Elizalde, R. Urteaga and C. L. Berli, *Lab Chip*, 2015, **15**, 2173–2180.
33 P. Yager, T. Edwards, E. Fu, K. Helton, K. Nelson, M. R. Tam and B. H. Weigl, *Nature*, 2006, **442**, 412–418.
34 B. M. Cummins, R. Chinthapatla, B. Lenin, F. S. Ligler and G. M. Walker, *Technology*, 2017, **5**, 21–30.
35 D. W. Inglis, J. A. Davis, R. H. Austin and J. C. Sturm, *Lab Chip*, 2006, **6**, 655–658.
36 S. H. Holm, J. P. Beech, M. P. Barrett and J. O. Tegenfeldt, *Anal. Methods*, 2016, **8**, 5726–5726.
37 A. F. Sarioglu, N. Aceto, N. Kojic, M. C. Donaldson, M. Zeinali, B. Hamza, A. Engstrom, H. Zhu, T. K. Sundaresan, D. T. Miyamoto, X. Luo, A. Bardia, B. S. Wittner, S. Ramaswamy, T. Shioda, D. T. Ting, S. L. Stott, R. Kapur, S. Maheswaran, D. A. Haber and M. Toner, *Nat. Methods*, 2015, **12**, 685–691.
38 J. L. Osborn, B. Lutz, E. Fu, P. Kauffman, D. Y. Stevens and P. Yager, *Lab Chip*, 2010, **10**, 2659–2665.
39 Y. Yang, E. Noviana, M. P. Nguyen, B. J. Geiss, D. S. Dandy and C. S. Henry, *Anal. Chem.*, 2017, **89**, 71–91.
40 K. Yamada, H. Shibata, K. Suzuki and D. Citterio, *Lab Chip*, 2017, **17**, 1206–1249.
41 Y. Temiz, R. D. Lovchik, G. V. Kaigala and E. Delamarche, *Microelectron. Eng.*, 2015, **132**, 156–175.
42 W. Herzberg, *Papierprüfung*, Springer, Berlin, Heidelberg, 1921, p. 109, DOI: 10.1007/978-3-662-25211-6_18.

Open Channel Deterministic Lateral Displacement for Particle and Cell Sorting

Trung S.H. Tran, Bao D. Ho, Jason P. Beech and Jonas O. Tegenfeldt

Electronic Supporting Information

Design and fabrication

The basic operational principle of DLD along with relevant parameters and critical separation diameters for our DLD devices are shown in Figure S1.

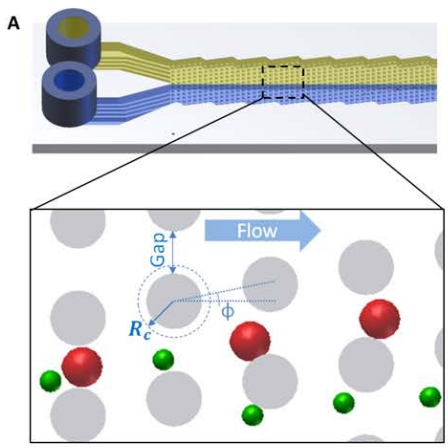

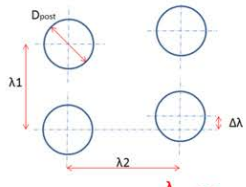

C

Device	Dpost	Gap	Dc	Depth
1	30	11	5.1	24
2	30	23	10.7	24
3	30	31	14.4	24
4	20	12	5	24
5	20	12	5	9

Figure S1. *(A) Schematic of a typical DLD device with particle trajectories, (B) Key parameters determining the critical diameter (D_c) of a DLD array, (C) List of DLD devices used in this report (length units are µm). Length of the devices is 20 mm and width is 4 mm.*

Several fabrication and surface treatment schemes were tested for our devices (Figure S2). Figure S2A shows the conventional method of fabricating closed PDMS/glass devices with a plasma-bonding step (that also renders the PDMS hydrophilic) and the attachment of reservoirs/pressure control connections.

Preparation of devices

For the open devices, if a drop of aqueous solution is applied at the end of an untreated (hydrophobic) DLD array, the droplet will stay on the surface and will not wet the channels or array area of the device. This can be overcome in two ways. Figure S2B shows an open device in which the channels are selectively rendered hydrophilic by use of a mask during oxygen plasma treatment. The untreated, hydrophobic PDMS surrounding the active area of the device serves to confine the sample, which would otherwise spread outside the features of the device. Another approach, that is simpler because oxygen plasma is not needed, is

shown in Figures S2C and D. By submerging the device in an aqueous solution (1% SDS for polystyrene bead sorting, AutoMacs™ for RBC, and complete Dulbecco's Modified Eagle's Medium (DMEM) for cancer cell experiments) at room temperature for 5 minutes, the entire surface of the device can be forced to wet. When the device is removed from the solution the flat PDMS surface is sufficiently hydrophobic to repel the aqueous solution, but the water inside the structures of the device remains. After the positioning of the paper capillary pump at the outlet and the addition of more sample at the inlet, flow is maintained and separation can be performed. The reservoir, shown in Figure S2D, is not essential but allows for greater control of the sample and the handling of larger sample volumes.

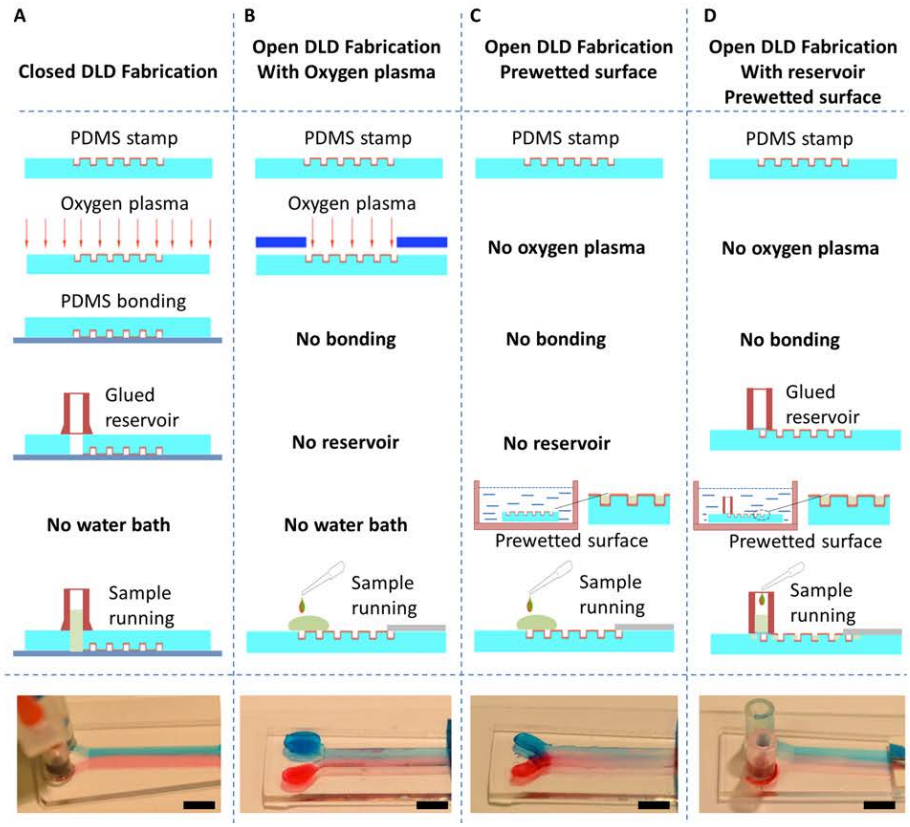

***Figure S2**. Comparison of different fabrication methods for closed and open DLD devices. (A) Conventional closed device fabrication. (B) Open device where the sorting structures are selectively treated with oxygen plasma to make them hydrophilic. (C) Rendering the PDMS hydrophilic by immersion (prewetting) in a water bath (plain water at room temperature in 5 minutes) instead of in an oxygen plasma. (D) Addition of a reservoir gives better control of the sample and allows for larger volumes. Scale bars 5 mm.*

The wetting of the devices using the different surface treatment strategies was characterized in more detail as presented in Figure S3. Selective oxygen plasma treatment gives a strongly hydrophilic surface with contact angle ~ 0°. Immersing the device in aqueous buffer gives a less hydrophilic surface (contact angle ~ 60° outside the device and an effective contact angle ~ 0° in the DLD array). The latter approach is fully adequate for the operation of the device and much simpler as it does not require any oxygen plasma equipment.

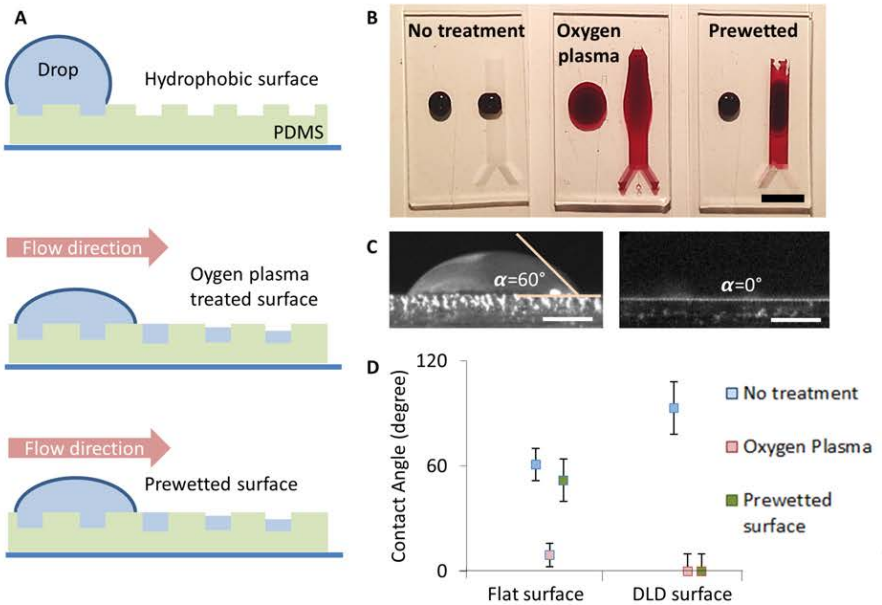

***Figure S3**. Hydrophobic and hydrophilic devices. (A) Schematic of a water droplet on an untreated (hydrophobic) surface and the two treated hydrophilic surfaces (B) Visualization of the wetting behavior of the three kinds of surface treatments on flat and patterned PDMS using an aqueous solution of red food coloring. (C) Cross-sectional view of water drop outside and on the DLD array for a prewetted surface. (D) Comparison of wetting angles on flat and patterned surfaces after no treatment, oxygen plasma and prewetting. The error bars represent the standard deviation of the measurement.*

Volume of a filled device

The volume of the liquid in a filled device is calculated based on the table in figure S1C. The ratio of the area of the fluid and the total area of the unit cell is 0.58, which is multiplied with the overall dimensions of the device (length 20 mm, width 4 mm and depth 24 µm), giving us the total volume of device 1 of 1.1 µL.

Uniformity of wetting

The characteristics and uniformity of the wetted array are characterized by confocal microscopy and direct imaging with a macro objective. In both cases device 3 was used with added reservoirs. For the confocal images fluorescein isothiocyanate (FITC) was first dissolved in methanol to 10% that was in turn diluted in water 100 times and the methanol

allowed to evaporate. The confocal microscope is based on a Yokogawa CSU22 spinning disc, Andor laser combiner and Andor iXon DU-897 CCD camera on an inverted Nikon Ti microscope. A Plan 50x ELWD Dry and a Plan Fluor ELWD 40x Ph2 ADL objective with NA 0.32 and 0.4 respectively where used for figures 2C-F. Since the microscope is inverted, the device was turned upside-down for imaging (surface tension dominates and so this has little to no effect on the shape of the liquid surface). The image contrast was adjusted such that scattered light was rejected from the image.

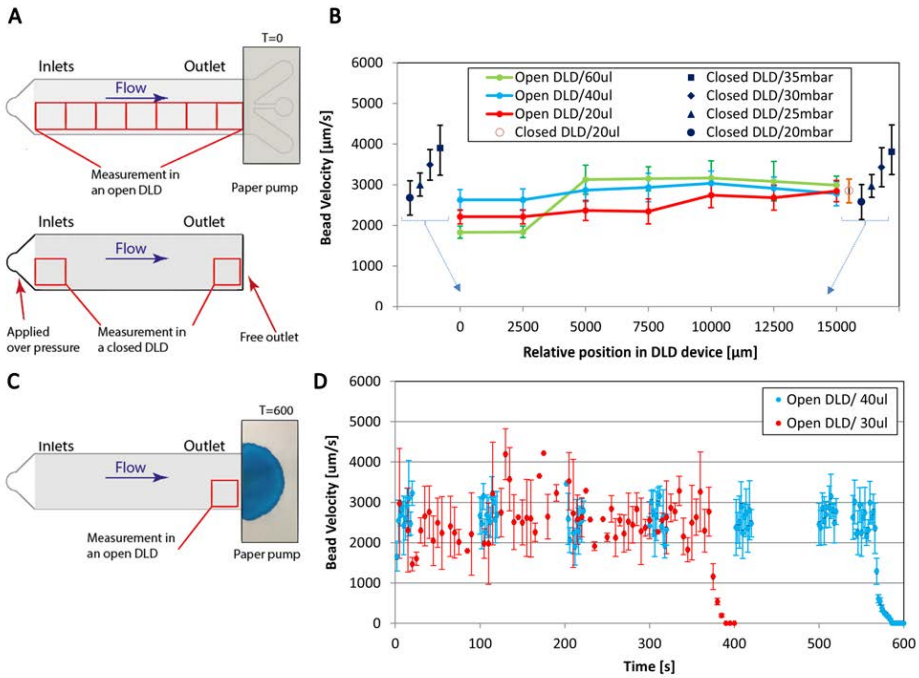

Figure S4. *Particle velocity measurements for open and closed DLD devices. The flow in the open devices is driven by a paper capillary pump without any wax-defined channels. The paper is shown at t=0 s in (A) and t=600 s in (C). The flow in the closed devices is driven by over pressure as well as by a paper capillary pump. The different sets of experiments took place using the same design of DLD (Device 1 (Figure S1)). The following microspheres were used at a dilution of 50x in deionized water: green fluorescent polystyrene beads with diameter 1.57 µm (CV 2%) and functionalized with carboxylate groups from Polysciences Inc. (Warrington, PA). (A) Schematic of measurement setup for velocity measurements at different locations for open and closed devices. (B) Velocity of the beads as a function of position for open and closed devices. For the data where a paper capillary pump was used the volume in the reservoir is indicated. For the pressure driven flow the applied pressure difference is given. (C) Schematic of measurement setup for velocity measurements as a function of time. (D) Velocity of beads as a function of time when 30 µL (red) and 40 µL (blue) of sample is added to the reservoir. The error bars represent the standard deviations of the measurements.*

For the images with the macro objective, the device is wetted with an aqueous food dye and imaged, with the liquid facing upwards, using a macro objective (Canon MP-E 65 mm f/2.8 1-5x) with a Canon 5D Mark II camera house. Basic contrast and brightness adjustments were made to ensure that the image reflects what is seen by the naked eye.

We could observe a tendency that the flow velocity (see below) is slightly lower for the first ~5 mm along the device. This indicates that the flow cross section is larger here, which is consistent with the flow extending above the posts since the volume flow rate is a conserved quantity. We observed that this effect vanishes as the fluid level drops, away from the reservoir and also decreases as the sample volume in the reservoir decreases with time.

Flow measurements

We measured the flow rates at different positions along open and closed devices using an applied overpressure or using a paper capillary pump (Figure S4). Velocities of fluorescent microspheres were observed between two neighboring posts in the same row.

The volumetric flow rates were measured directly by running the device with reservoirs filled with well-defined volumes and recording the elapsed time until the reservoirs were empty (Figure S4D). The volumes were corrected by subtracting the evaporated volume from the device based on figure S5 (8.5 nL/s). The time was measured until the velocity was half of the mean velocity. The remaining liquid in the device was crudely estimated to half the volume of the device, i.e. 0.5*1.1 µL. This volume was subtracted from the total volume considered. From these two measurements we obtain approximate values of 70 nL/s and 61 nL/s for the two different volumes tested. These results are consistent with the results of combining the velocity measurements (Figure S4B) with the total flow cross section based on the designed dimensions (Device 1 in Figure S1C) of the device giving flow rates of 71±19 nL/s. The correspondence of the two types of measurements indicate that the flow is indeed taking place such that it fills up the space between the posts without overflowing.

Equivalent pressures applied to the device

The equivalent pressure exerted by the paper capillary pump is found to be 21 mBar by comparing the applied over-pressure necessary across a closed device to achieve the same flow velocities as for a closed device with a paper capillary pump (Figure S4B). The pressure exerted by the paper capillary pump exceeds the pressure due to the water pillar in the reservoir. The pressure generated in the reservoir depends on the height difference between the inlet and outlet ($\rho\, g\, \Delta h$ ~ 1 mBar/cm with ρ = 1000 kg/m^3 density of water, g = 9.8 m/s^2 gravitational acceleration, Δh height of water pillar). The tested volumes, 30 µL, 40 µL and 60 µL, correspond to heights of 4.2 mm, 5.6 mm and 8.4 mm of sample respectively in the reservoir (inner diameter 3mm) giving hydrostatic pressures of 0.4 mBar, 0.6 mBar and 0.8 mBar which is much less than the involved estimated negative pressures exerted by the capillary paper pump pulling the sample. The capillary pumping effect of the paper therefore dominates the flow and the fluid is predominantly pulled through the device.

Flow resistance

Flow resistance for the closed devices is estimated based on the relationship

$$Q_{pump}^{closed} = \frac{\Delta P_{pump}}{R_{load}^{closed}}$$

where R is the fluidic resistance, Q is the volumetric flow rate and ΔP is the applied pressure difference across the device. From figure S4B we obtain R^{closed} = 30 10^{12} $kgs^{-1}m^{-4}$.

The flow resistance of the open device is expected to be slightly lower than that for the closed device. It is calculated below based on figure S5.

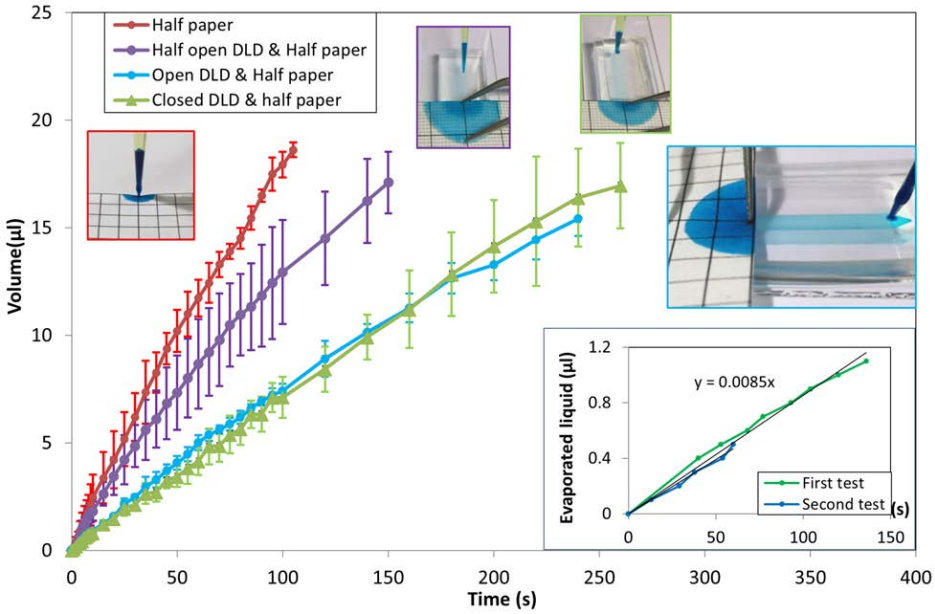

Figure S5. *Liquid flows versus time corrected for evaporation. The liquid is 0.5% food coloring diluted in deionized water. The graph shows four cases. From the left to the right we have: liquid added at the edge of a paper (half paper), open DLD device of length 10 mm (half device) connected to paper, open DLD of length 20 mm (whole device) connected to paper, closed DLD of length 20 mm (whole device) connected to paper. To be able to easily judge the extent of the drops on the paper, a grid pattern is printed on the paper using a standard laser writer. The inset shows the accumulated evaporated liquid from a filled device (device 1). From this graph we can conclude that the evaporation rate from the device is 8.5 nL per second.*

Characterization of the paper capillary pump

The paper capillary pump can be treated as a battery with an internal resistance and an internal negative pressure or, in analogy to electronics, a hydromotive force. To estimate the internal resistance and the hydromotive force the following system of equations (number 1 to 4) are considered. Note that we will obtain an estimate of the flow resistance of the open device from these calculations.

$$\begin{cases} Q_{paper} = \dfrac{\Delta P_{internal}}{R_{internal}} \\ Q_{paper}^{openHALF} = \dfrac{\Delta P_{internal}}{\frac{1}{2}R_{load}^{open} + R_{internal}} \\ Q_{paper}^{open} = \dfrac{\Delta P_{internal}}{R_{load}^{open} + R_{internal}} \\ Q_{paper}^{closed} = \dfrac{\Delta P_{internal}}{R_{load}^{closed} + R_{internal}} \end{cases}$$

We first calculate the internal resistance of the paper by combining equations 1 and 4 above to eliminate the internal pressure (hydromotive force).

$$R_{internal} = \frac{\Delta P_{pump}}{Q_{pump}^{closed}} \frac{Q_{paper}^{closed}}{Q_{paper} - Q_{paper}^{closed}}$$

Numerical data is extracted from Figures S4 (for the pump driven flow) and S5 (for the paper capillary pump driven flow) based on the initial flow rates for each case and combined with the flow resistance of the closed device as calculated above.

$$\Delta P_{pump} = 21 mBar$$
$$Q_{pump}^{closed} = 71 nL s^{-1}$$
$$Q_{paper} = 198 nL s^{-1}$$
$$Q_{paper}^{closed} = 71 nL s^{-1}$$
$$\Rightarrow R_{internal} = 16.5 \cdot 10^{12} kg s^{-1} m^{-4}$$

The hydromotive force is now calculated by using the number of the flow rate of the paper without any device (“Half paper”) in fig S5 combined with equation 1 above.

$$Q_{paper} = 198 nL s^{-1}$$
$$\Rightarrow \Delta P_{internal} = 32 mBar$$

Plugging the results above into equation 3 above, the flow resistance of the open device.

$$Q_{paper}^{open} = 80 nL s^{-1}$$
$$\Rightarrow R_{load}^{open} = 23.1 \cdot 10^{12} kg s^{-1} m^{-4}$$

Finally, as a simple control the flow rate of the device cut in half is estimated based on equation 2 above.

$$Q_{paper}^{openHALF*} = 113 nLs^{-1}$$

The value is lower but still consistent with the value obtained by measuring the initial slope of the corresponding curve in figure S5.

$$Q_{paper}^{openHALF} = 157 nLs^{-1}$$

Evaporation

To obtain rough estimates of the evaporation rates we measured the evaporation rates for different cases by using a precision balance (Ohaus Corp. Pine Brook, NJ USA, model Pioneer PA114C, minimal readout 1 µg).

An evaporation of 8 nL/s from the device can be compared to the typical flow rate through the device of 65 nL/s. Roughly 12% of the sample is thus evaporated from the device.

Due to nonuniform wetting and possible variations in the lab environment during the course of the experiments, the evaporation rates should be considered rough estimates to give a perspective of the relationship between the evaporation rate and the volumetric throughput in the devices.

The lab environment had a 60±5% RH and room temperature of 21°±1° C.

Biological samples

The size distributions of the biological samples used were determined by measurement in optical micrographs using ImageJ (Figure S6). The results are summarized in the following table.

Sample type	*Dimensions ± std dev*	*Shape*
MCF7 (cancer cell line)	17.3±2.1 µm	spherical
White blood cell	12.2±0.9 µm	spherical
Red blood cell	2.2±0.5 µm 7.8±0.6 µm	biconcave
Trypanosome cyclops	2.5±0.5 µm 12.8±3.3 µm	ribbon-like

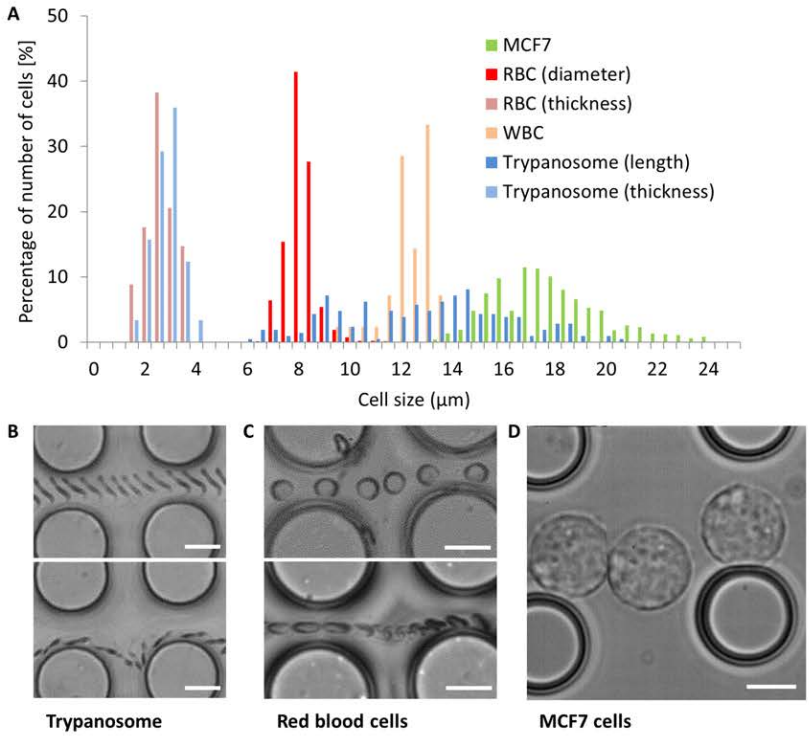

***Figure S6**. Size distribution of biological samples based on measurements in optical micrographs. (A) Histograms of size distributions. For the spherical cells (MCF7 and WBC) one number gives the relevant size (diameter). Red blood cells and the parasites are described by two numbers (thickness and overall diameter or length). (B) & (C) Optical micrographs of the non-spherical cells exhibiting different orientations depending on device depth (9 µm and 24 µm) (top images shallow device and bottom images deep device) (D) Optical micrograph of spherical MCF7 cells. All scale bars 10 µm.*

RBC Rotation in DLD

Paper IV

Dielectrophoretic effect on red blood cells in deterministic lateral displacement devices

Bao D. Ho,[a] Hasti Yavari,[b] Stefan H. Holm,[a] Si-Hoai-Trung Tran,[a] Jason P. Beech,[a] Jonas O. Tegenfeldt*[a]
[a] *Division of Solid State Physics and NanoLund, Lund University, Professorgatan 1, 22363 Lund, Sweden.*
E-mail: jonas.tegenfeldt@ftf.lth.se
[b] *Division of Atomic Physic, Lund University, Professorgatan 1, 22363 Lund, Sweden.*

Abstract. We report a biological application of dielectrophoresis (DEP) in controlling the orientation of red blood cells in deterministic lateral displacement (DLD) devices. Orientation has a large impact on the effective size of non-spherical cells in DLD devices but is normally decided by factors that are hard to decouple from the geometry of the device, such as fluid shear forces and steric interactions with the pillars. DEP has been shown in other work to have the ability of changing the effective size of spherical polystyrene particles in a DLD device by adding a force that is independent of shear and steric forces and that can be modulated to give the ability to tune separations. Our work demonstrates that DEP can also change the effective size of non-spherical particles, in this case red blood cells, via control of orientation. The experiments showed that by applying a low frequency AC voltage (100 Hz) of around 177 V_{RMS}/cm in an isotonic buffer, the RBCs exhibit negative dielectrophoretic properties, adopt specific orientations and thus have an increase of effective size by a factor of around 1.5, from below 3.47 µm to 4.44 µm. Since many important separations are performed on blood, any ability to improve the contrast in separation parameters between RBCs and other cells is promising. Our work indicates that DEP-DLD devices can find a wide range of applications in biological sorting, in particular for separation of RBCs from other kinds of cells and pathogens.

1. Introduction

Particle separation is important for various applications ranging from clinical pharmacology to diagnostic devices in the field of medicine and biology. One particular sample widely used in clinical studies is blood, consisting of different cells such as white blood cells (WBCs) a.k.a leukocytes, red blood cells (RBCs) a.k.a erythrocytes, and platelets. Under different physiological circumstances, distinct morphological changes are observed in RBCs affecting the cells' deformability. The extent of this deformation varies for different disease pathologies. For instance, cancerous blood cells are known to have a more deformable phenotype as opposed to healthy cells [1] whereas a less deformable phenotype is observed in the case of Sickle-cell disease (SCD) and Malaria [2]. In malaria higher stiffness of the parasitized RBCs is exhibited for more advanced stages of the disease. In addition, the physical and mechanical properties of a particle change with its size. Therefore, valuable information about the state of health or the phase in cycle of an individual cell can be extracted by investigating the cells' physical properties.

The techniques dominantly used for blood cell separation are fluorescence activated cell sorting (FACS) and magnetic-activated cell sorting (MACS) yielding high resolution results with the downside the necessary sample labeling may perturb the cells. In recent years different microfluidic particle separation devices have been introduced as a cheaper, more flexible and less time-consuming alternative technique. One particular advantage of these devices is the ability of working at nanometer or micrometer scale relative to the size of the particles being investigated.

Deterministic lateral displacement is a fundamental microfluidic separation technique introduced by Huang *et al.* in 2004, where particle separation based on size was reported with resolution as low as 10 nm [3]. The particle separation in this passive device is based on internal forces of the particular geometry of the design. One positive characteristic of DLD is that, being a continuous method, it can easily be integrated with upstream and downstream processes. In the first instance DLD was shown to be an extremely good size separation technique but advances in the method have since shown it to be more versatile with factors such as shape [4-7] and deformability [6]. In 2008, Chang and Cho introduced a virtual DLD device with varying critical size [8]. This tunability was achieved by employing a negative dielectrophoretic (DEP) virtual array of obstacles. In electrodeless or insulator-based DEP (iDEP) the varying electric field is present through the entire channel by insulating the microstructure between the electrodes using fabrication techniques such as soft lithography [9] or imprint lithography [10]. In this way the fabrication complexities involved with microelectrodes and other limitations commonly encountered in the presence of electrodes are avoided. Besides, by using iDEP the device can be operated at DC fields as well as low frequencies without the need to be concerned about causing electrolysis [11]. In 2003, Cummings *et al.* investigated the effect of iDEP in continuous separation of particles through an array of insulating obstacles in two separate studies [12, 13]. It was concluded that using DC fields, the flow of 200nm particles can be controlled from

ideal electrokinesis to streaming DEP to trapped particles. In 2009 Beech *et al.*, introduced a method called DEP-DLD where DEP and DLD are integrated together [14]. The particle separation behavior of the device was investigated using AC fields at low frequencies and it was shown that the critical size can be readily decreased by half or less. In a DEP-DLD device the high resolution of DLD is combined with the tunability of DEP. For example, by changing the applied frequency, different properties of the cells being investigated can be probed.

In 2014 Kruger *et al.* investigated the possibility of separating red blood cells (RBC) in DLD devices in a simulation study and obtained positive results [15]. The displacement path taken by the RBCs was predicted in the particular DLD design. Controlling the orientation of particles in a DLD device gives greater control over separation behavior and can make it possible to separate populations that vary in shape in a way that is otherwise not possible using DLD. Zeming *et al.* [16] used post shapes to gain some control over particle orientation and improve the separation of RBCs and Beech *et al.* used channel depth to control RBC orientation making it possible to choose to separate by cell diameter or cell thickness [6]. In the present work we show that we can use DEP forces to control cell orientation and show also the effect that this has on cell behavior in DLD devices. Using DEP in this way has the advantage over the above, geometry-based approaches in that it can be applied to any kind of existing DLD device fabricated in an insulating material and that it can be tuned to optimize separations under varying conditions without the need to fabricate new devices.

2. Theory

Deterministic Lateral Displacement

The geometry in a deterministic lateral displacement (DLD) device, as shown in Fig. 1, consists of an array of posts with λ spacing between the centers, shifted laterally by a distance $\Delta\lambda = \lambda/N$, where N is usually an integer number ($2 \leq N \leq 100$). N is called the period of the array since the array repeats itself after N rows.

Particles which are smaller than a critical diameter D_c flow in a zig-zagging pattern following the flow stream while ones whose size $D \geq D_c$ are transported in displacement mode. Fig. 2(a) shows the different trajectories of the particles depending on their size. The critical diameter can be calculated as:

$$D_c = 2\alpha \frac{d}{\sqrt{N}} \quad (1)$$

Where d is the distance between 2 posts and α is correction term.

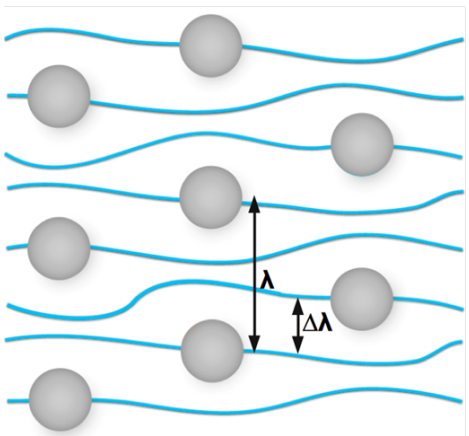

Fig 1 *A simplified bumper array with distance between two bumpers λ, row shift Δλ and period of N=3.*

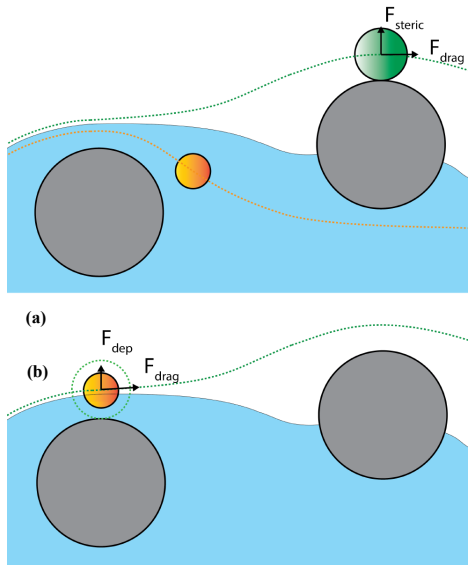

Fig 2 *(a) Trajectories of particles in a DLD device. The orange particle, which is smaller than the critical size, follows the stream while the big green particle "bumps" into the posts and switches to another stream. (b) Trajectories of a particle in a DEP-DLD device. Although it is smaller than the critical size, the dielectrophoretic force makes it appear larger and moves in displacement mode.*

Dielectrophoresis

Dielectrophoresis (DEP) is the motion of particles subjected to a non-uniform electric field. The interaction of the field with the particle's dipole moment exerts a force on the particle [17]. The force magnitude and direction are dependent on the particles' geometry (size and shape) and electrical properties of the particles and the buffer they are suspended in.

This property can be employed in microfluidic separation and sorting techniques, in particular DLD.

In the electrodeless DEP approach that we used in this project, the voltage is applied across the length of the device. Due to the presence of the PDMS posts inside the channel, the electric field is distorted around the posts. In particular, the maxima of electrical field are at the sides of each post. Fig. 2(b) illustrates the case the particle experiences negative DEP – it moves away from the particular post. In other words, although the particle is smaller than the critical diameter, it behaves like a larger particle and is deviated from the flow stream where it originally resided.

3. Experimental

Device

We used soft-lithography to make poly-(dimethylsiloxane) (PDMS) devices on glass for our experiments. The detailed procedure can be found in Holm *et al* [5]. We modified the design by Holm for sorting blood and *Trypanosoma cyclops* to run our DEP-DLD experiments with red blood cells. The layout of the original design is shown in Fig. 3(a). In order to achieve high electric field, we shortened the device by cutting it in half and pinched the outlet hole near the cut line.

The complete device after tubing is illustrated in Fig. 3(b). The device has four reservoirs: two buffer reservoirs and a sample reservoir (on top of the figure) and an outlet reservoir (at the bottom of the figure). The four blue cylinders showed in the figures are parts of the tubes connecting to the pressure pump and the four small wires are platinum electrodes.

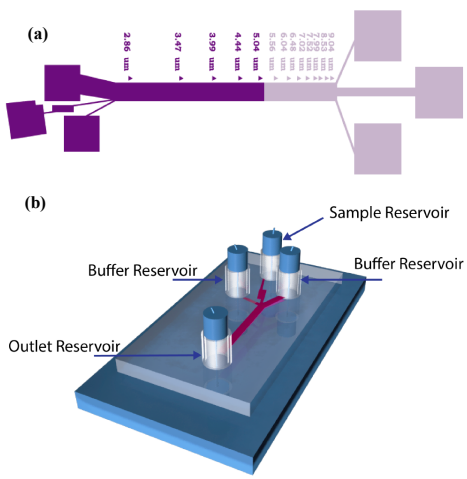

Fig 3 *(a) The DEP-DLD device modified from Holm's Trypanosoma design, the blurred half was cut out to shorten device length. (b) 3D model of the complete device.*

Equipment

The flow of blood sample and buffer inside the PDMS device was driven by pressure gradient. Pressure at the sample reservoir and the two buffer reservoirs was regulated by an over-pressure controller (MFCS-4C, Fluigent, Paris, France) via three plastic tubes and connectors (Fig. 4). The controller maintained a stable pressure difference in the range of 0 – 60 mBar between the sample/buffer reservoirs and the outlet reservoir, which was left open to atmospheric pressure. To supply a high-voltage bias across the channel of the device, we used a function generator (33120A, Hewlett Packard, Palo Alto, CA, USA) together with a 100X amplifier (BOP 1000M, Kepco, Flushing, NY, USA), yielding a sinusoidal AC voltage of up to 1000 Vpp. One terminal of the voltage source was connected to the two platinum electrodes immersed into the buffer at the buffer reservoirs and the other terminal was attached to the platinum electrode embedded into the buffer at the outlet reservoir. Since the cross-section of the buffer/outlet tubes is much larger than that of the fluidic channel, the electrical impedance of these tubes is much lower than the channel impedance and the voltage difference

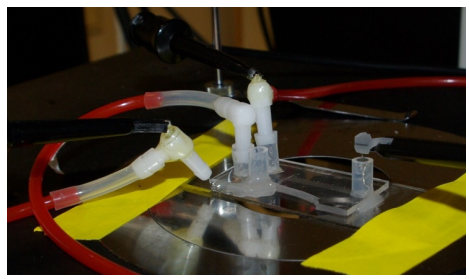

Fig 4 *The DEP-DLD device with microfluidic and electrical connections. The sample and buffer reservoirs (on the left of the device) were connected to an over-pressure pump by three plastic tubes; one of the tubes was unplugged for clarity. The buffer reservoirs and the output reservoir (on the right of the device) are connected to the AC voltage source through platinum electrodes.*

provided by the voltage source is assumed to be distributed across the channel only. Blood cells in the device were imaged through an inverted microscope (Eclipse TE2000-U, Nikon Corporation, Tokyo, Japan). The images and movies of the experiments were captured using a CMOS camera (Neo sCMOS, Andor Technology, Belfast, Northern Ireland).

Sample preparation

The blood sample was extracted from healthy donors following a standard procedure. A sterile needle (Haemolance+ low flow, Haemedic, Sweden) is used to prick the donors' finger. The blood drop (10 µL) is collected by a sterile pipette tip and then diluted into 1000 µL of autoMACS® running buffer (#130-091-221, Miltenyi Biotec, Bergisch Gladbach, Germany). The buffer (pH 7.2) contains phosphate buffered saline (PBS), bovine serum albumin (BSA), EDTA, and 0.09% sodium azide.

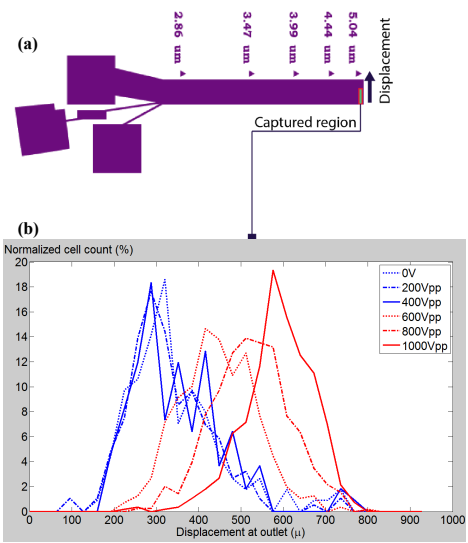

Fig. 5 *(a) The captured region where displacement of RBCs were analyzed. (b) Distribution of RBCs at the captured position. The graph shows cell count value at each displacement position along the chosen row for counting. There are six curves corresponding to six AC voltage values used in our experiments.*

Experimental procedure

Ten µL of diluted blood sample was added to the inlet reservoir and the buffer reservoirs were filled with autoMACS® running buffer. The outlet reservoir was also filled with the buffer to allow for electrical conduction. The experiment could be run with or without an applied voltage. Movies were taken all over the device. However, to quantify the displacement and effective size of the RBCs, we focused on a small region near the outlet reservoir, which has the nominal critical size of 5.04 µm (Fig. 5(a)). The AC voltage was ramped up from 0 V to 1000 Vpp, in steps of 200 Vpp. For each voltage value, we captured a corresponding microscopic movie. In each movie, we counted the number of RBCs passing through every gap between nearby posts of a chosen row. The cell counts were normalized and plotted as a function of the displacement.

4. Results and Discussion

Orientation of red blood cells in DEP-DLD device

RBCs have the shape of a biconcave disk, with diameter of around 6 – 8 µm and thickness of around 2 – 2.5 µm. Due to this specific geometry, orientation of the cells in a normal DLD device would change dependent on the fluid stream they reside in. When RBCs travel in a straight channel or in the middle of two posts, they align horizontally like Frisbees flying in mid-air. Looking at a microscopic image taken from the top of the device, one can observe the cells as circles. However, when the RBCs switch to the fluid streams near a post, they tend to lean against the post and orient vertically like bicycle tires. From the top of the device, one sees the cells as thin, rounded rectangles (Fig. 6 (a) and Movie 1. This phenomenon dictates the effective size of the cells in a DLD device, making them appear as small as their thickness [5].

With a sufficient electric field gradient applied across the device, this vertical orientation of the RBCs when they move near the posts is overridden. As can be seen in Fig. 6(b) and Movie 2, the cells appear consistently as Frisbees when they flow in the post array, disregarding their position with respect to posts. The effective size of the cells is near their diameter.

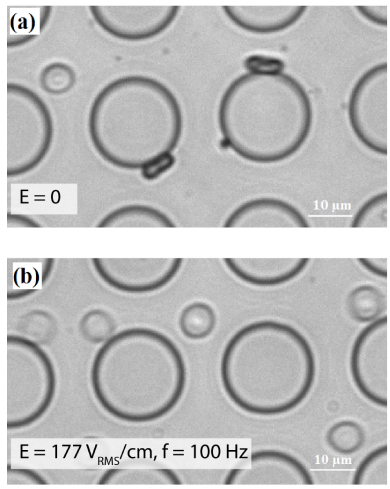

Fig. 6 *Orientation of red blood cells in a DLD device. (a) In the absence of an AC field (**E** = **0**), there are two types of orientation of RBCs depending on their positions with respect to a post. (b) When electric field was turned on (V = 1000 Vpp, |**E**| ≈ 177 V_{RMS}/cm), RBCs orient horizontally like Frisbees flying in mid-air, disregarding the fluid stream they were in.*

Distribution or red blood cells near the outlet reservoir

To quantify the dielectrophoretic effect on RBCs in DEP-DLD devices, we analyzed the displacement of the cells at a region near the outlet. Fig. 5(b) shows the distribution of RBCs measured at the end of our device. There are six curves corresponding to six AC voltage amplitudes we used, ranging from 0 to 1000 Vpp. As can be seen from the figure, when the applied voltage is increased to 600 Vpp, the displacement of the RBCs starts to change. This can be explained by the change in their orientation under dielectrophoretic effect, making them appear larger when in contact with a post, forcing them to move in displacement mode throughout the channel.

Effective size of RBCs in DEP-DLD

The bell-shaped curves in Fig. 5(b) can be fitted into normal distribution to estimate the effective size of RBCs in a DEP-DLD device. This work can be performed using the Curve Fitting application of MATLAB R2014a (The MathWorks, Natick, MA, USA). Fig. 7 shows the fitted data. The blue diamond marks represent the mean displacement of RBCs at each voltage value and the error bars correspond to one standard deviation. We also add the dotted lines noted with critical diameter values to help estimate the effective size of the cells in our device. For example, by looking at the graph one can see that when a voltage of 600 Vpp was applied, RBCs behave as spheres of diameters in the range between 3.47 µm and 3.99 µm.

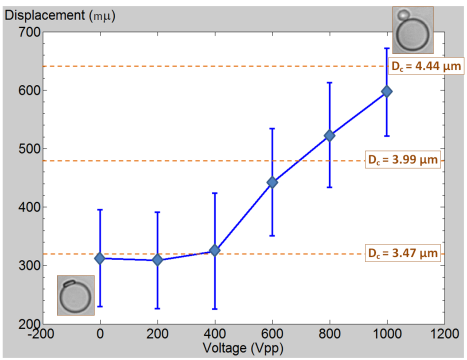

Fig. 7 *The displacement of RBCs as a function of applied voltage, assuming they have normal distribution. The dotted lines marked with critical diameter values are included to help estimate the effective size of the cells in our device.*

In Fig. 7, one can see that the error bars are larger as compared to the mean values. There are three possible factors causing this phenomenon. First, the RBCs already have their own size distribution, both in diameter and thickness. Second, the master we used to make PDMS device has some defects that make some posts disappear inside the device's channel and affect the flow profile. Finally, as can be seen from Movie 3, the orientation of RBCs while moving in the DLD arrays is quite stochastic. In particular, besides vertical and horizontal orientations they may also have inclined orientation that makes their effective size lies in the range between their thickness and their diameter. We believe that the third effect contributes the most to the variation seen in Fig. 7.

It should be noted that although the biggest size shown in Fig. 7 is 4.44 µm, it does not reflect the actual diameter of the RBCs. The reason for this is that we only use half of the device, which has highest critical size value of 5.04 µm, meaning that even if the cells were as large as 8 µm, they would be still displaced to the same position as the ones having the diameter of 5.04 µm. This drawback of the device can be avoided by a new DEP-DLD design that is more suitable for RBCs.

5. Conclusion and Outlook

In this work, we have shown the effect of dielectrophoresis on orientation of RBCs in DLD devices. This effect can be used as a tool to tune the effective size of RBCs by a factor of 1.5 (from below 3.47 µm to 4.44 µm in our work) or even better, with more suitable design, keeping in mind that the diameter of the cells can be three times as large as their thickness. This phenomenon can open a wide range of applications in sorting RBCs from other kinds of cells and pathogens, thanks to the unique geometric of the RBCs.

There is plenty of room for future work. For example, modelling and simulation of RBCs in the devices could help us gain more insight into the mechanism behind the DEP effect on orientation of the RBCs. The buffer we used in this work is isotonic. One can possibly treat RBCs with hypotonic buffer to make them more spherical, carry on similar experiments, and compare with our results to see whether the DEP force or torque (orientation change) is more pronounced.

In future work, *Trypanosoma cyclops* parasites can be tested in the same device and their displacement, as a function of voltage, can be compared with the current data of RBCs. If the difference in the effective critical diameter is significant, they can conceivably be separated by applying an AC voltage in DLD, as an alternative to fabricating DLD devices with specific depth [5]. The benefit would be that a deeper device with greater throughput could be used.

6. Electronic Supplementary Materials

A selection of videos of the results are available at http://bit.ly/RBCRotationVideos

Movie 1 - 0V_zoom_in.wmv: shows, at large magnification, the dynamics of RBC in the DLD device described in the main text when a pressure of 20 mBar was applied.

Movie 2 - 1000V_zoom_in.wmv: same as Movie 1, but with an additional AC voltage of 1000 V_{PP}, 100 Hz applied.

Movie 3 - 0Vpp_large_FOV.wmv: same as Movie 1, only at a larger field of view.

Movie 4 - 1000Vpp_large_FOV.wmv: same as Movie 2, only at a larger field of view.

References

1. Guck, J., et al., *Optical Deformability as an Inherent Cell Marker for Testing Malignant Transformation and Metastatic Competence.* Biophysical Journal, 2005. **88**(5): p. 3689-3698.
2. Suresh, S., et al., *Connections between single-cell biomechanics and human disease states: gastrointestinal cancer and malaria.* Acta Biomaterialia, 2005. **1**(1): p. 15-30.
3. Huang, L.R., et al., *Continuous particle separation through deterministic lateral displacement.* Science, 2004. **304**(5673): p. 987-90.
4. Holm, S.H., et al., *Simplifying microfluidic separation devices towards field-detection of blood parasites.* Analytical Methods, 2016. **8**(16): p. 3291-3300.
5. Holm, S.H., et al., *Separation of parasites from human blood using deterministic lateral displacement.* Lab on a Chip, 2011. **11**(7): p. 1326-1332.
6. Beech, J.P., et al., *Sorting cells by size, shape and deformability.* Lab on a Chip, 2012. **12**(6): p. 1048-1051.
7. Beech, J.P., et al., *Separation of pathogenic bacteria by chain length.* Analytica Chimica Acta, 2018. **1000**: p. 223-231.
8. Chang, S. and Y.H. Cho, *A continuous size-dependent particle separator using a negative dielectrophoretic virtual pillar array.* Lab on a Chip, 2008. **8**(11): p. 1930-1936.
9. Xia, Y.N. and G.M. Whitesides, *Soft lithography.* Annual Review of Materials Science, 1998. **28**: p. 153-184.
10. Chou, S.Y., P.R. Krauss, and P.J. Renstrom, *Imprint of Sub-25 Nm Vias and Trenches in Polymers.* Applied Physics Letters, 1995. **67**(21): p. 3114-3116.
11. Xing, X.X., M.Y. Zhang, and L. Yobas, *Interdigitated 3-D Silicon Ring Microelectrodes for DEP-Based Particle Manipulation.* Journal of Microelectromechanical Systems, 2013. **22**(2): p. 363-371.
12. Cummings, E.B., *Streaming dielectrophoresis for continuous-flow microfluidic devices.* IEEE Engineering in Medicine and Biology Magazine, 2003. **22**(6): p. 75-84.
13. Cummings, E.B. and A.K. Singh, *Dielectrophoresis in microchips containing arrays of insulating posts: Theoretical and experimental results.* Analytical Chemistry, 2003. **75**(18): p. 4724-4731.
14. Beech, J.P., P. Jonsson, and J.O. Tegenfeldt, *Tipping the balance of deterministic lateral displacement devices using dielectrophoresis.* Lab on a Chip, 2009. **9**(18): p. 2698-2706.
15. Kruger, T., D. Holmes, and P.V. Coveney, *Deformability-based red blood cell separation in deterministic lateral displacement devices-A simulation study.* Biomicrofluidics, 2014. **8**(5): p. 15.
16. Zeming, K.K., S. Ranjan, and Y. Zhang, *Rotational separation of non-spherical bioparticles using I-shaped pillar arrays in a microfluidic device.* Nature Communications, 2013. **4**.
17. Pethig, R., *Review Article-Dielectrophoresis: Status of the theory, technology, and applications.* Biomicrofluidics, 2010. **4**(2): p. 35.

Active post DLD

Paper v

Active Posts in Deterministic Lateral Displacement Devices

Jason P. Beech[1], Kevin Keim[2], Bao Dang Ho[1],
Carlotta Guiducci[2], Jonas O. Tegenfeldt[1]

1. *Division of Solid State Physics and NanoLund, Lund University, Sweden.*
2. *Laboratory of Life Sciences Electronics, École Polytechnique Fédérale de Lausanne, Switzerland.*

Abstract

Using electrically connected metal-coated posts in a Deterministic Lateral Displacement (DLD) device and applying electric fields, we use electrokinetics to tune separations, decrease the critical size for separation by a factor of 20 and increase the dynamic range by the same factor with switching times on the order of seconds.

The strength of DLD stems from its binary behavior. Particles move in one out of two trajectories based on their effective size. For particles that are close to the threshold size, a small external force is sufficient to nudge the particles from one trajectory to another. Our devices consist of arrays of cylindrical metal-coated SU-8 posts connected by an underlying metal layer. This allows us to generate electric field gradients around the posts, causing polarizable particles to experience dielectrophoretic (DEP) forces. These forces, that depend on the volume and polarizability of the particle, can be made sufficient to push particles from one trajectory into another.

We observe that by adding DEP in this way, multiple size fractions can be created simultaneously in a device that has only one fixed critical size.

Key Words: Dielectrophoresis, Deterministic Lateral Displacement, Vertical electrodes, Tunable separation, Particle sorting

Introduction

In many types of miniaturized integrated fluidics systems particle sorting is essential for sample preparation and analytical fractionation. Microfluidics simplifies the process considerably compared to standard methods such as FACS and MACS. For high-throughput applications, acoustophoresis and inertial focusing have been developed. However, they provide limited precision. For high-resolution fractionation, deterministic lateral displacement is excellent. It was first presented by Huang *et al.* [1] and is, in its original form, a passive and continuous particle separation technique for the separation of particles by size. “Passive” refers to the fact that separation functionality is built into the structure of the device and that no external fields or actuations other than the generation of flow are required to separate particles.

"Continuous" refers to the fact that a mixture of particles can be input into the device and continuously extracted from the outputs of the device. This is in contrast to batch methods. The passive nature of the technique means that DLD is ideal for integration into simple devices that require little to no power input and continuity means that this can be done easily with up/down stream preparative or analytical steps. However, "passive" also means that once designed and fabricated, the separation performance of a device is fixed.

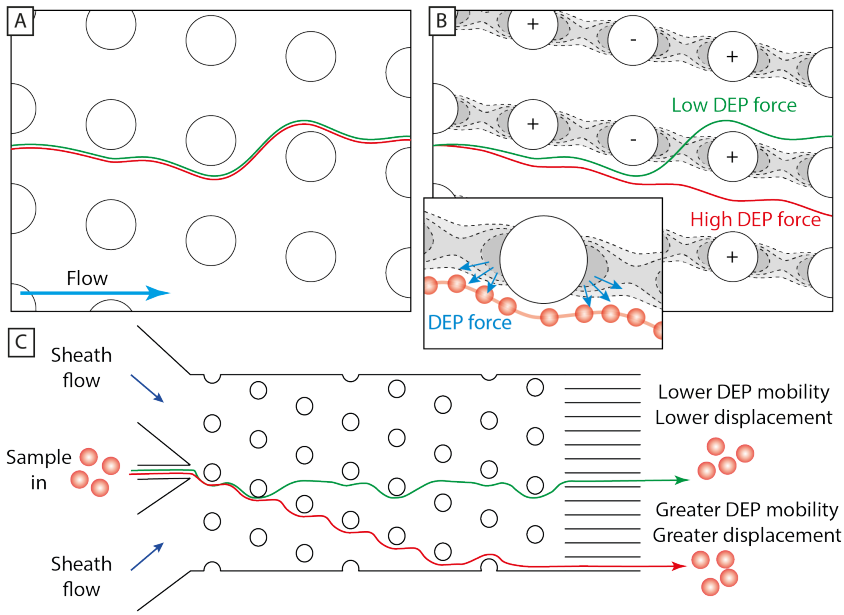

Figure 1. Device principle. (A) Particles smaller than the critical size in a DLD device move in the zigzag mode, following the average fluid flow direction (both red and green lines). (B) If the posts are active electrodes then electric fields can be generated between the rows of posts in such a way that DEP forces cause particles to transition to the displacement mode (the inset shows an illustration of the forces). (C) Using this principle, devices can be designed such that particles with differing DEP mobilities can be separated and then collected.

Tunability of separation functionality, a powerful tool, requires additional refinement. Beech and Tegenfeldt used the deformability of PDMS to change DLD device geometry and make devices tunable[2]. Zeming used innate, long-range electrostatic forces inside DLD devices, modulated via buffer ionic strength, to tune separations and achieve a large reduction of the critical size[3]. Zeming recently used this approach to detect the binding of proteins to the surface of micrometer sized beads[4]. In both of the above cases, nanometer-sized particles are separated in devices with micrometer-sized features. As the authors argue, this approach delivers powerful separations in devices that are easy to fabricate (large features) and easy to run (low pressures). Most relevant to the current work, Beech *et al.* used electric fields to modify the behavior of DLD devices[5]. This approach also enables the tuning of devices and the decrease of the critical size. It requires the application of electric fields but has the advantage that tuning can be done quickly and reversibly without the need to change the buffer. These devices were simple to fabricate and use, requiring only electrodes added at the inlets and outlets of devices. The insulating properties of PDMS generate insulator-based DEP forces[6] that tune the separations in DLD devices. This approach has now been refined by Ho *et al.* who have used buffer conditions and applied voltages and

frequencies to separate microspheres, bacteria and yeast based not only on size, but on surface charge and other dielectric properties (manuscript). However, generating high electric fields in devices using this approach requires high applied voltages (hundreds of volts), which can be problematic from a practical point of view, and it can be difficult to do this at high frequencies without specialized equipment.

Here we present a new approach to combine DEP and DLD by fabricating post arrays that are also electrodes. With our new design we are able to generate similar field gradients as in our previous work[5] using two orders of magnitude lower applied voltages due to the proximity of the electrodes, Figure 1 and Figure 2. This allows us to work with frequencies up to tens of MHz. Using this approach, we decrease the critical particle size in a device from 5.15µm to 0.25µm, a factor of >20. We also increase the dynamic range from 1 to 20.6, also a factor of >20. The switching times for the entire range (critical size from 5 to 0.25µm) are on the order of seconds.

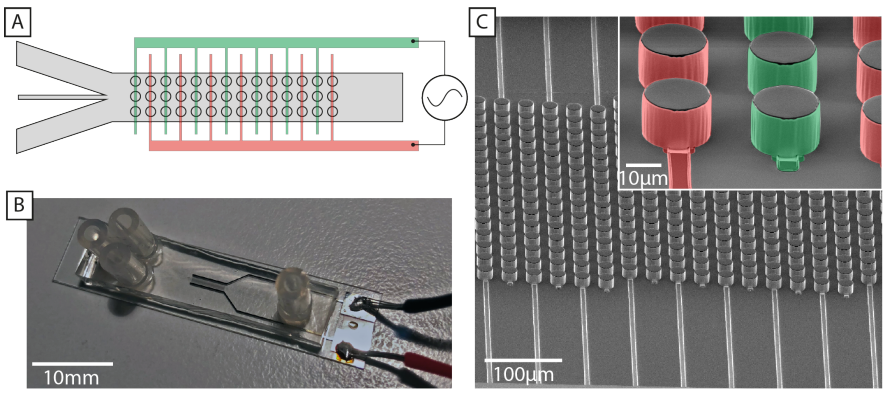

Figure 2. (A) Schematic of device design showing how the electrodes are coupled. (B) Photograph of a finished device showing inlet and outlet reservoirs and wires for fluid and electronic interfacing. (C) Colorized SEM image. The posts that constitute the DLD array are coated with metal (shown in both red and green) and connected via buried metal lines. The red and green colorized electrodes are connected as depicted in (A) to have opposite polarity.

Background and Theory

Deterministic Lateral Displacement

The critical particle diameter D_c in a DLD array with gap G and period N can be calculated using the empirical formula[7]:

$$D_c = 1.4 \cdot G \cdot N^{-0.48}$$

As shown in Figure E2 of the ESI, the measured gap in our device, $G = 11.10 \pm 0.14$ µm. With the period designed to be $N = 10$, the critical particle diameter is expected to be $D_c = 5.15 \pm 0.06$ µm.

This means that particles with diameters smaller than 5.15µm are expected to follow the fluid flow direction in the device (commonly referred to as non-displacement mode) and those larger than 5.15 µm will follow the geometry of the array (bumping or

displacement mode). Here we will refer to the two modes as displacement and non-displacement.

Dielectrophoresis

Dielectrophoresis (DEP), in turn, provides specificity based on both the volume and the dielectric properties of the particles.

The resistance to the formation of an electric field inside a material upon the application of an external alternating field ($\tilde{\varepsilon}$) is a function of frequency (f) and is given by the following where $\boldsymbol{\varepsilon}$ is the permittivity (in a static field) and σ is the conductivity.

Equation 1

$$\tilde{\varepsilon} = \varepsilon - \frac{j\sigma}{2\pi f}$$

The time-averaged force $\langle \boldsymbol{F}_{DEP} \rangle$ on a spherical particle of radius r and complex permittivity $\tilde{\varepsilon}_p$ suspended in a medium with complex permittivity $\tilde{\varepsilon}_m$ and an electric field with a peak amplitude of E_{pk} is given by:

Equation 2

$$\langle \boldsymbol{F}_{DEP} \rangle = \pi \varepsilon_0 \varepsilon_m r^3 Re(f_{CM}) \nabla E_{pk}^2$$

where the frequency dependence and the direction of the force is given by the real part of the Claussius-Mossotti factor (f_{CM}):

Equation 3

$$Re[f_{CM}] = \frac{\tilde{\varepsilon}_p - \tilde{\varepsilon}_m}{\tilde{\varepsilon}_p + 2\tilde{\varepsilon}_m}$$

A thorough treatment of DEP can be found in Pethig's textbook[8].

Active Posts

As mentioned above, the major advantage of placing electrodes inside devices is that the maximum field gradient can be generated exactly where it has the greatest effect on the trajectories of the particles, using the minimum applied voltage. While a similar effect could be achieved using a combination of 2D electrodes and 3D fluidics structures (metal electrodes on a surface with PDMS structures on top for example) three-dimensional electrodes have the major advantage that they provide a homogeneous electric field distribution over the complete depth of the device[9].

Combining DLD and DEP using active posts

In a DLD device, steric interactions between particles and posts cause particles to cross streamlines and to follow distinct trajectories through devices. As will be shown in the results section, a DEP force can be created that, together with the steric interaction, can be sufficient to force a transition from the non-displacement to the displacement mode. As described above, the DEP force is a function of the volume of the particle, the polarizabilities of the fluid and particles at the specific frequency and the gradient of the electric field squared. In contrast to previous work by Beech *et al.*[5] with electrodeless DEP in DLD devices, placing the electrodes onto the surface of the posts allows high field gradients to be achieved over a large range of frequencies (0-10 MHz with our current function generator). The significant advantages of combining DEP and DLD in this way are that we can tune the critical size in a device (that otherwise only has one critical size) by simply turning the knobs on our function generator. As will be shown below, we can decrease the critical size by a factor of 20, and do so with a response time of seconds. This means that we can separate 4 μm particles from 6 μm particles, or, 250 nm particles from 500 nm in the same device. What is more, the gaps between the posts in the device are 10 μm, making clogging negligible. We have run separations continuously for 10 hours without clogging being a problem. Also, while the focus in this report is on size-based separation, the dependence of the DEP force on the polarizability of particles means that we also have a handle on separations by dielectric properties which can further aid us in identifying different types of cells or microorganisms as well as in differentiating cells in different states, *e.g.* in live/dead assays.

Materials and Methods

Device Fabrication

The detailed fabrication process is described in the ESI (Figure E1). A metal layer (Ti/Pt/Ti 20 nm / 200 nm/20 nm) is first sputtered onto a plane glass substrate and patterned used ion beam etching. This is covered with an insulating SiO_2 layer (300 nm) and vias are opened. To create the active electrode structures SU-8 pillars are patterned (20 μm thick) and are subsequently coated by metal sputtering (Ti/Pt 20 nm/200 nm). The metal deposited on top of the pillars and on the planar substrate is removed by directional ion beam etching. This etching process preserves the metal-coated side walls of the electrodes [9]. A second SU-8 lithography step is used to define the fluidics channels and all other non-electrically active device features. Channels are sealed with a ~2 mm thick PDMS slab. Holes are punched through the slab for fluidic access and silicone tubes glued to the PDMS to function as fluid reservoirs and for interfacing with a pressure control unit. Wires are soldered to the device for electrical connection. The final device is shown in Figure 2. Further device details, such as the measured dimensions of the final device, can be found in the ESI (Figure E2).

Experimental Setup, Method and Materials

Flow in our devices was generated by applying over pressure in the range 1-10 mBar to device inlets using an MFCS-4C pressure controller (Fluigent, Paris, France). Outlet reservoirs are kept at ambient pressure. A function generator (15 MHz function/arbitrary waveform generator, model 33120A, Hewlett Packard, Palo Alto, CA, USA) is used for the application of AC signals. The voltage is measured with an

oscilloscope (Hewlett Packard 54603B 60MHz) with a 1x/10x probe (Kenwood PC-54, 600 Vpp). All images are captured through a microscope (Nikon Eclipse TE2000-U, Nikon Corporation, Tokyo, Japan), with an Andor Neo CMOS camera (Andor Technology, Belfast, Northern Ireland) using NIS Element software (NIS Element Advanced Research v4.51, Nikon). The conductivities of the media and the suspensions used in all experiments are measured using a B-771 LAQUAtwin Compact Conductivity Meter (Horiba Instruments).

1.7 mM KCl with 0.1% Pluronics F127 (conductivity measured at 25 mS/m) is used as a suspending medium for carboxylate modified latex beads of varied diameters below the critical size in the device. The bead suspensions are driven through the device using a ~5mBar pressure difference. Multiple frequencies between 1 Hz and several MHz at voltages between 0.5 V and 8 V are applied to the devices and the trajectories (exit positions) of the microspheres are measured.

DNA experiments are performed using YOYO-1 stained lambda-phage DNA suspended in 0.5 x TBE.

Particle counting and analysis

The separation of particles is determined by manual counting at the end of the DLD array. The process is described in detail in the ESI section 5. In short, the number of particles exiting the device through each of the 14 exit channels is established by manual inspection of recorded movies for each of the experimental conditions (varied voltage and frequency) and for each of the particle sizes.

Simulations

In order to gain insight into the distribution of the electric field and the shape of the gradients in our device, we performed finite element simulations using COMSOL Multiphysics 5.2. The results are shown in Figure 3 and complete details of simulations are given in the ESI section 4.

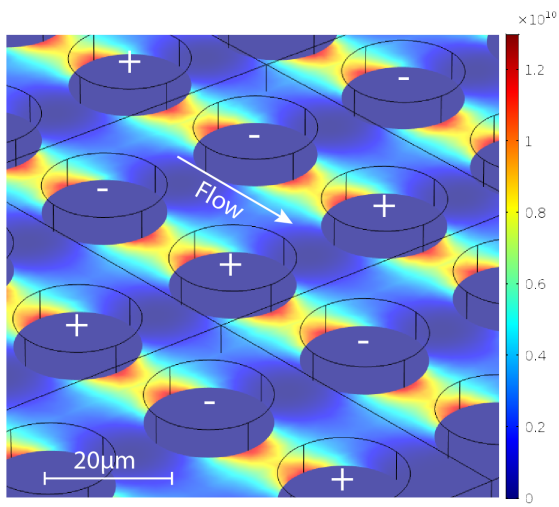

Figure 3. The DEP force is proportional to E^2. The plot shows a slice through a 3D finite element simulation of our device. The units are $(V/m)^2$. In this case the applied voltage is 1 Vpp. Although the maximum value of the color bar will scale with the applied voltage, the pattern of E^2 will always look similar.

Results and Discussion

Figure 4 shows an example of the switching of modes (zigzag to displacement) in our device. In (A) 2 µm beads, being smaller than the 5.15 µm critical size in the device move in the displacement mode. Upon the application of 3 V at 100 kHz (B) the beads switch to the displacement mode. When the particles are injected in a focused stream as in (C) the different trajectories mean that the particles can be collected at different positions at the end of the device.

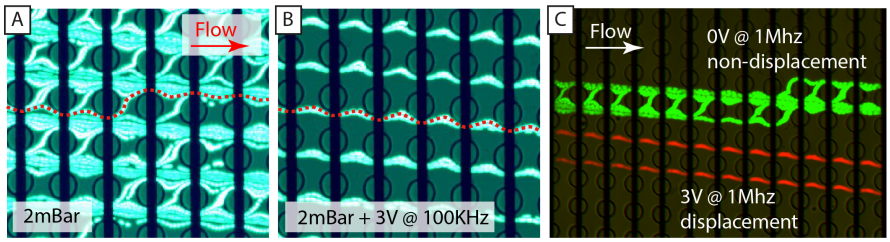

Figure 4. Typical separation results (A) 2 µm carboxylate beads are smaller than the native critical diameter (D_c = 5.15 µm) in the device and move therefore in the zigzag mode. (B) The same beads move in the displacement mode when 3V @ 100 kHz is applied. In both cases one trajectory is highlighted in red. (C) If the particles are focused into a stream then the change in trajectory leads to separation as the particle move through the device.

We tested the response of the device to voltage scans at frequencies ranging from 1-10^7 Hz. We find that at frequencies of 10 kHz and lower, at voltages above 3 Vpp, there is a tendency for microspheres to become trapped at the high field regions between the posts (see ESI figures E5 and E6). We attribute this to positive dielectrophoresis. We expect the optimal frequencies for tunable separation to depend on the types of particles being separated and frequency scans may well be the best approach at distinguishing bioparticles with differing polarizabilities. For the polystyrene microspheres we study here, all with the same polarizabilities, we find 10 MHz to be optimal (see ESI figure E5) and chose to keep the frequency fixed at 10 MHz and study the voltage dependence.

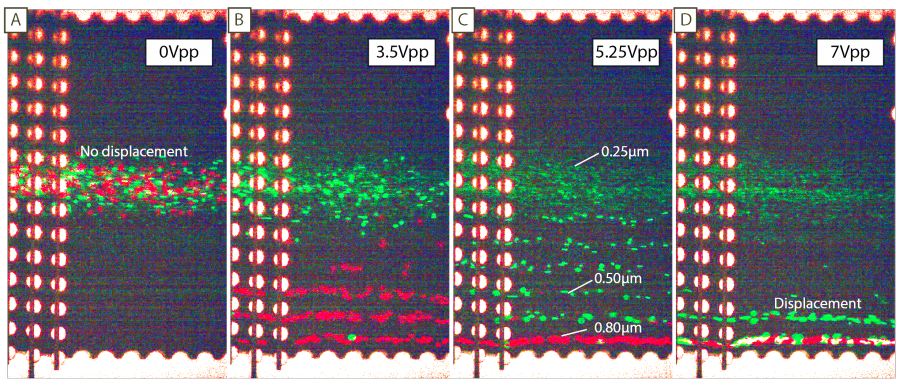

Figure 5. Tuned separation of 0.25 µm, 0.5 µm and 0.8 µm microspheres at 10 MHz and at (A) 0 Vpp (B) 3.5 Vpp (C) 5.25 Vpp and (D) 7 Vpp. 0.25 µm and 0.5 µm microspheres are green and 0.8 µm are blue and were imaged with separate filter sets. The images were extracted from a movie, colorized and recombined to show all particles simultaneously. See ESI for original movie.

Figure 5 shows the tuned separation of 0.25 µm, 0.5 µm and 0.8 µm microspheres at 10 MHz. At 0 Vpp all microspheres are in the non-displacement mode. At 3.5 Vpp the 0.8 µm microspheres move mostly in the displacement mode and become separated. At 5.25 Vpp the 0.8 µm microspheres are fully in the displacement mode, the 0.5µm half way between the non-displacement and displacement modes and the 0.25 µm still in the non-displacement. Here the three microsphere populations are fully separated. This is particularly interesting because the device has only one critical size and if used in the traditional way, without applied fields, can only generate two fractions. At 7 Vpp we are back to 2 fractions, one containing 0.25 µm microspheres and the other containing 0.5 µm and 0.8 µm microspheres.

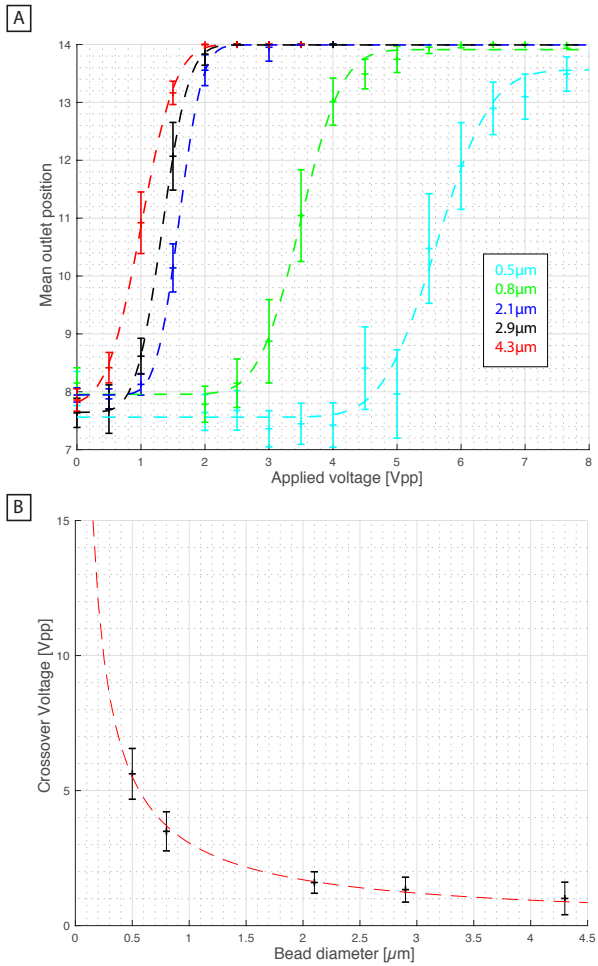

Figure 6. (A) Outlet position as a function of applied voltage for 0.5 µm, 0.8 µm, 2.1 µm, 2.9 µm and 4.3 µm microspheres at 10 MHz. Particles exit at channel 8 if they experience no displacement and at 14 if they experience maximal displacement. The dashed lines show fitted error functions (see ESI for more information on fitting). Error bars show one standard deviation. (B) Plot of the crossover voltage (mean of the fitted error function) as a function of beads diameter. Error bars are the standard deviation from the fitted error functions.

The trajectories (measured via outlet position) of 5 microsphere populations as at function of applied voltage at 10MHz are shown in Figure 6. As the voltage is increased each microsphere population, in decreasing size order, make the transition from the non-displacement to the displacement modes. This transition is described extremely well by an error function, shown fitted to the data. We believe the reason for this is the Gaussian size distribution of the microspheres. Voltages can be found at which all particles are either displaced, non-displaced or somewhere in between and this can be changed with a switching time of seconds (see ESI Figure E7). This is the fundamental principle of tuning using our method.

The obvious question is: How small can we make the critical size? Our function generator was able to provide 7.5 Vpp (at the device). At the 3 mBar applied pressure used in the measurement described in Figure 5 and Figure 6. This was not sufficient to displace the 0.25 µm microspheres. However, by decreasing the flow rate we can increase the relative strength of the DEP force. At 2 mBar applied pressure 0.25 µm microspheres became displaced, Figure 7. There are however limits on how slow we can flow the particles since, especially for small particle, diffusion becomes a problem as it works against separation. We believe that with a suitable amplifier, we can achieve up to 20 Vpp in our device and push the critical size down to 100nm or below.

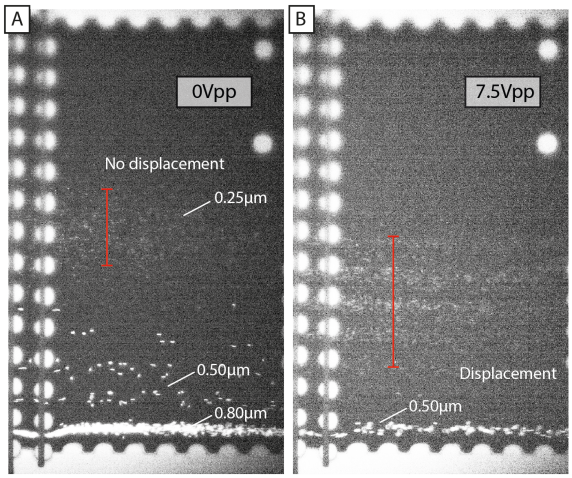

Figure 7. At 2 mBar applied pressure, 7.5 Vpp @10MHz it is possible to displace 0.25 µm particles for gaps between posts being ~12 µm. The red bars indicate the lateral distributions of the 0.25 µm beads for the two different voltages in (A) and (B).

The dynamic range of a DLD device can be defined as the ratio of the largest to smallest critical diameters that can be achieved[10]. Increasing this range is often done using so-called chirped arrays; multiple DLD array in sequence. However, as Davis discusses in his thesis [7], the maximum particle size that can be handled is limited to the smallest gap size in the device, which ultimately limits dynamic range to between 3 and 5. Cascaded devices have channels that remove large particles between the cascaded arrays and in these dynamic ranges of 20 can be achieved, but at the cost of increased complexity of both design and performing separations.

Because our device has only one critical size (D_C = 5.15 µm) it has a dynamic range of one, when not using the active post capabilities. However, since we are able to displace 0.25 µm particles in our device by applying electric fields, we have increased the

dynamic range to ~20. By combining our active post approach with the chirped and cascaded device approach we believe we could achieve dynamic ranges of ~100.

Finally, to demonstrate the manipulation of long polyelectrolytes, we used the device to trap DNA. By tuning the frequency, we could either trap the DNA onto the electrodes or through a dynamic process in between the posts, Figure 8.

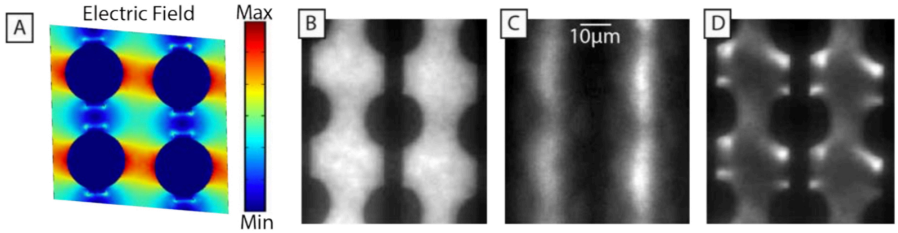

Figure 8. Trapping DNA in an electric field. (A) Finite Element simulation (COMSOL) showing the electric field between posts (in a plane close to the connecting electrodes) with 1 V_{RMS} applied across the electrodes. (B-D) lambda-phage DNA stained with YOYO1 (5:1 ratio) in 0.5x TBE buffer under different applied fields. In all cases the applied pressure is zero. (B) At 0 V the DNA is distributed homogeneously (C) At 4 V pp @ 1 Hz the DNA becomes concentrated between the rows of posts. The image shows a snapshot (0.1s exposure time). The distributions oscillate, shifting toward the positive electrode several micrometers during each cycle (D) 4 V pp @ 10 Hz. Here the DNA is trapped on the electrodes and no oscillations are observed.

Conclusion

We have successfully demonstrated proof of principle of a DLD device combined with electrodes directly integrated onto the posts. The short interelectrode distances allow us to reach high electric field strengths at high frequencies with small enough voltages to ensure simple and safe operation.

We have shown that we can change the critical size in our device from 5.15 µm to 250 nm, a decrease by a factor 20, which constitutes an increase in dynamic range by the same factor. We predict that at higher applied voltages we will be able to decrease the critical size further towards the 100 nm range. Switching times in our device depend on flow rates, but at the conditions presented here, they are in the range of several seconds. This means that we can immediately visualize the response to a change in voltage and tune separations in real time. At high flow rate/applied voltages the switching times will be shorter. To summarize, we change what is essentially a bimodal separation technique into a tunable multimodal separation tool.

Finally, we demonstrate the retention of DNA between the posts by applying an AC voltage between the electrodes on the posts. This allows us to trap DNA, for example for applications of DNA extraction and purification that are important for genomics studies.

Acknowledgements

The parts of this work carried out at NanoLund were supported by the BeyondSeq consortium (EU Horizon2020 project 634890), the evFOUNDRY consortium (EU Horizon2020 project 801367) and the Swedish Research Council (grant no. 2016-05739) and those carried out at EPFL by the Swiss National Science Foundation (205321_179086). We are thankful for support from the Center for Nano- and Microtechnology at EPFL where we fabricated the chips.

References

1. Huang, L.R., E.C. Cox, R.H. Austin, and J.C. Sturm, *Continuous Particle Separation Through Deterministic Lateral Displacement.* Science, 2004. **304**(5673): p. 987-990.
2. Beech, J.P. and J.O. Tegenfeldt, *Tuneable separation in elastomeric microfluidics devices.* Lab on a Chip, 2008. **8**(5): p. 657-659.
3. Zeming, K.K., N.V. Thakor, Y. Zhang, and C.H. Chen, *Real-time modulated nanoparticle separation with an ultra-large dynamic range.* Lab on a Chip, 2016. **16**(1): p. 75-85.
4. Zeming, K.K., T. Salafi, S. Shikha, and Y. Zhang, *Fluorescent label-free quantitative detection of nano-sized bioparticles using a pillar array.* Nature Communications, 2018. **9**(1): p. 1254.
5. Beech, J.P., P. Jonsson, and J.O. Tegenfeldt, *Tipping the balance of deterministic lateral displacement devices using dielectrophoresis.* Lab on a Chip, 2009. **9**(18): p. 2698-2706.
6. Chou, C.F., J.O. Tegenfeldt, O. Bakajin, S.S. Chan, E.C. Cox, N. Darnton, T. Duke, and R.H. Austin, *Electrodeless dielectrophoresis of single- and double-stranded DNA.* Biophysical Journal, 2002. **83**(4): p. 2170-2179.
7. Davis, J.A., *Microfluidic separation of blood components through deterministic lateral displacement*, PhD thesis, 2008, Princeton University
8. Pethig, R.R., *Dielectrophoresis: Theory, Methodology and Biological Applications, First Edition*. 2017: Wiley. 448.
9. Wang, L.S., L. Flanagan, and A.P. Lee, *Side-wall vertical electrodes for lateral field microfluidic applications.* Journal of Microelectromechanical Systems, 2007. **16**(2): p. 454-461.
10. Davis, J.A., D.W. Inglis, K.J. Morton, D.A. Lawrence, L.R. Huang, S.Y. Chou, J.C. Sturm, and R.H. Austin, *Deterministic hydrodynamics: Taking blood apart.* Proceedings of the National Academy of Sciences of the United States of America, 2006. **103**(40): p. 14779-14784.

Active Posts in Deterministic Lateral Displacement Devices – Electronic Supplementary Information

Jason P. Beech[1], Kevin Keim[2], Bao Dang Ho[1], Carlotta Guiducci[2], Jonas O. Tegenfeldt[1]

1. *Division of Solid State Physics and NanoLund, Lund University, Sweden.*
2. *Laboratory of Life Sciences Electronics, École Polytechnique Fédérale de Lausanne, Switzerland.*

1. Device Fabrication

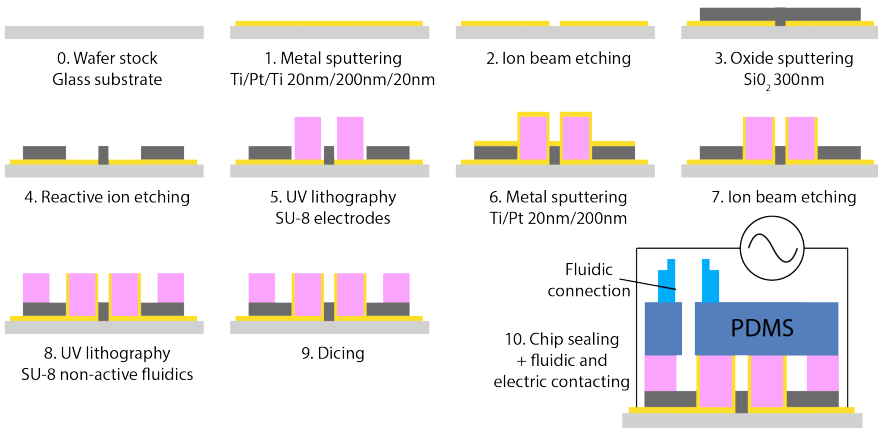

Figure 1. The process flow for the fabrication of devices containing metal-coated, three-dimensional electrode structures with insulated connection lines. These three-dimensional electrodes constitute the pillars that make up a DLD separation array.

2. Device Layout

The device is designed with the layout and dimensions shown in Figure 2. Using the fabrication method described above both the active electrode structures inside the DLD array (defined in step 5 in Figure 1) and the non-active features, such as the three inlets for particle focusing and the outlet for collection and counting of particles (defined in step 8 in Figure 1) are achieved. While the device was designed to have a D_c of 4.6µm (based on G=10µm and N=10, see section 3 below) the dimensions of the actual devices differed slightly from the designed parameters giving a somewhat larger D_c. Figure 2 D and E show how we determined the actual dimensions of our final devices.

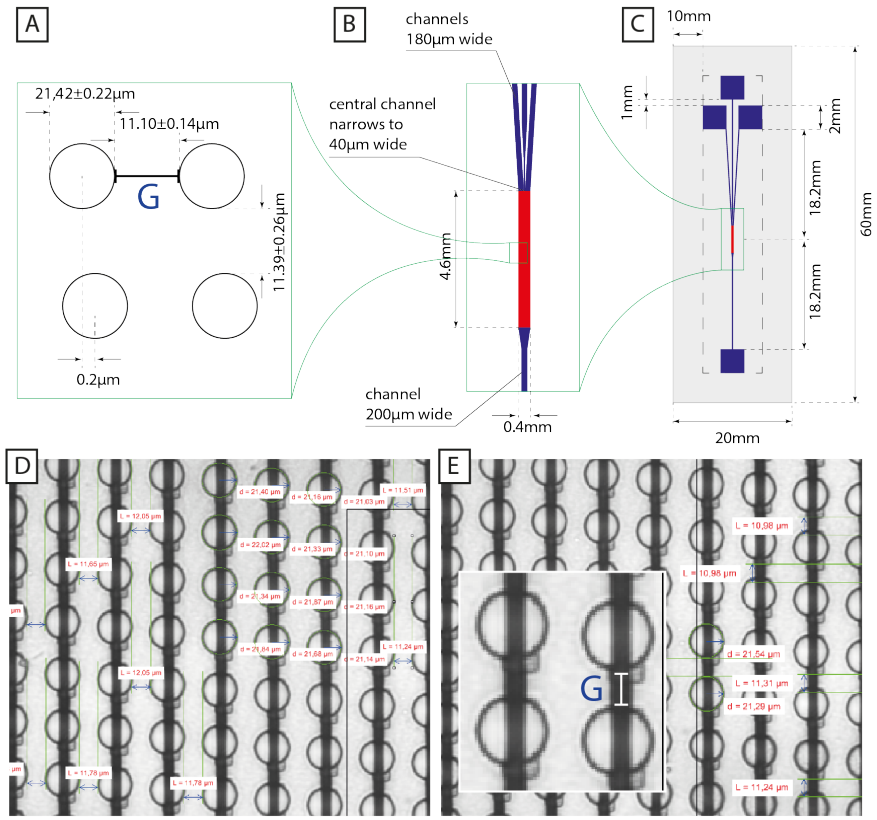

Figure 2. Designed and measured device and DLD array dimensions. A) Measured dimensions of fabricated DLD arrays. B) Dimensions of DLD array, inlet and outlet channels. C) Dimensions of the final, diced device with the inlet and outlet reservoir-connection areas shown. D) and E) Measurements are performed using NIS elements, 20x objective (NA 0.5, 2.0 mm WD).

3. Critical Size

The critical particle diameter D_c in a DLD array with gap G and period N can be calculated using the empirical formula[1]:

$$D_c = 1.4 \cdot G \cdot N^{-0.48}$$

As shown in Figure 2, the measured gap in our device, $G = 11.10 \pm 0.14$µm. With the period designed to be $N = 10$, the critical particle diameter $D_c = 5.15 \pm 0.06$.

4. Simulations

The electric field inside our device was simulated using COMSOL Multiphysics 5.2. A subset of the device with an array of 6x6 posts was generated in 3D with the same geometry (measured) as that of our final device. The simulation included the buried contacts. This was considered sufficient to generate a good picture of the electric field

around the posts without recourse to the considerable computational resources required to simulate the entire device.

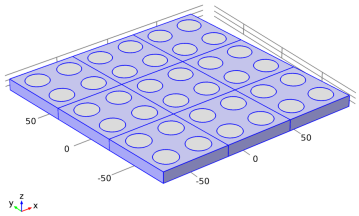

(A) Water

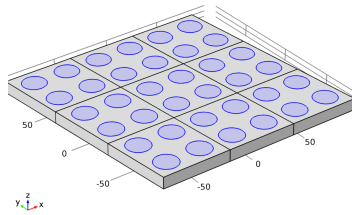

(B) PDMS

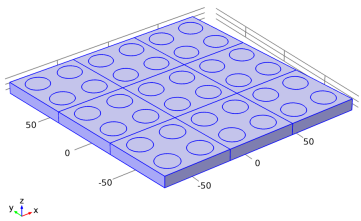

(C) Electrodes

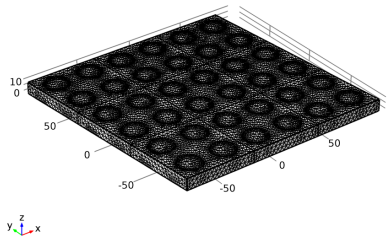

(D) Mesh

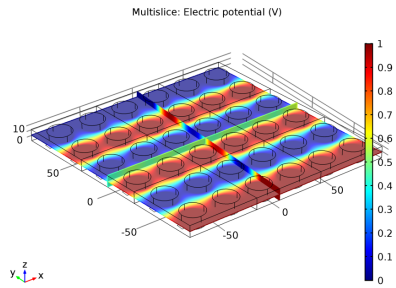

(E) Electric Potential

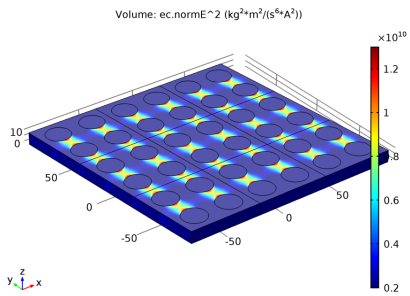

(F) Electric Field Squared

Figure 3. Simulation of electric field inside our device. Length units are µm.

The electric field in our device was simulated using the current conservation equations:

$$\nabla \cdot \mathbf{J} = Q_j$$

$$\mathbf{J} = \sigma \mathbf{E} + \mathbf{J}_e$$

$$\mathbf{E} = -\nabla V$$

The boundary condition for an insulating surface at the PDMS interface was:

$$\mathbf{n} \cdot \mathbf{J} = 0$$

The electric potential at the electrode are 0 V and 1 V.

5. Particle counting and Analysis

In order to establish the trajectories of particles (and determine the performance of the separations) the position of every particle was determined as they left the separation array in the device. The device was designed with 14 parallel channels in which to perform this measurement, see Figure 4. The measurement itself was performed by manual inspection of recorded movies. For each experimental condition (1 voltage, 1 frequency and 1 microparticle size) several hundred events were measured.

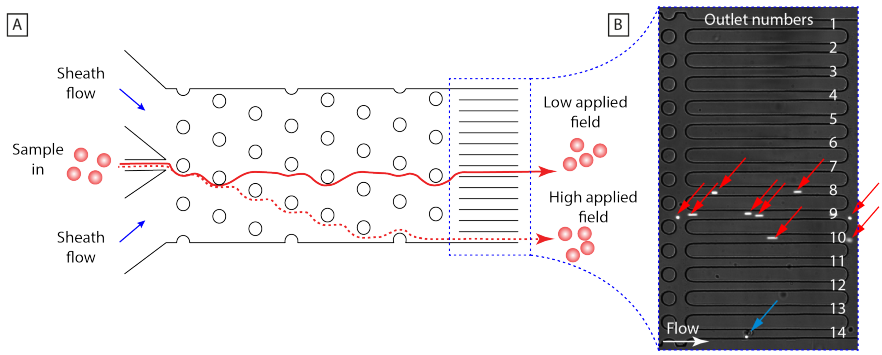

Figure 4. The device has 14 outlet channels where the particles are counted. Outlet #8 corresponds to no displacement in the DLD device. Outlet #14 corresponds to maximum displacement.

6. Frequency response

We measured the outlet distributions as a function of applied voltage for 4.3 µm, 2.9 µm and 2.1 µm polystyrene microspheres at frequencies between 1 Hz and 10^7 Hz. There are several results that are worth pointing out. The transitions between non-displacement and displacement modes are most well defined at 10^6 and 10^7. We chose therefore to study smaller microspheres at 10^7 Hz (see results in the main article). At 1 Hz and 10Hz there is no change in trajectories. At 100 Hz and 1000 Hz and 3 Vpp to 4 Vpp applied voltage, particles become trapped. Figure 6 shows particles 2.9 µm particles trapped at high-field regions implying positive DEP. There is a tendency for particle to be displaced in the "wrong" direction at lower frequencies. This is most apparent for the 2.9 µm microspheres here. We believe that this "negative" displacement is due to positive dielectrophoresis and that the trapping that occurs at 1000 Hz is occurring just prior to the crossover between positive and negative electrophoresis (as frequency is increased) although further studies are required to fully understand the true mechanisms at play.

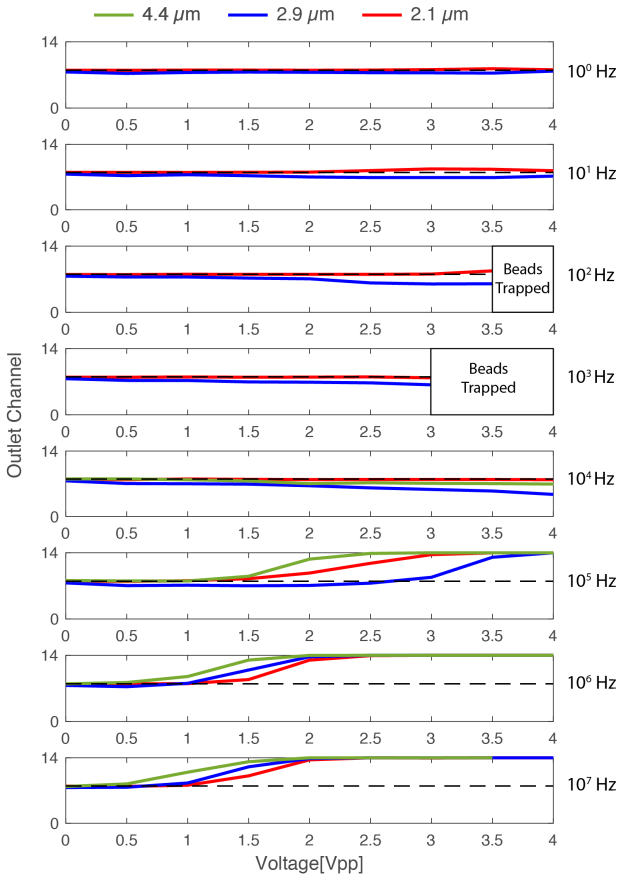

Figure 5. The outlet positions as a function of applied voltage for three beads sizes at frequencies ranging from 1 Hz to 10 MHz.

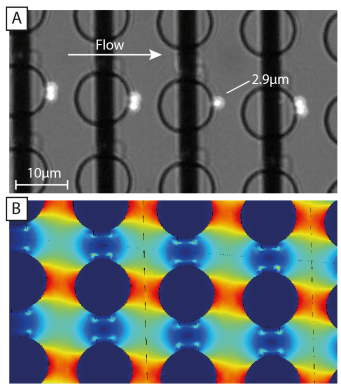

Figure 6. 2.9 μm microspheres become trapped at high-field regions at 1000 Hz and 4 Vpp applied voltage.

7. Switching time

In order to determine the results of a separation as parameters are tuned, short response times are preferable. Figure 7 shows the time evolution of particle distributions at the outlet of the device after the applied voltage is switched from 0 Vpp to 7.5 Vpp at time t = 0. The separation is fully developed after 4 s.

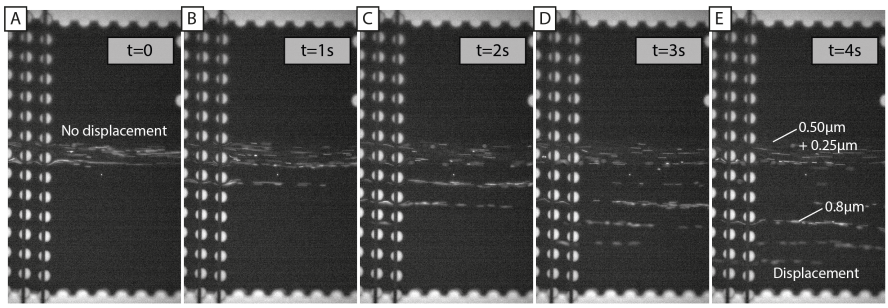

Figure 7. At t = 0 the 7.5 Vpp @ 10 MHz is applied. The response is immediate and the separation fully developed at 4 s. Measurement performed at 10 mBar where the displacement is less than that shown in previous results (3 mBar).

8. Videos

A selection of videos of the results are available at http://bit.ly/MetalDLDVideos

The following first four movies show tunable sorting (figure 5 is taken from here). The applied pressure is 3 mBar, frequency is 10 Mhz. The 250 nm and 500 nm microspheres are green and the 800 nm microspheres are red. Movies are played back at half speed. The first four movies with the respective applied voltages:

active posts ESI movie1: 0 Vpp
active posts ESI movie2: 3.5 Vpp
active posts ESI movie3: 5.25 Vpp
active posts ESI movie4: 7 Vpp

The fifth movie shows switching. The applied pressure is 10mBar, frequency is 10Mhz. 250 nm and 500 nm and 800 nm microspheres are all visible at the beginning of the movie. Movie is played back at actual speed. The applied voltage in the beginning of the movie is 0 Vpp and is switched to 7 Vpp at 1 s. At 15 s the excitation light is switched so that the 800 nm microspheres only are visible. Then at 16 s switched again so that the 250 nm and the 500 nm microspheres only are visible.

active posts ESI movie5: 0 Vpp – 7 Vpp

1. Davis, J.A., *Microfluidic separation of blood components through deterministic lateral displacement*, PhD thesis, 2008, Princeton University

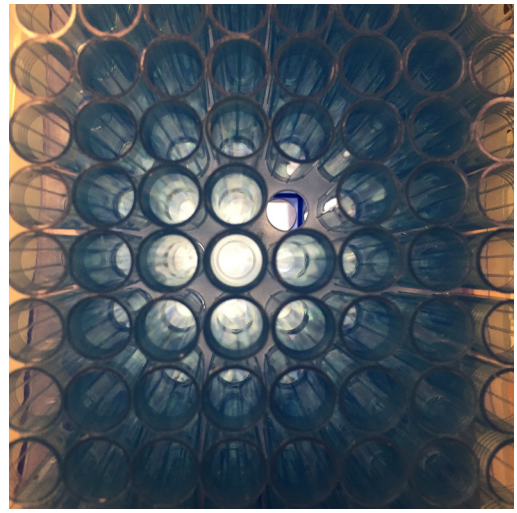

Printed by Media-Tryck, Lund 2018 NORDIC SWAN ECOLABEL 3041 0903

LUND UNIVERSITY

Lund University
Faculty of Engineering
Department of Physics

ISBN 978-91-7753-888-2